Electric Field Assisted Sintering of Gadolinium-doped Ceria

Tarini Prasad Mishra

JÜLICH
Forschungszentrum

Electric Field Assisted Sintering of Gadolinium-doped Ceria

Tarini Prasad Mishra

Abstract

10 mol% Gadolinium-doped ceria (GDC10) is a highly technological relevant material with potential application in electrochemical cells, oxygen transport membranes as a catalyst and other. However, one major drawback associated is that the processing of GDC10 requires high sintering temperatures (1300°C-1600°C) with dwelling time of several hours to achieve high relative density (>96%). Therefore, to improve the sintering behaviour of GDC ceramics, carefully study of the sintering conditions and optimization of sintering parameters are required.

The objective of this dissertation work is to understand the influence of electric field and current on the densification behaviour and microstructure evolution of GDC10. Furthermore, optimization of the sintering parameters for GDC10 powders and tailoring the microstructure by controlling the material synthesis and processing conditions were investigated.

In the beginning of the dissertation work, densification behaviour of GDC10 in conventional free sintering was systematically studied. Conventional free sintering of GDC10 in reducing atmosphere shows an enhanced densification, where the sintering temperature was lowered by approximately 200°C. However, the microstructure of the conventional free sintered samples under reducing atmosphere show a high concentration of micro-cracks. Controlled re-oxidation of the samples at high temperature (800°C), which were sintered in reducing atmosphere is beneficial in avoiding micro-cracks in the sample.

As next step, Field Assisted Sintering Technique/Spark Plasma Sintering (FAST/SPS) of GDC10 was investigated with a conventional tool configuration resulting in fragmentation of samples into several pieces due to severe reduction of GDC and related chemical expansion. An alternative tool configuration (without sample loading) was applied to eliminate the interaction between sample and graphite tool, which results in a stable and macroscopically crack free sample. The samples sintered in the specific tool configuration under vacuum or in reducing atmosphere were dense and visually homogeneous. However, still large number of micro-cracks was observed. The number and the size of micro-cracks were drastically reduced when the additional re-oxidation at elevated temperature (800°C) was used.

Finally a fundamental study on flash sintering study of GDC10 was carried out to understand the influence of different processing parameters involved in the flash experiment on the densification and grain growth behavior. Detailed investigation of the onset behavior of flash revealed Debye temperature to be the lower bound temperature for the onset of flash.

Furthermore, the emergence of electronic conductivity in the GDC10 material due to the application of DC field was found to be the trigger for the onset of flash. However, the microstructure of the flash sintered sample in voltage-to-current mode resulted in non-uniform microstructure along the gauge section of the sample.

Current rate (CR) flash sintering mode, where the power supply remain entirely under current control mode and the current is increased at a constant rate allows to control the densification rate and the degree of densification in flash sintering. CR flash sintering of GDC10 investigated by altering the current rate allows to tune the grain size of the sample, where slower current rate resulted in coarser grain size. The microstructure of the CR flash sintered sample showed a uniform microstructure along the gauge section of the sample.

In-situ X-ray diffraction experiments during the flash sintering of GDC10 were performed at the synchrotron facility in Brookhaven National Laboratory (BNL). The specimen temperature near each electrode (anode and cathode) for both voltage-to-current and current rate flash sintering experiments were measured in situ. The measured temperature found to be in a good agreement with the estimated sample temperature by a black body radiation (BBR) model.

Kurzfassung

10 mol% Gadolinium-dotiertes Ceroxid (GDC10) ist ein Werkstoff von hoher technologischer Relevanz für eine potentielle Anwendung in elektrochemischen Zellen, Sauerstofftransportmembranen und Katalysatoren. Ein wesentlicher Nachteil ist jedoch, dass die Verarbeitung von GDC10 hohe Sintertemperaturen (1300°C-1600°C) mit Verweilzeiten von mehreren Stunden erfordert, um eine hohe relative Dichte (>96%) zu erreichen. Um das Sinterverhalten von GDC-Keramiken zu verbessern, ist eine grundlegende Untersuchung des Sinterverhaltens und eine Optimierung der Sinterparameter erforderlich.

Das Ziel dieser Doktorarbeit ist es, den Einfluss von elektrischem Feld und Stromfluss auf das Verdichtungsverhalten und die Gefügeentwicklung von GDC10 zu verstehen. Darüber hinaus sollen die Sinterparameter für GDC10 optimiert und die Mikrostruktur durch Steuerung der Werkstoffsynthese und der Verarbeitungsbedingungen maßgeschneidert werden.

Im ersten Teil der Dissertation wurde das Verdichtungsverhalten von GDC10 beim konventionellen freien Sintern systematisch untersucht. Hierbei zeigte sich in reduzierender Atmosphäre ein verbessertes Verdichtungsverhalten, wobei die Sintertemperatur um ca. 200°C gesenkt werden konnte. Die Mikrostruktur der konventionell gesinterten Proben in reduzierender Atmosphäre zeigte jedoch eine hohe Konzentration von Mikrorissen. Eine kontrollierte Re-Oxidation der Proben bei erhöhten Temperaturen (800°C), die zuvor in reduzierender Atmosphäre gesintert wurden, erwies sich als vorteilhaft zur Vermeidung von Mikrorissen in der Probe.

Nachfolgend wurde das feldunterstütztes Sintern / Funkenplasmasintern (FAST/SPS) von GDC10 mit einem konventionellen Werkzeugaufbau untersucht. Dieser führte zu einer starken Fragmentierung der Proben aufgrund der Reduktion und der damit verbundenen chemischen Ausdehnung von GDC10 während des Sintervorgangs. Eine alternative Werkzeugkonfiguration (ohne externe Last) wurde entwickelt, um die Wechselwirkung zwischen Probe und Graphitwerkzeug zu verringern, was zu einer stabilen und makroskopisch rissfreien Probe führte, Die Proben, welche in der drucklosen Werkzeugkonfiguration unter Vakuum oder in reduzierender Atmosphäre gesintert wurden, waren dicht und visuell homogen. Eine Untersuchung der Mikrostruktur zeigte trotz verbesserter Stabilität eine große Anzahl von Mikrorissen. Die Anzahl und die Größe der Mikrorisse wurden durch eine zusätzliche Re-Oxidation deutlich reduziert.

Des Weiteren wurde ein Flash-Sinterstudie an GDC10 durchgeführt, um den Einfluss charakteristischer Versuchsparameter des Flash-Experiments auf das Verdichtungs- und Kornwachstumsverhalten zu verstehen. Eine grundlegende Studie, welche das Einsetzen des Flash Effekts untersuchte, zeigte dass die Debye-Temperatur die untere Grenztemperatur für diesen Effekt ist. Darüber hinaus wurde festgestellt, dass die zunehmende elektronische Leitfähigkeit innerhalb der GDC10 Probe bei Anlegen des elektrischen Felds der Auslöser für das Einsetzen des Flash-Sinterns ist. Die Mikrostruktur der durch Flash-Sintern verdichteten Proben im in zuerst Spannungs-, dann Storm kontrollier Modus führte jedoch zu einer inhomogenen Mikrostruktur entlang der Probenlänge.

Die Kontrolle des Flash Sinterns über die Stormrate (CR-Flash Sintern), bei dem die Stromregelung wahrend des gesamten Experiments erhalten bleibt und der Strom mit einer konstanten Rate erhöht wird, ermöglicht die gezielte Einstellung der Verdichtungsrate und des Verdichtungsgrades beim Flash-Sintern. Darüber hinaus zeigte das CR-Flash-Sintern von GDC10, dass es durch Änderung der Stromrate möglich ist, die Korngröße der Probe einzustellen, wobei eine geringere Rate zu einer gröberen Korngröße führte. Das Mikrogefüge der CR-Flash-Sinterprobe zeigte hierbei eine homogene Mikrostruktur entlang der Probenlänge.

Abschließend wurden in-situ-Röntgenbeugungsexperimente während des Flash-Sinterns von GDC10 am Synchrotron des Brookhaven National Laboratory (BNL) durchgeführt. Hierbei wurde die Probentemperatur in der Nähe der Elektroden (Anode und Kathode) sowohl für Spannungs-/Strom- als auch für CR-Flashsinterexperimente in situ gemessen. Es zeigte sich, dass die gemessene Temperatur in guter Übereinstimmung mit der errechneten Probentemperatur ist, nach dem Modell der schwarzem Körperstrahlung bestimmt wurde.

Contents

Abbreviations

AC   Alternating Current

BNL   Brookhaven National Laboratory

CHR   Constant Heating Rate

CR   Current Rate

CTE   Coefficient of Thermal Expansion

DC   Direct Current

DTA   Differential Thermal Analysis

ECAS   Electric Current Activated/Assisted Sintering

FAST/SPS   Field Assisted Sintering Technology/Spark Plasma Sintering

FCC   Face Centered Cubic

FS   Flash Sintering

GDC   Gadolinium-doped Ceria

GDC10   10 mol% Gadolinium-doped Ceria

HIP   Hot Isostatic Pressing

HP   Hot Press

MIEC   Mixed Ionic and Electronic Conductivity

Mol%   Molecular Percentage

MSCs   Metal Supported Fuel Cells

$P(O_2)$ Partial Pressure of Oxygen

PECS   Pulsed Electric Current Sintering

SEM   Scanning Electron Microscopy

SOEC   Solid Oxide Electrolyze Cell

SOFC   Solid Oxide Fuel Cell

TEM	Transmission Electron Microscopy
TG	Thermo-Gravimetry
TZM	Titanium-Zirconium-Molybdenum Alloy
XRD	X-ray Diffraction
YSZ	Yttria Stabilized Zirconia

Chapter 1 Introduction

1.1. Statement of Problem and Motivation

Energy is essential for economic and social development and improved quality of the human life. Today, human life critically depends on supply of energy to cover all the essential needs. The U.S. Energy Information Administration's International Energy Outlook 2019 (IEO2019) projected that the world energy consumption will grow by nearly 50% by 2050, rising from approximately 525 quadrillion Btu in 2010 to nearly 900 quadrillion Btu (3412.14 BTU = 1 kWh) in 2050 [1].
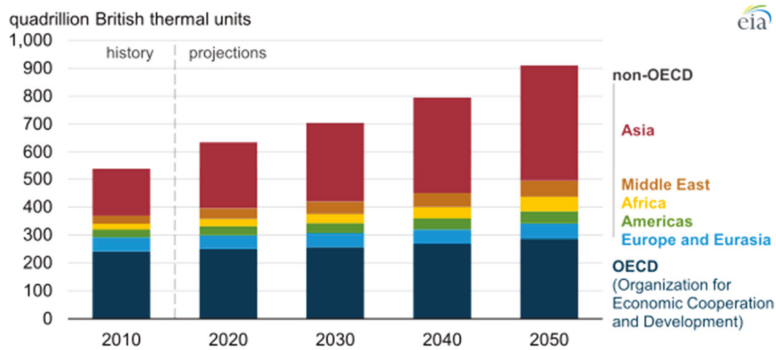
Figure 1-1 : Global primary energy consumption by region between 2010 and 2050 [1]

The higher energy demand is largely met with the fossil fuel reserves that are also responsible for emissions of greenhouse gases (GHGs). Since Climate change and global warming are fundamentally associated with energy consumption and greenhouse emissions, a sustainable and efficient energy supply that is largely CO_2 neutral is necessary way forward to environmental problems that we face today. Among various renewable energy generation technologies, fuel cells are a promising technology that depends on converting an electrochemical energy to generate electricity and heat [2–4]. The operating principle of fuel cells is based on the electrochemical combination of a gaseous fuel (e.g. hydrogen) and an oxidant gas (e.g. oxygen from air) to generate electricity. Unlike batteries, fuel cells do not required electrical recharging, they continue to generate power as long as the fuel supply continues [3]. Nevertheless, for high efficiency operations and successful commercialization of such new technologies, selection of suitable materials plays a vital role.

Materials are the backbone of the current technological advanced society. In the industrial product design, the relationship between material properties and its application promote each other [5]. Cerium oxide or ceria (CeO2) with high abundance, is one of the most technological relevant material due to its wide applications in oxygen gas sensors, catalysis, oxygen permeable membrane and electrochemical devices [6–11]. Fully oxidized, stoichiometric ceria (CeO2), has the crystal structure of fluorite AO2, where A = Ce4+. Cerium (Ce) belongs to the lanthanide group and possesses 4f electrons, and this property is responsible for its powerful redox behaviour when cycling between the smaller atomic radius Ce^{4+} ion and the larger atomic radius Ce^{3+}. When combined with oxygen, it forms a series of nonstoichiometric $CeO_{2-\delta}$ compositions (with $0 < \delta < 0.5$) characterized by adopting the face-centered cubic (fcc) fluorite lattice. Where a 50% of the total Ce^{3+} population in Ceria ($Ce_2O_{1.5}$) would result in 100% reduced Ceria (Ce_2O_3) [12]. A fully oxidized, stoichiometric ceria (CeO2) is the upper limiting composition; it consists of a cubic closed-packed array of metal atoms with all tetrahedral holes filled by oxygen atoms. The ejection of oxygen from the fluorite lattice is fully reversible, and it give the material its fascinating and unique properties in the broad field of applications [11]. Due to its strong redox behavior, ceria based materials possess mixed ionic and electronic conductivity (MIEC), where the MIEC properties of ceria-based materials can be tuneable by A-site doping of ceria with rare earth elements [11] or reduction of the material system by low partial pressure of oxygen P(O_2) [13].

Amongst the various ceria-based material systems, gadolinium-doped ceria (GDC) is an attractive material that has one of the highest ionic conductivity among all ceria based oxides [11]. In GDC, the substitution of Ce^{4+} ion by trivalent Gd^{3+} dopant causes the formation of oxygen vacancies to maintain electro-neutrality as denoted by Kröger-Vink notation in equation (1.1) and illustrated in Fig. 2.

$$Gd_2O_3 \xrightarrow{CeO_2} 2Gd'_{Ce} + 3_O^x + V_O^{\cdot\cdot} \qquad\qquad\qquad \text{eq. (1.1)}$$
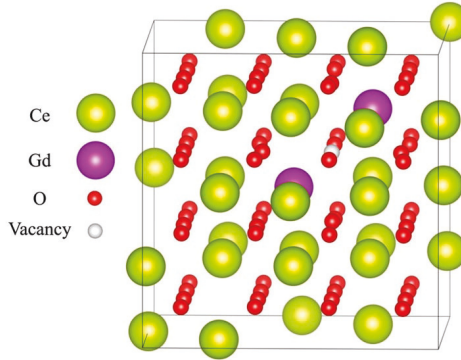
Figure 1-2 : The lowest-energy GDC configuration with one vacancy and two Gd cations, adapted from Asher et. al. [14]

Due to their good chemical stability, high ionic conductivity below 600°C and good catalytic activities in redox processes, GDC is one of the most technological relevance ceria-based material that has huge potential to be used in different applications as mentioned before [12,15–19]. However, one major drawback is in the case of conventional processing of GDC is the need of high sintering temperatures (1300°C-1600°C) with dwelling time of several hours in air to achieve very high density (>96%) [12,20]. Sintering is a high temperature process below the melting temperature of the material, based on diffusion. Lowering the sintering temperature for producing GDC could be beneficial for lowering the energy consumption and avoiding possible reaction with other materials during co-firing, (e.g. for manufacturing of solid oxide fuel or electrolysis cells). A minimal reduction of the sintering temperature can be achieved by optimization of the processing conditions like reduction of particle size [21,22], application of sintering aids [23] or increase of the density of the powder compact in the non-sintered state. Recently, studies show that conventional sintering temperature for GDC can be lowered to about 200 °C by densifying the material under reducing atmosphere [12,20]. The enhanced in densification of the GDC was explained as a result of creation of the oxygen vacancy ($V_O^{\cdot\cdot}$) and electronic defects (Gd'_{Ce}) in the material under reducing atmosphere. But even if sintering was done at temperatures around 1100°C, a controlled re-oxidation of the samples at high temperatures in the range between 800°C and 1100°C was mandatory to avoid cracking of the samples reliably [20].

Recent advancement in the sintering technology involves electric field/current assisted densification. Electric current activated/assisted sintering (ECAS) techniques are promising for

processing of high performance ceramic materials due to significant improvement of sintering kinetics [24,25]. ECAS technologies like field assisted sintering technology/spark plasma sintering (FAST/SPS) [26] or flash sintering [27,28] enable to reduce furnace temperature and dwell time making them highly promising regarding energy efficiency compared to conventional sintering technologies. Furthermore, the possibility of tuning of microstructures down to the nanoscale is attractive with respect to improving the materials performance. A detailed description of each process is provided in the following chapter.

Electric field assisted sintering techniques like, FAST/SPS is defined as a low voltage, direct current (DC) pulsed-activated pressure-assisted sintering technique [29]. The sample (if conductive) is heated internally by the joule heating as the current is directly pass through the sample and the tools (typically made of graphite), on the contrary for the non-conductive samples, the current is passed through the tools and the heat is transferred to the sample from the tool. This makes possible achieving high heating rates up to 1000 °C/min. However, densification of GDC by FAST/SPS is rarely reported in the literature. A non-uniform reduction of ceria pellet was reported during the sintering of ceria by FAST/SPS technique. A successful sintering of ceria by FAST/SPS was only achieved by using an alumina encapsulation between the tool and pellet [30].

Flash sintering (FS) is a novel field/current-assisted sintering techniques for rapidly densifying ceramics at low furnace temperatures [31–35]. It is usually described by three stages. First, a constant electric field is applied to the green body while it is heated inside a furnace (Stage I). Then, the flash event is signaled by a non-linear rise in the sample conductivity at a critical furnace temperature (Stage II). Here, the electric power source switches from voltage to current control and the sample densifies in a few seconds while emitting a bright glow. This switch from voltage-to-current control is required to avoid melting of sample as consequences of the electric conductivity of the ceramic. Flash sintering of GDC to nearly full density at furnace temperature between 500 – 700 °C has been reported in the literature [36–38]. Nevertheless, these studies mostly focused on the densification process of GDC. An important insight was presented by Jha et al. [39], who measured abnormal lattice expansion by in-situ X-ray diffraction during FS. However, a comprehensive densification and microstructure evolution study of GDC during FS is still missing.

1.2. Objectives and Scientific Approach

The focus of this dissertation is to study the densification behavior and microstructural evolution of 10 mol% Gadolinium-doped Ceria (GDC10) by applying ECAS technologies, with the goal of tailoring the grain size.

Densification of GDC10 by conventional technique in air required high temperature and longer dwelling time [12]. The required sintering temperature for GDC10 may be lowered by using low oxygen partial pressure $P(O_2)$ atmosphere. However, densification of GDC10 under low $P(O_2)$ required controlled re-oxidation at high temperature to avoid micro-cracks in the microstructure of the sintered samples [20]. In this context, lowering the sintering temperature of GDC10 by electric ECAS techniques is significant. Additionally, GDC10 due to its strong redox properties, which results in intrinsic defects in the lattice give additional complexities during different sintering routes. While in conventional sintering route, very high temperature can influence the defect chemistry in the material, electric field/current can also influence the defect chemistry of the GDC10. In FAST/SPS, direct contact of the sample with the graphite tools may act as an oxygen getter which may reduce the sample during the densification process. The reduction of the sample coupled with the volume expansion inside the FAST/SPS tool could have a catastrophic effect on the mechanical integrity of the pellet. Densification of GDC10 by flash sintering, which is a highly dynamic process, results in rapid densification of the material. However, utilizing this novel processing technique commercially with a controlled densification and tunable microstructure is still an open question. Furthermore, the application of a high electric field could result in generation and redistribution of the point defects leading to a non-uniform microstructure near different section of the sample depending on the electrical polarity of the electrodes. This effect may have a pronounced effect on the microstructure of highly active materials like GDC10.

In this work, a systematic investigation of densification behavior of GDC10 was carried out. Primarily two different electric field assisted sintering techniques was used, (i) FAST/SPS, which is a low electric field and high current technique and (ii) Flash sintering, which is characterized by a moderate to high electric field and low current. The densification behavior, microstructure evaluation and grain growth behavior were compared with the conventional sintering of GDC10.

The sintering behavior of the materials is greatly influenced by physical properties of the starting powder particles. Therefore, in the beginning of the dissertation, benchmarking of the

starting powders was conducted. Four different commercially available GDC10 powders were investigated to identify the optimum starting powder that shows best densification behavior by conventional sintering technique. Effect of sintering atmospheres (with respect to the partial pressure of oxygen) on the densification behavior and the sintering temperature of GDC10 was investigated. Fundamental studies on the influence of low partial pressure of oxygen $P(O_2)$ on formation of oxygen vacancies was investigated by Differential Thermal Analysis (DTA) / Thermogravimetric Analysis (TGA). Furthermore, the associated chemical expansion due to the formation of oxygen vacancies was estimated by High-Temperature X-Ray Diffraction.

Later, sintering of GDC10 by FAST/SPS technique was investigated. Influence of the sintering atmospheres on the densification behavior of GDC10 in FAST/SPS was studied by operating FAST/SPS device under different atmospheres. As part of this work topic, a special tool set-up was designed to allow the FAST/SPS chamber atmosphere to reach the sample.

Last but not the least, a detailed investigation of the densification, microstructure and grain growth of GDC10 by flash sintering was carried out. The flash sintering study of GDC10 began by understanding the influence of electric field and current density on the onset of flash and final density of the flashed specimens. A processing map for safe flash sintering of GDC10 was developed. During flash sintering the densification occurred very rapidly, where the control of densification and grain growth is a major challenge for its successful commercialization. As a step beyond, flash sintering was carried out by an alternating method, known as Current Rate (CR) flash sintering, a detailed description of the process is discussed in chapter 4. It was shown for the first time that, the grain size and densification of GDC10 could be tailored by controlling the rate of current density. To understand the mechanism of flash sintering, in-situ flash sintering of GDC10 were performed at the synchrotron facility at the Brookhaven National Laboratory.

1.3. Organization of Dissertation

Chapter 2 gives a general introduction to the sintering theory based on two particle model system. A summary of the current knowledge of different sintering techniques with there working principle, and mechanisms is discussed. Chapter 3 details the experimental procedures used in this work, including the materials, equipment, as well as different characterization techniques. Chapter 4 comprise the results and their discussions. Finally, conclusions and outlook of the work will be given in Chapter 5.

Chapter 2 Theoretical Background of Sintering

Sintering is a fabrication method which utilizes thermal energy to consolidate loose powders into a bulk solid. Sintering has been applied to oxides for 26000 years, which started with clay and pottery [40]. In this process, the consolidation of loose particles occurred due to the thermodynamic nature of the particle system to decrease its total surface and interfacial energy [41,42]. Sintering of ceramics is primarily a solid-state process. However, sintering process can be classified as liquid-phase sintering and viscous flow sintering [41]. In this work, sintering studies are carried out entirely in solid-state therefore, in the following text sintering always referred to as solid-state sintering.

This chapter introduces the theory of sintering and different sintering mechanisms, with a simple two particle model in conventional free sintering case. Sintering is primarily a solid-state diffusion process by which the matters are being transported to the pores. The different diffusion paths, which explained the sintering mechanism will be discussed in this chapter. Sintering process is still evolving to satisfy the 21st century mankind needs, which demand high performance sintered parts to meet new property requirements. Sintering technologies that are predominantly depends only on thermal energy, currently advances by utilizing pressure, electric and magnetic field and laser technology to enhance the densification rate. In the end of this chapter, ECAS techniques used in this dissertation are introduced to give the reader a basic background knowledge of these techniques.

2.1. General Sintering Theory

2.1.1. Driving Force and Basic Phenomena

Sintering is usually driven by reduction of the total interfacial/surface energy of the powder compacts [43]. The total interfacial/surface energy of the powder compact is expressed as γA, where γ is the surface (interface) energy and A is the total surface (interface) area of the compact. Therefore, the reduction of the total energy is given by;

$$\Delta(\gamma A) = \Delta\gamma\, A + \gamma\, \Delta A \qquad\qquad \text{eq. (2.1)}$$

From the equation (2.1), the change in the interfacial energy ($\Delta\gamma$) usually results in densification, while the change in the interfacial area (ΔA) is responsible for the grain growth of the powder compact [43]. For solid-state sintering, $\Delta\gamma$ is related to the replacement of solid/vapor interfaces at the surface of the powder particles by solid/solid interfaces in the sintered compact. Basic phenomena of sintering the decrease of total surface (interface) energy via densification and grain growth is shown schematically in Figure 2-1.
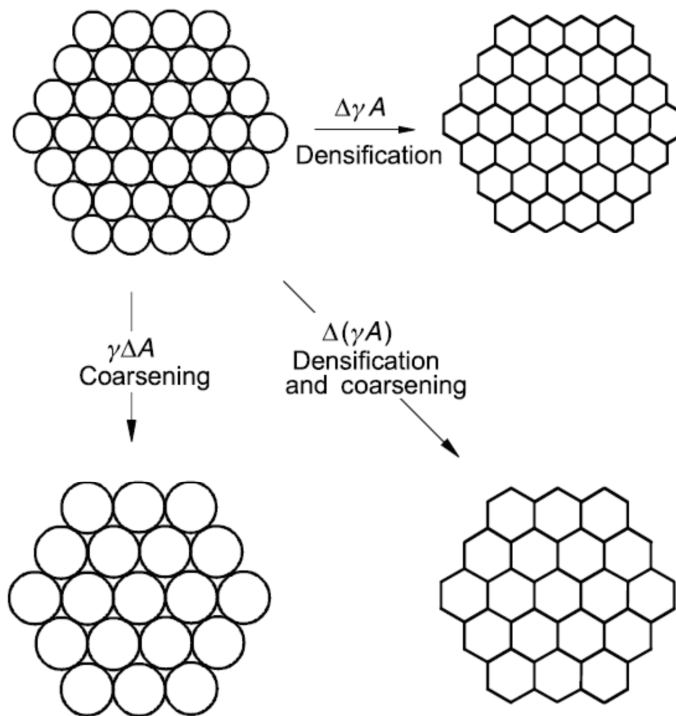
Figure 2-1 : Schematic representation of densification and coarsening from powder compact. [43]

2.1.2. Defects in Crystalline Solids

The driving force of sintering is lowering of the free energy of the system. In case of a powder compact, the lowering of the free energy is achieved by lowering the surface or interfacial energy. However, the solid-state sintering can only happen by transportation of matter via diffusion of atoms, ions or molecules in crystalline solids. Crystalline solids are defined as a perfect crystal solid array of atoms, which are arranged in a three-dimensional periodic array

of perfect order [44]. However, in real world crystalline solids are not ideal in structure. These imperfections in the regular geometrical arrangement of the atoms in a crystalline solids are known as defects [45]. Defects in crystalline solids occur due to the imperfection in the arrangement of the atoms or defects can occur due to chemical reasons, when the inorganic compounds may deviate from the ideal composition determined by the valence of the atoms. For example, pure ceria (CeO_2) has a cubic fluorite structure. When trivalent cation dopants are added to pure ceria lattice, oxygen vacancies (defects) are being created [46]. The presence of these defects in crystalline solids allows diffusional matter transport to take place during sintering and grain growth. Defects in a crystalline solid are broadly classified into three groups:

(i)   Point defects, which are generally associated with one lattice point. Point defects are missing atoms (vacancies), atoms occupying the interstices between two atoms (interstitials) and atoms replaced and occupied the parent atoms (substitution).

(ii)   Line defects, which are generally many atom lengths. Line defects are called dislocations.

(iii)   Planar defects, which are generally the discontinuity of the perfect crystal structure across a plane. Grain boundary is a general planar defect that separates two distinct oriented crystals.

Point defects in pure crystals are generally the vacancies and the interstitials. A perfect crystal is thermodynamically stable at absolute zero temperature. At any higher temperature, the crystal always contains certain number of point defects. Point defects in ceramics usually expressed by the Kröger-Vink notation [47]. In this notation, the main symbol represents the species (A), its subscript represents the site (B) and its superscript represents the effective charge (C), in the form of A_B^C. A positive effective charge is denoted as • and a negative effective charge is denoted as ′. Table 2-1 lists some typical defects in Kröger-Vink notation present in a compound MX. Due to thermodynamic in in nature, point defects are important features in ionic solids (ceramics) and plays an important role in the rate of matter transport, which takes place during sintering. Different point defects in crystalline solids are shown in Figure 2-2 [41]. A detailed discussion about defects in ceramics can be found in the literature [41,43,44,48].

Table 2-1: Different types of point defects in a compound MX [43,47]

Defect type	Kröger-Vink notation
Vacancies	$V_M , V_X , V_X^{\bullet} , V_M^{''} , V_X^{\bullet\bullet}$
Interstitials	$M_i , X_i , X_i^{''} , M_i^{\bullet\bullet}$
Misplaced atoms	X_M , M_X
Associated centres	$(V_M , V_X), (X_i , X_M)$
Foreign atoms	$L_M , F_M^{\bullet} , L_i^{\bullet\bullet}$
Free electrons and holes	$e^{'} , h^{\bullet}$
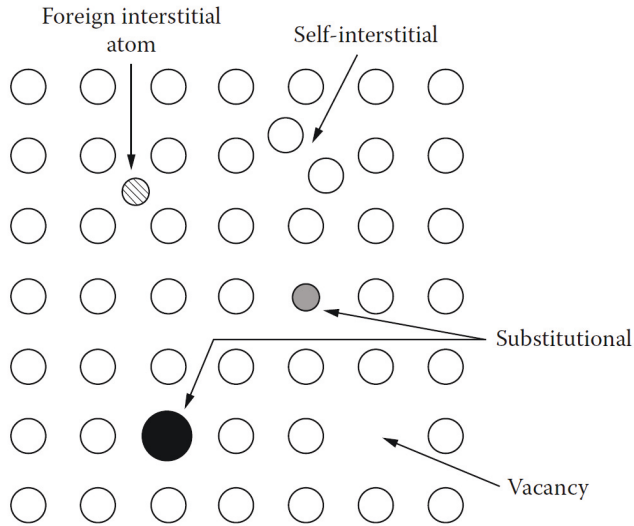
Figure 2-2 : Schematic illustration of different point defects in a crystalline solid [41]

In addition to the temperature, the concentration of point defects in a crystallite solid can also be influenced by the partial pressure of oxygen $P(O_2)$ and the concentration of dopants. Ting and Lu studied the effect of Al_2O_3 and MgO doping percentage on the defect chemistry and the kinetics of sintering of the Magnesium Aluminate Spinel [49]. They observed that with increase in the amount of MgO in the Mg-Aluminate Spinel, oxygen vacancies (anion defects) are generated in the lattice system, which enhanced the densification rate during conventional

sintering [49]. Whereas the excess Al₂O₃ content in the Spinel system, which increases the cation defects in the system, inhibit the densification rate. The densification rates of the Magnesium Aluminate spinel system having different stochiometric compositions due to the MgO and Al₂O₃ content at a relative density of 90% are shown in Figure 2-3 [49]. The excess MgO composition leads to a five times higher densification rate than the stochiometric composition. Comparing the densification rate result with the concentration of oxygen vacancy shows that the concentration of the oxygen vacancies also increased by the same ratio with increased MgO content while keeping the temperature and P(O₂) similar. While excess Al₂O₃ content decreased the densification rate.
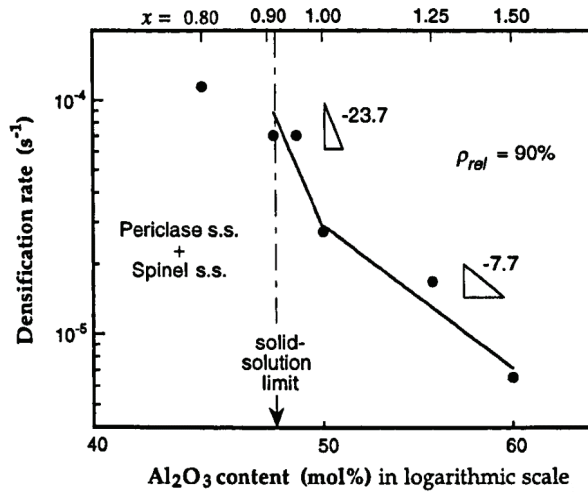
Figure 2-3 : Dependence of densification rate on MgO and Al₂O₃ content at 1600°C, Reprinted with permission from [49].

It is remarkable to see by careful addition of the dopant, intrinsic defects in the lattice system can be influenced, which indeed can be used to tune the densification and grain growth. Sintering of oxides in low P(O₂) atmospheres results in an increase of the concentration of point defects in the crystallite solid and the diffusivity of the oxygen and metal ions. This concept is applied to many oxide to lowering the sintering temperature or to achieve a high densification rate and grain growth [11,20,46,49–51]. It is also necessary to point out here that other factors, such as the starting powder physical properties, compaction process and green density have a considerable influence on the densification rate and final microstructure of the sintered pellets.

2.1.3. Mechanism of Sintering

Sintering process generally combines the densification and grain growth of the initial powder compacts. Densification or shrinkage can be defined as the ratio between the change of the porosity after sintering and the initial porosity of the powder compact. Grain growth is defined by the increase in the average grain size. In either case, the matter needs to be transported from the regions with higher chemical potential (the source) to the regions with lower chemical potential (the sinks). Sintering of polycrystals occur by matter transport by diffusion along a defined path during the process. The diffusional matter transport can happen along different paths, which are defined by the sintering mechanism involved [41,43]. There are six different mechanisms of sintering in polycrystalline materials, as shown in a simpler assembly of three particles system in Figure 2-4.
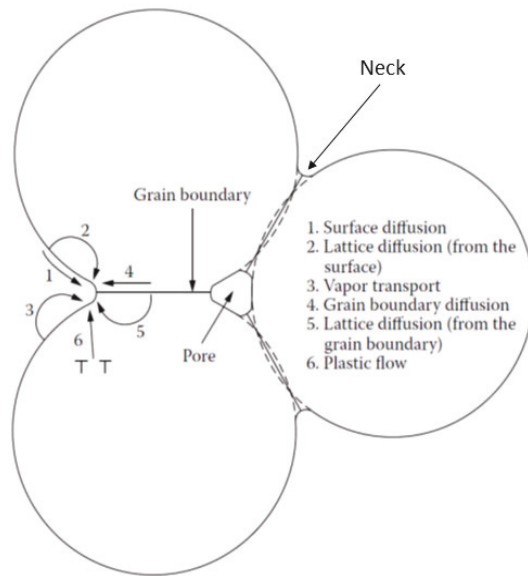
Figure 2-4 : Material transport paths during sintering and associated six different mechanisms [41]

All the six material transport mechanisms lead to bonding and growth of necks between particles whereas, only three mechanisms contribute to densification or shrinkage of the initial powder compacts. Surface diffusion, lattice diffusion from the surface and vapor transport are referred as non-densifying mechanisms while grain boundary diffusion, lattice diffusion from the grain boundary (volume diffusion) and plastic flow are classified as densifying mechanism. Table 2-2 summarizes different sintering mechanisms in polycrystalline solids, characterized by the source and the sink and contribution to the densification or shrinkage.

Table 2-2: Material transport mechanisms in polycrystalline solids [41]

Sintering Mechanism	Source of Matter	Sink of Matter	Densifying
Surface diffusion	Surface	Neck	No
Lattice diffusion	Surface	Neck	No
Vapor transport	Surface	Neck	No
Grain boundary diffusion	Grain boundary	Neck	Yes
Lattice diffusion	Grain boundary	Neck	Yes
Plastic flow	Dislocation	Neck	Yes

2.1.4. Stages of Sintering

Sintering in general can be categorized by three different stages; initial, intermediate and final stage. Fig. 2-5 shows a general densification as a function of time, illustrating different stages of sintering and its corresponding micrographs. During the initial stage, interparticle neck growth occurs as the sintering time increases. In this stage the large difference in the surface curvature is removed by diffusion, vapor transport or plastic flow. It is assumed that the shrinkage is appeared at the later period of the initial stage, when the radius of the interparticle neck has reached a value of 0.4-0.5 of the particle radius. During this stage a linear shrinkage of 3-5% is expected [41,43].

After the interparticle neck growth is achieved and the pores have reached their equilibrium shapes, the intermediate stage begins. As the sintering proceeds, the pore channels are disconnected, and isolated pores start to form due to the dihedral angle is much larger than 60°.

Densification is assumed to occur simply by shrinkage of the pores to reduce their cross-section. Major part of the densification occurs during the intermediate stage of the sintering [41,43,51].

The final stage of sintering begins when the pores become increasingly spheroidised, isolated and remained on the triple boundary of the grains. Depending on the temperature and time, the pore may continue to shrink at a slower rate during this stage. Grain growth can also take place in the final stage which reduce the driving force for sintering. However, no further densification is possible if pores become isolated from the grain boundaries and entrapped inside a grain.
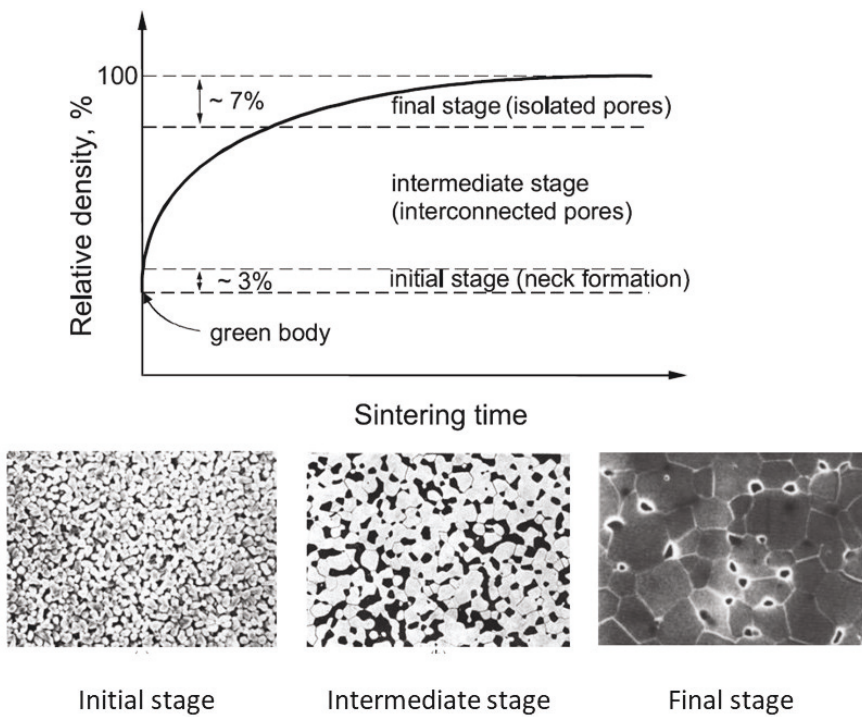
Figure 2-5 : Schematic representation of three different sintering stages of a powder compact and example of associated microstructure and grain size evolution [41,43]

2.2. Sintering Techniques

Traditionally, the primary sintering parameters for the densification and grain growth are the temperature and dwell time. High technological advancements in many industries demands high performance sintered products with novel properties. Additionally, industries seek to fabricate material with increased energy efficiency by reducing the sintering temperature and dwell time. Thus, the limitations of the conventional sintering method are overcome by superposition of other process control variables, like, pressure, electric field/current etc.

In this section, overview of different sintering techniques and the possible sintering mechanisms is provided. Due to the relevance for the present work, the focus lies on the ECAS techniques, more specifically Field Assisted Sintering Technique/Spark Plasma Sintering (FAST/SPS) and Flash Sintering (FS). Therefore, a detailed background information and state of the art will be described for the two field assisted sintering techniques, while, only brief theoretical background of the other sintering techniques will be provided.

2.2.1. Pressure Assisted Sintering

The development of high-performance fully dense ceramics with a controlled microstructure are necessary for different applications from tool industry to space industry [42,43,52]. Conventional pressure less sintering technology has limitations regarding fabricating fully dense ceramics with controlled microstructure. For example, fabrication of fully dense high melting point compounds such as carbides, nitrides, borides and some oxides with a melting temperature above 2000°C [51,53–56] are difficult by conventional sintering techniques . The challenge of inadequate densification of such materials can be overcome by the simultaneous application of pressure and temperature during sintering process.

In conventional pressure less sintering, the driving force for sintering comes from the reduction in total interfacial energy, as discussed in section 2.1. An application of the simultaneous external pressure during the sintering increases the driving force which results in enhanced densification. The sintering stress (σ_S) is proportional to the surface energy (γ) divided by the grain size (G), mathematically it can be written as [57]:

$$\sigma_S = \frac{g\,\gamma}{G} \qquad\qquad\qquad \text{eq. (2.2)}$$

where g is a geometrical parameter.

Depending on the initial particle size and the surface energy, the sintering stress can be calculated by using equation 2.2. The sintering stress can be increased by applying an external pressure to the green compact body during the sintering process. During the initial stage of sintering, an external applied pressure increases the inter-particle contacts, which enhances the internal sintering stress. When external pressure is applied, the particles are flattened at the contact points. Due to the small inter-particle contacts, even a small applied pressure can have a huge impact on the stress at the inter-particle contacts, as a result of stress concentration. During the initial stage of the pressure assisted sintering techniques, the contact stress is much higher than the applied pressure [41]. The higher contact stress due to the external applied pressure enhance the densification at a lower sintering temperature [57,58]. Sintering techniques that utilizes a simultaneous external pressure with the thermal energy are know as pressure-assisted sintering techniques. The pressure-assisted sintering techniques can be classified by the manner in which the pressure is applied to the sample during sintering, as schematically shown in Fig. 2-6.
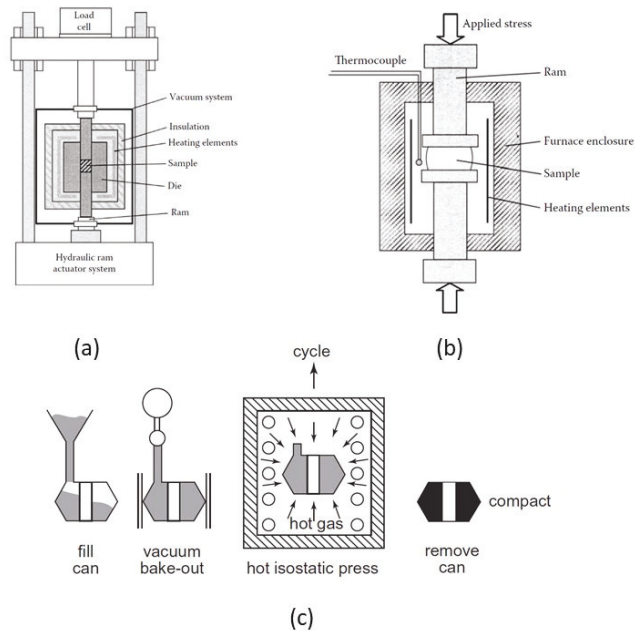

Figure 2-6 : Schematic of pressure assisted sintering techniques; (a) hot pressing, where pressure is applied along the vertical axis [41], (b) sinter forging [41] and (c) hot isostatic process, illustrating different steps involved in the HIP process [57]

Hot pressing: In hot pressing, an external uni-axial pressure is applied simultaneously to the green compact in a die addition to the temperature. Among different pressure-assisted sintering techniques, hot pressing is one of the widely used fabrication method for ceramics. Depending on the furnace, operating temperatures typically range between 1400°C – 2000°C and applied pressures range from 10 to 75 MPa. The temperature is transferred by radiation from the furnace to the die and to the sample. Typically, graphite is used as the tool material in hot pressing due to material cost, ease of machinability and excellent creep resistance at higher temperature, for an operating pressure up to 50 MPa. Otherwise, for higher operating pressure other tool materials like tungsten carbide can be used (i.e., > 50 MPa), various tool materials that can be use are summarized in the literature [41]. A typical set-up for the hot-pressing process is shown in Fig. 2-6 (a). As shown in the figure, due to the significant axial strain in hot pressing, a textured microstructure may develop in the sintered pellets.

The primary mechanisms responsible for the densification during hot pressing are lattice diffusion, grain boundary diffusion, plastic deformation by dislocation motion, particle rearrangements and grain boundary sliding [41,59,60]. During the initial stage of the hot pressing, particle rearrangement contributes to the densification. During the intermediate and the final stage of sintering in hot press, grain boundary sliding is activated in addition accommodating the diffusion-controlled shape changes. Nevertheless, the grain boundary sliding and the diffusional mass transport are not independent mechanisms during the hot pressing.

Sinter forging: The sinter forging process, which is also known as hot forging, is similar to the hot pressing concept except that the sample is not confined in a die. Therefore, a uni-axially pressed powder compact or even a pre-sintered body is usually applied to be densified by sinter forging technique [61,62]. The externally applied uni-axial pressure during the sinter forging technique provides an additional driving force for sintering. As in the tool set-up no die is involved, uniaxial strains in the direction of the applied stress are significantly higher than in hot pressing. One of the disadvantages of the process is the limitation of the externally applied pressure as higher pressure can destroy the sample. A general schematic of the sinter forging set-up is shown in Fig. 2-6 (b).

Hot Isostatic Pressing: Hot isostatic pressing (HIP) is a pressure assisted sintering technique, where an isostatic pressure together with temperature is utilized to densify a reconsolidated powder compact. In the HIP process, the reconsolidated powder compact is placed in an

enclosed glass or metal container (known as can) that is sealed under a high vacuum and the can is placed in a high-pressure vessel. The schematic of the HIP process is shown in Fig. 2-6 (c). The isostatic pressure during HIP is generated by an inert gas like N_2 or Ar, which is compressed by an external compressor [63]. In HIP devices, the number of gas atoms moving through a unit area and their velocities are same in all directions, which results in a uniform densification in all directions. Additionally, unlike the uni-axial pressure assisted sintering, complex shape materials can be fabricated by HIP.

2.2.2. Field Assisted Sintering Techniques – an overview

Conventional pressure less sintering is a well-established method for fabricating ceramics at high temperatures. Enhanced densification during sintering can be achieved by simultaneous application of external pressure. Therefore, primarily temperature and pressure are the traditional measures to densify and optimize microstructure of ceramics. Another way to enhance the densification is the addition of electric or magnetic field to the sintering process, which results in reduction of sintering temperature and dwelling time. The additional degree of freedom to densify materials and in some techniques, tailoring of microstructures and properties has large potential for the industrial application, also due to providing significant reduction in processing costs and energy savings in the fabrication of ceramics. Many review articles and books underline the history and the high current interest in the scientific community on the field assisted sintering techniques [28,29,42,64–67].

Various attempts were made in the literature to unifying different field assisted technologies under a single acronym [66,68–71]. However, in the literature we often find different techniques that utilizes electric field/current also grouped under Electric Current Activated/Assisted Sintering (ECAS) [68,69]. As suggested by Grasso et. al. [69], the term "field" in the field assisted sintering techniques, is attributed to any field such as mechanical, electric, magnetic and electromagnetic etc. Nonetheless, ECAS, is a subclass of field assisted sintering techniques and is more related to the techniques that utilizes electric field/current to achieve enhanced densification during sintering.

Electric current activated/assisted sintering (ECAS) techniques are very promising for processing of high-performance ceramic materials due to significant improvement of sintering kinetics [69]. Fig. 2-7 shows primary processing parameters involved in the ECAS methods. One primary distinction is the heating method, where the heating of the sample can be achieved by directly passing current through the green body e.g., in flash sintering. Alternatively, in

some ECAS methods the temperature of the sample is raised by passing the current through a tool and transferring the temperature by convection or conduction e.g., FAST/SPS. ECAS technologies due to the reduction in the sintering temperature and dwell time are highly promising techniques regarding energy efficiency, when compared to conventional sintering technologies. Furthermore, the possibility of tuning of microstructures down to the nanoscale is attractive with respect to improving the materials performance.
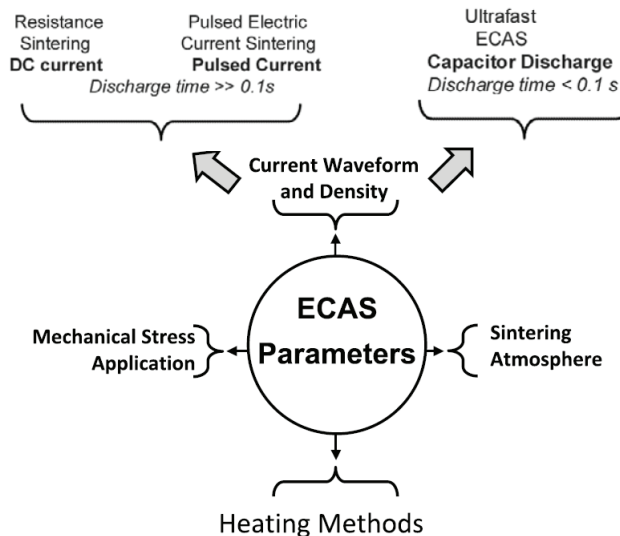
Figure 2-7 : Primary ECAS processing parameters: current density, current wave form, heating method, mechanical pressure and sintering atmosphere, Reprinted with permission from [69].

Recent advancements in development of suitable FAST/SPS devices made the process well established in the industry [72], but there are still a lot of open questions regarding sintering of complex ceramics, such as the ceramic's sensitiveness to low oxygen partial pressure or reaction with the tool material. On the other hand, ECAS techniques like Flash sintering and Flash SPS in the last decade attract significant attention due to further reduction in the required furnace temperature and dwelling time to few seconds [33]. A wide variety of oxide materials are densified by flash sintering methods. Nevertheless, on fundamental research perspective the underlying physical mechanisms of flash sintering remains under consideration.

2.2.3. Field-Assisted Sintering Technology/Spark Plasma Sintering (FAST/SPS)

▪ **Introduction**

The Field-Assisted Sintering Technology/Spark Plasma Sintering (FAST/SPS) comes under rather broad field of Electric Current Activated/Assisted Sintering (ECAS) techniques [69]. FAST/SPS, also known as pulsed electric current sintering (PECS), is a low voltage (electric field), direct current (DC) pulsed current activated uni-axial pressure-assisted sintering, and synthesis technique [70]. FAST/SPS process set-up is similar to the hot pressing method (see section 2.2.1), with a difference in the heating of the tool material and sample. In FAST/SPS, very high current (typically from 1 to 10 kA) is used to achieve heating at a very high heating rate by joule heating. Generally, graphite is used as a tool material due to its high electrical conductivity and operating temperatures. The electrical property of the processing materials may influence the current pathways, which affects the densification behavior. A general schematic of the FAST/SPS process set-up is shown in Figure 2-8 [70]. Densification of the powder is achieved by the simultaneous application of pressure and heat at a very high heating rate. One of the most remarkable features of the FAST/SPS technique is that full densification is achieved while maintaining a finer grain size [73,74].

(a)   (b)
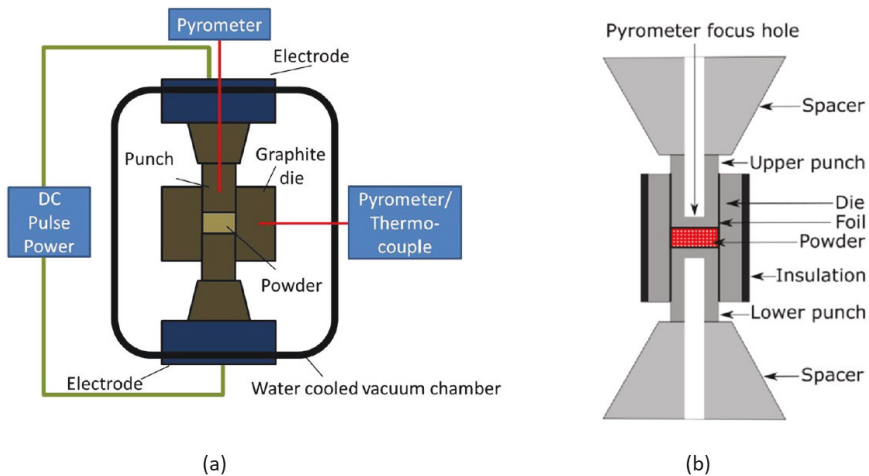
Figure 2-8 : General schematics of the (a) FAST/SPS process set-up [70] and (b) general tooling assembly

§   **Principles of FAST/SPS**

FAST/SPS consists of a mechanical loading system similar to the hot pressing with a difference in the way the heat is generated, as shown in Fig. 2-8. A conductive tool is used in a FAST/SPS device, which is placed between two water cooled electrodes inside a chamber for application of uni-axial pressure and simultaneously act as a high-power electrical circuit. A water-cooling system is used to regulate the system temperature throughout the process. Graphite based materials are commonly used for the tool in FAST/SPS devices due to high electrical conductivity and low thermal expansion coefficient (CTE) [75]. The starting powder is poured inside the die between the two punches. The temperature can be regulated by a pyrometer either from the top or from the side. A hole is drilled in the graphite tool until very close proximity of the sample as illustrated in Figure 2-8 for the pyrometer.

FAST/SPS is a low voltage, typically below 10 V and high DC pulsed current, typically between 1-10 kA leading to efficient joule heating. When a conductive material is employed for sintering in FAST/SPS, the current is passed through the sample which increase the sample temperature internally. However, even when a nonconducting material is employed for sintering, the high pulsed current is passed through the graphite tool to produce heat by joule heating, heat is then transferred to the sample by conduction. Guillon et. al. [70] in a review paper on the FAST/SPS process shown the current density profile for three different tool and sample material assembly i.e., (i) conductive tool and powder, (ii) conductive powder and insulating die and (ii) non-conductive powder and conductive die. From which, the flow of current for two widely used tool and sample assembly is shown in Figure 2-9.

(a)   (b)

Figure 2-9 : Schematic of the current flow for the tool and sample assembly; (a) conductive powder and die, (b) non-conductive powder and conductive die, Reprinted with permission from [70].

Most of the ceramics have electrical conductivity much less than the electrical conductivity of the tool material (e.g., graphite). Therefore, during the FAST/SPS cycle, the current primarily flow through the tool material as depicted in Figure 2-9 (b), where the heat is then transferred to the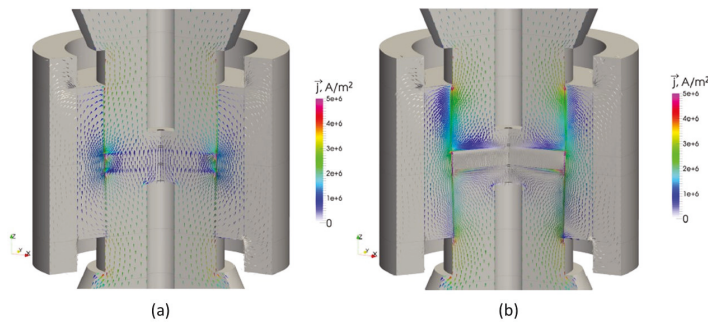 sample from the tool by conduction mechanism. As the heating is achieved due to the joule heating by the power dissipation in the tool material or in the sample, sintering cycle with very high heating rates (e.g., 1000°C min^{-1}) is possible by FAST/SPS process. Similarly, a controlled cooling with very high cooling rate (100-200 °C min^{-1}) is also possible, due to the cooling system used in the FAST/SPS process. Due to a very high heating and cooling rates, significant reduction in the sintering cycle is possible by FAST/SPS process, which reduces the energy consumption and processing cost as compared to other sintering processes discussed above.

Another unique feature apart from a very high rates is simultaneous application of an uni-axial pressure in the FAST/SPS process. The maximum pressure that can be applied during the FAST/SPS cycle primarily depends on the compressive strength of the tool material. For example, typically a mechanical pressure of 10-100 MPa can be applied when graphite is used as the tool material. The externally applied pressure can be increased by using different tool materials. Laptev et. al., uses tool material based on molybdenum alloy (TZM) for applying high pressure of 440 MPa to fabricate half-cell for all solid state battery [76]. Simultaneous application of external pressure during the FAST/SPS cycle enhances densification and lower the sintering temperature as compared to the conventional sintering process. Typically, in FAST/SPS the sintering cycle is realized under vacuum atmosphere, to avoid oxidation of the tool material. Nevertheless, protective gas as Argon at atmospheric pressure can also be used during the FAST/SPS cycle.

In last decades, extensive efforts have been made in understanding the FAST/SPS process and developing it as a promising techniques for fabrication of advanced new materials [70,76–82]. However, limited literature is available on the exact sintering mechanism involved in the FAST/SPS process. During FAST/SPS process, different factors such as thermal, electrical and mechanical effects involved simultaneously for densifying the powder compacts. Although not verified, several different mechanisms such as plastic deformation, vaporization and condensation and surface, grain boundary and volume diffusion are assumed for the densification mechanisms involved in the FAST/SPS process [83,84]. In particular the existence of the plasma due to the spark generate at the inter-particle contacts is not yet proved [67,77,85–87].

- **Mechanisms involved in FAST/SPS**

As one of the most successful electric field assisted sintering techniques, which has the potential for upscaling at the industrial level, understanding the sintering mechanism behind the FAST/SPS process is important. Many researchers contributions help in understanding the underlying possible mechanisms with respect to plasma [77,85], electric field [88,89], high heating rate [90] and mechanical pressure [88,89]. Nevertheless, a universal mechanism for the rapid densification by FAST/SPS is still under consideration [70,72,85,91]. However, the early claims of active role of plasma that enhanced the densification mechanism is widely accepted not to be true [92]. It is therefore important to understand the effect of each processing parameter and its influence in the densification behavior in FAST/SPS in its totality.

- **Electrical effects:**

The presence of plasma in FAST/SPS and its contribution on the densification of the powder was introduced by Tokita in 1993 [93]. He hypothesized that the high current flow through the sample might induce the formation of electric sparks between the particles of the green pellets, generating plasma clouds and micro scale temperature increase. However, direct experimental evidence was never provided for the possible mechanisms. Furthermore, when an oxide material is used to densify by FAST/SPS, the green body electrical conductivity is negligible as compared to the electrical conductivity of the tool, which facilitate all the current flow through the tool and not through the sample itself. Hulbert et al., investigated the presence of plasma by a complex approach involving the use of electrical and optical techniques but failed to find any presence of plasma [85,86].

Another electrical effect often discussed in the FAST/SPS literature is electromigration effect [94]. Electromigration is a mass transport phenomenon observed mainly in metals and resulting from the momentum transfer between the conducting electrons and the metal ions [95]. The hypothesis of electromigration during the processing of materials in FAST/SPS suggested an acceleration of the mass transport due to the high intensity current pulses (up to several 100 kA cm^{-2}). Nevertheless, in a typical FAST/SPS geometry only a small amount of current flows through the sample even when the sample is highly conductive materials, as shown in Figure 2-10 [70].

Electrical fields, without current flow can also affect the matter transport, grain boundary migration and in ionic materials, it can generate point defects and polarize them near the appropriate electrode regions. The matter transportation due to the electrical field effect may

also play a crucial role in controlling or enhancing the sintering mechanisms in FAST/SPS [96]. The applied electrical field in an ionic conductor, as well as mixed electronic and ionic conductors can produce a chemical potential gradient. However, the electrical fields applied in FAST/SPS are very low to observe such effects. A direct comparison study in sintering of alumina and fully stabilized zirconia by HP and FAST/SPS suggests negligible field effect [89,97]. Although the effect of electrical field shows negligible for most of the materials, in some materials, it can play a role in the densification of powders by FAST/SPS.

(a)   (b)
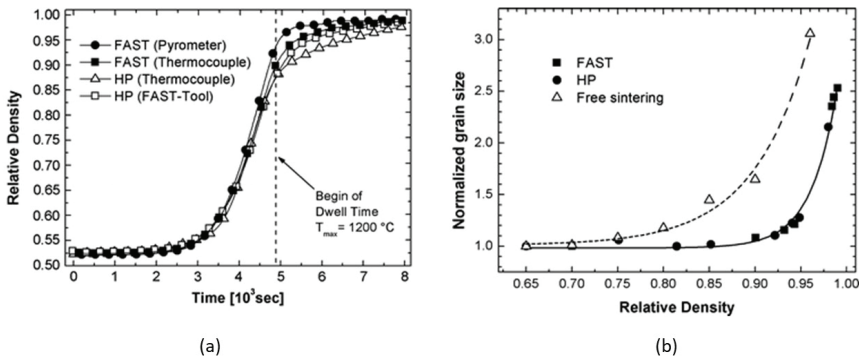
Figure 2-10 : Comparison between HP and FAST/SPS of submicron alumina: (a) Densification curve and (b) sintering trajectory, Reprinted with permission from [98].

Direct comparison between HP and FAST/SPS of pure submicron size alumina, keeping the sample geometry and the processing parameters e.g., heating rate 10°C/min, resulted similar densification behaviour for both processes [98], shown in Fig. 2-10. Similar densification results have been observed for ionic conductor fully stabilized zirconia as well [97], where in both process densification is controlled by grain boundary diffusion. This suggests that no separate densification mechanisms induced by the electric field or current in FAST/SPS process for oxides.

- **Thermal effect:**

One of the significant differences between the Hot pressing (HP) and FAST/SPS process is the heating rate. In FAST/SPS heating rate as high as 1000°C/min can be achieved due to the high current that generate joule heating. The effect of heating rate on sintering has been extensively investigated for conventional pressure less sintering technique [99]. In conventional sintering high heating rates results in enhanced densification and impede grain growth, due to high

activation energy for densification than the grain coarsening mechanism [99]. Surface diffusion typically dominates sintering at low temperature in conventional pressure less sintering. The low temperature surface diffusion results neck growth without densification. High heating rates is found to be effective for lowering the surface diffusion and supressing the grain growth.

The effect of heating rate on the densification and grain growth in the FAST/SPS led to conflicting results in the literature. Stanciu et. al., [100] studied the effect of heating rate on the densification and grain growth in FAST/SPS. Sintering studies of two types of powders Al_2O_3 (electrical non-conductor) and $MoSi_2$ (electrical conductor) were done in FAST/SPS using heating rate from 50°C to 700°C/min. The final relative density of the samples sintered at the same temperature and dwelling time, shows no effect of heating rates. Nevertheless, the grain size of alumina shows to have an inverse relationship with the heating rates, whereas $MoSi_2$ samples had no dependence of the grain size with respect to the heating rates [100]. In contrast to the above observations, Shen et al. [73] did sintering study on alumina in FAST/SPS. It was shown that the heating rate has a negligible effect on the final relative density up to a value of about 350°C/min and above that had a negative effect on the final relative density until 600°C/min. The grain size results however in a good agreement with previous findings. A general findings from the literatures on the effect of heating rates on the densification and grain growth of different oxides by FAST/SPS, suggest that the heating rate has a negligible effect of the final relative density of the sample, while the grain size has an inverse relationship with the heating rate [88].

In FAST/SPS process typically, the current flows through the die and a high temperature is generated in the die by joule heating, which is then transferred to the sample by conduction. A high heating rate may influence the thermal distribution in the sample during the FAST/SPS process. A non-uniform temperature distribution, where the core of the sample have a lower temperature as compared to the surface close to the tool die may results in non-uniform microstructure and thermal stresses [101,102]. A homogeneous thermal distribution in the sample can be achieved by using advanced thermal distribution and increase the energy efficiency of the FAST/SPS cycle [102].

▪ **Pressure effect:**

As described earlier, sintering is a thermally activated process where the driving force is provided by the lowering of the free energy of the powder compact. Sintering can be also enhanced by application of an external pressure, as described in section 2.2.1. In FAST/SPS, a

uni-axial pressure is applied with addition to the temperature. The simultaneous application of the uni-axial pressure leads to a better contact between the particles. The applied pressure has primarily two roles during the sintering in FAST/SPS. First, mechanically the applied pressure helps in the destruction of soft agglomerates (specifically in non-sized powders) and promotes intensive particle re-arrangements at the initial stage of the process [103]. Second, the applied pressure can also influence the driving force for sintering by activation different sintering mechanisms, such as plastic deformation or grain boundary sliding [41].

In FAST/SPS the powder is confined in a die like the condition in HP process. The effective stress in these conditions is significantly higher than the sintering stress, during higher porosity stage. Previous works have clearly shown that the dominant mechanism of densification in pressure assisted sintering of material is creep [104,105]. An analytical model was developed, which was based on the power-law creep successfully applied to determine the mechanism(s) controlling the densification of the granulated zirconia powders during the FAST/SPS process [106]. In this study it is proposed that at low temperature and pressure (10-20 MPa), a pure diffusion mechanism is responsible for the densification. At intermediate macroscopic compaction pressure and/or temperature, a stress exponent of 2 with an apparent activation energy of the mechanism controlling densification is 450 kJ mol^{-1}, suggested grain boundary sliding to be primary densification mechanism. For high temperatures and/or higher pressure, stress exponent between 3 and 4.8 was determined, which suggested the densification proceeds by a dislocation-climb controlled mechanism [106]. Generally, the effect of applied pressure on the densification in FAST/SPS is dominant during lower density and higher porosity of the sample [104]. A detailed description on the effect of applied stress during the sintering in FAST/SPS and the responsible mechanism can be found here [92].

- **Role of atmosphere**

The composition of sintering atmosphere and the partial pressure of oxygen have an influence on the defect structure of the material, which may have a pronounced effect for highly active materials like ceria. As discussed in section 2.1.2., these intrinsic defects in the material have an influence on the diffusivity in the sintering material. Therefore, densification kinetics, grain growth phase stability, oxygen stoichiometry and sample coloration are affected by the sintering atmosphere [107–109].

In most cases, FAST/SPS is carried out at a low vacuum conditions, in the range of 10^{-4} to 10^{-5} bar. However, the sample is enclosed in the pressing tool, which results in almost complete

isolation of the sample from the FAST/SPS chamber. The atmosphere near to the sample might be therefore completely different from the FAST/SPS chamber atmosphere. Due to the tool assembly, it is difficult experimentally to analyse the actual gas composition near the sample. Furthermore, the residual oxygen present in the low vacuum condition or inert gas atmosphere, may react with the tool material to produce carbon monoxide (CO), which is reducing in nature. Therefore, it is safe to assume that the actual sample atmosphere consists of uncontrolled reducing in nature. In the literature one such report is found, where thermoelectric perovskite material $Ca_{0.9} Yb_{0.1} MnO_{(3-x)}$ sintered by FAST/SPS in vacuum showed significant oxygen deficiency. While the oxygen deficiency can be lowered by conducting FAST/SPS of the same material in air at low temperature (900°C) with non-graphite based pressing tools [110].

The role of atmosphere in FAST/SPS is specifically critical during the processing of oxide materials that are prone to loose oxygen by reduction, e.g. Ceria based materials. In this work, we focused our attention to understand the role of FAST/SPS sintering atmosphere and its effect on the densification and grain growth of GDC10.

To summarize the FAST/SPS technique, over the last decade many experimental findings contributed on identifying the sintering mechanisms occurring during FAST/SPS process. It was observed under same experimental condition, that there are no significant differences in the densification and grain growth of the sample between HP and FAST/SPS for different oxides. The external mechanical pressure plays a significant role for enhanced densification due to the activation of additional sintering mechanisms. By increase external mechanical pressure in FAST/SPS, the sintering temperature can be lowered, while the densification rate is enhanced. The effect of heating rates in sintering of materials by FAST/SPS shows contradicting results. However, in general it can be concluded that the heating rate has a negligible effect of the final relative density of the sample, while the grain size has an inverse relationship with the heating rate.

2.2.4. Flash Sintering

▪ Introduction

Flash sintering is a recent development in the broad category of field assisted sintering, which comes under the ECAS sintering technique [69]. Flash sintering distinguished from the FAST/SPS process by forcing the current to pass through the green body directly and the current causes joule heating [71]. Flash sintering process since its discovery in 2010 [33], have emerged as an interesting technique for densifying ceramics at significantly lower furnace temperature and shorter processing time (usually < 5 s) compared to the conventional free sintering [31,32,34,35]. Fig. 2-11 shows influence of electrical field on the densification rate for 3YSZ material, where a rapid densification was observed above an electric field of 60 V/cm known as flash sintering. One of the primary concern of the conventional sintering technology is associated with high energy consumption due to the higher temperature and longer dwelling time required for fabrication of ceramics [111]. Therefore, flash sintering has the potential to significantly reduce the energetic cost to fabricate ceramics.
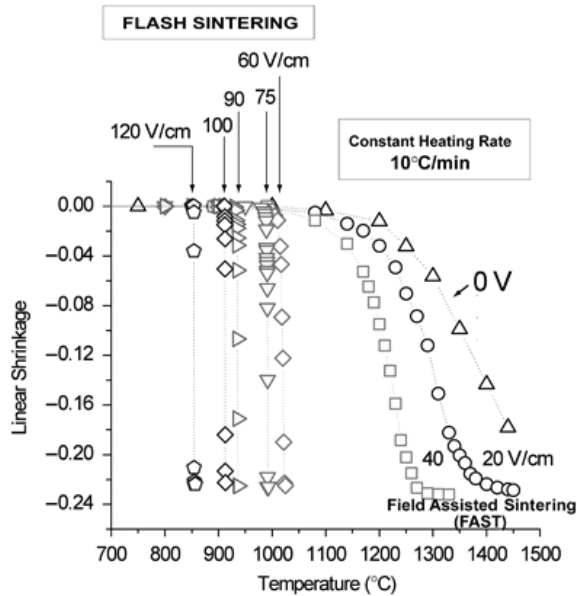

Figure 2-11 : Flash sintering of 3 mol% Yittria Stabilized Zirconia (3YSZ); flash sintering occurred at >60 Vcm^{-1} DC electric field, Reprinted with permission from [33].

The exact mechanism responsible for the onset of flash and a rapid densification is still under debate [112–116]. Even though the onset of flash occurred due to the thermal runaway by joule heating in the materials with a negative temperature coefficient for electrical resistivity, the question remains whether Joule heating alone can explain all the characteristics observed during the flash sintering process [114,117,118]. Flash sintering process has four characteristic phenomenon: (i) sharp rise in the sample conductivity (ii) a bright light emission and (iii) rapid densification (in couple of seconds) and (iv) which is currently evolving, the Debye temperature of the material is the lower bound temperature for the onset of flash [119,120].

A typical flash sintering process is carried out by applying a constant electric field to the green body specimen from the beginning. At a critical furnace temperature (i.e. onset temperature) for the specific electric field a sharp rise in the conductivity of the sample leads to an uncontrolled current flow through the sample [121]. The electrical power to the specimen is then switched from voltage control to current control, which is set to a maximum current density in order to prevent electrical /thermal runaway (voltage-to-current flash).

The voltage-to-current flash sintering process can be carried out in different ways: by heating the furnace at a constant rate until the specimen flashes (constant heating rate flash), or if the onset temperature is known for the material and for the applied electrical field, keeping the furnace at a isothermal temperature (iso-thermal flash).

Very recently, a novel method for flash sintering is discovered, where the flash is initiated by injecting current through the green body from the beginning and increased at a constant rate until the desired maximum current density [122]. The method of flash sintering is known as Current Rate (CR) flash sintering. The power density profile shown to increase linearly, where a rapid increase in the power density in voltage-to-current flash is avoided. As the power density increases steadily as the current density increases, the densification occurred steadily that depends on the instantaneous value of the current density not on the rate at which the current was increased.

- **Principle of flash sintering**

The sample temperature, voltage and current control are fundamental features of the flash experiment. The process is therefore run by software that is interfaced with the various components of the flash system. It controls the process in real time. The experiments can be carried out in two modes, voltage-to-current and current-rate. Most experiments are carried out in the voltage-to-current mode, were an electric field is applied to a powder-pressed "green

specimen" held at a certain furnace temperature. The flash is signaled by a sharp rise in the conductivity of the sample and a rapid increase in the current flowing in the sample. The current is then controlled by switching the power supply from voltage to current control, which is set to a prescribed limit.

The voltage-to-current experiments can be carried out by holding the furnace at a constant temperature (Iso-thermal flash experiment) and applying the electric field as a step voltage, or by heating the specimen at a constant rate with an electric field applied to the specimen from the start (constant heating rate flash experiment). In either case a combination of furnace temperature and electric field characterize the onset of the flash, while the magnitude of the current limit determines the extent of densification [123,124]. It is interesting to note that the lowest temperature for the onset of flash has been shown to correspond the Debye temperature of the material [119,120]. The flash experiment embodies additional features such as highly non-linear rise in conductivity [121] and electroluminescence [125,126].

- **Stages in flash sintering**

Most of the flash sintering experiments are carried out in the voltage-to-current mode. The voltage-to-current experiments can be carried out by holding the furnace at a constant temperature and applying the electric field as a step voltage (Iso-thermal flash), or by heating the specimen at a constant rate (constant heating rate flash) with an constant electric field applied to the specimen from the start. In either case a combination of furnace temperature and electric field characterize the onset of the flash, while the magnitude of the current limit determines the extent of densification.
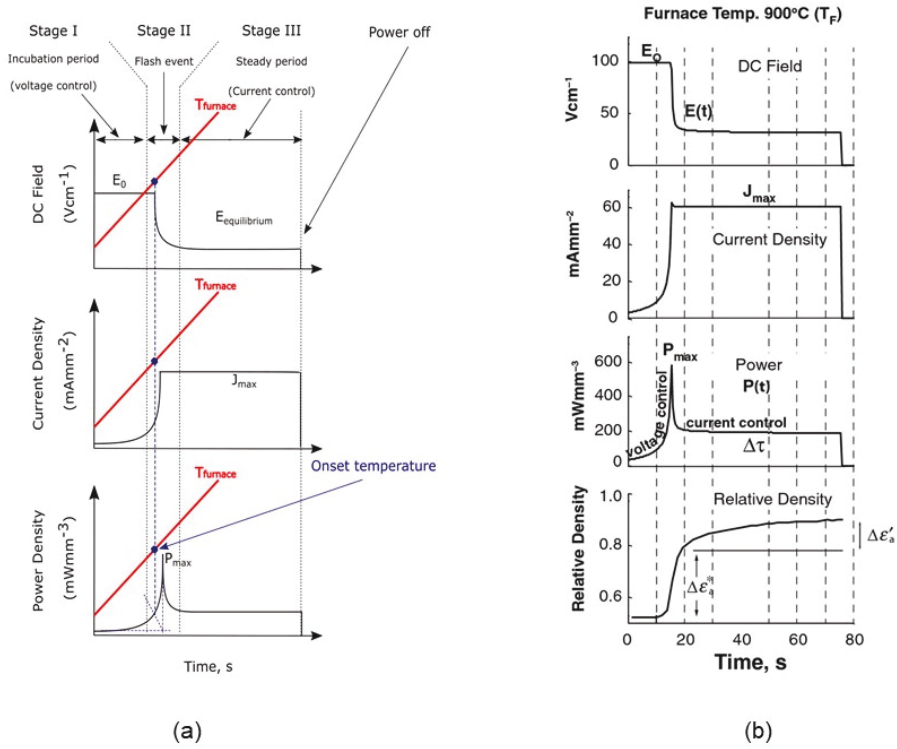
Figure 2-12 : (a) Schematic sketch of three distinct stages in a constant heating rate (CHR) flash sintering experiment, where the furnace temperature is raised at a constant rate (typically 10°C min^{-1}) and (b) Interplay between electrical field, current density, power density and densification for a real iso-thermal flash sintering cycle for 3YSZ dog-bone sample, Reprinted with permission from [124].

The voltage-to-current control flash sintering can be summarized by three distinct stages, as shown in Fig. 2-12 [127]. For a constant heating rate flash experiment the stages can be defined as:

- Stage I: Initially, a constant voltage is applied to the sample at room temperature, where the power source is operated in voltage control mode. At room temperature the ceramic is an insulator and negligible current flow through the sample. The temperature of the furnace is the raised at constant rate, typically 10°C min^{-1}. At a specific furnace temperature that depends on the applied electrical field strength, the conductivity of the

sample rises nonlinearly. Stage I corresponds to the incubation time between the application of a constant electrical field and just before the onset of flash. Depending on the flash sintering experiment and parameters, the incubation time can vary from 1 second to several hours [128].

- Stage II: At a critical combination of the electrical field and the furnace temperature, the conductivity of the ceramic sample rises abruptly, also known as onset of flash. The power supply is the switched from the voltage control to current control, to the predefined current density value. The furnace temperature at which the onset of flash occurs known as the onset temperature. Here it is important to note that at this stage some joule heating may already took place and the actual sample temperature is expected be higher than the furnace temperature. During this stage most of the densification occurred at a very high rate, as shown in Fig. 2-12 (b) and electroluminescence is observed. The time duration in this stage is generally, 1-5 s [128].

- Stage III: When the prescribed current limit is reached, the power supply is completely under current control mode at this stage. The voltage finds a quasi-steady-state value in stage III. The sample is sintered (some residual densification may still occur), grain growth can occur, and electroluminescence is observed. At this stage the furnace temperature is not required and if the current is provided the sample can held in flash mode at this stage [124].

In an iso-thermal flash experiment, the sample is submerged into the hot zone of the furnace that is already at required temperature. After some stabilizing period (usually 10-15 minutes), which ensure a homogeneous thermal distribution in the specimen, an electric field is applied. If the electric field is high enough, the onset of flash may occur immediately that results in a very short incubation period (stage I). Nevertheless, the question remains during the incubation period or in more generalist term stage I period, what happens in the material system which led to the abrupt change in the conductivity of the sample.

- **Flash sintering apparatus**

Flash sintering is a relatively simple process with respect to technical requirements. Flash sintering setup constitutes of four basic components.

i. High temperature furnace: the furnace is required to heat the green specimen to the required onset temperature

ii.   Power supply: either AC or DC power supply for providing electrical power to the sample

iii.   Multimeter: multimeters are required for precise measurements of the electrical parameters

iv.   Metal electrodes: the electrodes are connected with the oxide sample and power source

The optimum condition for carrying out flash sintering experiments are not established yet. Nevertheless, most of the flash sintering experiments reported in the literatures are with small volume samples e.g., dog-bone shaped. Different research groups around the globe are using different shaped sample and different experimental setup, which consists of the basic components as mentioned above.

Schematics of different flash sintering setup is shown in Fig. 2-13.
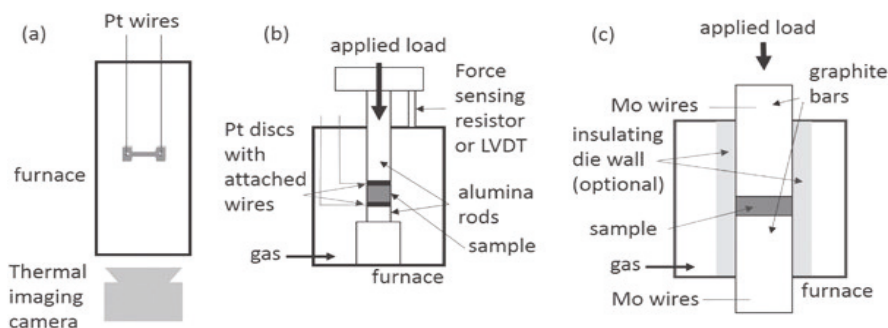
Figure 2-13 : Different flash sintering setup; (a) vertical tube furnace with dog-bone sample, (b) adapted dilatometer/mechanical loading frame and (c) flash spark plasma sintering/adapted hot press, Reprinted with permission from [31].

The first and most widely used flash experiments are carried out by using a standard high temperature tube furnace (vertical or horizontal) with a dog-bone or bar shaped sample. These green specimens were connected to a pair of metal (e.g. platinum) wires wrapped through the holes in the ears of the dog-bones or edge of the bars. The metal wire used in the flash setup should have good electrical conductivity, good oxidation resistance (typically flash experiments are carried out in air) and high melting temperature. Conductive paste was applied to the ears for good electrical contact (typically Pt, Au, Ag or C). The specimen was hung with these platinum wires into the hot-zone of a tubular vertical furnace [129]. The specimen

shrinkage is recorded through a digital camera with optical filters placed at the bottom of the furnace.

The second and third approach to carryout flash experiments by using a custom made dilatometer [130], mechanical loading frame [131] or FAST/SPS [132]. In this setup, a pellet shaped sample is used, where a very low uni-axial force is applied to put the sample in place and ensure good electrical contacts with the electrodes. The electrodes are metallic disks or grids pressed on the flat surface of the specimen, which are connected through the wire electrodes to the power source. The specimen shrinkage can be recorded using displacement sensors or linear variable differential transformer (LVDT).

Fig. 2-14 illustrates three most widely used sample geometries in flash sintering experiments. In all the setups, electrical field and current were fed to the specimen through these metallic wires (electrodes), from a power source. Multimeters are used in the circuit for measuring the voltage and current in real time during the flash experiment.
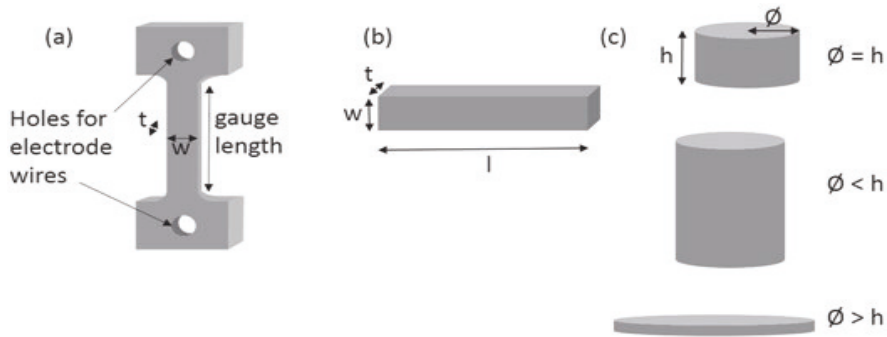
Figure 2-14 : Different specimen geometries used in flash sintering studies; (a) dog-bone shaped, (b) rectangle bar and (c) pellets, of different height: diameter ratios, Reprinted with permission from [31].

Although the dog-bone shaped specimens are the most complex geometry among the three, it is the most suitable shape for studying the flash behavior in lab scale. The dog-bone shaped with two holes are easy to connect to the electrodes and the current can easily flow homogeneously through the thinner cross-section (gauge/gage section). The bar shaped specimens are the best alternative to the dog-bone shaped specimens, where the metal wire is

wrapped around the edges for the electrical contact. Nevertheless, dog-bone shaped samples have no practical applications. The disc shaped samples with larger diameter can be used for practical applications. However, limited literature reported successful densification of disc shaped sample by flash sintering. To our knowledge, a large contact area between the electrode and surface of the specimen can lead to non-uniform contact. In addition, a large volume of the sample may lead to an inhomogeneous temperature distribution in the specimen. The above challenges often lead to current localization, where the current is passed through a preferential path in the specimen. The current localization results in partial densification of the specimen [32].

Flash sintering experimental setups are also constituted by some additional components based on the flash study requirements.

i- Optical pyrometer: due to the very high heating rate employed in flash sintering, optical pyrometer is used to measure the specimen temperature [125]. However, using of a pyrometer to measure the sample temperature often required exact emissivity of the material. Furthermore, it is not possible to integrate a pyrometer in all experimental setups.

ii- Spectrometer: a distinct characteristic of the flash sintering experiment is the bright light emission from the specimen. The emission of the bright light occurs not only during the flash sintering but also in pre-sintered, dense and single crystal specimens. Spectrometer have been used by different research group to characterize the bright light emission during the flash experiment [119,125,126,133].

iii- Diffractometer (x-ray or synchrotron): diffractometry techniques are used to study the evolution of different phases during the flash sintering. Furthermore, the lattice expansion of the material is measured in-situ to accurately measure the specimen temperature during the flash experiment [39,134,135]. More recently, analysis of the mean square displacement of the ions during the flash sintering by pair distribution function (pdf) measurement in synchrotron revealed non-linear movements of the ions from the thermal equilibrium state [136].

iv- Thermal imaging camera: the temperature distribution of the specimen along the gage section are measured by the thermal imaging camera. Liu et. al. and Biesuz et. al., independently reported asymmetric temperature distribution during the flash experiment of a dog-bone shaped zirconia specimen [126,137].

▪ **Influence of processing parameters**

Despite the relatively simple technology and setup, the interpretation of the flash phenomenon occurred during the flash experiments are still very complex. Various processing parameters, their interaction with each other and the effect on the flash sintering process required careful consideration [32,123]. For example, the onset temperature for the flash is inversely related to the applied electric field, while the maximum current density is directly affecting the final relative density of the flash sintered specimen [123,131]. An overview of the primary processing parameters that affect the densification and grain growth behavior in flash sintering are summarized in Fig. 2-15. The most important processing parameters and its influence on the flash sintering behavior is discussed in more detailed below.
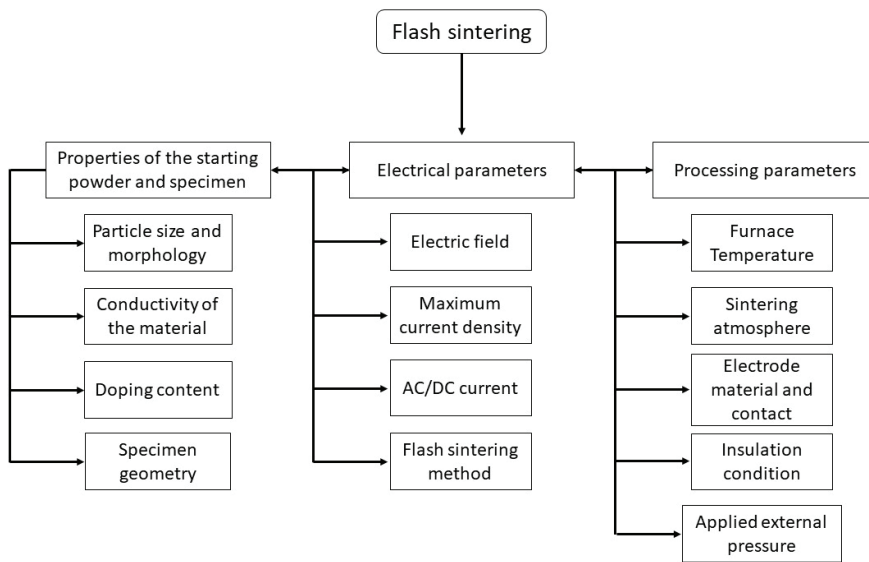
Figure 2-15 : Different processing parameters that influence the flash sintering behavior

Properties of the starting powder and specimen geometry: In conventional free sintering, the densification rate of powder compacts strongly depends on the particle size, where smaller particle size enhances in the densification rate [41]. Until now there are not many specific studies on the effect of particle size on the flash sintering available. One of such specific study was carried out by Francis et. al. [138], they observed that the onset temperature for flash increases as the particle size increased for 3mol% yttria stabilized zirconia. Furthermore, the coarser particle size achieved less final relative density as compared to the finer particle size

sample, while flash occurred at same parameters. They also studied the particle size effect on the densification behavior by conventional free sintering method on the same set of powders. The conventional free sintering results show the densification occurred at lower temperature for finer particle size, as shown in Fig. 2-16 (a).

(a)

(b)
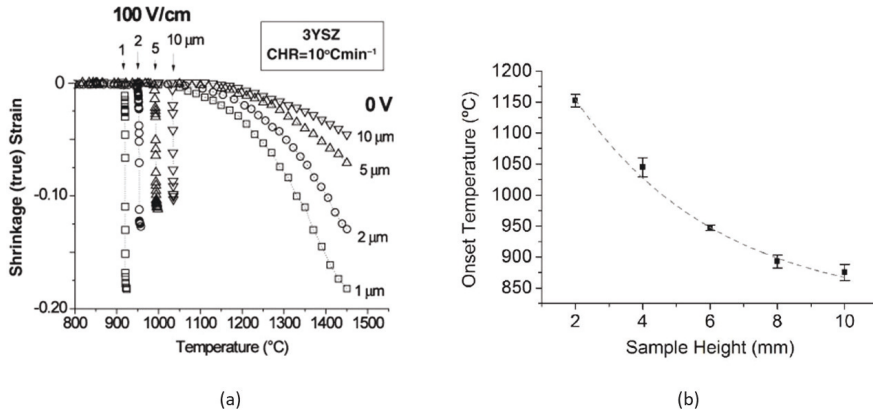
Figure 2-16 : Experiments with 3mol% yttria stabilized zirconia (3YSZ) material (a) Dog-bone shaped samples, uni-axial shrinkage strain in four different particle size from 0 to 100 Vcm^{-1}, the furnace temperature was raised at a constant rate of 10°C min^{-1}, Reprinted with permission from [138], (b) Onset temperature of flash for different cylindrical pellet shaped sample heights, applied AC electric field 90 Vcm^{-1} [139].

Like the particle size effect, most of the flash sintering studies has paid little attention to the effect of sample geometries on the flash and densification behavior. This is also because different research group focuses on different sample geometries. Campos et. al., [139] presented the influence of the sample height on the onset temperature of flash. It was shown for cylindrical pellet shaped 3mol% yttria stabilized zirconia (3YSZ) sample, the onset temperature of flash is lowered as the sample height is increased, Fig. 2-16 (b). Similarly, Avila and Raj [140] reported that for 3YSZ dog-bone shaped specimens, the volumetric power density for the onset of flash increases as the surface to volume ratio is increased. The effect is attributed to Black Body Radiation (BBR) effect during the early onset of the flash transition

in samples [140]. In summary, the onset temperature for flash can be lowered by increasing the height of the cylindrical pellets and decreasing the surface area in dog-bone shaped sample.

Electrical parameters: Electrical field (unit: Vcm^{-1}) is used in flash sintering to have a better comparison of results. The electrical field can be defined as the voltage applied to the specimen divided by the length between the electrodes. Electric field is one of the primary processing parameters in the flash sintering process. The applied electric field inversely influence the onset temperature for flash, where the onset temperature can be defined as the furnace temperature at which the specimen electrical conductivity rises nonlinearly. The nonlinear rise in conductivity occurred only if the applied electric field is above a critical value, which depends on the material, e.g. an electric field of at least 60 Vcm^{-1} was required for 3YSZ to initiate the onset of flash, shown in Fig. 2-11. The effect of the electrical field on the onset temperature for flash is found to be universal behavior for all the materials, shown in Fig. 2-17 (a) [32,66,121]. The onset of flash is not only limited to the powder samples but also occurred in dense polycrystals and single crystals [141].

Wide range of ceramics, which includes semiconductors, electronic conductors, ionic conductors and insulators show the onset of flash at a critical combination of applied electrical field and the furnace temperature. Surprisingly, Arrhenius plots of the power expenditure in the wide variety of specimens revealed the power density at the onset of flash remains in the narrow range of 10 to 60 mW/mm^3, shown in Fig. 2-17 (d) [121].
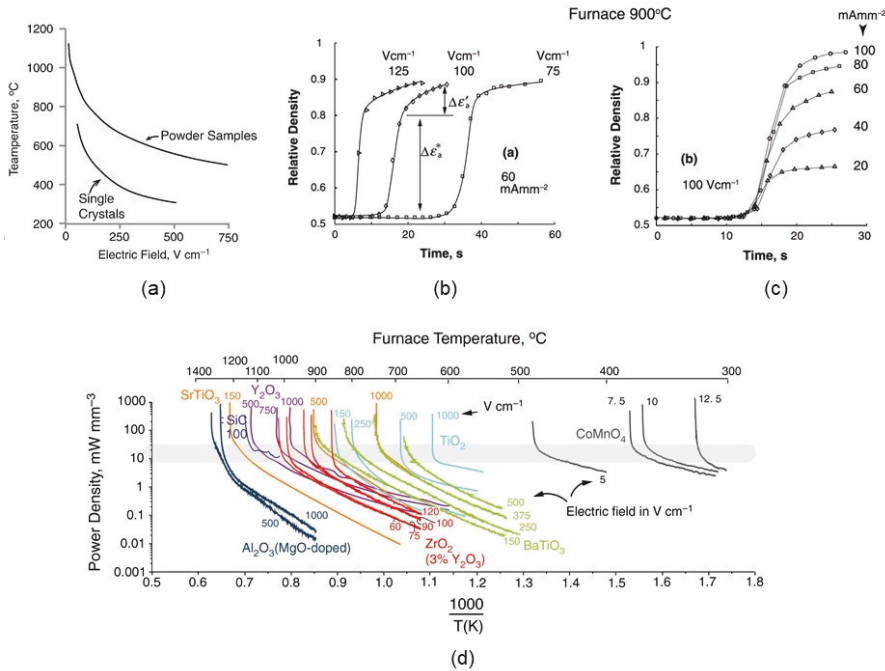
Figure 2-17 : (a) comparison of the onset temperature for single crystal and powder pressed 8-10 mol% yttria stabilized zirconia (YSZ) dog-bone shaped samples in one graph, Reprinted with permission from [141], (b) Influence of the electrical field on the incubation time and densification for 3YSZ samples, (c) influence of the maximum current density on the densification for 3YSZ samples, Reprinted with permission from [124] and (d) Arrhenius plots of power density for several ceramics showing the onset of flash occurred within a narrow band of power density, Reprinted with permission from [121].

While the electrical field is responsible for initiating the nonlinearity in the conductivity (onset), the current density is responsible for the densification kinetics and grain growth. Furthermore, the maximum current density influences the final relative density of the flash sintered specimens, as shown in Fig. 2-17 (b & c) [124,131].

Both AC and DC power source can be used for flash sintering experiments. However, flash sintering experiments with DC power have shown to change the electrochemical properties in the material. Biesuz et al. [142] reported electrochemical blackening due to the partial reduction of the 8YSZ samples under DC biased flash sintering. Whereas, the partial reduction under AC

bias flash sintering with higher frequencies (f > 10 Hz) becomes negligible. Such phenomenon attributed in the literature to a partial reduction of the cation's oxidation state due to the generation of oxygen vacancies under a strong electrical charge polarization [143]. Qin et. al. studied the densification behavior and grain growth of 3YSZ under both AC and DC current. The observed a significant grain growth near the cathode when the samples were flash sintered under DC current [144]. A schematic summarizing the primary electrochemical reactions taking place upon flash sintering of YSZ under DC bias is illustrated in Fig. 2-18 [142].
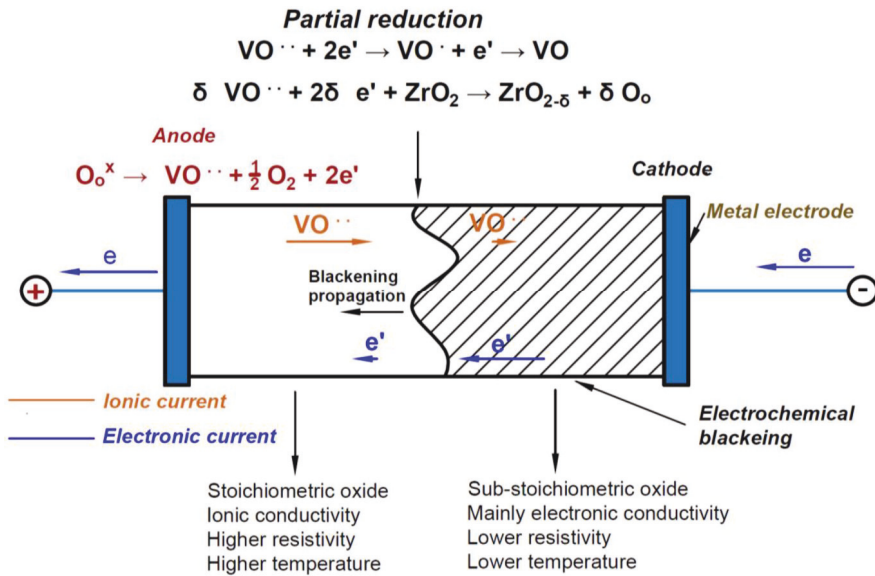
Figure 2-18 : Schematic representation of the electrochemical reactions and the propagation of the electrochemical blackening in 8YSZ during DC flash sintering [142].

Processing parameters: Generally, in most of the flash sintering experiments platinum (Pt) metal is used as the electrode material, due to its melting temperature and good electrical conductivity. The electrode material influences the conductivity of the ceramic, which affect the onset behavior of the sample. There is still a great scope in understanding the influence of the electrode materials on the flash sintering process. Up to now two such studies available in the literature which gave some insight to this effect. Caliman et al. [145] compared both platinum and silver electrodes for the cylindrical pellet shaped β-alumina (MgNa$_2$Al$_{10}$O$_{17}$). They observed that the Pt acts as a blocking electrode for the charge transfer between the electrode and the sample. In this case no flash sintering occurred, due to the incompatibility

between the sodium-ion conducting β-alumina and the platinum metal. On the other hand, use of silver (Ag) electrode allowed more efficient electrochemical transfer at the interface, which resulted in flash sintering. Recently, Biesuz and Sglavo [123] reported the effect of different paste material (Pt, C and Ag) between the platinum electrode and the α-alumina (Al_2O_3) dog-bone shaped sample material on the flash sintering behavior. It was found that the onset temperature for flash sintering for a given electric field was lowered by 250°C when silver paste was used, while the highest temperature was observed using Pt paste, shown in Fig. 2-19 (a). The effect was explained by the electrochemical reaction, which was catalyzed by the silver and carbon paste, which improved the conductivity of the material. These studies indicate the importance of the electrode materials in the flash sintering process. Where not only the high melting temperature and oxidation resistance are important factors but also other factors such as the electrochemical interaction between the sample and the electrode obviously plays a significant role [31].

The sintering atmosphere can induce defects in some of the oxides. For example use of reducing atmosphere changes the stochiometric composition in Ceria based materials [12]. This has an influence on the electrical conductivity, which can directly affect the onset conditions for flash sintering. Most of the flash sintering experiments were carried out in ambient conditions and not many studies on this regard are available in the literature. Nevertheless, Zhang and Luo [146] observed a strong dependence of the onset temperature in ZnO under different flash sintering atmosphere. The onset of flash occurred approximately 120°C lower in Ar/5mol% H_2 atmosphere as compared to in air. They attributed this effect to the higher electronic conductivity of ZnO under reducing atmosphere [146].
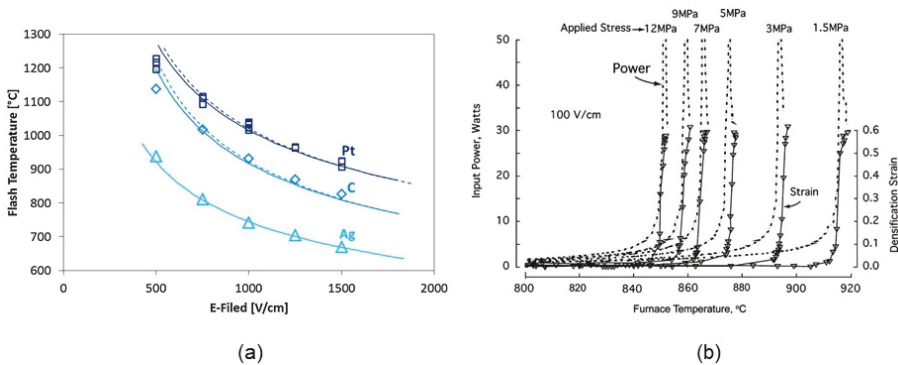

(a)   (b)

41

Figure 2-19 : (a) Onset temperature for Flash sintering of α-alumina (Al_2O_3) dog-bone shaped sample as a function of the applied electrical field for three different conductive paste used, Reprinted with permission from [123], (b) For the same applied electrical field (100 Vcm^{-1}), the onset temperature for flash as a function of applied pressure for 3YSZ pellets in flash sinter forging, Reprinted with permission from [147].

Biesuz et al., [148] studied the effect of thermal insulation of the sample (8YSZ) during the flash sintering enhanced densification. Analytical calculation, which was validated by experimental results, showed an improvement up to 10% of the final relative density by using a thermal insulation around the sample. Application of external pressure has been known to enhance the densification in sintering [57]. It was found that application of uni-axial stress in sinter forging affects the onset temperature. As the stress is increased, the temperature for the onset of flash sintering is lowered [147]. Axial strain was found to be higher than radial strain as the applied pressure was increased, shown in Fig. 2-19 (b).

One of the biggest challenges remains in flash sintering is the accurate measurement of the specimen temperature in real time. Many efforts are being made to accurately measure the specimen temperature during the flash sintering.

- **Proposed mechanisms for flash sintering**

Flash sintering, which comes under the broader group named as electric current assisted sintering technology (ECAS), demonstrate to densify a wide variety of materials at a lower furnace temperature and within very short time. Due to this novelty, scientific interest has been generated to understand the exact physical mechanism of the high sintering rate. Several theories explaining the mechanism behind flash sintering either based on empirical findings or hypothesis have been proposed. However, the exact mechanism responsible for the flash sintering is still under consideration [31,32,34]. One of the primary reasons is also because of the high heating rate and flow of current, it is difficult to measure the specimen temperature accurately in real time, especially during the stage II, where the maximum sintering rate was observed. From the literature, the proposed mechanism can be broadly categorized in three different types: (i) Joule heating, (ii) Grain boundary melting, (iii) Nucleation of Frenkel pairs and (iv) Electrochemical effect.

It is important to point out that a singular mechanism explaining the flash sintering may not enough. More than one mechanism described below may be act simultaneously during the flash sintering, which also strongly depends on the material properties.

(i)   Joule heating

When an electrical current is passed through a material, depending on the resistance and the time, the heat is produced known as the Joule heating. Most ceramics, whether the conduction mechanism is ionic or electronic, have a negative temperature coefficient (NTC) of resistivity in flash sintering condition. It was therefore proposed that the thermal runaway due to the Joule heating leads to increased power dissipation (V^2/R). Two independent works from Todd et al. [114] and Zhang et. al. [118] proposed thermal runaway concept due to the joule heating to explain the flash sintering mechanism. Todd et. al. [114] developed a model by solving the heat equation taking into account the electrical and thermal properties of the material in question (3YSZ) and was able to accurately predict the onset behavior. Zhang et al. [118] have also developed a thermal runaway model for ZnO to explain flash sintering. The model is based on comparing the Joule heating with the heat dissipation. Their model enabled to successfully predict the onset temperature of flash as well.

The modelling results suggested that the peak in the power dissipation curve at the onset of flash could results in higher temperature, which is enough to obtain a rapid densification of the green body [114]. However, Raj and co-workers [149] measured the sample temperature during the flash sintering process by in-situ synchrotron radiation for 3YSZ. They observed a maximum temperature of 1500°C under a peak power dissipation of 1700 mW mm^{-3}. While Joule heating certainly necessary for the onset behavior of flash, it is still not sufficient to entirety explain the flash sintering behavior [112,114,118,150].

(ii)   Grain boundary melting

The second mechanism that is proposed to explain flash sintering is based on the local melting at the interparticle contacts [115,151]. The current density applied during the flash sintering process is measured with respect to the bulk sample. However, the surface area at the interparticle contacts is much smaller as compared to the bulk specimen. Therefore, the current density in microscale could lead to much higher temperature as compared to the macroscale, which may lead to local melting of the sample.

The proposed mechanism based on grain boundary melting suggest that the temperature at the particle to particle contact could be much higher, which may lead to melting and form a liquid phase. The formation of a liquid capillary film could account for rapid densification in flash

sintering. Furthermore, the formation of the liquid film at the interparticle contacts can enhance the electrical conductivity as well [151]. Narayan et. al. [152] developed a grain growth model for flash sintered 3YSZ materials based on free energy calculations. Their analysis suggest that the application of an electric field contributed to the creation and segregation of vacancies at the grain boundaries, which reduce the grain growth rate.

The proposed mechanism of grain boundary melting to explain the flash sintering process is very interesting suggestion. Due to the technological limitations, it is difficult to measure the actual temperature and phenomenon occurred at a microscale. However, the question remains if the grain boundary or interparticle contacts are necessary for the onset of flash, then how can the flash happened not only in dense specimens but also in single crystals [141]. Therefore, further experiment with simulation work is required to validate the proposed mechanism.

(iii) Nucleation of Frenkel pairs

One of the first mechanism that proposed by Raj and co-workers on the flash sintering process was based on the generation of Frenkel defects that are far from equilibrium. They proposed a unified mechanism that explain all the three characteristics of flash sintering, such as high densification rate, abrupt increase in conductivity and electroluminescence. , The mechanism suggested as an electric field induced formation of Frenkel pairs within the lattice [33,119,120,125,129,140,141,147,153–155]. They hypothesized that due to the applied electrical field and moderate temperature Frenkel pairs (a vacancy and interstitial) are created simultaneously both cations and anions and have opposite relative charge. The Frenkel pairs then lose their charge to form holes and electrons, which migrates towards opposite electrode and account for electronic conduction. The recombination of some of the electron-hole pairs give optical luminescence of fixed wavelength. The two uncharged defects (interstitial and vacancy) are driven into the grain boundary and the interstitials to the pores, which contributed in densification. Under the flash conditions, avalanche of these Frenkel pairs are generated which is responsible for the flash sintering process.

The hypothesis of electrical field induced Frenkel pairs nucleation is appears quite interesting mechanism, as it can singularly explain all the three characteristics associated with flash sintering. However, no direct experimental evidence of generation of such defects are reported in the literature. Furthermore, the ionization of single charged ions, e.g. intertitles, requires electric field that are much larger than used in flash experiments [156].

In any of the proposed mechanisms responsible for flash sintering, a direct experimental evidence is still lacking.

(iv)   Electrochemical effect

Application of electric field can change the electrochemical properties of the materials. Blackening of yttria stabilized zirconia caused by electrochemical reduction is a well know phenomenon [143]. The formation of partially electrochemical reduced phases in 8YSZ has been proposed for the flash sintering mechanism [157]. This mechanism is mostly suggested for ionic conductor materials like YSZ. The partial electrochemical reduction in 8YSZ during flash sintering is illustrated in Fig. 2-18. The partial reduction in the ionic conductor materials would result in reduction of the oxidation state of the cations, which will increase the electron density in the material [158]. The enhance electron density may be responsible for the sudden rise in conductivity, which is known as the onset of flash. Moreover, the charged cations under the influence of electric field may diffuse rapidly, which increases the densification rate during the flash sintering.

2.2.5. Flash Spark Plasma Sintering (FSPS)

FAST/SPS as discussed above have become an technologically attractive process to densify a wide variety of materials [70]. It is technologically beneficial to further shorten the sintering time to fabricate fully dense material by FAST/SPS. On the other hand, Flash sintering is very attractive as the densification occurred in some seconds at much lower furnace temperature. However, up to now, flash sintering has been only successfully demonstrated on lab scale. Typical sample geometries are dog bone shaped, small bars and cylindrical pellets with a length in the range of less than 30 mm and an active volume of only a few 100 mm^3. Use of the technology on larger scale was restricted by a lack of fully understanding how parameters required to initiate flash like electric field, furnace temperature, current density and processing parameters like sample size, density of powder compact, kind of electrical contact, atmosphere and thermal radiation interact during the flash event. Therefore, if applying this technology to larger samples, formation of hot spots was observed which prohibits homogenous densification. The limitation was overcome by combination of two technology i.e., FAST/SPS and flash sintering, which is named Flash Spark Plasma Sintering (FSPS) [132,159].

Flash Spark Plasma Sintering (FSPS) is an interesting method to densifying materials shown by Grasso et. al. in 2014 [132]. This process simply involves using Spark Plasma Sintering (SPS) equipment without using the die so that the current is forced through the sample

[66,132,159]. The control of the process is achieved by limiting the maximum power, which is defined as a percentage of the maximum power capacity of the machine. This process has an advantage regarding scaling up the sample geometry and eliminated the need of sample preheating as in flash sintering, for an electronic conductor material. In FSPS process, a pre sintered sample is placed between the graphite punches either without a die or an insulated inlay between the die and punch. Nevertheless, with small modification in the FAST/SPS tool, pre-heating of the sample until the onset temperature can also achieved in FSPS process, schematic of the FSPS setup is shown in Fig. 2-20. Due to the difficulties in measuring the actual temperature during the FSPS, the process is controlled by limiting the power. The sample is discharged under a pre-defined peak power for some seconds. The power is rapidly decreased after the discharge and maintained for a few seconds.
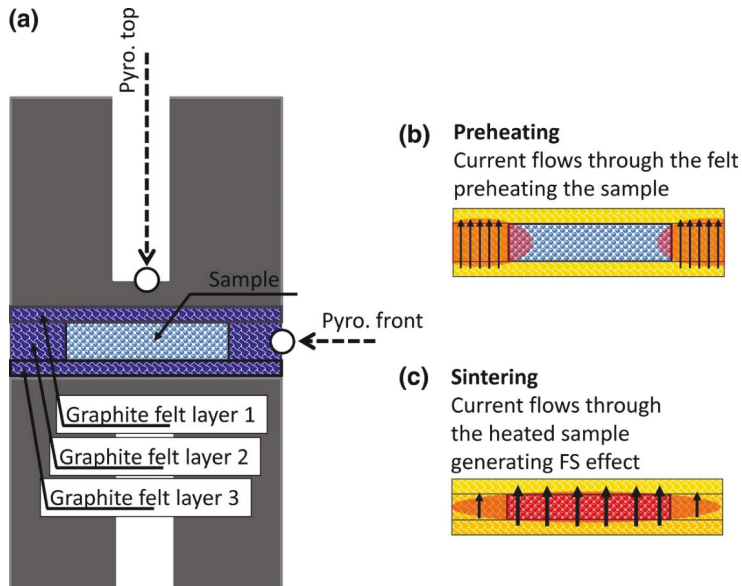
Figure 2-20 : (a) Schematic of the FSPS experimental set up used by Grasso et. al. to densify SiC, (b) The preheating of the sample was achieved with current flowing through the graphite felt and (c) The sintering was achieved by current flowing through the SiC sample [160]

Recent studies show that by using Flash-SPS (FSPS) non-oxide compounds such as ZrB_2 and SiC materials can be densifying in very short time. Additionally, nearly fully dense (Relative density = 98%) crack free SiC sample with diameter of 60 mm has been produced in a hybrid

SPS furnace [132,160]. Nevertheless, their FEM simulation study of the sample temperature shows a temperature gradient of 200-300 °C between the core and the surface of the SiC specimen. Demirskyi et. al. [161] also reported densifying SiC material by FSPS method has showed a bimodal grain size distribution. Using FSPS approach Vasylkiv et. al. [162] successfully densified oxides (i.e. 3YSZ) with a diameter of 20 mm. SEM micrographs of the FSPS YSZ sample revealed the sample exhibit initial crystallite size as the starting particle. However, FSPS is a two-step process where a pre sintering step is necessary for the sample to bear the applied pressure during the process. Also, when a large sample is densified a temperature gradient is observed in the sample.

Unlike flash sintering, FSPS might be industrially attractive process as it can be easily implemented on a larger scale in a conventional FAST/SPS device [25].

2.2.6. Microwave Sintering

Microwave sintering is a field assisted sintering technology, where the microwave energy, which is a nonionizing electromagnetic radiation is utilized to densify a powder compact. Microwave energy is a form of electromagnetic energy with a frequency range between 300 MHz and 300 GHz [65,163–166]. In microwave sintering, electromagnetic energy is supplied directly and penetrates the material volumetrically through molecular interaction to produce internal heat in the powder compact. Microwave sintering is distinguished from the conventional sintering, where heat is transferred to the powder compact by conduction, radiation and convection. In conventional sintering for a large volume sample with a higher heating rate would generate temperature gradient between the core and the surface of the sample. However, in microwave sintering, the heat is generated within the material and heats the entire volume of the sample [165].

 Microwave sintering process is a relatively simple technique to densify powder compacts into bulk products, involving instantaneous transfer of electromagnetic energy into thermal energy rapidly and with high efficiency. The powder compacts are usually placed in an insulated alumina chamber or tube for achieving good thermal insulation. A microwave sintering set-up consists of microwave generator or magnetron, susceptor, heating system and program controller [164]. Schematics of heating pattern in conventional as well as in microwave sintering is shown in figure 2-21 (a and b), while figure 2-21 (c and d) shows the different heating mechanisms in the sample in conventional and microwave sintering.
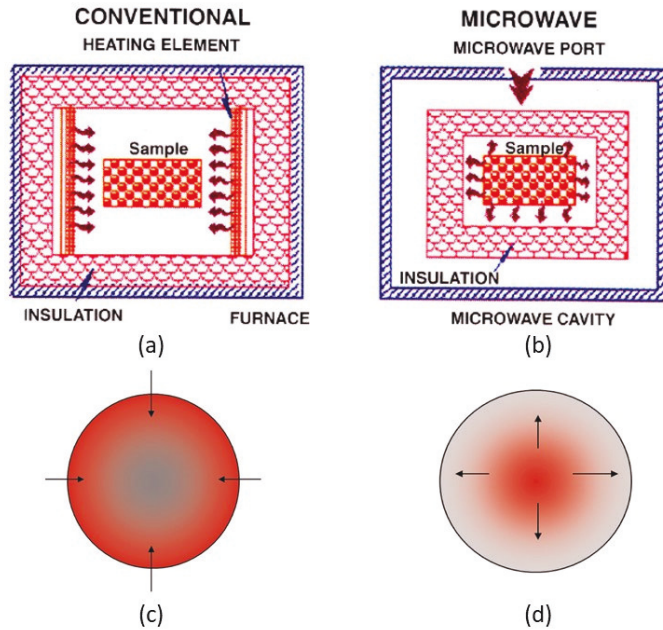
Figure 2-21 : Schematic sketch of the heating procedure (a) conventional sintering and (b) microwave sintering; heating mechanism of the specimen (c) conventional sintering where the heat is transferred from the outer surface to the inner bulk and (d) microwave heating from the inner bulk to the outer surface [164]

Microwaves cause molecular motion by migration of ionic species and/or rotation of dipolar species [163]. The heat generation in the material by microwave sintering greatly depends on the dissipation factor also known as loss factor, which is the ratio between dielectric loss and the dielectric constant of the material. The dielectric constant is a measure of the ability of the to sample retard microwave energy as it passes through and the dissipation factor is the amount of energy that is dissipated in the material. Therefore, a material with high dissipation factor, can be easily heated by microwave energy. Metals, as the microwaves are reflected from the surface do not produce any heat. Materials which transmit the microwaves are classed as insulators and do not produce any heat. On the other hand, materials which are excellent absorbers of the microwave energy can be easily heated and are classified as dielectrics. Figure 2-22 shows different interactions of microwave with materials and resulted heat generation [163].
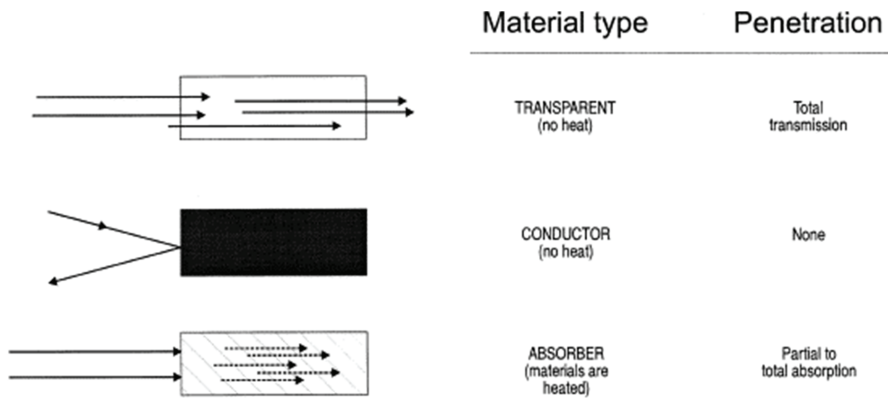
Figure 2-22 : Interaction of microwave with different materials type [163]

Microwave sintering has the potential over conventional sintering processes as a rapid sintering process with a shorter processing time. Usually, microwave energy is more expensive than the electrical energy, primarily due to the low conversion energy efficiency from the electrical energy [164].

Chapter 3 Experimental Methods and Materials

3.1. Starting Powder & Binder

The dissertation focuses on the effect of the electric field/current on the densification behavior of Gadolinium-doped Ceria (GDC), specifically 10mol% Gadolinium-doped Ceria (GDC10). It is already established that physical properties of the starting powders e.g., agglomeration state, particle size distribution etc. greatly affect the sintering behavior [167]. In the beginning of the work, four different commercially available powders were benchmarked with respect to their sintering behavior. From the benchmarking study, a suitable commercially available powder that shows good and reproducible densification behavior is selected. After the benchmarking study all the further studies have been carried out with the selected powder.

Table 3-1: Classification of different GDC10 powders

Name	Manufacturer	Batch No.	Lot No.	Specific surface area (m^2/g)	Particle size distribution (μm) after 3 min ultra-sonification		
					d_{10}	d_{50}	d_{90}
GDC10_C	CerpoTech, Heimdal, Norway	1	#170119A-CGO91	16.83	0.09	0.73	31.44
GDC10_T	Treibacher, Althofen, Austria	1	#EA35/12.1	7.86	0.05	0.07	20.46
GDC10_D	DKKK*, Osaka, Japan	1	#12640	7.64	0.35	1.03	4.07
GDC10_F	FuellCellMaterials, Ohio, United States	1	#AB050	10.57	0.09	0.50	3.14
		2	#CB080	10.50	0.07	0.13	1.9

*DKKK: DAIICHI KIGENSO KAGAKU KOGYO CO., LTD

Table 3-1 summarizes four different commercially available GDC10 powders which are used in the current work. It is obvious that the powders differ in particle size distribution and specific surface area. GDC10 powder with same specifications from FuelCellMaterials, USA was purchased two times therefore, they are defined as batch 1 and batch 2.

Commercially available organic binder Duramax B-1000 (Rohm and Haas France SAS, BP, France), ready to use as aqueous emulsion was used as binding agent for preparing the dog-bone shaped samples, which were used in the flash sintering studies [168]. The binder is supplied as pre-dispersed in water with 55% solids content. It has low glass transition temperature (-26°C), density of 1.05 g/ml at 23°C, with pH in a range of 9.0-9.8 and viscosity of <140 cP (Brookfield # 2.60 rpm). The B-1000 binder is used for enhancing strength of the green ceramic samples. The powder was mixed with a 2 wt% binder and pressed uniaxially in a die to the shape of a dog-bone under a pressure of 100 MPa (more details in section 3.2.1). The weight loss profile of binder starts at 350°C and end completely at 550-600°C [168]. The burnout of the binder from the dog-bone shaped samples were carried out at 600°C (heating /cooling rate: 3° C/min) in air by holding at this temperature for 1 hour.

3.2. Processing Techniques

3.2.1. Sample Preparation

- **Conventional free sintering**

For conventional free sintering experiments, pellet shaped samples were prepared by uni-axially cold pressing of the starting powder. The conventional free sintering experiments were carried out in two different methods:

    (i)   Free sintering in a high temperature furnace (bench-top type, Nabertherm)

    (ii)   Vertical Dilatometer (TMA 402 F1 Hyperion, Netzsch GmbH)

The sintering studies in conventional free sintering experiments were carried out with 20 mm diameter sample and the dilatometer experiments were carried out with a 8 mm diameter sample, which are pellet shaped. In both experiments the height of the sample was between 5-7 mm. For both experiments, the green pellets were prepared by pouring the dry starting powder in a commercially available evacuable die, with respective diameter [169].
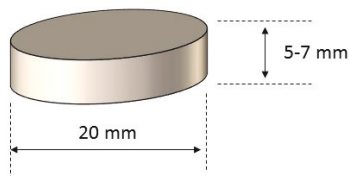
Figure 3-1 : (a) Evacuable pressing tool used for preparing pellet shaped samples and (b) sketch of the pellet used for conventional free sintering studies

Figure 3-1 shows the pressing tool used for uni-axially cold pressed pellet shaped green body samples and a sketch of the sample used for conventional free sintering studies. The pellets were prepared by using no external additives or binder. The green relative density of the green samples varies between 45-55 % depending on the applied uni-axial pressure used for compaction.

- FAST/SPS

The tools for FAST/SPS consisted of a die and punch, which were made of graphite material (graphite type R7710, SGL Carbon GmbH, Germany). A graphite foil with a thickness of 0.34 mm (SGL Carbon) is placed between the die and punch and between the powder and punches (only for the tool shown in Fig. 3-2 (a)), which ensured good electrical contact and easy remove of punches and sample after the FAST/SPS cycle. In the current study, two different types of FAST/SPS tool configuration are used, shown in Fig. 3-2.

- (i) Pressure Assisted (PA) tool
- (ii) Pressure Less (PL) tool

The PA tool has a wall thickness of 10 mm and an internal diameter of 20 mm, as shown in Fig. 3-2 (a). The PA tool is the conventional FAST/SPS tool configuration [70]. In the case of PA tool, 6 g of powder is poured into the die between two graphite punches (upper and lower

punch). Then the powder was pre-compacted at room temperature with an uni-axial pressure of 50 MPa, achieving a relative density of the green compact of approximately 52-55%.
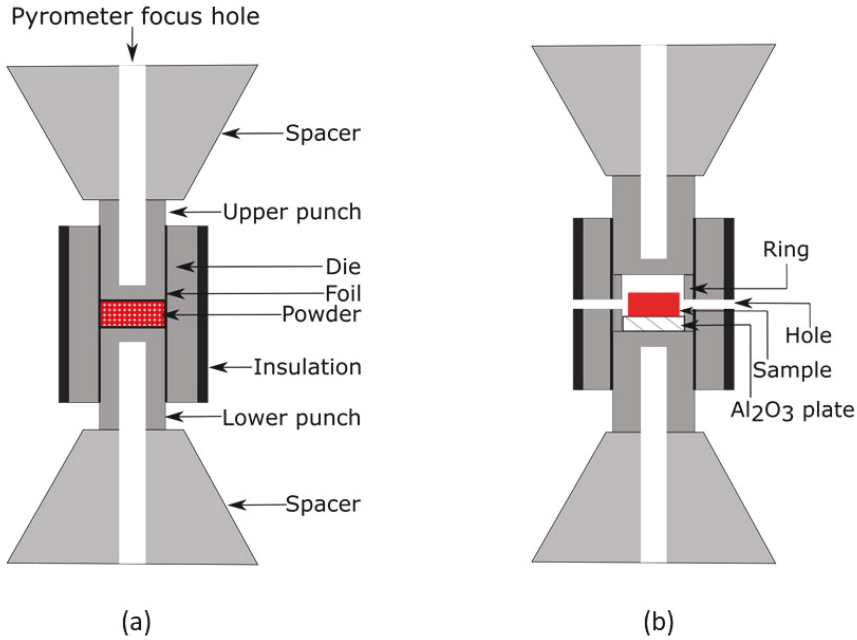

Figure 3-2 : FAST/SPS tool configuration: (a) pressure assisted (PA) tool set up and (b) pressure less (PL) tool set up.

The PL tool configuration consist of a die with an internal diameter of 30 mm, two punches and a graphite ring with external and internal diameter of 29.8 mm and 24 mm respectively. The ring is placed inside the die between the two punches, forming a cavity between the two punches. In case of PL tool configuration, a pellet shaped sample uni-axially cold pressed at 50 MPa with a diameter of 20 mm (mass 6 g), a height of 3.6 mm and a relative density of around 50% was placed inside the cavity, as shown in Fig.3-2 (b). To avoid any contact between the sample and the tool (lower punch), the sample was placed on an alumina plate (thickness 4 mm). Two 4 mm holes were drilled through the die and the ring, which enables gas exchange through the cavity. With PL tool configuration, no load was applied on the sample. It was completely isolated from the tool and sit freely inside the cavity.

- **Flash sintering**

Four different sample geometies were used in the flash sintering study. Dog-bone shaped samples (with a gage length of 15 mm) were used for most of the flash sintering experiments. However, for electrochemical blackening experiment at Prof. Sglavo's laboratory, University of Trento, dog-bone shaped sample with a gage length of 20 mm was used. Additionally, some fundamental studies on flash sintering i.e., role of Debye temperature and in-situ flash sintering experiments in synchrotron, Brookhaven National Laboratory, USA were carried out with a rectangular bar shaped sample. The four different samples are defined for simplification.

  i.   Dog-bone-1
 ii.   Dog-bone-2
iii.   Rectangle bar-1
 iv.   Rectangle bar-2

i.   Dog-bone-1: Flash sintering studies at University of Colorado Boulder, were carried out with dog-bone shaped samples. The powder was mixed with a 2 wt% binder (Duramax B-1000 binder) and pressed uniaxially in a die to the shape of a dog-bone under a pressure of 100 MPa. Fig. 3-3 shows the dimensions of the dog-bone die configuration. The die was made from stainless steel. Dog-bone-1 samples had a gage length of 15 mm, a width of 3.3 mm, and a thickness of 1.95±0.15 mm. The amount of powder used for these specimens was 1.0±0.1 g.

The green body samples were too fragile to connect to the electrodes. Therefore, they were heated to 600° C for 1 hour to remove the binder, and then pre-sintered at 1000°C for 30 minutes with a heating and cooling ramp of 3°C min^{-1}. The density of the pre-sintered samples, measured from the weight and the physical dimensions, was approximately 62.5% for sample design (i) and (iii).
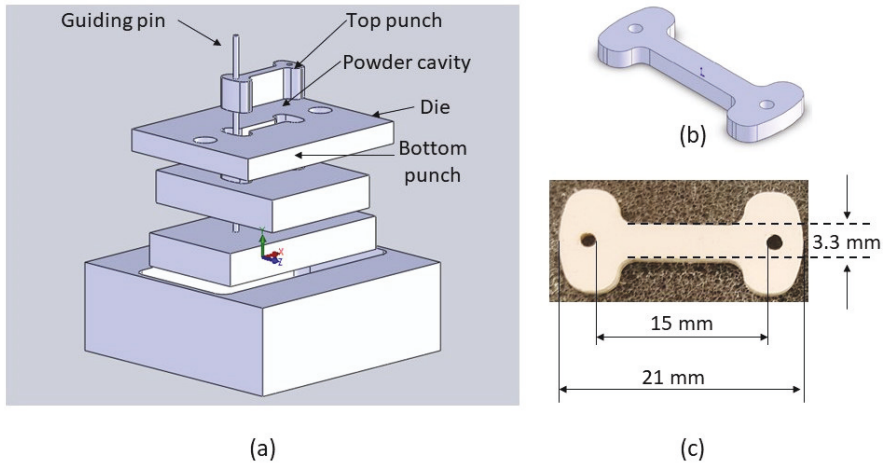
Figure 3-3 : (a) Schematics of the dog-bone die design, (b) schematic of the dog-bone shaped specimen and (c) actual uni-axially pressed dog-bone specimen with dimensions

ii. Dog-bone-2: Electrochemical blackening experiments were carried out at Prof. Vincenzo M. Sglavo's lab, Department of Industrial Engineering, University of Trento, Italy. Dog-bone samples were produced (uni-axially pressed of 100 MPa) with a gage length and cross section of 20 mm and 3.0 x 2.0 mm², respectively. The samples were sintered at 1250°C for 2 h (heating rate of 10 K min^{-1}) in air. The relative density of the sintered dog-bone shaped samples were around 90%.

iii. Rectangle bar-1: The sample for the in-situ flash sintering study in synchrotron were prepared from a die, with a rectangular cavity for producing rectangular bar shaped sample of 7 mm length, 1.6 mm width and 1 mm in height. The processing conditions for producing the rectangle bar-1 was same as in for dog-bone-1 samples.

iv. Rectangle bar-2: The fundamental study on the role of Debye temperature were carried out on a dense rectangular shaped sample. The GDC10 powder was uniaxially pressed at 50 MPa into a pellet, 20 mm in diameter and 5 mm height. The green pellet was then pressed again by a cold isostatic pressing (CIP) at 300 MPa. The CIPed samples were free sintered in a high-temperature furnace (Nabertherm, Germany) at 1500 °C, 4 hours dwell, heating and cooling rate 3°C/min in air to achieve full density. The relative density of the sintered samples was 99%, measured by the Archimedes method. 7 mm length, 1.6 mm width and 1 mm in height, rectangular samples were carved from the dense pellets.

3.2.2. Sintering Equipment and Experiment

- **Conventional sintering and dilatometry**

Conventional free sintering of the pellet shaped samples produced by uni-axially cold pressing of the GDC10 powders were carried out in a Nabertherm LH30/14 high temperature chamber furnace [170]. Sintering was carried out either under ambient atmosphere conditions or under Argon or Ar/2.9% H_2 by flowing of the respective gas throughout the complete sintering cycle.

Dilatometry of the pellets was performed by thermo-mechanical analysis (TMA 402 F1 Hyperion, NETZSCH, Germany) for monitoring the in-situ shrinkage of the sample. In the dilatometer experiment only the axial shrinkage as a function of temperature was measured.

Sintering cycles in the conventional free sintering (both in conventional high temperature furnace and dilatometer) were always carried out at a heating and cooling rate of 3°C/minute. The sintering temperature and the dwelling times were varied for specific experiments and will be mentioned in the results section.

- **Field Assisted Sintering Technology/Spark Plasma Sintering (FAST/SPS)**

Field Assisted Sintering Technology/Spark Plasma Sintering (FAST/SPS) process was carried out using a FCT-HP D 5/2 device, (FCT System GmbH, Rauenstein, Germany) [102]. The equipment is shown in Fig. 3-4. The FAST/SPS device is equipped with a uniaxial hydraulic press (pressing force up to 50 kN) and with a 37 kW power source. The FAST/SPS device can achieve a maximum temperature of 2400°C at a maximum voltage of 8V. The temperature was controlled by an axial pyrometer, which measured the temperature from the upper punch.

Figure 3-4 : FAST/SPS FCT-HP D 5/2, FCT system GmbH at IEK-1, Forschungszentrum Jülich GmbH

The FAST/SPS device can be operated under intermediate vacuum (around 0.6 mbar) wich was achieved by an inbuilt vacuum pump. Furthermore, different gases e.g. Ar, Ar/2.9%H_2, N_2 and technical air can also be used in the device, which enables FAST/SPS cycles under different atmospheres. Operating with gases is generally done at a chamber pressure 30 ±5 mbar higher pressure than the atmospheric pressure. All experiments were done under dynamic gas flow, which means the gas is constantly flowing through the chamber during the whole FAST/SPS cycle.

In addition to the above mentioned FAST/SPS device, some of the FAST/SPS cycles, specifically the densification and grain growth as a function of temperature study were carried out at our project partner at Institute for Materials Applications in Mechanical Engineering (IWM), RWTH Aachen. FAST/SPS cycles were carried out in vacuum using FCT HP D-25-2, FCT system GmbH. All the processing parameters e.g. graphite tool geometry and materials remains same as described above.

To sinter the GDC10 material in reducing atmosphere followed by controlled re-oxidation, it is necessary to measure and control the partial pressure of oxygen of the FAST chamber.

The partial pressure of oxygen was monitored during the FAST/SPS cycle under reducing and oxidation atmospheres. Oxygen sensor (SGM7) from ZIROX has been used for measurement of the oxygen partial pressure. In figure 3-5, sketch of the FAST/SPS chanmber and the position

of the oxygen sensor is shown. Please note that the oxygen sensor does not function in vacuum conditions as a continuous gas flow of 5-10 l/h is required for the measurement.
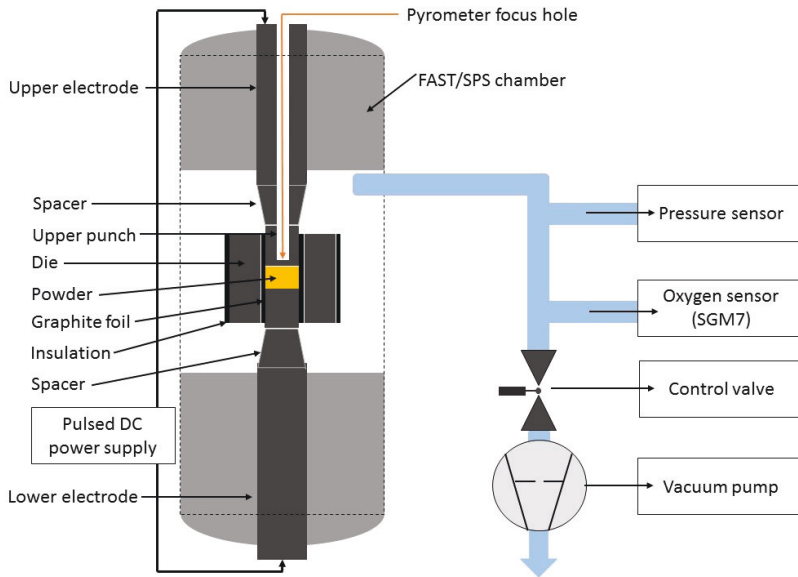

Figure 3-5 : Sketch of the FAST/SPS device showing the position of the oxygen sensor.

- **Flash sintering**

Flash sintering of GDC10 materials were carried out at three different locations, (i) Prof. Rishi Raj's laboratory, University of Colorado Boulder, USA, where the majority of the flash sintering work was carried out, (ii) beamline XPD 28ID-2 of the National Synchrotron Light Source II (NSLS II) at Brookhaven National Laboratory, USA and (iii) Prof. Vincenzo M. Sglavo's lab, Department of Industrial Engineering, University of Trento, Trento, Italy. The flash experimental set up at each of the location is described below:

(i)   Set up at Prof. Rishi Raj's laboratory, University of Colorado Boulder, USA

The flash sintering experiments were carried out in a vertical tubular furnace custom made set up, as shown in Fig. 3-6. The tubular furnace used is a Barnstead Thermolyne 21100 tube furnace, with a maximum operating temperature of 1400°C. The pre-sintered specimens were connected to a pair of platinum wires wrapped through the holes in the ears of the dog-bones.

Platinum paste was applied by a brush for good electrical contact. The specimen was hung with the platinum wires into the hot-zone of the tubular vertical furnace. Electrical power was fed to the specimen from a Sorensen DLM 300-2 (AMETEK Programmable Power, San Diego, CA, USA) power source. The current was measured with a digital multi-meter (Keithley 2000, Keithley Instruments, Cleveland, OH). The communication and control of the power supply was achieved by DAQ USB-6008 (National Instruments). The General Purpose Interface Bus (GPIB) was used to communicate with the multimeter, the device that monitors the current.
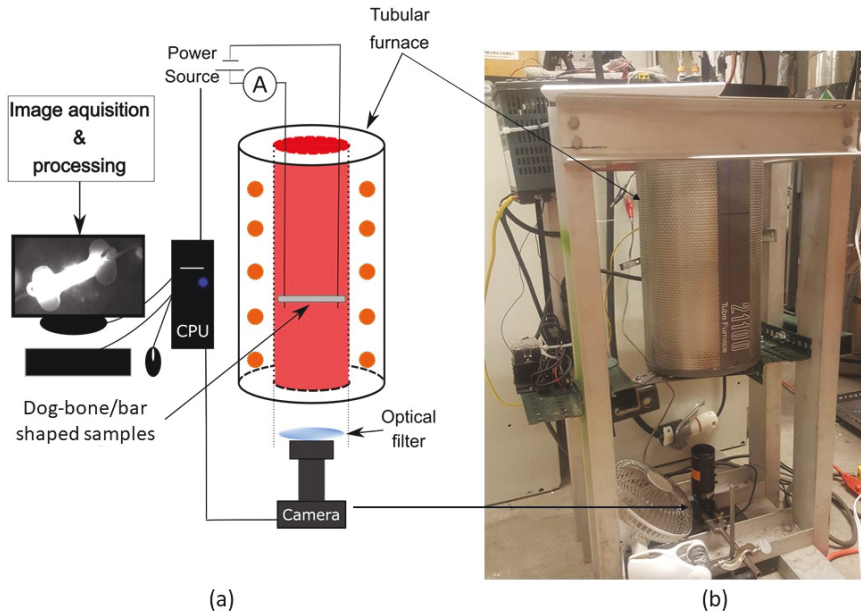
Figure 3-6 : Flash sintering set up at University of Colorado Boulder, USA; (a) sketch of the flash sintering set up and (b) photo of the vertical tubular furnace used for the flash sintering experiment

Data were acquired through a graphical user interface (GUI) developed in-house at Boulder, running on the MATLAB platform. The voltage expressed across the specimen was measured at the power supply. The power consumed in the sample (per unit volume) was calculated as the product of current density and electric field. The sample shrinkage was recorded through a digital camera with optical filters placed at the bottom of the furnace.

(ii)　　NSLS II at Brookhaven National Laboratory, USA

The in situ flash sintering experiments at the beamline XPD 28ID-2 of the National Synchrotron Light Source II (NSLS II) at Brookhaven National Laboratory using a wavelength of 0.18203 Å (68.112 keV), USA were carried out in a quadrupole lamp furnace [171,172]. The set up consisted of a sample holder, made with an alumina rod, which was place within the furnace, as shown in Fig. 3-7. The furnace can be operated at a maximum temperature of 2000°C. Platinum wires were wrapped around the rectangular bar shaped samples with some platinum paste to obtain good electrical contact. The diameter of the incident beam was approximately 500 μm. A monochromatic X-ray beam travels through the rectangular bar shaped specimen. The experimental set up used for the experiment is explained in the literature [136].
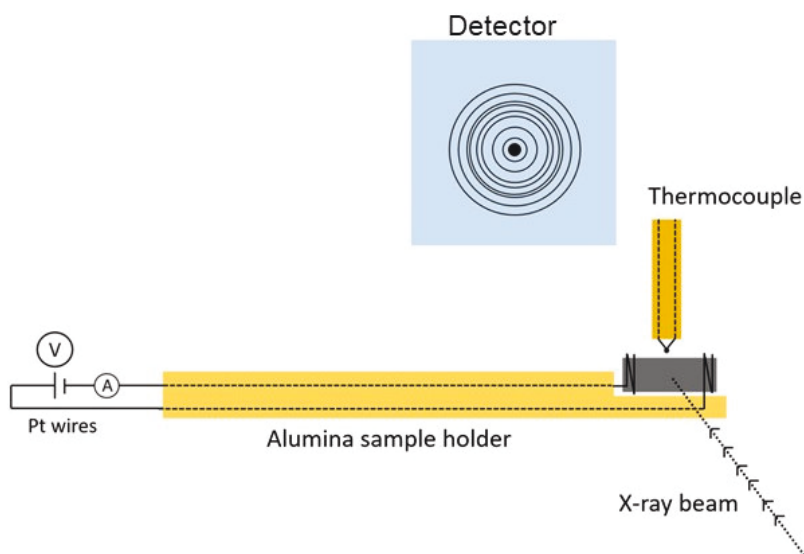
Figure 3-7 : Experimental set up for the in situ flash sintering experiment at NSLS-II [136]

The pre-sintered samples were place on a sample holder, which was made with an alumina rod. Power was supplied from a 600 W DC power supply (Sorensen 300-2) and the current was measured with a Keithley multimeter. Data was acquired through a graphical user interface (GUI) developed in-house at Boulder, running on the MATLAB platform. All the experiments were carried out at constant furnace temperature of 680°C.

(iii)   At Prof. Vincenzo M. Sglavo's lab, University of Trento, Italy

The flash experiment was carried out in air on a hot plate at about 280°C (constant temperature). The dog-bone sample was placed on the hot plate on an alumina disc. The temperature of the hot plate was monitored by a thermocouple, as shown in Fig. 3-8. Platinum wires served as electrodes and were connected to a DC power supply (Sorensen DLM 300-2). To improve the ceramic-metal contact Platinum paste was spread at the interface. An electric field of 175 V cm^{-1} was used to activate the flash and the current limit was fixed at 25 mA mm^{-2}. Electric data were monitored using a Keitheley 2100 multimeter (Keithley Instruments, Cleveland, USA) and a video of the experiment was taken using a digital camera with the aim to check the presence of electrochemical blackening.
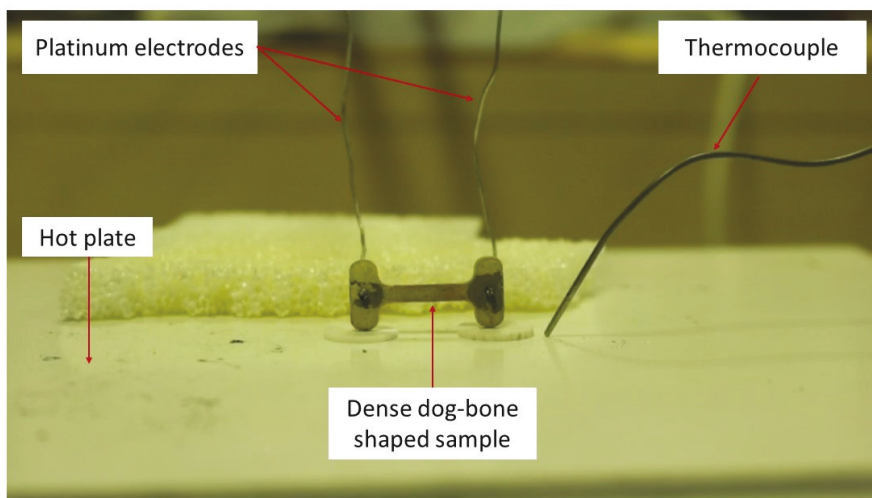
Figure 3-8 : Iso-thermal flash experiment on a hot plate with dense GDC10 sample at a constant temperature of 280°C, applied DC field 150 Vcm^{-1} and maximum current density 25 mA mm^{-2}. The chromatic alteration of the sample is observed by using a CCD camera.

▪ **Flash experiment mode used in this study**

The voltage and current control is a fundamental feature of the flash sintering method. The process is therefore running by software that is interfaced with the various components of the flash system. It controls the process in real time. The experiments can be carried out in two modes, voltage-to-current and current-rate. Most experiments are carried out in the voltage-to-current mode, where a constant electric field is applied to a powder-pressed "green specimen".

The furnace temperature is then raised at a constant rate, typically 10°C/min. The flash is signaled by a sharp rise in the conductivity of the sample and a rapid increase in the current flowing in the sample. The current is then controlled by switching the power supply from voltage-to-current control, which is set to a prescribed limit, which is known as constant heating rate (CHR) flash experiment. The furnace temperature at which the abrupt increase in the specimen conductivity is observed is known as onset temperature.

The voltage-to-current experiments can also be carried out by holding the furnace at a constant temperature and applying either a constant electric field or as a step voltage, known as Iso-thermal flash experiment. In either case a combination of furnace temperature and electric field characterize the onset of the flash, while the magnitude of the current limit determines the extent of densification.

Second flash mode, which was developed very recently, called as current-rate (CR) flash is an alternative way to initiate flash. In CR flash mode, the current is controlled from the beginning of the experiment and raised at a constant rate. After certain current density (incubation time) the self-generated voltage of the sample drops rapidly and the saturated. The highest peak in the voltage profile in current control mode is defined as the onset of flash.

In the current work, three different mode of flash sintering experiments were carried out as shown in Fig. 3-9. All the flash sintering experiments were carried out in direct current (DC) power mode. The maximum current density applied electrical field and furnace temperature were varied for different experiments. These values will be specifically discussed in the result section for individual experiments.
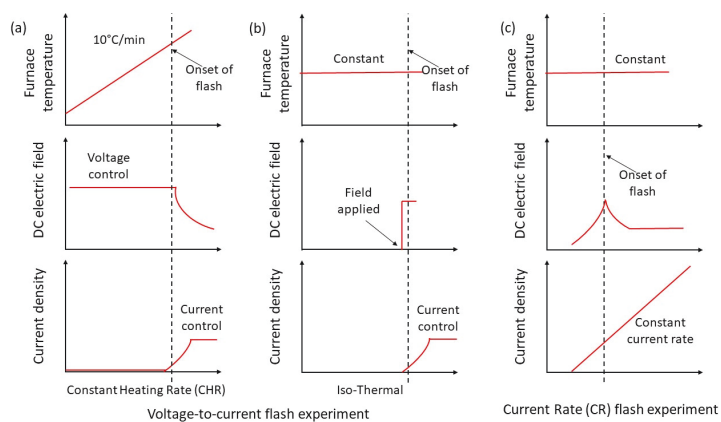
Figure 3-9 : Different flash mode used in the current work: (a) constant heating rate, voltage-to-current flash experiment, (b) iso-thermal, voltage-to-current flash experiment and (c) current rate flash experiment

The exact flash sintering parameters used for each experiment is discussed in the results and discussion section. However, the range of flash sintering parameters used during this work is summarized in Table 3-2.

Table 3-2: Flash parameters range used during this work

Flash experiment mode	DC electric field (V/cm)	Current density (mA/mm^2)	Furnace temperature (°C)
Voltage-to-current flash (constant heating rate)	50 - 2000	100- 200	Constant heating rate (10°/C)
Voltage-to-current flash (isothermal)	90	50 - 800	680°C
Current rate flash (isothermal)	Self-generated by the electrical resistance of the specimen	200	680°C

3.3. Characterization

3.3.1. Particle Size Distribution (PSD)

The particle size distribution of the starting powder was characterized with the laser diffraction particle sizing LA-950 (2 laser diodes, HORIBA analyzers). The particle size was measured with the as received powder and then the powder was mixed with ethanol and dispersed for 3 minutes for measuring the particle size distribution for the second time. The initial particle size distribution provides information about the agglomerated state of the powder, whereas the particle size distribution after the ultra-sonification, which results in breaking of the soft agglomerates in the starting powder, provides information about the primary particle size.

Laser diffraction is a widely used particle sizing technique for materials ranging from hundreds of nanometres up to several millimetres in size [173]. From laser diffraction analysis, diffraction patterns of a laser beam passed through an object. When a light beam strikes a particle, it may diffract, reflect, refract or be absorbed and radiate. Laser diffraction particle size analysis is based on the principle that particles of a given size diffract light through a given angle, the angle increasing with decreasing particle size [174]. The principle of a general laser diffraction technique is shown in Fig. 3-10.
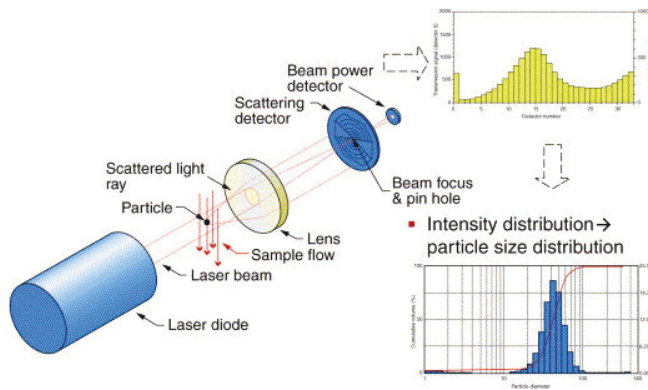

Figure 3-10 : Schematic representation of the principle of the laser diffraction analysis for measuring the particle size distribution (PSD), Reprinted with permission from [174].

A general laser diffraction equipment for measuring the particle size distribution has (a) a light source (usually a laser) and a beam processing unit, typically a beam expander with integrated

filter to generate a monochromatic, coherent and parallel beam having a diameter of a few millimeters, (b) a stream of dispersed particles (in liquid or air) at an appropriate concentration, usually between the windows of a sample cell, crossing the laser beam within the focal distance of (c) a positive Fourier lens or set of lenses that focus the laser beam onto (d) a multi-element detector, located in the focal plane of the lens, to measure the intensity of the original or remaining light beam and the intensities of the scattered light by the particles at different angles, (e) an interface and a computer to process the measured detector signals, usually after averaging a number of detector read outs (sweeps) , into an average particle size distribution. This procedure needs an appropriate optical model for the light scattering by the particles and some mathematical de-convolution procedure, because several particles are simultaneously present in the beam.

3.3.2. Density Measurement

Correct density measurements are an important characterization for analysing the sintering property of the sample. In the current work, relative density of the samples was measured by two methods. The bulk density of the powder compact (green density) was measured from the physician dimension and the mass of the sample.

ρ (g/cm^3) = mass (g)/volume (cm^3)   eq. 3-1

where, ρ is the density of the sample.

The second method used for measuring the bulk density of the samples, specifically the dense samples was by Archimedes' principle. Archimedes' principle states that the buoyant force on a submerged object is equal to the weight of the fluid that is displaced by the object. The bulk density of the sample was calculated from precise measurement of the mass of the sintered samples in dry, saturated and suspended state. According to the Archimedes' principle, the bulk density of the sample is given by equation 3-2:

$$\rho_{bulk} = \frac{m_{dry}\, \rho_{liquid}}{m_{saturated} - m_{suspended}}$$ Eq. 3-2

Where, ρ_{bulk} is the bulk density of the sample, m_{dry}, $m_{saturated}$, $m_{suspended}$ is the mass of the sample in dry, saturated and suspended state respectively. ρ_{liquid} is the density of the suspending liquid with distilled water as a liquid medium. Here it should be noted that for the density calculation of the flash sintered dog-bone shaped sample, only the gage sections were considered.

The relative density ($\rho_{relative}$) of the sample is then measured from the ratio between the bulk density of the sample and the theoretical density of the material, assuming a theoretical density for GDC10 of 7.22 g cm^{-3}.

3.3.3. Microstructure Analysis

The starting powder, microstructure and the grain size of the sintered samples were analysed from the Scanning Electron Microscopy (SEM) micrographs. Additionally, primary particle morphology of the starting powder (only for GDC10, FuelCellMaterials) was also imaged by Transmission Electron Microscopy (TEM) techniques, FEI Titan G2 80-200 ChemiSTEM microscope.

For imaging the micrographs of the starting powder (both in SEM and TEM), the powder was dissolved in ethanol and dispersed for 10 minutes by ultrasonic dispersion. A monolayer of the solution is carefully spread onto the surface of the conductive graphite foil, which was placed on the sample holder. For microstructure analysis of the sintered samples, the samples were embedded with epoxy. After having the embedded samples, they were cut exactly in the middle using ATM "Brillant 221" precision cutting machine. After cutting, the samples were then grinded and polished by standard metallography technique.

- Metallography procedure

The standard metallography steps include grinding of the sample, which was done on the ATM "Saphir 550" programmable grinding machine. The grinding of the sample was done starting from 80 grade grit SiC paper and followed by 120, 400, 800, 1200, 2500 and 4000 grade grit paper. After grinding, the final step was polishing of the samples. The grinded samples were polished by 3μm, 1μm diamond solution and finally with 50nm colloidal silica suspension with Buehler "Minimet1000" polishing device for individual samples, with planetary motion.

- Thermal etching procedure

After polishing, the samples were then removed from the embedded epoxy resin by carefully removed the epoxy by cutting them. The samples were then thermally etched by annealing at 150 °C below the sintering temperature for 20 minutes, to reveal the grain boundaries. The heating and cooling rate used during the thermal etching process was 3°C per minute. The specimens with then sputter coated with platinum, achieving a thickness of approximately 1 nm.

- SEM micrograph

The microstructures were imaged with a table top SEM (Phenom, Fei Company, Oregon, USA) and an Ultra 55 SEM (Carl Zeiss Microscopy, Oberkochen, Germany) for different magnifications. The former one used primarily for the grain size analysis of the flash sintered samples, in which only back-scattered electron (BSE) images can be obtained. The latter one is equipped with both secondary electron (SE) and BSE imaging modes to obtain micrographs with high magnification. The morphology of the starting powder were imaged by Ultra 55 SEM.

3.3.4. X-ray Diffraction (XRD) Analysis

X-ray powder diffraction (XRD) is a rapid analytical technique primarily used for phase identification of a crystalline material and can provide information on unit cell dimensions. The analyzed material is finely ground, homogenized, and average bulk composition is determined.

Max von Laue, discovered in 1912 that crystalline substances act as three-dimensional diffraction gratings for X-ray wavelengths similar to the spacing of planes in a crystal lattice. X-ray diffraction is now a common technique for the study of crystal structures and atomic spacing. X-ray diffraction is based on constructive interference of monochromatic X-rays and a crystalline sample. All diffraction methods are based on generation of X-rays in an X-ray tube. These X-rays are directed at the sample, and the diffracted rays are collected. X-ray diffractometers consist of three basic elements: an X-ray tube, a sample holder, and an X-ray detector. Detailed theory and application of X-Ray diffraction technology can be found in literature [175]. The interaction of the incident rays with the sample produces constructive interference (and a diffracted ray) when conditions satisfy Bragg's Law:

$$2d \sin \theta = n\lambda \qquad\qquad (3.3)$$

This law relates the wavelength of electromagnetic radiation to the diffraction angle and the lattice spacing in a crystalline sample. These diffracted X-rays are then detected, processed and counted. By scanning the sample through a range of 2θ angles, all possible diffraction directions of the lattice are attained due to the random orientation of the powdered material. Conversion of the diffraction peaks to d-spacing allows identification of the phase composition because each phase has a set of unique d-spacing. Typically, this is achieved by comparison of d-spacings with standard reference patterns [175].

In the present work, the phase analysis and lattice parameters of the starting powder and sintered samples were investigated by X-ray diffraction technique in two different experimental set-ups.

(a) Standard X-ray diffraction at room temperature

The phase analysis of the starting powder as well as sintered specimens were investigated by using a standard X-ray diffraction device (XRD, D4; Endeavor-Bruker AXS GmbH, Germany).

(b) High Temperature X-ray diffraction (HTXRD)

Ceria based materials, like GDC10 is prone to loose oxygen from its original lattice sites under reducing atmosphere [176]. The reduction of GDC10 material under reducing atmosphere depends both on the partial pressure of oxygen $P(O_2)$ and temperature [12]. The reduction of GDC10 is accompanied by lattice expansion, which leads to the macroscopic volume change of the sample. This volume change during the constrained sintering (like in FAST/SPS) under low oxygen partial pressure could generate high internal stresses in the sample, which could disintegrate the sample.

HTXRD technique is used to study the behaviour of GDC10 powder in air, vacuum and reducing atmosphere (Ar/2.9% H_2) at a constant partial pressure of oxygen. Powder X-ray diffraction data in the scanning range of 2θ between 25–145° were collected using a high-temperature X-ray diffraction spectrometer (Diffractometer: EMPYREAN, PANalytical) using CuKα irradiation.

The HTXRD measurement temperature was programmed as follows:

Heating and cooling rate: 3°C/ minute

Temperature steps: 25°C, 100°C, 200°C, 300°C, 400°C, between 400°C to 1000°C at each 50°C interval.

Dwelling time: at each temperature step above 200°C, measurements were taken after a 20 minutes thermal stabilization time.

The same temperature interval and dwelling time is followed during cooling cycle as well

3.3.5. Differential Thermal Analysis (DTA) / Thermogravimetric Analysis (TGA)

Differential thermal analysis/thermogravimetry analysis (DTA/TGA) provides information about the enthalpy, thermal capacity, mass changes and the coefficient of thermal expansion. In the current work, DTA/TGA analysis were carried out to study the non-stochiometric information of the GDC10 powder under reducing atmosphere. The DTA/TGA was done with the thermal analyzer STA449 F1 Jupiter coupled to the mass spectrometer QMS 403C, Aëolos both from the company Netzsch. The DTA experiment records the temperature differences between the sample and a reference during the thermal treatment. During a TGA experiment, the changes in weight are measured in dependence on temperature and give information about the thermal stability, the purity and the presence of humidity in a sample.

3.3.6. Data Analysis

- Shrinkage in flash sintering

The shrinkage strain was measured during the live flash sintering experiments with the equation given below. The strain is plotted as a function of time, current density or temperature for all flash sintering experiments. The linear strain is translated into the sinter density by

$$\ell n\left(\frac{\rho}{\rho_g}\right) = 3\ell n\left(\frac{L_0}{L}\right)$$

(3.4)

where ρ is the sinter density and ρ_g is the green density, while L_0 and L are the initial and the time dependent gage lengths. The equation assumed that the dog-bone shaped specimens have isotropic shrinkage in all the directions.

- Grain size measurement

Average grain size of the sintered body was determined by the linear intercept method from the SEM micrographs. The method involved measurements on the microstructural images of thermally etched polished samples with clear visible grain boundaries. The test line was drawn on the SEM micrographs with known distance and number of grains (intercept) within that line was counted. For generating the statistics minimum 500 randomly selected grains were measured for each sample. Linecut for Matlab software was used for determining the average grain size from the SEM micrographs [177].

Chapter 4 Results and Discussion

4.1. Benchmarking of GDC10 Powders

4.1.1. Overview

A successful sintering technique should fabricate highly dense samples (usually above 95% of the theoretical density) with small grain size. The microstructure of the final sintered products affects properties of the material and therefore the potential for technological applications. It is well established that the processing steps prior to the sintering step have a significant influence on the microstructural development of the sintered products [41,43]. Specifically, the densification rate and the ability to achieve high final density with homogeneous microstructure strongly depends on the particle size distribution particle packing of the green body, which will influence the green body density. The effect of particle size on sintering is well explained by Herring's scaling law [178], which states that starting powders with similar morphology but smaller sizes results in high sintering rate as compared to the coarser particle size. For example reduction in the starting particle size is expected to result in enhanced densification at lower sintering temperature [179].

Similarly, the particle size distribution can also have a significant effect on the sintering and microstructure of the sintered samples [180]. The use of a broad range of particle size distribution can result in an increase in the packing density, which may enhance the sintering rate. However, the heterogeneous particle size distribution could lead to nonuniform pore and grain size distribution in the sintered sample. On the other hand, a homogeneous particle size distribution with suitable particle sizes result in homogeneous packing of the particles. In this case a high sintering rate with homogeneous grain size can be achieved.

In this work, before starting the sintering studies of GDC10 material, benchmarking of different commercially available GDC10 powder was carried out. As discussed above, the physical properties of the starting powder together with the processing parameters before sintering could influence the densification behaviour and the microstructure of the sintered sample. The aim of the study is that to identify the most suitable commercially available starting powder that shows high densification behaviour among all the investigated powder. The selected GDC10 powder will be used for all sintering studies in this conducted work.

4.1.2. Characterization of the Starting Powder

Commercially available GDC10 powders from four different manufacturers have been acquired at the beginning of this dissertation work. The details of the powders with the manufacturers name and lot number is mentioned in section 3.1. The morphology of the starting powders was analysed by the SEM analysis. SEM micrographs of the GDC10 powders from the different manufacturers are shown in Fig. 4-1.
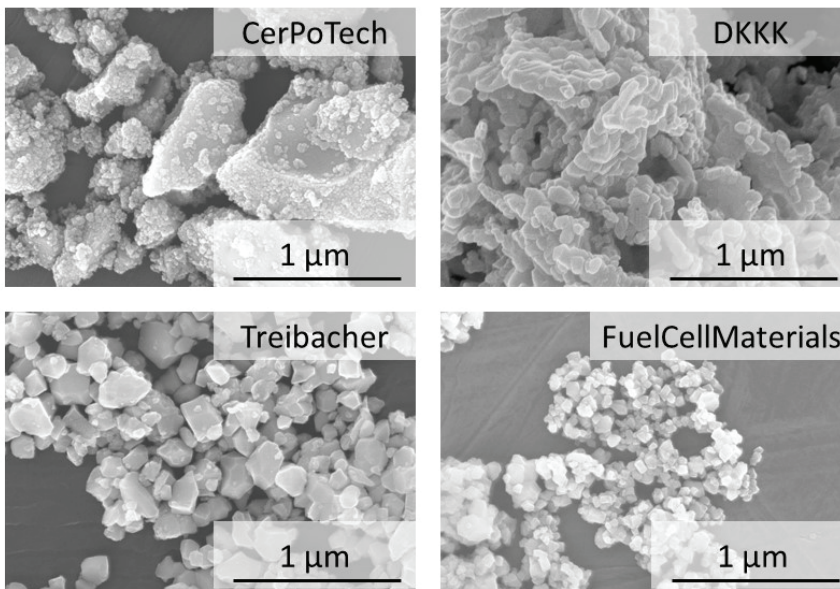

Figure 4-1 : SEM micrographs of the commercially available GDC10 powders from four different manufacturers, showing the primary particle morphology.

It should be noted that the starting powders were dispersed by an ultrasonic treatment to break any soft agglomerates present in the as received powder. It becomes obvious that the powders have quite different primary particle sizes, morphologies and degrees of agglomeration. GDC10 powder from CerPoTech has a quite irregular and inhomogeneous shapes, hinting on a strong agglomeration of very fine primary particles. This assumption is supported by the high specific surface of 16.83 m^2/g. The GDC10 powder from DAIICHI KIGENSO KAGAKU KOGYO CO., LTD (DKKK) has a unique morphology and a specific surface of 7.64 m^2/g.

GDC10 powders from Treibacher and FuelCellMaterials (FCM) have similar morphology. However, FCM powder has smaller primary particle size as compared to the Treibacher powder. This is also confirmed by the specific surface area of the powders, FCM powders have higher specific surface area (10.572 m^2/ g) as compared to the Treibacher powder (7.863 m^2/ g). To conclude if the coarser particles of CerPoTech powders are hard agglomerates, TEM analysis has been conducted for CerPoTech and for FCM powders, as shown in Fig. 4-2.
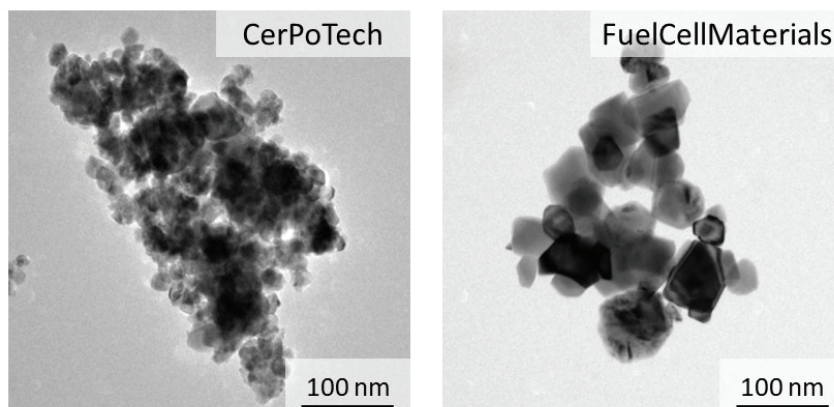

Figure 4-2 : TEM micrographs of GDC10 powders from CerPoTech and FCM, showing the primary particle size.

The primary particles of the FCM powder shows similar morphology as seen from the SEM micrographs. However, TEM micrograph of the GDC10 powder from CerPoTech confirms that the primary particles are much finer and are strongly bonded to form hard agglomerates.

Figure 4-3 shows the cumulative volume percentile results indicating the particle size distribution (PSD) of GDC10 powders from the four different manufacturers. In the PSD graphs, the black lines are the results from the as received powders and the pink lines are the results which were obtained after dispersion of the particles by ultrasonic treatment for 3 minutes. The soft agglomerate states of the powders can be seen from results of the as received powders, which were dispersed by the ultrasonic treatment, indicating the primary particle size distribution.
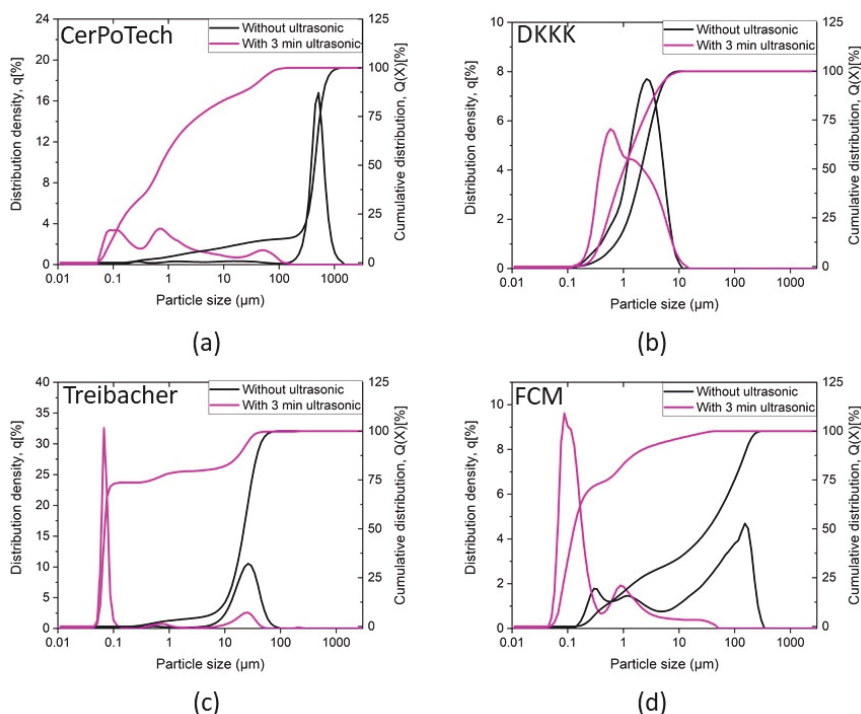
Figure 4-3 : Cumulative volume percentile results indicating particle size distribution for GDC10 powder from (a) CerPoTech, (b) DKKK, (c) Treibacher and (d) FuelCellMaterials.

The PSD result for GDC10 powder from CerPoTech shows the as received powder has very large amount of agglomerates, while after ultrasonic treatment the PSD moves towards finer particle size. However, it still has a very wide range of particle size distribution ranging from few nano meters to 100 micrometre scale. However, we know from the TEM and specific surface area result that the primary particle size lies in nano sized (10-100 nm) range. This suggests the powder consists of many hard agglomerates, which may be difficult to break during the compaction step. On the other hand, PSD data for the GDC10 powder from DKKK, Treibacher and FCM suggests that the as received powder has agglomerates which are easy to disperse by ultrasonic treatment.

The powder characterization study suggests that it is necessary to combine different techniques and careful analysis to make correct interpretation about the physical characteristics of the powder.

4.1.3. Compaction and Conventional Sintering Study

A systematic compaction study at room temperature of all four GDC10 powders was carried out. The compaction study of the powders helps to understand the densification behaviour of the powders. Furthermore, it is beneficial to decide about the optimum handling of starting powder and green pellets.

For understanding the effect of uniaxial compaction pressure, four GDC10 powders were pressed at room temperature at different pressures, as shown in Fig. 4-4. The powders were uni-axially pressed at three different pressures; i.e., 48 MPa, 110 MPa and 254 MPa additionally, the powder was uni-axially pressed at 110 MPa and followed by pressed using cold iso-static pressing (CIP) at 300 MPa.
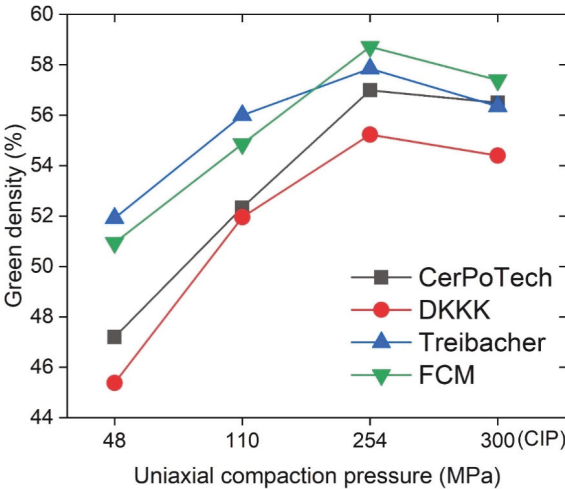

Figure 4-4 : Uniaxial compaction of four different powders at room temperature, the graph shows the green density (measured from the mass and volume of the green sample) as a function of three different uniaxial pressures and one cold isostatic pressure of 300 MPa.

The relative densities of the green samples were calculated by the sample dimensions and mass and using the formula described in equation 3.1. The relative density of the green sample of FCM and Treibacher powders reached above 50% with a compaction pressure of 48 MPa as compared to the powder from CerPoTech and DKKK. The GDC10 powder from FCM and Treibacher have a greater relative density (green body) at all the compaction pressures except in the case of the sample prepared with CIP. The green samples prepared from CerPoTech and FCM are found to be more suitable for handling, where no binder is required as compared to the green sample prepared from Treibacher and DKKK, where the green samples during handling were broken. A comparison of the green sample, which were easier to handle (GDC10 powder from FCM) and difficult to handle sample (GDC10 from Treibacher) is shown in Fig. 4-5.
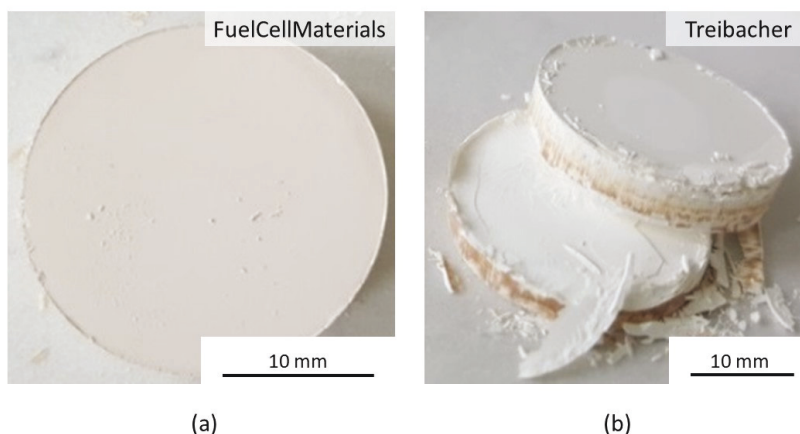

(a)   (b)

Figure 4-5 : Optical images of the green samples uniaxially compacted at 110 MPa; (a) GDC10 powder from FuelCellMaterials and (b) GDC10 powder from Treibacher.

At high uniaxial pressure of 254 MPa, all the samples were difficult to remove from the die. During the ejection of the die, they were disintegrated from the middle. The sample compacted at uniaxial pressure of 110 MPa followed by cold isostatic pressing (CIP) at 300 MPa does not show any increment in their green density as compared the uniaxially pressed samples at 254 MPa. This suggest that the green compacts reached their maximum achievable density at around 250 MPa and further increment in the pressure could not increase the green density further.
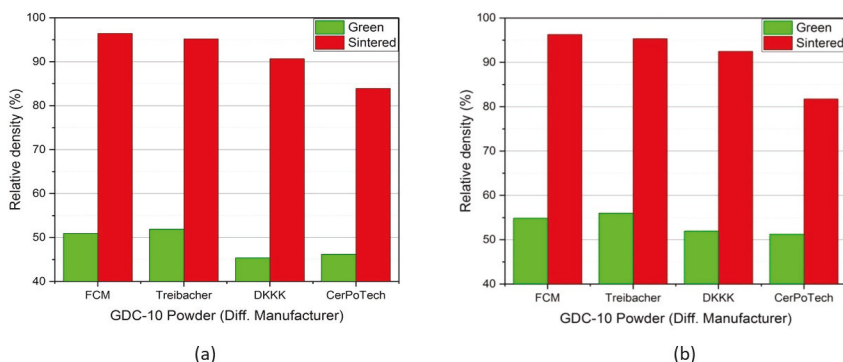
Figure 4-6 : Conventional free sintering study in air of different GDC10 powders showing different final relative density of the samples when compacted and sintered (1400°C, heating/cooling rate 3°C/minutes and dwelling time 30 minutes at 1400°C) with same parameters; (a) uniaxial compaction pressure 48 MPa and (b) uniaxial compaction pressure 110 MPa.

All the four commercially available GDC10 powders were uniaxially pressed at 48 MPa and 110 MPa and then sintered in the conventional sintering route at 1400° C in air as shown in Fig. 4-6. The sintering parameters are mentioned in Table 4-1.

Table 4-1: Conventional sintering parameters in air

Sintering Atmosphere	Air
Heating Rate	3 °C/ min
Sintering Temperature	1400° C
Dwelling time	30 minutes
Cooling rate	3 °C/ min

The FCM powder shows better final relative density (above 95% relative density) among all the powders when sintered at same parameters. On the other hand, the CerPoTech powder has shown the poorest densification among all the powders. Even if uniaxial compaction pressure has a clear influence on the green density, it has a negligible effect on the final densification of the samples.

The micrographs of the pellets sintered at 1400°C (uniaxial compaction pressure 110 MPa) shown in Fig. 4-7. The sintered sample from CerPoTech has highest porosity, which were

distributed non uniformly. Contrary, the pore distribution in other three samples was relatively uniform. Among all the GDC10 powders, higher degree of densification was achieved with FCM powder. Furthermore, the pore distribution was more homogeneous as compared to other sintered samples.
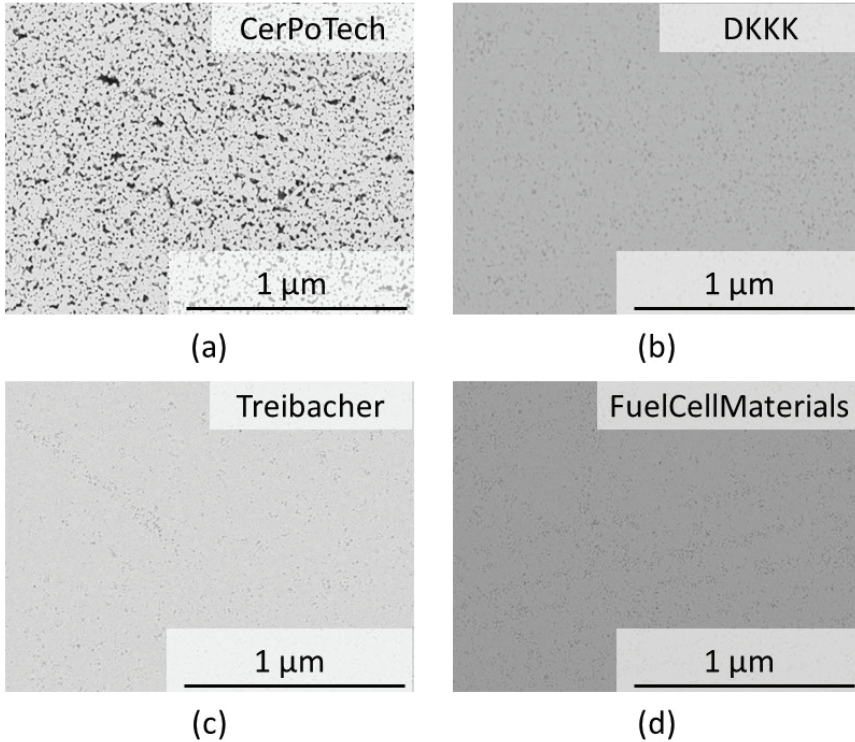

Figure 4-7 : SEM micrographs of the sintered pellets at 1400°C (uniaxial compaction pressure 110 MPa).

The results if looked in its entirety from starting powder characterization to the sintering study, it is clear that the physical properties of the starting powder greatly influence the densification behaviour and the microstructure of the sintered sample. GDC10 powders from CerPoTech, has an irregular shape with a broad agglomerate size range from nanometre scale to micrometre scale. The inhomogeneous particle size distribution results in an inhomogeneous microstructure with nonuniform pore distribution. On the other hand, GDC10 powder from DKKK has a narrow particle size distribution as compared to the CerPoTech powder. Therefore densification was slightly improved and the pore size distribution is uniform in the sample.

When comparing GDC10 powders from Treibacher and FCM, they both have similar particle morphology with mostly unimodal particle size distribution in the nano size range, while the FCM powder is finer as compared to the powder from Treibacher. The microstructure of the Tribacher sample shows more uniform distribution of pores while the sample from FCM powder shows highest densification.

From the benchmarking of starting powder study, it was concluded that GDC10 powder from FuelCellMaterials is most suitable starting material for the future sintering study done in this work. Furthermore, to understand the densification and grain growth behaviour of the GDC10 powder, conventional free sintering was carried out at different temperatures and dwelling times. The final relative density as a function of sintering temperature and dwelling time in air is shown in Fig. 4-8 and 4-9.
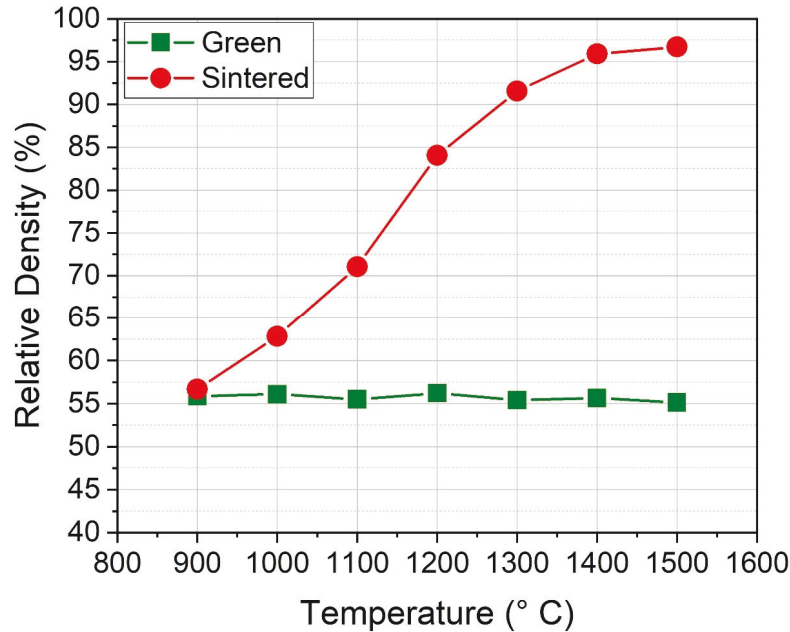
Figure 4-8 : Conventional free sintering study of GDC10 powder from FCM showing the final relative density as a function of sintering temperatures, dwell time 30 minutes.

In the beginning, green samples (compaction pressure 100 MPa) were sintered at different temperatures between 900°C to 1500°C, as shown in Fig. 4-8. To achieve good densification, a sintering temperature of 1400°C with 30 minutes dwelling time in air is required. After

1400°C the densification curve saturates. For studying the grain growth behaviour three temperatures were selected which produces samples with high densities. The temperatures were 1350°C, 1400°C and 1450°C. The dwelling time was varied from 30, 60, 90, 120, 150 minutes for each sintering temperature, as shown in Fig. 4-9 (a).
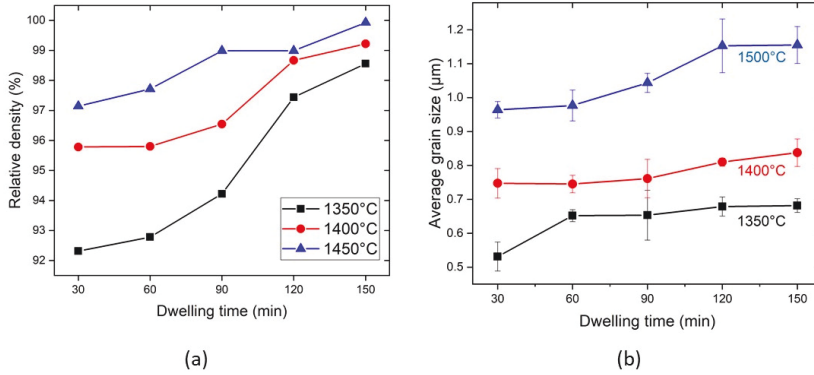

(a)   (b)

Figure 4-9 : Conventional free sintering study of GDC10 powder from FCM in air; (a) final relative density for sample sintered at different dwelling time for three different sintering temperatures and (b) average grain size of the sintered samples at different dwelling time for three different sintering temperatures, all the samples were compacted at 110 MPa.

From all samples considered in Fig. 4-9 (a), microstructure was analysed regarding the grain size. Average grain size values are plotted in Fig. 4-9 (b). It was found that at a given temperature there is no significant grain growth observed when varying the dwell time. However, at a given dwell time, increase of grain size is observed with increase of sintering temperature. The densification and grain growth results shows that at a constant temperature with increment of dwell time, densification with negligible grain growth occurred.

Selected SEM micrographs of the sintered samples at three different sintering temperature i.e., 1350°C, 1400°C and 1450°C with a dwelling time of 30 minutes in air are shown in Fig. 4-10.
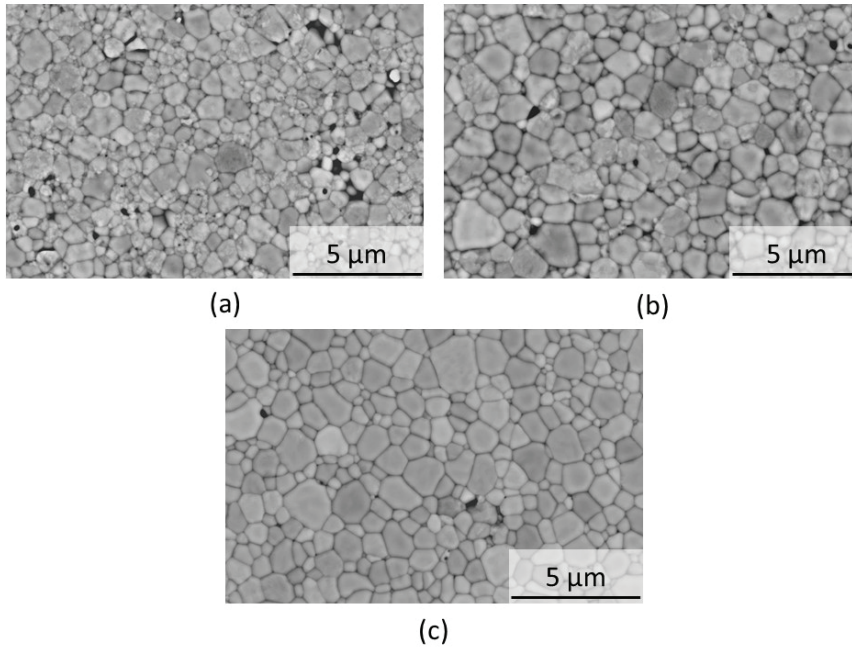
(a)

(b)

(c)

Figure 4-10 : SEM micrograph of the polished and thermally etched surface showing the grain, microstructure of samples sintered at (a) 1350°C, (b) 1400°C and (c) 1450°C with 30 minutes dwelling time in air.

In the case of conventional sintering, optimized parameters for achieving densification >95% in air are a compaction pressure of 100 MPa and a sintering temperature of 1400°C for 30 minutes.

4.1.4. Summary of Benchmarking GDC10 Powder

10mol% Gadolinium doped ceria (GDC10) powder from four different manufacturers (FCM, Treibacher, CerPoTech & DKKK) has been characterized to study their physical properties. Summarizing the results of particle size distribution, SEM and TEM analysis it becomes obvious that the CerPoTEch powder has wide range of particle size distribution from few nanometres to 100 micrometres scale, which consists of hard agglomerate. The powder from DKKK has a unimodal particle size distribution in the coarser particle size range (between 5-10 µm). On the other hand, GDC10 powders from Treibacher and FCM has similar morphology with a unimodal particle size distribution in the nano size (100-500 nm) range, where Treibacer powders are coarser than the FCM powders.

A systematic conventional sintering study of different powders as a function of sintering temperature and compaction pressure has been conducted. From the conventional sintering studies, GDC10 powder from FCM has shown most promising densification behaviour. The relative density above 95% has been achieved when sintered at 1400° C for 30 minutes in an air. From the SEM micrographs of the different sintered samples, it is observed that the sintered sample from FCM powder has no large pores as compared to the sintered sample from CerPoTech powder. While the starting GDC10 powder from CerPoTech does not have optimum properties like morphology and particle size distribution, it resulted in less densification as compared to other powders. Where the microstructure consists of many large pores which are again distributed randomly in the sample.

The GDC10 powder from FCM was found to be most suitable powder for the current sintering study with highest densification behaviour among all the powders investigated. The processing parameters for the starting powder like compaction pressure and sintering temperature has been identified. The GDC10 powder from FCM required and uniaxial compaction pressure of 100 MPa and a sintering temperature of 1400°C, dwelling time 30 minutes in air is necessary to achieve a good densification (>95%) of the sample. The grain growth study with three different sintering temperature and various dwelling time shows that the densification and grain growth occurred concurrently as the temperature increases. However, the at constant sintering temperature and longer dwelling time no significant grain growth is observed but the densification is occurred.

The benchmarking of starting powders from the beginning of the dissertation work ensure the avoidance of the processing effects on the densification behaviour and microstructure during sintering. A systematic investigation of the densification and grain growth study of the starting powder in conventional sintering route concluded, sintering of GDC10 material required very high sintering temperature and longer dwelling time to achieve full densification. The densification and grain growth of the sample occurred concurrently with increment of sintering temperature, with no abnormal grain growth.

4.2. Effect of Reducing Atmosphere and Chemical Expansion of GDC10

4.2.1. Overview

Conventional sintering study in air showed that full densification of GDC10 material required higher sintering temperature and longer dwelling time. In the literature it was found that GDC powder that sintered under low oxygen partial pressure ($P(O_2) < 10^{-12}$ atm), showed enhanced mass diffusion mechanisms that led to a full densification and rapid grain growth at low temperatures [12]. At these conditions, enhanced densification behaviour of GDC is activated by high volume diffusion due to the formation of a large concentration of oxygen vacancies ($V_O^{\bullet\bullet}$), electronic defects(Ce'_{Ce}) due to the reduction of Ce^{4+} to Ce^{3+} and reduced cation Gd/Ce size mismatch [12]. It has been shown also that such mechanisms can influence the viscoelastic properties of the material during sintering [181].

The enhanced mass diffusion could lead to lowering the processing temperature for GDC materials, which would be greatly beneficial for lowering the energy consumption and minimizing the potential of interdiffusion of materials if fired together as e.g. SOFCs. However, GDC when sintered under reduced atmosphere could experience high volume expansion due to the generation of oxygen vacancies and changing of the valence state of the cerium ions to Ce^{3+}, which has a large radius (1.14 Å) as compared to the Ce^{4+} ions (0.97 Å). This additional volume expansion which increases with lowering partial pressure of oxygen and increasing temperature, could lead to high stresses inside the material during cooling. It is reported that the internal stress generation is so high during cooling, that cracking of the sample might occurs [20]. One suggestion proposed in the literature is that the controlled re-oxidation of GDC10 at 800°C could be beneficial to avoid cracking of the sample.

In this section, systematic investigation of the densification behaviour of GDC10 powder from Fuelcellmaterials, which was selected as the suitable powder for the sintering study, was carried out. Conventional free sintering of the powder under low oxygen partial pressure (approximately $P(O_2) <10^{-23}$ mbar), which was realized by using Ar/2.9%H_2 gas was done. The densification behaviour was compared with the densification behaviour under air. The microstructure and grain size of the samples sintered under reducing atmosphere was compared with the sample sintered in air. As expected from literature, the sintering study shows an enhanced densification under reducing atmosphere as compared to the sample sintered in air.

Furthermore, in a dilatometer study the shrinkage curve and the onset temperature for densification was compared for three different atmospheres i.e., air, Ar and Ar/2.9%H$_2$. During cooling cycle re-oxidation experiments at 800°C are carried out, by switching the sintering atmosphere from Ar/2.9%H$_2$ (reducing atmosphere) to Ar/20%O$_2$ (oxidizing atmosphere). The aim was to take advantage of the reducing atmosphere for enhanced densification and using the oxidizing atmosphere to put oxygen into the lattice at higher temperature to reduce the internal stress that may generated due to the chemical expansion/contraction during the complete sintering cycle.

Later in this section, fundamental studies on the reducing behaviour of the GDC10 was carried out. DTA/TGA analysis under different atmospheres were done to study the reduction/oxidation behaviour of the material. Oxygen deficiency was calculated from the weight loss behaviour of the sample under reducing atmosphere. Additionally, high temperature X-ray diffraction study under reducing atmosphere was done to quantitatively analyse the chemical expansion of GDC10. The chemical expansion of the sample was then correlated with the non-stoichiometry of GDC10.

The sintering and grain growth study of the material under reducing atmosphere together with the fundamental studies to characterise the reduction/oxidation behaviour of the material is important for future experiments in FAST/SPS. Under FAST/SPS condition, the sample experienced an uncontrolled reducing atmosphere inside the die, which might be significantly different from chamber atmosphere. Amongst others, the difference is caused by the direct contact with the graphite foil/tool. Here, the graphite can act as an oxygen getter and further reduce the sample. As the sample is clamped in the tool, this might have consequences on the stability of the sintered sample. The fundamental study on the reducing/oxidizing behaviour of the sample will help to overcome these challenges while densifying by FAST/SPS process.

4.2.2. Conventional Sintering Study under Reducing Atmosphere

Conventional free sintering of GDC10 powder in reducing atmosphere (Ar/ 2.9%H$_2$) and in air were carried out at five different temperatures (1000°C – 1400°C). The densification behaviour of the samples was characterized by measuring the final relative density of the sintered samples. All sintering parameters are summarized in the Table 4-2.

Table 4-2: Parameters of conventional sintering in air and Ar/2.9%H$_2$

Sintering Atmosphere	Air and Ar/2.9%H$_2$
Heating Rate	3 °C/ min
Sintering Temperature	1000, 1100, 1200, 1300 and 1400 ° C
Dwelling time	30 minutes
Cooling rate	3 °C/ min

Figure 4-11 shows the degree of densification of the GDC10 powder under reducing atmosphere (Ar/2.9%H$_2$) compared with the degree of densification in air. Significant enhancement of the degree of densification was achieved at temperatures below 1200° C (i.e. 1000°C, 1100°C & 1200°C) when sintered in reducing atmosphere (Ar/ 2.9% H$_2$). However samples, which were sintered at 1300°C and 1400°C, had lower relative density as compared to the sample sintered in air at same temperatures.
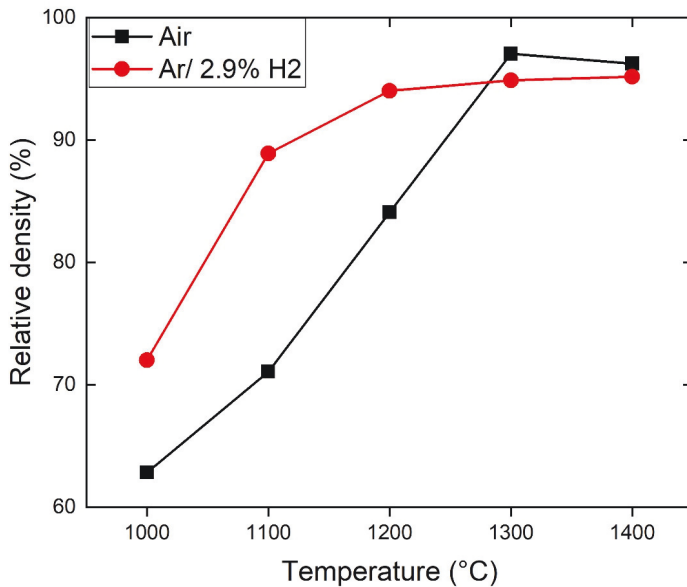

Figure 4-11 : Conventional free sintering study of GDC10 powder from FCM showing the final relative density as a function of sintering temperatures in air and Ar/2.9%H$_2$.

The conventional study under reducing atmosphere and air shows that an enhanced degree of densification can be achieved by using reducing atmosphere during sintering. However, it raised a question, why above 1200°C the degree of densification almost saturates, even resulting in a lower density than the samples sintered in air. To understand the conventional sintering result, microstructure of all the sintered samples were analysed. The SEM micrographs at low magnification of the sintered samples under Ar/ 2.9% H_2 at four different sintering temperatures i.e. 1100,1200,1300 and 1400 °C are shown in Fig. 4-12. The sample which was sintered at a temperature of 1000°C has a very low density and could therefore not investigated by SEM.
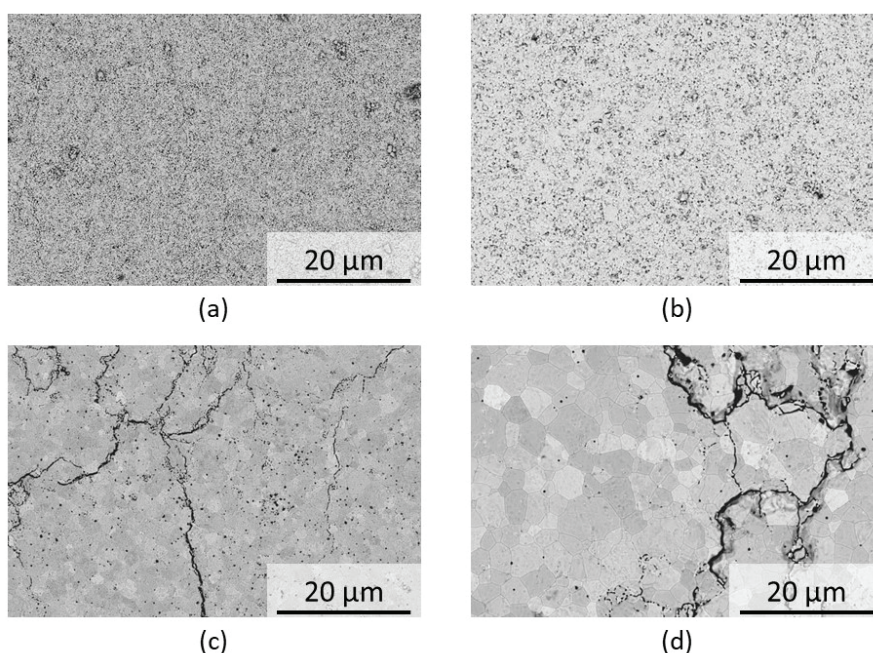

(a)   (b)

(c)   (d)

Figure 4-12 : SEM micrograph at low magnification of the polished and thermally etched surface showing the grains and micro-cracks formation, sample sintered at (a) 1100°C, (b) 1200°C, (c) 1300°C and (d) 1400°C with 30 minutes dwelling time under Ar/2.9% H_2.

All other samples were mechanically sufficiently stable without obvious macroscopic cracking. Nevertheless, it is observed that the sample sintered at 1100°C and 1200°C has no micro-cracks however, the samples which are sintered at 1300°C and 1400°C has severe micro-cracks. These observations are in accordance with the literature [20]. It is reported that the chemical expansion during sintering and successive contraction in oxidation at room temperatures could generate high stresses in the sample due to the heterogeneous re-oxidation in the sample, which can cause micro-cracks in the microstructure [20]. Therefore, it may be possible that the sample sintered above 1200° C in Ar/ 2.9%H$_2$ atmosphere and cooled in the same atmosphere may develop a high amount of stress. Exposing the sample to ambient oxygen partial pressure at room temperature may lead to sudden contraction that generate micro-cracks in the sintered samples. The presence of excessive micro-cracks in the samples could be a reason for the lower final relative density of the samples. On the other hand, no micro-cracks were observed for the samples sintered below 1300°C, which can be due to high residual porosity of the sample. Alternatively, the chemical expansion of the GDC material depends both on the partial pressure of oxygen and temperature. In the sintering study the partial pressure of oxygen was constant, but the sintering temperatures were varied. The sample sintered above 1200°C may have experienced very high reduction, which may be coupled with very high chemical expansion. Therefore, the samples sintered below 1200°C may have experienced only moderate amount of reduction and subsequent contraction that was not enough to generate high stresses in the sample.

The grain size of the sample sintered in air and Ar/ 2.9% H$_2$ was evaluated by image analysis from the SEM micrographs. The effect of the sintering atmosphere on the grain growth is shown for one temperature (1400°C) in Fig. 4-13. The average grain size of the sample sintered in reducing atmosphere is approximately 2.4 µm. The sample which was sintered in air had an average grain size of 0.45 µm when keeping the other processing parameters constant. The use of reducing atmosphere not only shows enhanced degree of densification but also enhanced grain growth (approximately 5 times higher). Moreover, careful analysis of the grains revealed that most of the pores are entrapped inside the large grains, in the samples that were sintered under reducing atmosphere. Whereas, the samples which were sintered in air has the pores near to the triple grain boundary. Addition to the micro-cracks, the entrapped pores inside the grains could be a reason for the lower final relative density of the sample sintered under Ar/ 2.9% H$_2$ atmosphere.
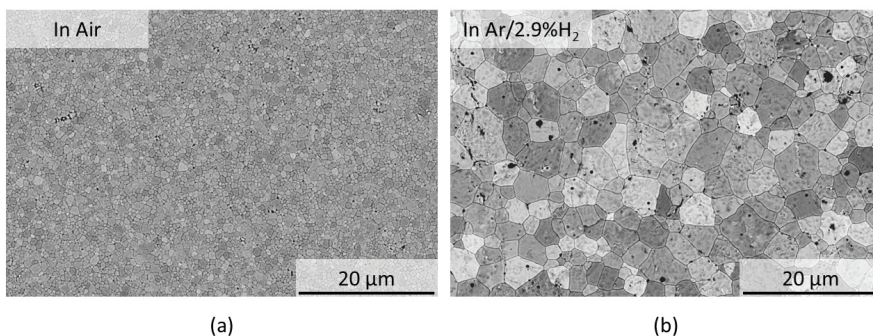
Figure 4-13 : SEM micrographs of the GDC10 samples sintered at 1400°C with a dwelling time of 30 minutes (a) in air and (b) in Ar/2.9%H$_2$ illustrating the enhanced grain growth in the sample sintered in Ar/2.9%H$_2$.

The conventional sintering study shows that the high degree of densification is achieved under reducing atmosphere, with an enhanced grain growth. However, the sintering rate of the sample sintered in reducing atmosphere cannot be studied in such kind of experiments. To understand the effect of oxygen partial pressure on the sintering rate for GDC10 material, dilatometry measurements were done in addition. Here, re-oxidation at higher temperature (i.e. 800°C) was studied as well aiming on to understand if abrupt volume changes might be the main reason for crack formation.

4.2.3. Thermometric Analysis with Re-oxidation

Pellet shaped samples with diameter of approximately 8 mm and height of approximately 5 mm were prepared by uniaxially cold pressing at 100 MPa. The green density of the uniaxially pressed samples was around 55%. Dilatometer experiments were conducted in a push-rod vertical dilatometer (TMA 402, NETZSCH) for monitoring the insitu shrinkage of the sample. In the dilatometer experiment only the axial shrinkage as a function of temperature is measured. Therefore, before the main series of experiments several samples (d= 13 mm & h= 4-5 mm) were sintered by dilatometer in air as well to assure the isotropic character of the shrinkage at different temperatures. The axial shrinkage was measured during the dilatometer experiment and the final radial shrinkage was calculated by measuring the change in the diameter of the sample after the experiment by a Vernier calliper. The results comparing the final shrinkage in axial and radial directions are shown in Fig.4-14. The shrinkage was approximately same in

both axial and radial direction. Therefore, it is safe to assume that the densification is isotropic in the GDC10 sample.
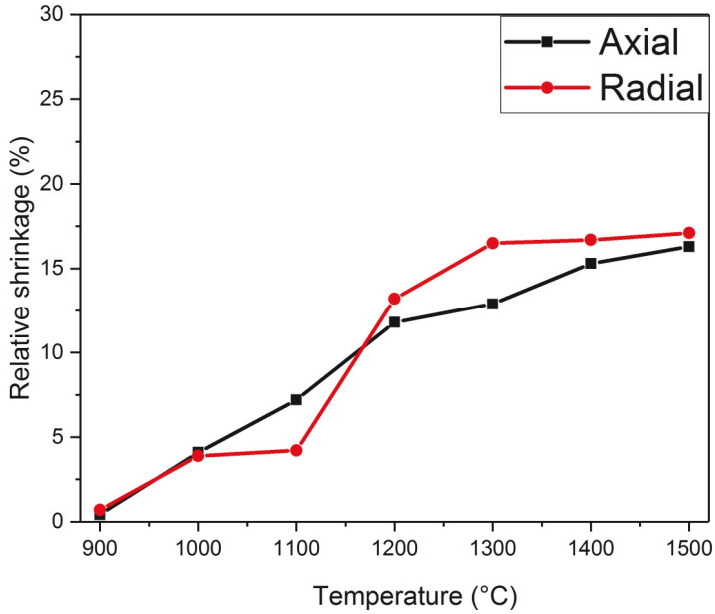

Figure 4-14 : Relative shrinkage of the conventionally sintered GDC10 samples at different temperatures both in axial (dilatometer result) and radial (manual measurement) direction in air.

Afterwards three different samples were sintered in a dilatometer under three different atmospheres i.e. air, argon and Ar/2.9%H_2. The samples were sintered at 1400°C with a dwelling time of 30 minutes and a heating/cooling rate of 3°C/minute. During sintering a negligible load of 50 mN is applied for the whole cycle to record the live axial shrinkage data. The evolution of density as a function of time and temperature is shown in Fig. 4-15 (a). The measured shrinkage curves were corrected for thermal expansion known as true shrinkage, the densification was calculated from the true shrinkage, so the densification rate (true densification rate) presented show only the effect of sintering and/or lattice volume changes from oxidation or reduction [182]. The densification rate as a function of sintering temperature is shown in Fig. 4-15 (b).
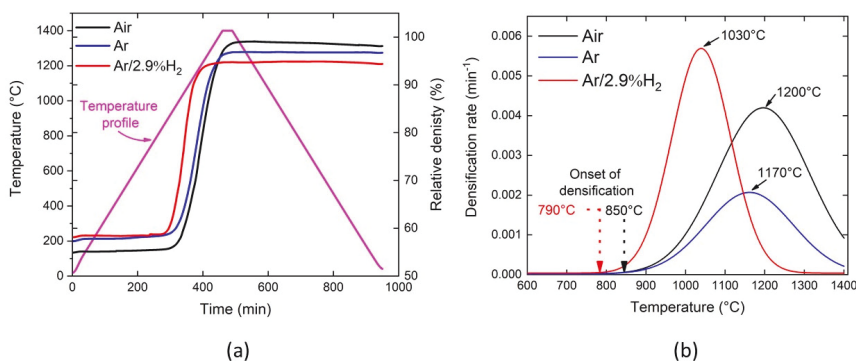
Figure 4-15 : (a) The evolution of density as a function of time and temperature for sample sintered in three different atmospheres and (b) the true densification rate as a function of sintering temperature showing the onset temperature and temperature of maximum sintering rate for three different sintering atmospheres [183].

As found previously from the conventional free sintering experiments, the densification of GDC10 under reducing atmosphere starts approximately 60°C earlier than in air and argon. However, under reducing atmosphere the densification saturates at around 1200°C, when the density of the sample was approximately 94%. With increasing the temperature higher than 1200°C, a negligible increase in the relative density of the sample was observed. On the other hand, sintering under air and argon atmosphere shows much less difference in the densification behaviour. In both cases, the onset of densification starts at 850°C. The densification continues until the highest temperature and completion of dwelling time. The densification rate provides more information about the sintering activity under different atmosphere. It was observed that the sample sintered in reducing atmosphere has a maximum densification at around 1030°C, while the sample sintered under argon and air shows maximum densification at around 1200°C [183].

First, the densification of GDC10 under argon atmosphere (inert in nature) shows no significant difference in comparison to the densification behaviour in air. The partial pressure of oxygen in argon atmosphere is slightly reducing, which was approximately 10^{-4} mbar [184]. On the other hand, the partial pressure of oxygen in Ar/2.9%H$_2$, which was approximately 10^{-22} mbar is highly reducing in nature [184]. This suggest that the residual oxygen concentration in argon atmosphere is high enough to impede clearly pronounced reduction of the material. Whereas, the oxygen vacancies in the material are generated at much lower oxygen partial pressure

atmosphere. The generation of defects is necessary to provide enhanced mass diffusion during sintering.

Second, under reducing atmosphere the sintering starts earlier than in argon and air. Furthermore, higher sintering rate was observed at around 200°C lower temperature in reducing atmosphere than in argon and air. The densification in reducing atmosphere continues until approximately 1200°C, further increment in temperature does not show any further densification. When comparing the densification in air and argon atmosphere, the densification continues till 1400°C and during the complete holding time. Densification and grain growth are competing process during sintering, in case of reducing atmosphere where no densification is observed after 1200°C grain growth obviously starts much earlier. This results in a much coarser grain size in the sample sintered in reducing atmosphere under same processing parameters and entrapment of residual pores by the large grains. Since the oxygen lattice diffusion is faster at lower oxygen partial pressure, an increase of the pore mobility leads to faster grain growth since the boundary mobility is controlled by the pore motion [185].

Furthermore, XRD patterns were obtained from the sintered GDC10 pellets in air and Ar/ 2.9% H_2 atmosphere. These XRD patterns were compared with the green pellet's pattern. There is no decomposition in the sintered pellets in both atmospheres. Nevertheless, in case of sintered sample in Ar/ 2.9% H_2 atmosphere, the sample shows a remaining micro-strain of 0.046%. The micro-strain is the deviation of the lattice parameters with respect to the starting pellet (green body). During the heat-treatment of GDC10 materials in reducing atmosphere, the strain is due to the thermo-chemical expansion. The micro-strain in the sintered pellet in reducing atmosphere suggests that the re-oxidation process at room temperature can lead to a residual strain in the sample after cooling as a result of remaining chemical expansion in the sample. A high residual strain in the sample can easily cause mechanical failure of the sample.
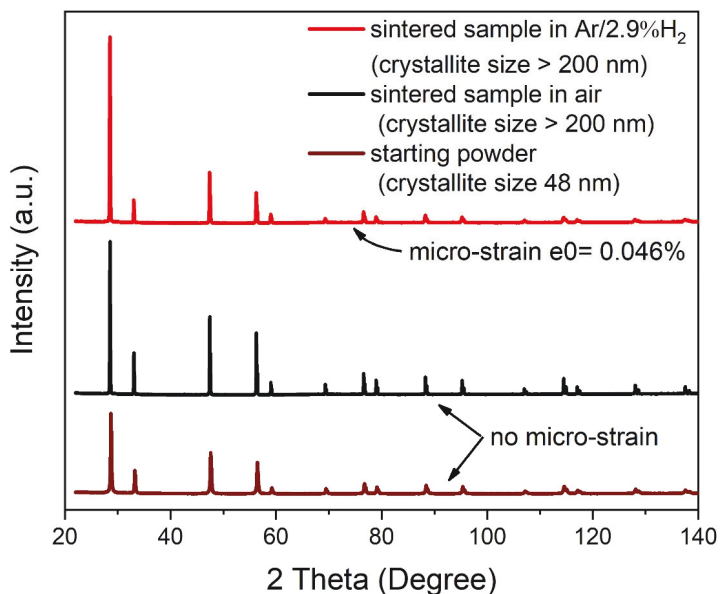
Figure 4-16 : XRD patterns of sintered GDC10 sample in air, Ar/ 2.9% H2 and starting powder.

As expected from previous results (Fig. 4-12), the microstructure of the sample sintered in reducing (Ar/2.9%H_2) leads to excessive micro-cracking of the sample. To overcome this micro-cracking in the sample, while taking advantage of the enhanced densification at reducing sintering conditions, controlled re-oxidation at 800°C was performed. Therefore, the sintering atmosphere was kept reducing by plunging Ar/2.9%H_2 during heating cycle and dwelling cycle. While cooling, when the temperature of the furnace reached at 800°C, the temperature was kept constant for 10 minutes and at this stage the atmosphere was switched from Ar/2.9%H_2 (reducing) to Ar/20%O_2 (oxidizing). Then the cooling from 800°C to room temperature was entirely carried out under oxidizing atmosphere. All measurements were performed using a respective gas flow of 50 ml min^{-1}. For these experiments, a sintering temperature of 1400° C and heating rates and cooling rates of 3° C min^{-1} were used for all samples. The temperature dependence on the true uniaxial shrinkage in two different atmospheres (i.e. air and Ar/2.9%H_2) and re-oxidation condition is shown in Fig. 4-17.
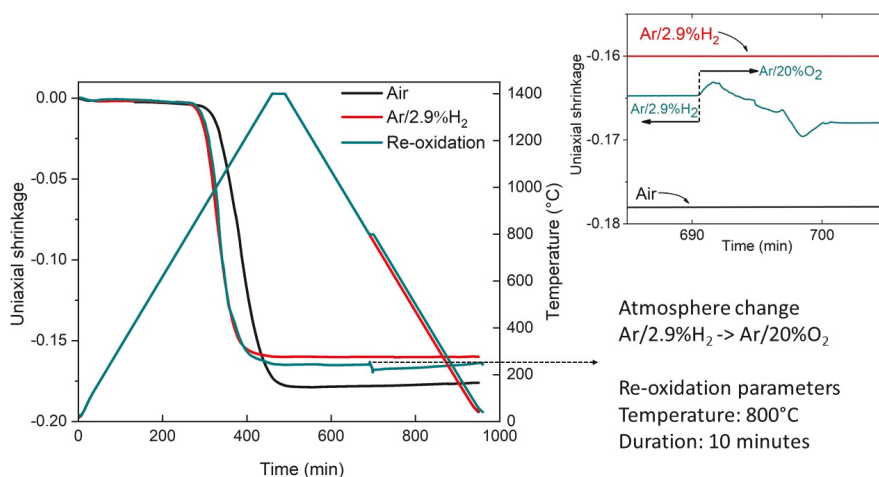
Figure 4-17 : True uniaxial shrinkage of GDC10 under entirely air, entirely Ar/2.9%H$_2$ atmosphere and partially under Ar/2.9%H$_2$ atmosphere and during cooling at 800°C re-oxidation, the inset graph shows with higher resolution the shrinkage during the re-oxidation.

Figure 4-17 shows the linear uniaxial shrinkage curves at three different sintering atmospheres. The measured shrinkage curves were corrected for thermal expansion known as true shrinkage. Therefore, the dimensional changes ($\Delta L/L0$) presented in the Fig. 4-17 shows only sintering and/or lattice volume changes from oxidation and/or reduction. As seen in the previous dilatometer studies, the shrinkage of GDC10 starts earlier (lower temperature) under reducing atmosphere as compared to when sintered in air. The final relative densities of the samples sintered in air, under Ar/2.9%H$_2$ and under Ar/2.9%H$_2$ with subsequent re-oxidation were 97.41%, 94.45% and 95.6% respectively.

In the inset graph of the Fig. 4-17 shows the shrinkage profile only between the experiment time 685 to 705 minute, to better illustrate the shrinkage profile during the re-oxidation condition. The cyan line is corresponding to the shrinkage profile during the re-oxidation experiment. After 690 min the temperature was held at 800°C for 10 minutes. At the beginning of this period the atmosphere is switched from Ar/2.9%H$_2$ (reducing) to Ar/20%O$_2$ (oxidizing) remaining this atmosphere until the end of the experiment. The observed rapid shrinkage in this period corresponds to the volume changes in the sample due to the chemical expansion/contraction behaviour of GDC material, which is due to the release of oxygen

(chemical expansion) and insertion of the oxygen back into the lattice in the oxidizing condition (chemical contraction). The diffusion of oxygen into the whole sample took approximately 9 minutes which is approximately the iso-thermal time (10 minutes) used for the re-oxidation cycle. It can be concluded from this experiment that at 800° C, Po_2 of 212.24 mbar, the 8mm sample can be fully re-oxidized in less than 10 minutes.
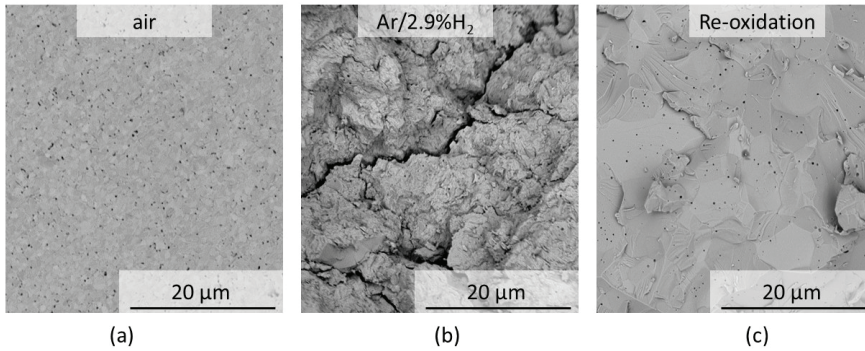

(a)   (b)   (c)

Figure 4-18 : SEM micrographs of the fractured cross-section surface of the GDC10 samples; (a) sintered in air, (b) sintered entirely under Ar/2.9%H$_2$ atmosphere and (c) sintered in Ar/2.9%H$_2$ atmosphere with re-oxidation during cooling at 800°C.

Figure 4-18 shows the SEM micrograph of the fractured surface of the GDC10 sample sintered in air, entirely under Ar/2.9%H$_2$ and under Ar/2.9%H$_2$ atmosphere with re-oxidation during cooling at 800°C. The sample which was sintered in Ar/ 2.9%H$_2$ has a relative density of 94.45% but was severely cracked, whereas the sample which was sintered in air has no cracks. The cracking in the microstructure for the sample sintered in low P(O$_2$) (Ar/2.9%H$_2$) is caused by higher P(O$_2$) (air) at room temperature when the furnace was opened. Abrupt and heterogeneous volume changes are starting from the sample surface and low oxygen diffusion at room temperature leads to stress gradient in the sample. To avoid the cracking in the sample re-oxidation at 800°C was carried out, the SEM micrograph (c) show no cracks in the sample.

4.2.4. Quantification of Oxygen Defects and Chemical Expansion

The diffusion mechanisms and defect chemistry for pure ceria (CeO$_2$) showed that the generation of oxygen vacancies due to the reduction of the material can control the cation mobility and the related sintering and grain growth mechanism [186,187]. Current sintering study of GDC10 materials shows enhanced densification when sintered under reducing

atmosphere (Ar/2.9%H$_2$). Therefore, it is important to understand and quantify the oxygen deficiency of GDC10 under the processing condition used in this dissertation.

GDC10 can have a wide range of nonstoichiometric GdCeO$_{2-\delta}$, which can be influenced by the partial pressure of oxygen and temperature. Due to this property, GDC10 is capable of absorbing or releasing oxygen, while maintaining its original phase. In order to evaluate the reduction behaviour, kinetics of the re-oxidation and quantification of the amount of nonstoichiometric of GDC, thermogravimetry analysis (TGA) was used. The results are shown in Fig. 4-19.
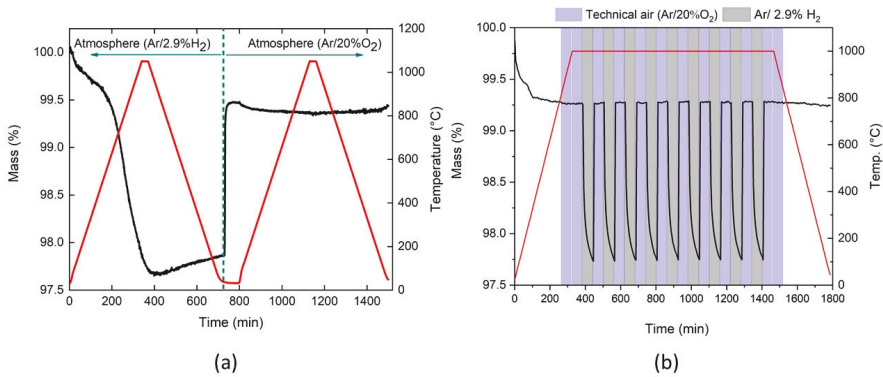

Figure 4-19 : (a) TG curves for GDC10 powder to see the redox behavior of the material, the powder sample was heated and cooled in Ar/2.9%H$_2$ and then atmosphere was switched to Ar/20%O$_2$. The maximum temperature was 1000°C and the dwelling time was 30 minutes at the maximum temperature with a heating/cooling rate of 3°C/minute, (b) change in mass due to the change in atmosphere under isothermal temperature of 1000°C [183].

Fig. 4-19 (a) shows change in mass as a function of time with two consecutive thermal cycles where the initial cycle was performed under Ar/2.9%H$_2$ atmosphere and the subsequent cycle on the sample was carried out under Ar/20%O$_2$. Initially in the first thermal cycle in Ar/ 2.9%H$_2$ atmosphere, a mass loss in the powder was observed, which may be due to the evaporation of moisture contents from the powder. However, after exceeding 600° C, continuous mass loss was observed as a function of temperature, which is due to the removal of the oxygen from the lattice. A total mass loss of 2.3% was measured during the heating period in the first thermal cycle. During the cooling period in the first thermal cycle (under Ar/ 2.9%H$_2$) a mass gain is observed, as the degree of reduction of the material depends both partial pressure of oxygen

and temperature. Therefore, when the temperature was lowered the degree of reduction of the sample was changing by incorporation of oxygen back into the lattice. After the first thermal cycle in Ar/ 2.9%H$_2$ atmosphere is finished and the sample reached room temperature, the atmosphere is now switched from Ar/ 2.9%H$_2$ to technical air (Ar/20%O$_2$). At room temperature, a sudden mass gain is observed when the atmosphere is switched to technical air (higher Po_2). This mass gain (around 1.57%) is due to the incorporation of the oxygen back into the lattice. During the second thermal cycle in technical air atmosphere the mass remains more or less same. The difference between the results obtained in Ar/2.9%H$_2$ and technical air atmosphere can be ascribed to the deviation from oxygen stoichiometry of GDC10 sample, according to the reaction equation (4.1)

$$CeGdO_{1.95} + \delta H_2 = CeGdO_{1.95-\delta} + \delta H_2O \qquad\qquad \text{Eq. (4.1)}$$
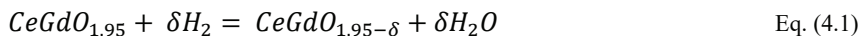
Surprisingly, it is observed that even a room temperature the re-oxidation of GDC10 powder happened in 7-8 minutes. The TGA analysis confirmed that re-oxidation at high oxygen partial pressure (Po_2 = 212.24 mbar) can happen in few minutes (7-9 minutes) in powder sample. Therefore, the abrupt change in oxygen partial pressure during the processing of GDC10 material can lead to mechanical failure of the sample, as observed in the Fig. 4-18. A controlled re-oxidation is therefore required at higher temperature to avoid unnecessary cracks in the sample.

Thermogravimetric analysis (TGA) has been recognized as one of the most valuable technique for directly measuring the oxygen deficiency in the material by measuring the weight change of oxide caused by the redox reactions. The weight change can then be directly converted into the corresponding variation of oxygen non-stoichiometry (δ). However, despite the direct working principle of the TGA analysis for measuring the oxygen deficiency, it is important to consider several other factors (e.g. environment) which can influence the weight change of the sample.

The change in mass due to the removal of the oxygen ions in reducing atmosphere and the incorporation of the oxygen ions in oxidizing atmosphere were confirmed by series of atmosphere switch experiments at isothermal temperature of 1000°C, as shown in Fig. 4-19 (b). GDC10 powder was used for this experiment. The initial atmosphere was technical air, the temperature was raised to 1000°C at a heating rate of 3°C/min. The initial atmosphere was kept for one hour, then the atmosphere was switched to reducing by flowing Ar/2.9%H$_2$ for 30 minutes. After that the atmosphere is again switched to technical air. This cycle was repeated

18 times. Mass loss and re-oxidation kinetics were the same in all the cycles, which confirms the mass loss is only due to the oxygen removal and incorporation in the lattice.

Another set of TGA experiments were carried out for quantifying the oxygen nonstoichiometry under reducing atmosphere. The thermal cycle used in this TG analysis has eight complete cycles with alternating furnace atmospheres (i.e. Ar/ 20% O_2 an Ar/ 2.9% H_2) and in each thermal cycle, the powder sample was heated until 1000 °C with a heating rate of 5 °C/ min and a dwelling time of 30 minutes. The sample was then cooled with a cooling rate of 5 °C/ min. After each cycle, the atmosphere was changed from technical air to Ar/ 2.9% H_2 or vice versa. Fig. 4-20 shows the thermal cycles and TG measurement as a function of time. Each cycle is named as 1, 2, 3 etc. and the first thermal cycle was carried out in air atmosphere.
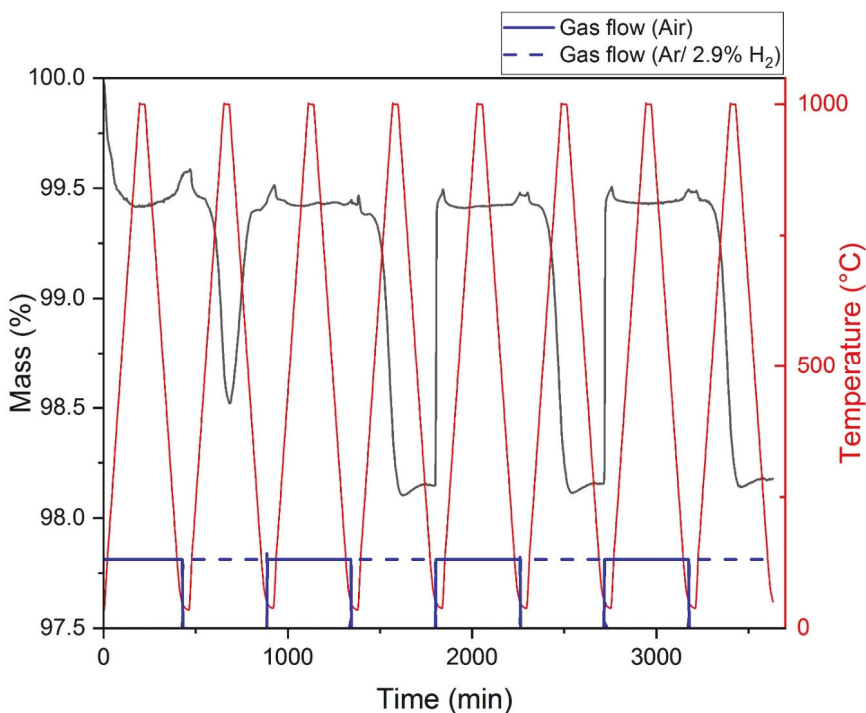

Figure 4-20 : Weight change profile of GDC10 as a function of temperature and $P(O_2)$.

From the weight profile in the first thermal cycle of the GDC10 material, it can be observed that the weight loss in air is due to the evaporation of any organic compound and moisture in the sample. In the second thermal cycle, the atmosphere was changed from technical air to Ar/

2.9% H_2 and after 30 minutes, the temperature was increased with 5 °C per min rate. The weight of the sample was further decreased in Ar/ 2.9% H_2 which suggest that the weight loss of the sample was due to the removal of the oxygen. However, when analyzing the complete thermal cycles, deviation in the weight loss in the first three cycles is observed. After the fourth cycle the weight profile of the GDC10 sample as a function of both temperature and $P(O_2)$ is found to be consistent. Therefore, for calculating the non-stoichiometry of the oxygen (δ) the weight profile from the last two cycles (thermal cycle 7 and 8) have been used. The non-stoichiometry value was determined by using the formula shown in equation 4.2 [188]. Where, Δw is the weight change of the sample, W_S is the initial sample weight, M_O is the oxygen atomic weight, and M_S denotes the molecular formula weight of the sample (i.e. GDC10).

$$\delta = \frac{\Delta w}{W_S} * \frac{M_S}{M_0} \hspace{5cm} \text{Eq. (4.2)}$$

Fig. 4-21 shows the calculated oxygen non-stoichiometry (δ) as a function of temperature in air and Ar/ 2.9% H_2 atmosphere. The black line represents the oxygen non-stoichiometry as a function of temperature in air whereas, the red line represents the δ in Ar/ 2.9% H_2 atmosphere. Under reducing atmosphere, the δ values remains constant up to approximately 500 °C however if exceeding 500°C, the material progressively looses oxygen until the highest experimental temperature (1000°C) and even during the holding time.
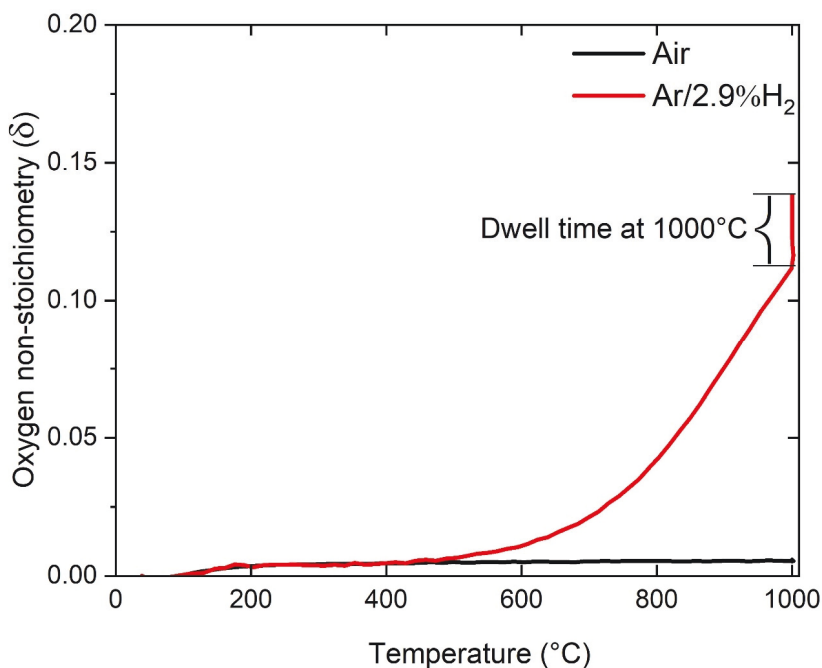
Figure 4-21 : Oxygen non-stoichiometry as a function of temperature in air and Ar/ 2.9% H$_2$ atmosphere.

Sintering under reducing atmosphere leads to an enhanced densification of GDC10 material. However, the effect of chemical expansion during the sintering in reducing atmosphere and the successive contraction in oxidizing conditions at low temperature results in cracked microstructure. Series of thermogravimetric analysis suggest a strong redox behavior of the GDC10 material. Furthermore, accurate quantification of the oxygen non-stoichiometry uo to 1000°C has been obtained. High temperature X-ray diffraction experiment in different atmosphere was carried out to quantify the theoretical volume expansion of the GDC10 materials.

Figure 4-22 shows the in-situ high temperature X-ray diffraction measurements in technical air and reducing atmosphere, showing the lattice parameter as a function of temperature. The GDC10 powder was heated until 1000°C at a heating and cooling rate of 3 °C/min.
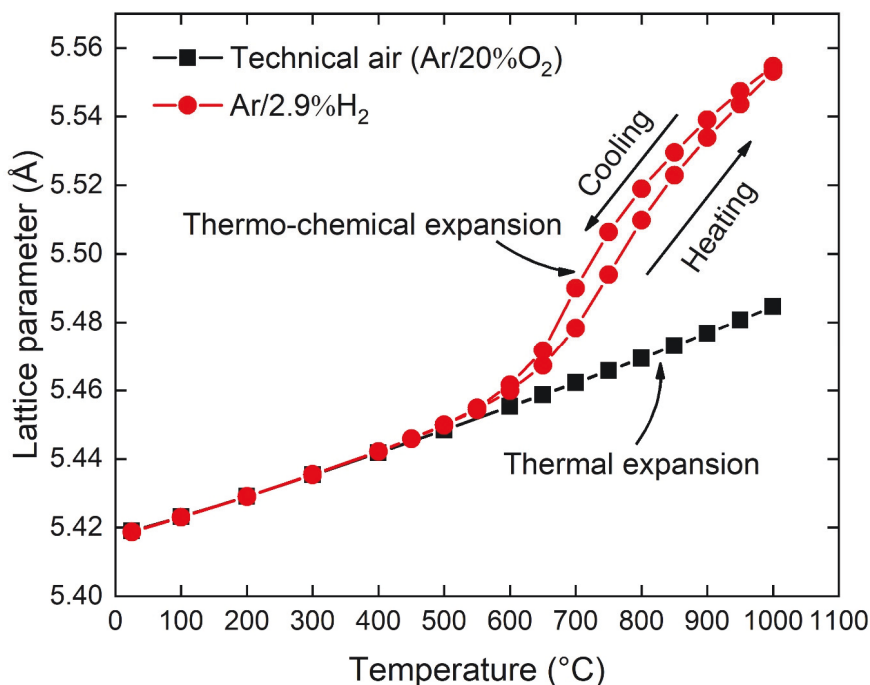
Figure 4-22 : Comparison of the lattice expansion behavior of GDC10 powder under technical air and reducing atmosphere showing volume expansion of up to 4% under reducing conditions at 1000°C [183].

When the sample was heated under technical air (high $P(O_2)$), the lattice parameter increased linearly and during the cooling cycle the lattice parameter follows the same path and came down to the initial lattice parameter. The increase in lattice parameter in the GDC10 material while treating in air is simply because of thermal expansion. When the sample was fired under reducing atmosphere (Ar/ 2.9%H_2), the lattice increments has a linear behaviour until 500°C, which is only due to the thermal expansion. After exceeding 500°C there was an abrupt increment in the lattice parameters as a function of temperature, which abruptly increases at temperature higher than 600°C. In low $P(O_2)$, when exceeding 500°C the material continuously looses oxygen and the increased in lattice parameter is due to both thermal and chemical expansion.
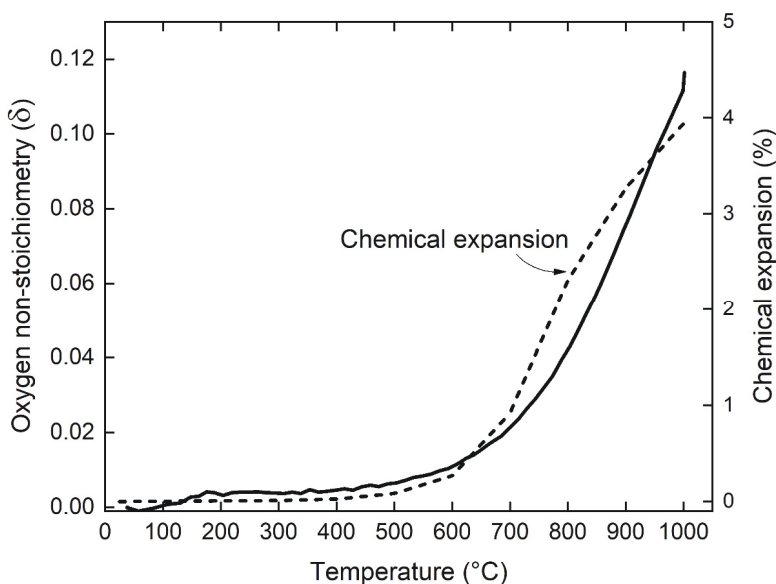
Figure 4-23 : Oxygen deficiency in GDC10 under reducing atmosphere as a function temperature corelated with the volume change in the sample.

The subtraction of the lattice expansion under reducing atmosphere by the lattice expansion in air, gives the exact volume change only due to the chemical expansion. It was measured that the release of oxygen from the lattice above 600° C results in a volume expansion as high as 4% at 1000°C, which will further increase at higher temperature. Combining the non-stoichiometry calculation with the lattice expansion data, chemical expansion due to the oxygen vacancies under reducing environment is quantified (Fig. 4-23). The temperature at which the change in the non-stoichiometry is observed exactly matches with the temperature when a non-linear rise of chemical expansion is observed.

4.2.5. Summary

To summarize the section, GDC10 samples sintered under reducing atmosphere (Ar/2.9%H_2) shows enhanced densification as compared to the samples sintered in air. Such enhanced densification behaviour of GDC under low oxygen partial pressure of oxygen (PO_2 < 10^{-15} mbar) activated high volume diffusion due to the formation of a large concentration of oxygen vacancies ($V_O^{\bullet\bullet}$), electronic defects (Ce'_{Ce}) due to the valance change of Ce^{4+} to Ce^{3+} and reduced cation Gd/Ce size mismatch [12,20,189]. Schematic representation of the generation

of oxygen vacancies in the lattice and reduction of Cerium ions and the constituted defect equilibria equation under reducing atmosphere is shown in Fig. 4-24.
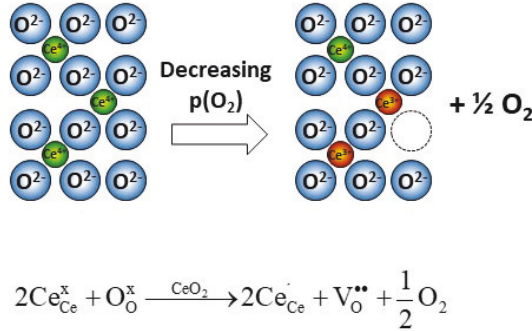

$$2Ce_{Ce}^{x} + O_{O}^{x} \xrightarrow{CeO_2} 2Ce_{Ce}^{'} + V_{O}^{\bullet\bullet} + \frac{1}{2}O_2$$

Figure 4-24 : Schematically representation of generation of oxygen vacancies and reduction of Cerium ions under reducing atmosphere.

However, samples conventionally sintered above 1200°C under reducing conditions has micro-cracks in the microstructure due to internal stress generated by the abrupt volume change starting from the sample surface at low temperature in oxidizing atmosphere.

The dilatometer study of GDC10 sample shows the progression of density as a function of temperature in three different atmospheres i.e. air, argon and Ar/2.9%H$_2$. There was no significant difference in the densification behaviour of the GDC10 sample if sintered in argon and air. However, in the case of the sample sintered under Ar/2.9%H$_2$ atmosphere it was found that the onset of densification already starts at lower temperature. The densification rate of the three samples shows that the maximum sintering activity of GDC10 under reducing atmosphere is lowered by approximately 200°C.

The grain size analysis was carried out by SEM micrographs, shows that the sample sintered under reducing atmosphere experienced a higher grain growth as compared to the sample sintered in air. The average grain size of the sample sintered under reducing atmosphere was five times coarser (2.4 µm) than the average grain size (0.45 µm) of the sample sintered in air. Furthermore, sample which was sintered entirely under reducing atmosphere has several cracks in the microstructure. For taking advantage of the reducing atmosphere effect at the same time avoiding the micro-cracks in the sample was obtained by a re-oxidation at 800°C during the cooling cycle.

The crack formation in the microstructure for the sample sintered in low $P(O_2)$ (Ar/2.9%H_2) after exposing it to higher $P(O_2)$ (air) at room temperature corresponds to abrupt and heterogeneous volume changes starting from the sample surface. To better understand the chemical expansion behaviour of the GDC10 material due to the generation of oxygen vacancies, series of thermogravimetric and high temperature X-ray diffraction experiments were carried out. The quantification of the oxygen non-stoichiometry and the chemical expansion shows that the GDC10 sample may experience a volume change of above 4% at 1000°C under the reducing environment used during this dissertation.

4.3. Densification of GDC10 by FAST/SPS with Atmosphere Control

4.3.1. Overview

Field Assisted Sintering Technology (FAST) also known as Spark Plasma Sintering (SPS) is an efficient technology for fabricating ceramics. The very high heating rate due to the heat generation by joule heating, enables densify materials in a very short time as compared to the conventional sintering technologies. The high heating rate together with simultaneous application of mechanical pressure during the complete sintering cycle offers the possibility of tuning of microstructures down to the nanoscale, which is attractive with respect to improving the materials performance. FAST/SPS has been well established in the industry, but there are still a lot of open questions regarding sintering of complex ceramics, such as the ceramic's sensitiveness to low oxygen partial pressure or reaction with the tool material [29,30].

In this section, densification behavior of GDC10 in FAST/SPS, which is a low field and high current density technique will be studied. The redox behavior of GDC10 materials due to reduced atmosphere and associated volume change (chemical expansion) during the sintering process will be studied. Furthermore, sintering under reducing atmosphere and its effect on the densification and grain growth will be evaluated. A processing challenge for fabricating active oxides like GDC, which tends to easily loose oxygen under reducing conditions in FAST/SPS due to the direct contact with graphite tool and the atmosphere near the sample can have catastrophic effect on the mechanical stability of the material. The re-oxidation at higher temperature (800°C) have been investigated on a fundamental level with powder in the section 4.2.3 before. The re-oxidation experiment at 800°C will be carried out in FAST/SPS to overcome the cracking of the sample. The complete cycle was carried out by measuring the partial pressure of oxygen in real time during the experiment.

Later in the section, FAST/SPS cycles with an alternate tool design have been conducted to better facilitate the atmosphere near the sample. The densification behavior and the microstructure evaluation of the sintered samples were investigated. The application of controlled re-oxidation and its direct effect on the microstructure will be discussed.

4.3.2. Densification Behavior and Microstructure Evolution of GDC10 in FAST/SPS

In the beginning GDC10 was sintered in conventional FAST/SPS mode. Therefore, a conventional tool configuration (PA tool design, Fig. 3-2) and vacuum atmosphere were used. Several sintering cycles with different temperatures and holding time were carried out. A uniaxial pressure of 50 MPa is applied for the entire FAST/SPS cycle except the cooling period.

The processing conditions for the FAST/SPS cycle were described in section 3.2.1. Different set of experiments varying the sintering temperature between 800°C to 1400°C and with different dwelling period at the maximum temperature (0, 2, 4 and 6 min) was carried out for studying the densification and grain growth behavior of GGDC10 in FAST/SPS technique, which is shown in Fig. 4-25 [190]. These sets of FAST/SPS experiments were carried by Mr. Sree Koundinya Sistla at the Institute for Materials Applications in Mechanical Engineering (IWM), RWTH Aachen.
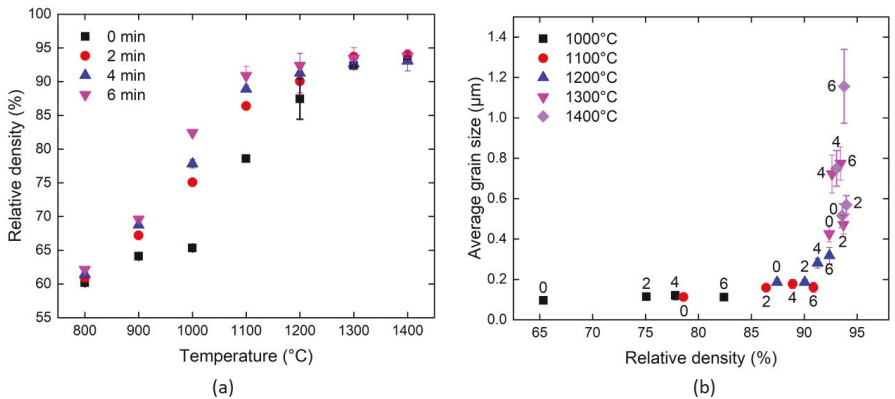

Figure 4-25 : (a) Relative density as a function of sintering temperature (800°C – 1400°C) and (b) evolution of grain size plotted against the relative density for the sintered samples at different temperatures (1000°C-1400°C) and dwell time (0-6 min) [190].

The densification of GDC10 as a function of temperature and four different dwelling time is shown in Fig. 4-25 (a). The initial green relative density of the powder compact, which was measured from the difference in the plunge heights before the uniaxial compaction and after uniaxial compaction at room temperature prior to the FAST/SPS experiments was approximately 50%. As concluded from the conventional sintering study in the dilatometer experiment (see section 4.2.3. Fig 4-17), the densification in argon and air starts approximately at around 850°C and in Ar/2.9%H_2 the densification starts at around 800°C. However, in FAST/SPS an increment of 10% in the relative density is observed at 800°C in all FAST/SPS cycle at different dwell time. The densification increases with increase in temperature from 800°C onwards, where the densification saturates at around 1200°C. After 1200°C, until 1400°C there was no significant densification observed for all the dwelling times [190].

Figure 4-25 (b) shows the sintering trajectory of GDC10 in FAST/SPS, where the grain growth behavior of GDC10 as function of sintering temperature and dwell time can be observed. In conventional FAST/SPS and vacuum atmosphere and 50 MPa pressure, the densification is dominant until a relative density reaches around 90%. After that a grain growth in the sample is observed, which is as a result of either higher temperature or longer dwelling time. The SEM micrographs shows the grain growth at 1400°C with different dwelling time in Fig. 4-26.
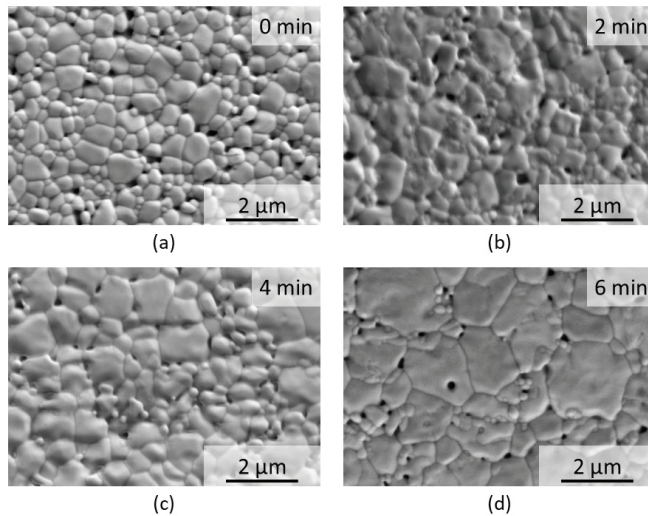

Figure 4-26 : SEM micrographs of the GDC10 sample sintered at 1400°C and different dwelling time: (a) 0 min, (b) 2 min, (c) 4 min and (d) 6 min showing the grain growth with dwelling time [190].

The sintering trajectory of GDC10 shows that the similar degree of densification can be achieved at a 200°C lower temperature by utilizing FAST/SPS as compared to conventional sintering route. The enhanced densification is obtained primarily because of the additional uniaxial pressure, which was applied during the FAST/SPS process. Furthermore, it may also be supported by the reduction of the GDC10 material due to the direct contact with the graphite tool (according to equation 4.3) and reducing atmospheres near the sample during the FAST/SPS process.

$$CeGdO_{1.95} + \delta C = CeGdO_{1.95-\delta} + \delta CO \qquad\qquad\qquad Eq. (4.3)$$

However, most of the sintered pellets were fragmented into many small pieces once ejected from the graphite die. All the sintered pellets were changing their colour from the original pale-yellow colour to dark bluish colour. The chromatic alteration of the sintered pellets colour hints reduction of the sample during the FAST/SPS process [191]. The change in the sample colour can be completely restored by annealing in air at high temperature (i.e. above 800°C). The fragmentation of the sintered pellets shows no specific dependence on either sintering temperature or the dwelling time. Very few times, a crack free sintered samples pellets were also produced by conventional FAST/SPS but the results were not reproducible. An optical image of the FAST/SPS sintered sample, which was fractured after ejection from the die is shown in Fig. 4-27.
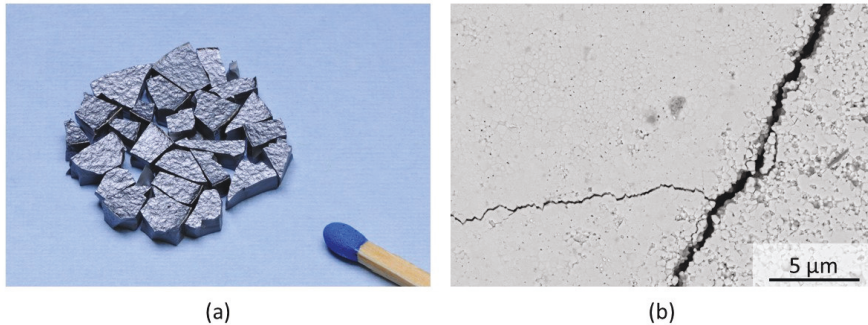

(a)   (b)

Figure 4-27 : (a) Optical image of the dense GDC10 sample fabricated by FAST/SPS at a sintering temperature of 1200°C with a dwelling time of 6 minutes and (b) SEM micrograph of the sample showing presence of typical micro-cracks in the FAST/SPS sintered GDC10 sample.

The redox behavior of GDC10 material accompanied by volume change, known as chemical expansion behavior, is extensively characterized in this work. It was observed that the sample under Ar/2.9%H_2 atmosphere at 1000°C could change the stoichiometry of GDC10 which results in a volume expansion of 4%. The change in coloration into a dark blue color hints towards a high degree of reduction of the sample during the FAST/SPS cycle. Furthermore, the sample is clamped inside the tool die and plunge, which does not allow the sample to accommodate such volume expansion and contraction, which resulted in fragmentation of the sample. In addition to the macroscopic failure, the microstructure of the FAST/SPS sintered pellets shows high degree of micro-cracks present in the sample, an example of such micro-cracks is shown in Fig. 4-27 (b).

4.3.3. Influence of Atmosphere on the Densification of GDC10 in FAST/SPS

The challenges of fabricating dense and crack free GDC10 samples by FAST/SPS technique was well anticipated from the beginning of the project. The generation of micro-cracks was shown to be avoided by putting oxygen back into the lattice at 800°C, so called re-oxidation experiments was achieved in dilatometer (see section 4.2.3). Similar re-oxidation experiments were carried out during FAST/SPS cycle. When taking advantage of the reducing atmosphere to enhance the densification kinetics of GDC10 and controlled re-oxidation at 800°C in a FAST/SPS to avoid the cracking of the sample was proposed for the first time.

In this section, effect of the reducing atmosphere on the densification kinetics in conventional FAST/SPS set-up (PA tool setup shown in fig. 3-2) was carried out. Furthermore, re-oxidation experiments at 800°C by introducing technical air (Ar/20%O_2) into the FAST/SPS chamber were carried out. The microstructures of the re-oxidized samples and not re-oxidized samples were compared. In addition, the partial pressure of the oxygen was monitored during the complete duration of the experiment, when operated under reducing atmosphere.
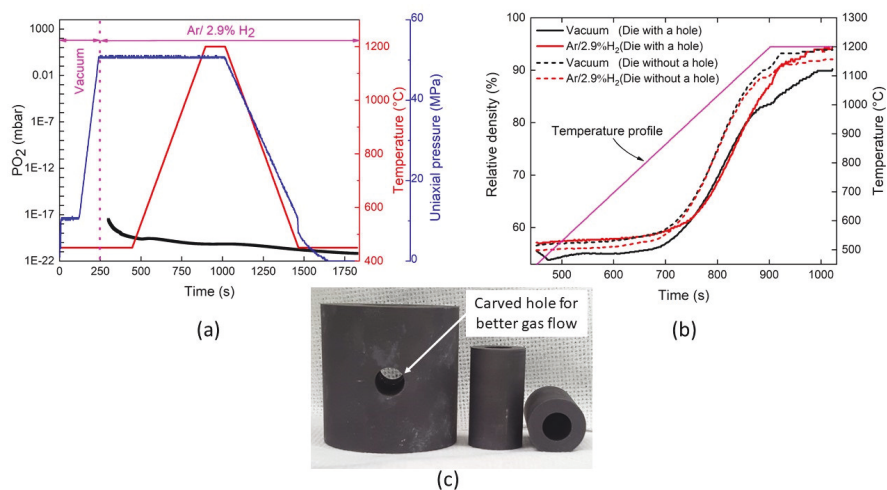
Figure 4-28 : (a) FAST/SPS cycle under reducing atmosphere showing the temperature, pressure, FAST/SPS chamber pressure and measured (PO_2) (b) evolution of density under vacuum and Ar/2.9%H2 for conventional tool configuration (PA) with and without a hole and (c) image showing the carved out hole in the die for better gas flow to the sample.

FAST/SPS cycle for GDC10 is carried out in a conventional tool configuration (PA tool, shown in Fig. 3-2) in vacuum and Ar/2.9%H$_2$ atmosphere. The sample is sintered at a temperature of 1200°C under simultaneous application of a uniaxial pressure of 50 MPa. The temperature and uniaxial pressure profile are shown in Fig. 4-28 (a). During the FAST/SPS cycle under reducing atmosphere (Ar/2.9%H$_2$) the partial pressure of oxygen was measured, which is shown in Fig. 4-28 (a). From the partial pressure of oxygen measurement, it was confirmed the sample was sintered under very low partial pressure of oxygen environment, where the PO$_2$ value was around 10^{-22} mbar.

Figure 4-28 (b) shows the evolution of relative density under vacuum and Ar/2.9%H$_2$ atmosphere. No difference in the densification profile under reducing atmosphere and vacuum is observed. In a conventional tool configuration (PA, Fig. 3-2), the sample is clamped inside the tool, moreover, the use of a graphite foil between the tool and sample avoids gas exchange between sample and gas chamber. Therefore, it is supposed that the actual atmosphere near the sample is different to the atmosphere in the FAST/SPS chamber. There was no exchange of gas between the sample and the FAST/SPS chamber atmosphere. To ensure direct exchange of the FAST/SPS chamber atmosphere to the sample, a hole (8 mm in diameter) was carved out

in the tool, as shown in Fig. 4-28 (c). The dashed line in the Fig. 4-28 (b) profile shows the evolution of relative density as a function of temperature. It was observed that there was no effect of the atmosphere on the densification behaviour of GDC10 in FAST/SPS.

In all the experiments in a conventional tool setup independent if $Ar/2.9\%H_2$ or vacuum are used, the sample fractured into many pieces after ejection from the die, as shown in Fig. 4-27. The microstructure of the sintered samples shows high amount of micro-cracks presence. Therefore as next step, controlled re-oxidation experiments at three different temperatures, i.e. 450°C, 600°C and 800°C were carried out on the conventional tool configuration with hole.

The FAST/SPS cycle with controlled re-oxidation at 800°C is shown in Fig. 4-29. In the beginning of the sintering cycle, the FAST/SPS chamber is evacuated completely approximately 0.6 mbar pressure. The uniaxial pressure is then applied on the sample and the FAST/SPS chamber was purged with $Ar/2.9\%H_2$ until a stable oxygen partial pressure is achieved. The partial pressure of oxygen was constantly monitored during the complete sintering cycle, except when the FAST/SPS chamber was in vacuum as the oxygen sensor can only work with a gas flow. The heating cycle starts at a heating rate of 100°C/min to 1200°C under controlled reducing atmosphere ($Ar/2.9\%H_2$). When reaching 1200°C, the temperature was held for 5 minutes, after which the cooling cycle started at a cooling rate of 100°C/min until it reached 800°C. At 800°C the temperature was held isothermally for 13 minutes. The FAST/SPS chamber was then evacuated for three minutes, which ensured all the $Ar/2.9\%H_2$ gas were evacuated from the chamber. After 3 minutes, the FAST/SPS chamber was purged with technical air ($Ar/20\%O_2$) for the complete cooling cycle, which included 10 minutes isothermal temperature at 800°C and until it reached room temperature. The measured oxygen partial pressure was around 10^{-21} mbar during the heating, dwelling and cooling until 800°C period. During the re-oxidation period the partial pressure of oxygen was around 206 mbar, which ensured an oxidizing atmosphere.
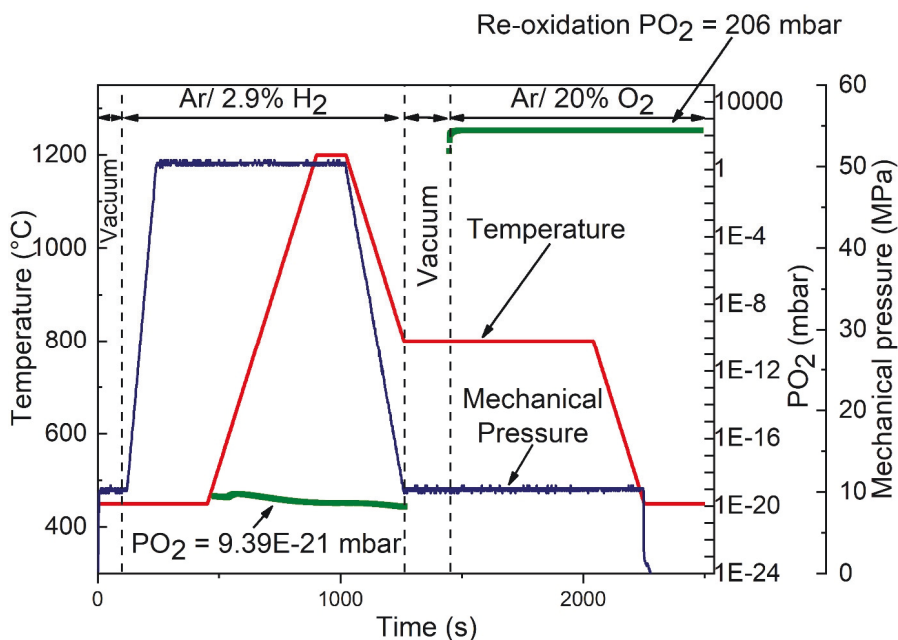
Figure 4-29 : FAST/SPS cycle under reducing atmosphere and controlled re-oxidation at 800°C during cooling showing the temperature, pressure, FAST/SPS chamber pressure and measured $P(O_2)$ [183].

The sintered sample nevertheless fractured into many pieces as observed during conventional FAST/SPS cycle without re-oxidation. This suggest that, no matter what is the FAST/SPS chamber atmosphere the actual atmosphere near the sample remains reducing. Additionally, due to the direct contact with the graphite foil, the GDC10 react with the graphite and looses oxygen as per equation (4.3). Another challenge is that, the reduced environment is quite uncontrolled with respect to the partial pressure of oxygen. Therefore, it is hard to evaluate in-situ the actual reduced state of the sample. The sample experience an uncontrolled high reducing environment near to its periphery inside the tool. Due to the PA tool design, exchange of the FAST/SPS chamber atmosphere with the sample was restricted. Therefore, no effect of atmosphere on the densification was observed. Furthermore, during the re-oxidation process the oxidized atmosphere could not reach the to the sample, which was clamped inside the PA tool. At room temperature when the sample is ejected from the die, an inhomogeneous re-oxidation is expected in accordance with the conventional sintering study (see section 4.2.2),

where the surface was re-oxidised rapidly as compared to the core of the sample. The sample then experience a sudden contraction starting from the surface, which disintegrated the dense sample into many pieces.

Similar results were obtained by Prasad et al. [30] during FAST/SPS of pure Ceria. Pure CeO_2 powder was sintered in the temperature range of 900-1500°C, under a pressure of 50-70 MPa, in vacuum. A standard graphite tool was used. Three important results from the XRD analysis were reported. First, the overall stoichiometry of ceria was significantly changed due to reduction by graphite. Second, the large inhomogeneity in stoichiometry was noticed. The samples were much less reduced in the centre then on surfaces contacting graphite punches. The largest loss of oxygen was observed on the surface contacting the positive electrode. Evidently, the related inhomogeneous chemical expansion led to the large internal stresses. Third, the samples were fractured into several pieces during ejection from the die due to abrupt release of internal stresses and additional stresses arisen during uncontrolled oxidation. Improved sintering was achieved only if the samples were encapsulated and isolated in an alumina powder bed [30].

Therefore, as a next step sintering of GDC10 sample, which was encapsulated with alumina powder was done. The goal of the experiment was to isolate the sample both electrically from passage of any current through the sample and chemically by inhibiting direct contact with the graphite tool. To do a related experiment, in this work a conventional tool (PA) with internal diameter of 30 mm was used. The external diameter of the punches was 29.6 mm. The GDC10 powder was uniaxially compacted at room temperature and the green body was placed inside the tool, where the green body was completely encapsulated by pure alumina powder. The alumina powder used for the encapsulation was high purity coarse alumina powder, #183 Alumina, Saint Gobain coating solution, France. The average particle size of the alumina powder was between 15-45 μm. The FAST/SPS tool configuration is shown in Fig. 4-30 (a).

Different FAST/SPS cycles, with varying sintering temperature, heating/cooling rate (here only 5°C/min), uniaxial pressure and atmosphere (i.e. vacuum and Ar/2.9%H_2) were carried out. In all the experiments, the sample disintegrated into many pieces or at least severe macroscale cracks were observed on the sample. In some of the experiments the sample fractured completely, and some experiments resulted cracks only on the surface without disintegration of the sample. The results obtained from these experiments were not reproducible. However,

the original coloration of the samples does not change when sintered with an alumina encapsulation, as shown in Fig. 4-30 (b, c and d).
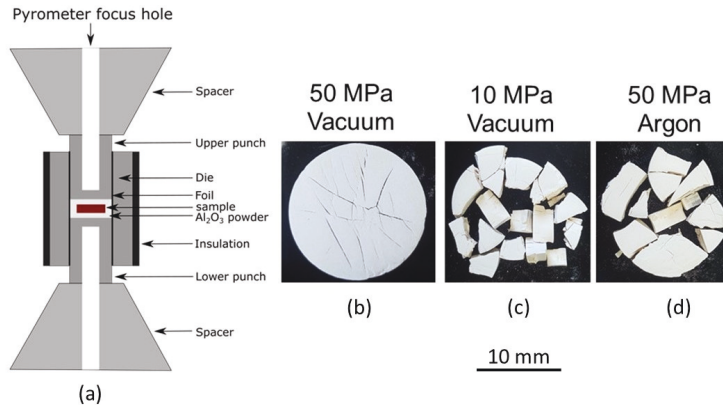

Figure 4-30 : (a) Schematics of the FAST/SPS tool configuration for the experiments with alumina encapsulation and sample from three different experiments, where sintering temperature of 1200°C and a dwelling time of 2 minute and heating /cooling rate 100°C/min, was used: (a) in vacuum and uniaxial pressure of 50 MPa, (b) in Vacuum and uniaxial pressure of 10 MPa and (C) in Argon atmosphere and a uniaxial pressure of 50 MPa [183].

Fig. 4-30 (a) shows the schematics of the FAST/SPS tool configuration and Fig. 4-30 (b - d) the images of the sample from three different experiments. In these experiments, a sintering temperature of 1200°C and a dwelling time of 2 minute and heating /cooling rates of 100°C/min, was used , where (a) in vacuum and uniaxial pressure of 50 MPa, (b) in vacuum and uniaxial pressure of 10 MPa and (c) in Argon atmosphere and a uniaxial pressure of 50 MPa. These three images represent the state of the sample integrity for all the experiments carried out by alumina encapsulations.

The disintegration of the GDC10 sample when sintered in a conventional tool configuration can be due to the following reasons:

- Thermal shock (high heating/ cooling rate)

- Temperature gradients/ non-homogenous temperature field

- Friction during sample removal

- Pressure profiles

- Phase transformation with significant volume change

- Chemical reactions with graphite/ sintering die

- Volume change due to chemical expansion

In this study, all the possible reasons for the disintegration of the GDC10 samples were systematically studied to avoid above mentioned reasons. For example, conventional FAST/SPS with a low heating and cooling rates (e.g., 5°C/min) was carried out to avoid any thermal shock. A modification to the PA FAST/SPS tool was done, where two dies were used, the internal die was made from two pieces which was inserted in an external die (sketch of the tool is not shown here). In this tool design, the sample can be easily ejected from the die without application of any external load, which ensure no friction during sample removal. FAST/SPS experiments with different pressure profiles were carried out to study the effect of external pressure on the stability of the sample. Ex-situ XRD study of the GDC10 specimens densified by FAST/SPS show that the samples retained its original phase after sintering in FAST/SPS, shown in Fig. 4-34. The chemical reaction with graphite (tool material) was also avoided by using alumina encapsulation during the FAST/SPS cycle. Controlled re-oxidation experiments were carried out to avoid any abrupt volume changes at room temperature. However, with all the variations in the processing parameters, a stable crack free GDC10 sample could not be fabricated.

Therefore, it was concluded that in case of conventional FAST/SPS tool configuration, graphite tool act obviously as an oxygen getter which reduce the sample in an uncontrolled way, as per the reaction equation (4.3). Moreover, due to the graphite tool, the sample environment near the sample is highly reducing in nature, which was also confirmed by analyzing the FAST/SPS chamber gas, which shows high concentration of CO gases (the results are not shown). The re-oxidation experiment might result in even more reducing atmosphere due to the reaction between graphite and oxygen that generates carbon monoxide gas, which is more reducing in nature. The reduction of the GDC10 sample in the FAST/SPS coupled with chemical expansion and abrupt contact to highly oxidizing atmosphere when ejecting the sample at room temperature from the die leads to an inhomogeneous re-oxidation of the sample from its surface to the core. As consequence, a nonuniform volume contraction occurs, which results in fragmentation of the pellets into many pieces.

4.3.4. Alternate Tool Design for Successful Processing of GDC10 by FAST/SPS Technique

To overcome the challenges of processing of GDC10 in a conventional tool configuration, an alternative tool configuration (PL tool) was proposed in this work. The objective of the alternate tool design servs two purposes, (i) fabrication of stable crack free GDC10 samples in FAST/SPS device and (ii) elimination of any possible micro-cracks in the microstructure by re-oxidizing at higher temperature. The goals were realized by designing a tool configuration where some space allowed to avoid clamping of the sample and direct contact with the tool material. Furthermore, by carving a hole a better gas flow was achieved near the sample. The detailed tool setup (named PL tool for "pressure less") was explained in section 3.2.1 and shown in Fig. 3.2.

Specific detail of this tool is that no pressure can be applied on the sample during the FAST/SPS cycle. High densification by PL FAST/SPS technique was achieved only at a temperature of 1400°C with 15 min dwelling time. FAST/SPS cycles were carried out with high heating and cooling rate of 100°C/min. A minimum load of 3 kN was applied on the PL tool configuration to ensure good electrical contacts between the cone, punches and die. Uni-axially pressed powder compact sample (green density of 50-55%) was used for densification in FAST/SPS by PL tool.
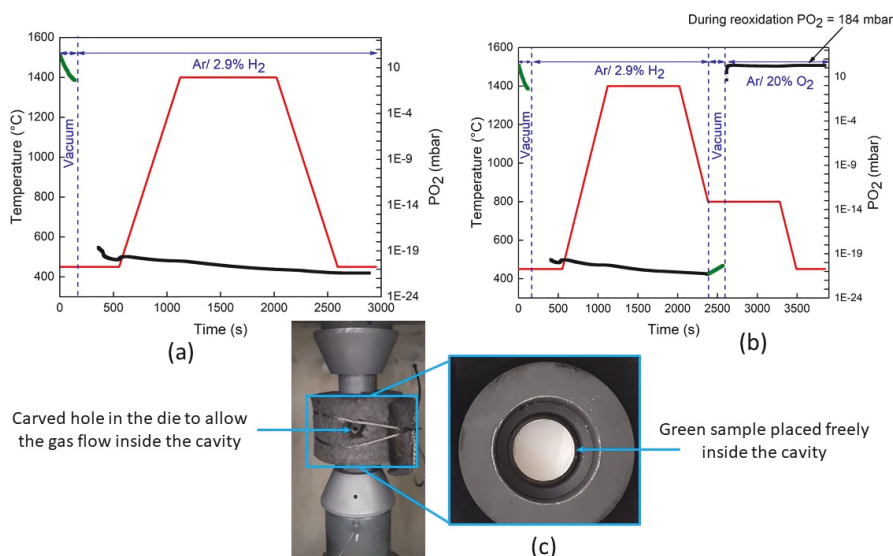
Figure 4-31 : FAST/SPS cycle with the pressure less (PL) tool configuration: (a) FAST/SPS cycle entirely under reducing atmosphere, (b) FAST/SPS cycle under reducing atmosphere and re-oxidation at 800°C and (c) image of the tool showing the carved out hole in the die for better gas flow and placement of the sample freely to allow volume expansions.

This tool enabled non-constrained sintering and better atmosphere control in the vicinity of the sample. However, it is expected that sintering of GDC10 under vacuum and in the vicinity of the graphite tool results in some degree of reduction. Occurrence of this effect was also evident from the sample colour, which turns out to be light blue in colour. The samples sintered in vacuum were mechanically stable, but SEM analysis revealed many micro-cracks in the microstructure. Similar result was obtained after FAST/SPS in Ar-2.9% H_2 atmosphere, Fig. 4-31(a). Different PL FAST/SPS processing parameters and the final relative density with the integrity of the sintered samples are summarized in Table 4-3.

Table 4-3: Parameters and results of GDC10 densification at different conditions by PL FAST/SPS

Temperature, °C	Dwell, min	Atmosphere	Rel. density	Integrity
1400	15	Vacuum	0.92	Micro-cracks
1400	15	Ar-2.9%H_2	0.91	Micro-cracks
1400	15	Redox	0.93	Nearly crack-free

Figure 4-32 : Comparison of the FAST/SPS sintered pellets: (dark yellow and stable) with pressure less (PL) tool configuration under Ar/2.9%H_2 atmosphere and re-oxidation at 800°C and (black and fractured) with conventional pressure assisted (PA) tool under Ar/2.9%H_2 atmosphere [192].

In contrast, re-oxidation at 800°C (FAST/SPS cycle shown in Fig. 4-31 (b)) was found to be an effective measure to drastically reduce the micro-crack formation. Nevertheless, the colour of sintered samples was dark yellow, indicating a certain change in stoichiometry, as shown in Fig. 4-32.
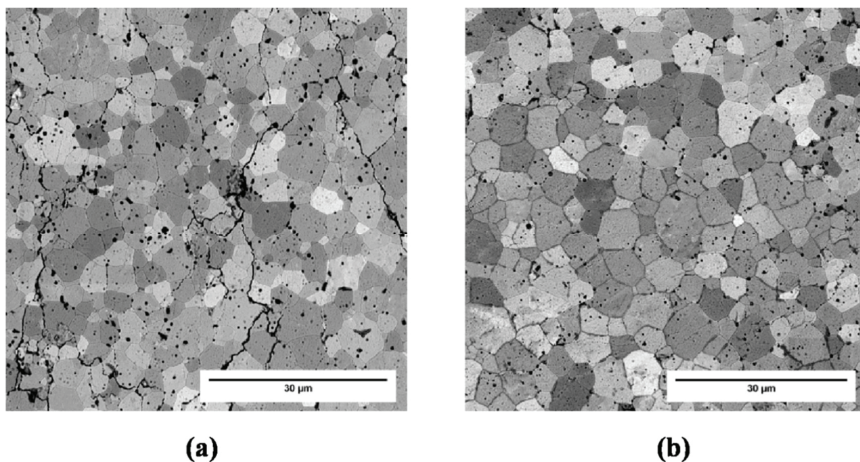
Figure 4-33 : Micrographs of pressure less (PL) sintered samples: (a) cracks formation after sintering in Ar/2.9%H_2, (b) nearly crack-free structure after sintering in Ar-2.9%H_2 with subsequent re-oxidation [183].

Figure 4-33 shows the SEM micrographs of the pressure less (PL) FAST/SPS sintered pellets in (a) Ar/2.9%H_2 and (b) Ar/2.9%H_2 with controlled re-oxidation at 800°C. The sample which was sintered entirely under Ar/2.9%H_2 atmosphere has high amount of micro-cracks. This result suggests that the reduction of the sample took place under better controlled reducing conditions with defined oxygen partial pressure. More importantly, the atmospheres which was purged in the FAST/SPS chamber obviously reaches the sample environment. Which becomes evident from the almost crack free microstructure of the re-oxidised sample and is in accordance with the dilatometer experiments.

The effect of sintering atmosphere and re-oxidation was further characterized by XRD analysis in Fig. 4-34. The cross section of the samples was analysed by X-ray diffraction to obtain possible degree of reduction from calculating the micro strain present in the sintered samples. All the sintered samples maintained the initial fluorite structure.
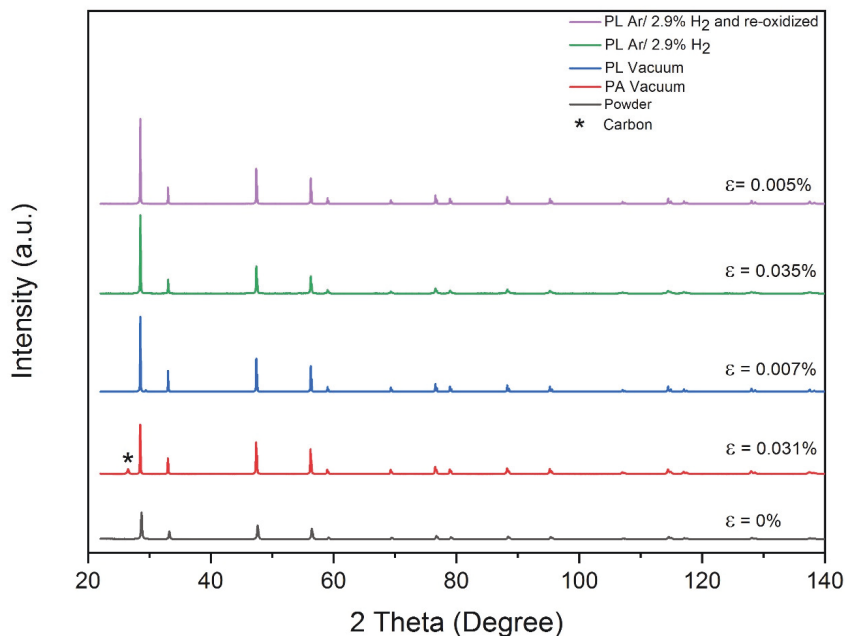
Figure 4-34 : XRD patterns of the GDC10 raw powder and FAST/SPS pellets sintered under different atmospheres and different tool configurations [183].

Fig. 4-34 shows XRD patterns of the sample sintered by conventional FAST/SPS (PA) tool in vacuum, pressure less FAST/SPS (PL) tool in vacuum, pressure less FAST/SPS (PL) tool under Ar/ 2.9% H_2, pressure less FAST/SPS (PL) tool with controlled re-oxidized sample and the raw powder. XRD patterns of the sample sintered in a PA tool set up in FAST/SPS shows traces of carbon as compared to the sample sintered by FAST/SPS in PL tool. The broadening of the XRD peaks is due to the contribution of crystallite size, micro-strain (ε), and the instrument itself. The micro-strain of the sintered samples was calculated from the peak broadening and by subtracting the effect from the instrument and crystallite size. The micro-strain results show that, GDC10 material when sintered in PA tool in vacuum, has higher micro-strain of about 0.031% as compared to the sample sintered by PL tool set up ($\varepsilon = 0.007\%$). Which suggest that by isolating the sample from the direct contact with the graphite tool, the degree of reduction of the sample can be minimized significantly. Furthermore, in PL tool configuration, when GDC10 is sintered under reducing atmosphere (Ar/ 2.9% H_2) without a re-oxidation step shows even higher micro-strain ($\varepsilon = 0.035\%$). That confirms that the reducing atmosphere is reached to the sample, which is why the degree of reduction was higher than in PL tool in vacuum. The

re-oxidation of GDC10 at 800 °C shows significant reduction in the micro-strain ($\varepsilon = 0.005\%$) in the sintered pellet. This shows the effectiveness and importance of the re-oxidation step at higher temperature [183].

The XRD analysis data confirms the assumption that GDC10 material in conventional PA tool set up with direct contact to the graphite tool underwent high degree of reduction. The chemical expansion and successive contraction due to the reduction and oxidation of the sample respectively results in dense but splintered into many pieces and has micro-crack in the microstructure.

4.3.5. Summary

The Field Assisted Sintering Technique/Spark Plasma Sintering (FAST/SPS) has emerged as an effective method for densifying a wide range of materials [70]. The FAST/SPS process utilizes low voltage, pulsed direct current (DC) and uniaxial pressure to consolidate powders by joule heating. The tool material is in most cases made of graphite, the sample (when sufficiently conductive) is heated internally by the joule heating as the current is directly pass through the sample and the tools on the contrary for the non-conductive samples, the current is passed through the tool and the heat is transferred to the sample from the tool by thermal conduction. Therefore, this experimental setup enables high heating rates up to 1000 °C/min. It has been reported in the literatures that higher densities and lower sintering temperature can be achieved by FAST/SPS process as the densification of the material is achieved by simultaneous application of temperature and pressure.

Conventional FAST/SPS is utilized to fabricate GDC10 samples. The densification behaviour of GDC10 suggest that the sintering temperature can be lowered by 200°C in FAST/SPS process as compared to the conventional sintering route. Nevertheless, the conventional tool setup (PA tool) has several challenges for fabricating stable crack free GDC10 samples by FAST/SPS.

Primarily due to the direct contact with the graphite tool that act obviously as an oxygen getter, which reduce the sample in an uncontrolled way. Furthermore, in conventional tool configuration the sample is completely isolated from the external atmosphere, which hinder exchange of any processing gas to reach to the sample.

For the first time, sintering of GDC10 with controlled re-oxidation in a FAST/SPS device has been demonstrated. An alternative tool design was applied, which enabled unhindered gas

exchange in the vicinity of the sample. By feeding technical air at 800°C to the sample, GDC10 samples were almost free of residual strain and did not show any micro-crack formation. Additionally, this pressure less tool design allows stacking up more than one sample, which enables sintering of many samples in one FAST/SPS cycle. Nevertheless, simple tool design did not allow taking advantage of uniaxial pressure usually applied in conventional FAST/SPS cycles. In conclusion, the developed FAST/SPS method can be applied for sintering of other oxides that are prone to the chemical expansion, such as $Ba_xSr_{1-x}Co_yFe_{1-y}O_{x-d}$ (BSCF) or $La_xSr_{1-x}Co_yFe_{1-y}O_{x-d}$ (LSCF).

4.4. Fundamental Study of GDC10 in Flash Sintering

4.4.1. Overview

Flash sintering (FS) is another field assisted sintering technology, which has high potential for sintering of GDC. More specifically, flash sintering belongs to the electric current assisted sintering (ECAS) processes. Contrary to FAST/SPS process, in flash sintering the current is forced to flow through the ceramic sample. The most important aspect of the flash sintering process is its ability to significantly lower the required furnace temperature and shorten the sintering time, usually down to a few seconds to fully densify ceramics. While the mechanisms of the flash sintering process remain under consideration, they encompass three characteristics: (i) an abrupt increase in conductivity, (ii) electroluminescence, and (iii) rapid densification.

In this work, comprehensive flash sintering study of 10 mol.% gadolinium-doped ceria (GDC10, $Gd_{0.10}Ce_{0.90}O_{1.95}$) was carried out. The current section is dedicated to a fundamental study of the flash sintering of GDC10 in the established voltage-to-current control mode. This part of the thesis contributes to the ongoing debate on the physical mechanisms responsible for flash sintering. First, the onset characteristics for initiating flash (non-linear rise in conductivity) was examined. It is well known that higher electric fields lower the temperature for the onset of flash. We explore the question "what can be the lowest temperature for initiating flash?". Constant heating rate experiments at increasing electric fields revealed a surprising characteristic: the Debye temperature emerges as a lower bound for the onset of flash. Data for flash onset temperature for GDC10 together with three other oxides (i.e. 8mol.% Yttria stabilized zirconia, 3mol.% Yttria stabilized zirconia and Titania) are shown to exhibit this behavior in a universal plot.

The second question which was explored was, to understand what triggered the onset of flash in GDC10 sample under DC electric field. The flash transition in GDC10 is correlated with the

generation of *n-type* electronic conductivity in ambient air under DC bias. Its origin is attributed to a partial reduction of the material which propagates from the cathodic to the anodic region, during the incubation period. The phenomenon was observed by an, *in-situ* experiment, by monitoring the occurance of electrochemical blackening during the incubation period of the flash experiment. Anomalous features, including a shift in the valence band edge, shrinkage of the band gap and a change in the oxidation state of Ce in flashed samples was confirmed by XPS and diffuse reflectance measurements. The results prove that flash sintering can alter the electronic structure of GDC10, and that such alterations being partially retained after the flash.

Finally, the effect of different flash processing parameters in the densification behavior of GDC10 was systematically studied. Higher electric fields lower the onset temperature, but it does not affect the degree of densification of the sample. The degree of densification depends on the maximum current density applied to the sample. Here, the effect of current density, electric field and holding time after initiating flash on the densification and microstructure was studied. Based on this results, a processing map for safe flash sintering of GDC10 sample was developed.

4.4.2. Influence of Electric Field on the Lower Bound Temperature for the Onset of Flash

The onset of flash in the voltage-to-current controlled mode is signaled by an abrupt increase in the conductivity of the specimen, which is related to the applied electrical field and the furnace temperature. It is now accepted that the onset temperature for flash is inversely dependent on the applied electrical field [121,139,139,141]. The flash phenomenon takes place not only in powder sample during sintering but also in dense polycrystalline specimen and even in single crystals [120,141]. It is interesting that at a given applied field the flash temperature for single crystals of cubic zirconia is lower than in dense polycrystals. This temperature is even higher for powder compact samples. Previous studies on the flash sintering of GDC showed that the onset temperature of flash was lowered by applying higher electric fields [36,38]. Additionally, preliminary experiments in the current work also showed the onset temperature of flash on green GDC10 samples was lowered with higher electric field. Surprisingly, it was found that at very high electrical fields the onset temperature was saturated.

The onset behavior of dog-bone shaped green GDC10 samples (dog-bone-1 samples as discussed in section 3.2.1) on the applied electrical field shows that the onset temperature for flash is lowered with higher electrical field, shown in the inset plot of the Fig. 4-37. Surprisingly, it was found that at very high electrical fields the onset temperature saturated.

In this section, the lower bound temperature for the onset of flash and the possible mechanism that determined the lower bound temperature for the onset of flash is systematically studied. The experiment is designed based on the hypothesis suggested by Yadav and Raj [119] that onset of flash is occurred due to the generation of Frenkel defects, These defects arise in concentrations far above thermal equilibrium as a result of non-linear lattice vibrations [116]. Related to this hypothesis the onset of flash would only be possible at phonon wavelengths that are equal to or less than the lattice parameter. The Debye temperature (Θ_D) is defined as the temperature for the crystal's highest normal mode of vibration [193]. It follows that, if this theory is correct, the Debye temperature would be the lower bound for the onset of the flash. To study the role of Debye temperature on the onset of flash, dense GDC10 samples in rectangular shape was used (rectangle bar-2 as mentioned in section 3.2.1).

The experiments were carried out in constant heating rate mode, where a constant electric field was applied at room temperature and then heating the furnace at a constant rate of 10°C min^{-1}. In total 15 different electric fields were applied ranging from 80 V cm^{-1} to 2000 V cm^{-1}. After the flash event the experiment was switched from voltage control to current control, with the current limit set to 100 mA mm^{-2}. After holding the specimen at this current for 120 seconds the power was switched off. This study was primarily concerned with the stage I of the flash sintering process.

The real time data for the power density are shown in Fig. 4-35. Power density profile for constant heating rate experiments at 15 electric fields is shown. The peak of the power density, which is the product of the electric field and the current density, increases with the field up to 500 V cm^{-1}. At higher fields the samples splintered before reaching the maximum current limit (100 mA mm^{-2}). At very high electric fields, 3000, 4000 and 5000 V cm^{-1}, which are not included in this figure the samples splintered with only a few mA current flowing through them.
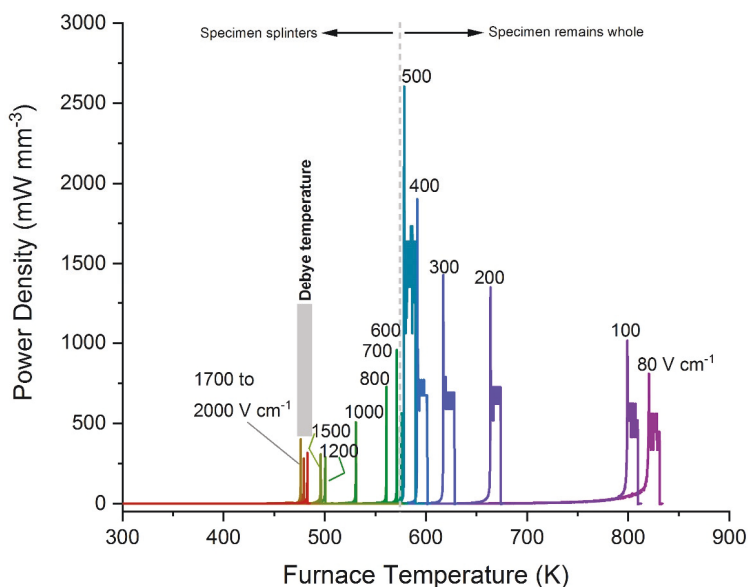
Figure 4-35 : The data for the change in power density depending on temperature in constant heating rate experiments with 10°C min^{-1} for dense GDC10 bar shaped samples, variation of electric field between 80 and 2000 V cm^{-1} [120].

There are two possible explanations for the cracking of the samples: It may be related to the non-uniform lattice expansion from non-uniform defect generation [194]. The resulting gradient in lattice expansion could lead to elastic stresses which caused the fracture. Another possibility would be thermal shock [148]. The power surge happens quickly. At high fields and low furnace temperatures, the power surge can produce thermal gradients and thereby, heterogeneous stress distribution might lead to mechanical failure. Specimen splintering during flash at high fields is a new finding, which required more study to understand the effect. Such studies are planned for the future.

Before discussing the results, it is important to address one of the biggest challenges in flash sintering in general, which is measuring the actual temperature of the sample during the flash event. The temperature of the sample at the onset of flash can rise above the furnace temperature by Joule heating. Therefore, it is important to look at the power density at the onset of flash and standardize a method to measure the onset temperature.
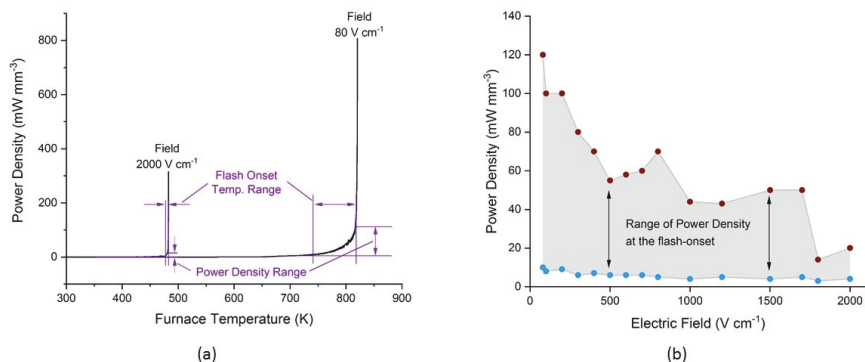
Figure 4-36 : (a) The method for measuring the range of temperature and power density at the flash-onset. The range became narrower at higher applied fields, (b) the range of power density encompassing the onset of flash at 15 different electric fields. The range varied up to 40 – 60 mW mm^{-3}, although it is wider at the lowest fields and narrower at the very high fields [120].

The onset temperature for flash was measured as a range from the power density profile as a function of furnace temperature. Tangents were drawn to the Stage I and Stage II period in the power density curve. Two examples of this method, one at low and the other at high electric field, are shown in Fig. 4-36 (a). The data yield values for the range in temperature and the range in powder density for the onset of the flash at different electric fields.

The range of the power density for the flash-onset at different electric fields, is shown in Fig. 4-36 (b). Note that the lower limit of the range is almost the same for all electric fields. The flash-onset is wide at low electric fields but narrows as the field is increased. Table 4-4 summarizes the range of the flash onset temperature at different electric fields.

Table 4-4: The onset temperature range for the applied electrical field for dense GDC10

Experiment No.	Electric Field (V cm^{-1})	Onset temperature range (K)
1	80	740 – 818
2	100	730 – 800
3	200	650 – 665
4	300	610 – 617
5	400	585 – 590
6	500	570 – 575
7	600	570 – 575
8	700	565 – 570
9	800	550 – 560
10	1000	520 – 530
11	1200	490 – 500
12	1500	490 – 495
13	1700	470 – 475
14	1800	470 – 475
15	2000	473 – 480

The upper bound power density value at the onset of flash was highest ~100 mW mm^{-3} among all the experiments with different electric fields. Recently, Cao et. al. [195] have measured the sample temperature for 10 mol.% yttria doped ceria by applying a low electric field during Stage I. They used a cylindrical shaped sample with a diameter 8 mm and height 13 mm. The experiment was conducted on a custom-made sinter forging device. An insulating mantle thermocouple was used to measure the temperature inside the sample [195]. They found that at a power density of 63 mW mm^{-3} the sample temperature was only 22°C higher than the furnace temperature. Therefore, in the current study, it is assumed that the sample temperature is similar to the furnace temperature at the onset of flash.

The main graph in Fig. 4-37 shows how the flash temperature lowers with increase in the electric field. At very high electrical field i.e., above 1200 V cm^{-1}, the temperature approaches a lower bound. Above an electrical field of 1200 Vcm^{-1}, the onset temperature of flash remains more or less constant even when the electric field was almost doubled i.e. 2000 Vcm^{-1}. Direct

measurements of the Debye temperature for GDC 10 has not been reported in literature. However, Hisashige et al. [196] report on the Debye temperature of rare earth-doped ceria. They found that the Debye temperature with different doping elements (10 mol. %) changes by less than ± 20 °C from the Debye temperature of pure Ceria, which is reported to be about 480 K. Therefore, for the current experiments with GDC the Debye temperature was taken as 480±20 K.
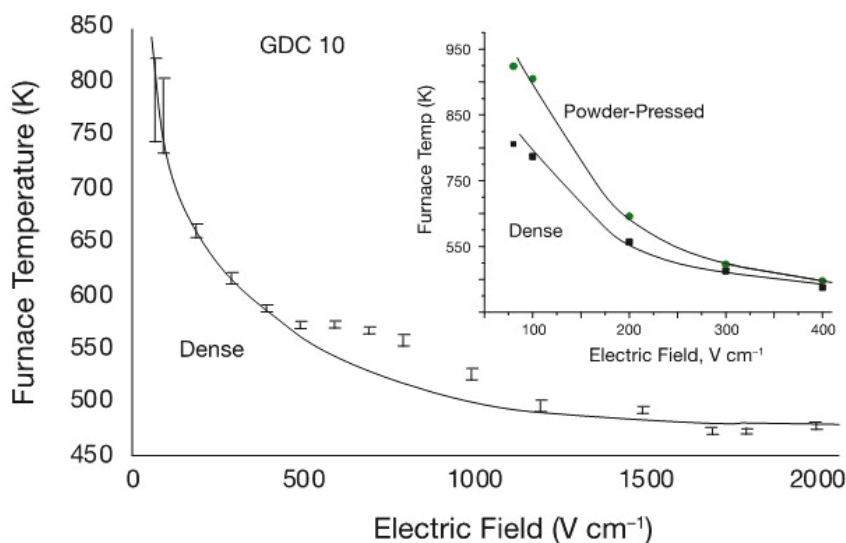

Figure 4-37 : Plots of the onset temperature of as a function of the electrical fields. The error bars were calculated from the procedure outlined in Fig. 4-36. The numerical data are included in Table 4-4. The inset compares the data from powder-pressed and dense polycrystalline samples. The main graph shows the temperature to approach an asymptotic values at high electric fields [120].

Data for the lower bound flash temperature from literature [119] for 3YSZ, 8YSZ and Titania are gathered and together with the current onset results for GDC10, a universal plot was prepared (Fig. 4-38). The plot shows the flash onset temperature, which is normalized with respect to the Debye temperature of each material. The plot shows that the Debye temperature for several ceramics may indeed serve as the lower bound for the onset of the flash.
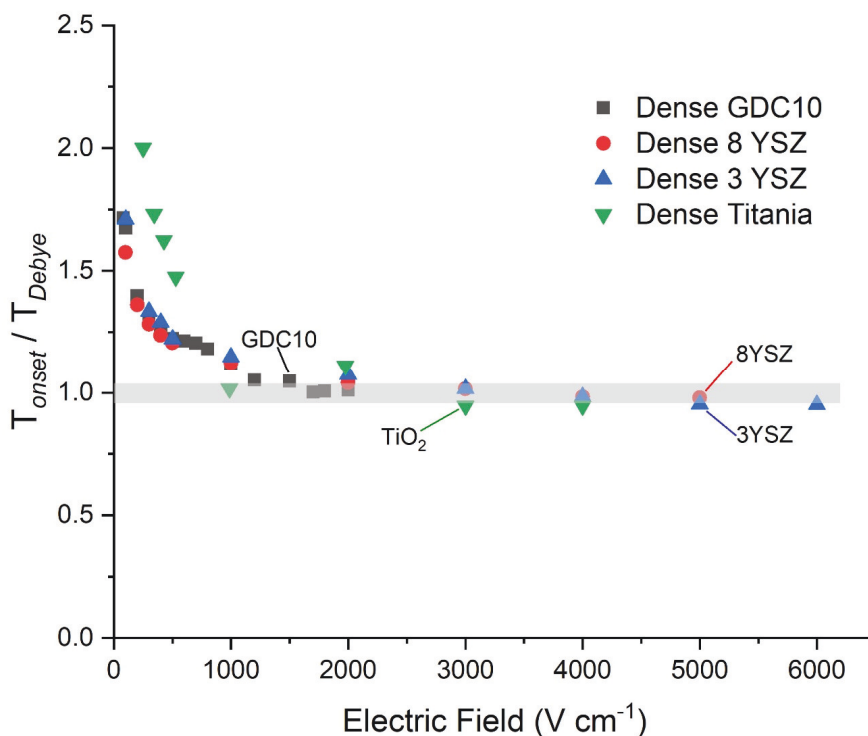
Figure 4-38 : Normalized plot of the flash onset temperature, with respect to the Debye temperature for three oxides measured on dense polycrystalline samples. The result confirms the hypothesis that Debye temperature is the lower bound for flash [120].

This is a novel finding in the flash sintering process that would support the idea that point defects are generated during the onset of flash. The role of these defects in the sintering process is still under consideration. The empirical finding that the Debye temperature is the lower bound temperature for the onset of flash does not entirely explain the mechanism, but it is another characteristic effect, which must be added to the already accepted three characteristics of the flash sintering process (see section 2.2.5).

### 4.4.3. Understanding the Mechanism of the Onset of Flash in GDC10

A suggestion has been made that the time of stage I (incubation period) in the flash sintering experiment may be the time required for the joule heating of the sample to balance surpass the heat loss due to radiation [114,118]. The stage II starts with the onset of flash, when the joule heating in the sample is larger than the heat loss due to the radiation. The onset of flash is

signaled by a non-linear rise in conductivity. This causes a surge in power dissipation in the specimen also known as thermal runaway. The question remains what may trigger the onset of flash? Is the Joule heating occurring first that led to nonlinear rise in conductivity or is the enhanced conductivity appearing first that causes Joule heating?

In this study, the progression of flash sintering in 10 mol% gadolinium-doped ceria specimens (GDC10) was studied to understand the onset mechanism in flash sintering. GDC10 is mixed ionic an electronic conductor, where the electronic conductivity of GDC10 depends on the partial pressure of oxygen and temperature [197]. Therefore, here we question whether electronic conductivity (n-type) of GDC10 could be activated also in air and changes its flash onset temperature. In summary, we seek a deeper understanding of the origin of flash transition for GDC10. This goal is achieved by exploring the electrochemical effects and the related enhancement in electronic conductivity under DC field in air.

To answer this question, flash experiments were carried out on a hot plate in ambient air atmosphere to check the presence of chromatic alterations associated to a partial reduction under the effect of electric loading (the so-called electrochemical blackening) [143].

Figure 4-39 reveals that a visible chromatic alteration develops in the early stage of the FS incubation from the negative electrode (cathode) and propagates towards the positive one (anode). The alteration appears faint in the first experiment (Figure 4-39 (a)) and better visible in the second run on the same sample (Figure 4-39 (b)), where the flash sintering was conducted on the same sample but with reverse electrical polarity. Electrochemical blackening is attributed to the fact that the electric loading under DC bias forces an accumulation of oxygen vacancies in the cathodic region (-) where their charge is balanced by electrons injected from the metal electrode [198]:
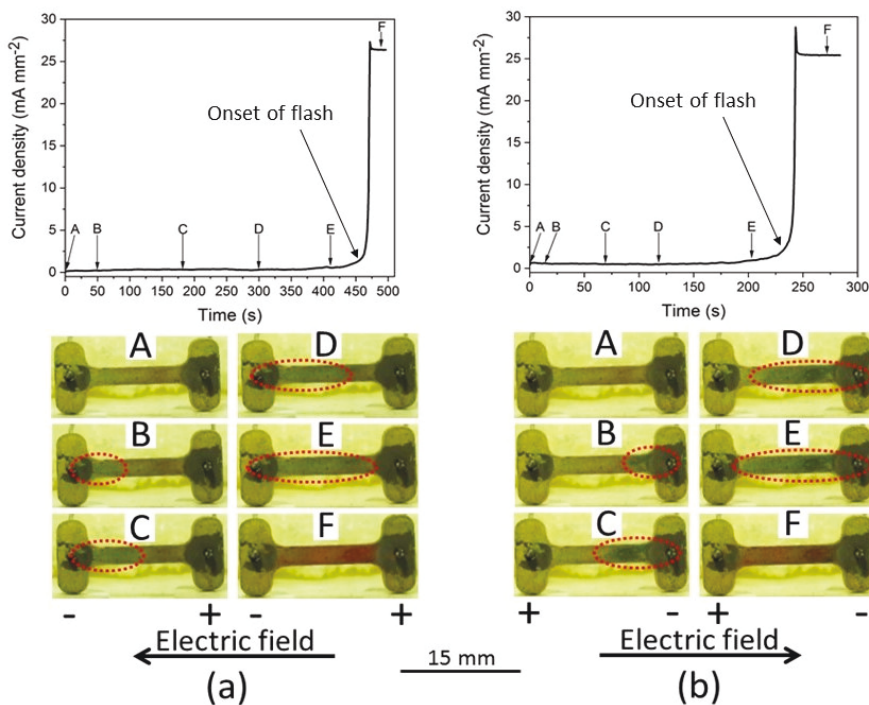
$$\delta V_O^{\cdot\cdot} + CeO_2 + 2\delta\, e' \;\rightarrow\; CeO_{2-\delta} + \delta\, O^x \qquad . \qquad\qquad\qquad \text{Eq. 4.4}$$
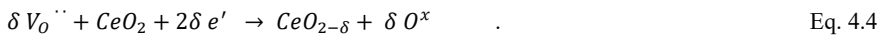
Figure 4-39 : Chromatic alteration in the dense polycrystal GDC10 samples during the incubation time of the flash experiment in air (280°C, 150 V cm^{-1}, 25 mA mm^{-2}). Current density profile in real time and optical images of the samples during different stages of the flash experiment reveal the generation and propagation of the blackening from the negative electrode to the positive electrode (a) First flash experiment and (b) repeated flash experiment on the same sample with reverse electrical polarity [199].

Therefore, the material starts to be partially reduced from the cathode. The partially reduced region becomes electronically conductive and allows the reduction reaction to propagate through the sample. At the reduction front, the electronic current is continuously converted into ionic current. Electrochemical blackening suggests a change in the material stoichiometry due to the applied electric field, thus leading to the formation of electronic defects beyond the simple effect of temperature and molecular oxygen activity. The electronic conductivity is enhanced in the partially reduced state (Eq. 4.5) and, therefore, the current flow rises abruptly when the blackened region propagates to most of the gage length. The partial reduction of the

oxide can be therefore considered a co-triggering mechanisms for the onset of flash in GDC10, along with Joule heating.

$$O_O^X \leftrightarrow \frac{1}{2}O_2 + V_O^{\cdot\cdot} + 2e'$$
Eq. 4.5

Figure 4-39 (b) shows a second flash experiment on the same sample but with a reversed polarity. It can be clearly observed that the blackening again starts at the cathode and propagates towards the anode. More interestingly, the incubation time for FS (i.e., the time needed to initiate the flash) is lowered by about 50% when compared to the first flash experiment. This suggests that, after the flash, the specimen retains a non-stoichiometric and free electrons-enriched state. In other words, there is a sort of "memory" of the previous flash process. This might be useful in the next future to tailor the electronic properties of both semiconducting and insulating oxides.

The flashed samples (flashed twice as shown in Fig. 4-39) were further characterized ex situ to study the origin of the blackening in the GDC10 sample, which is expected to be partially retained after the flash experiment due to change of incubation time. Initially the crystalline structure of the flashed sample was investigated by XRD analysis to verify that the reduction process did not cause the development of new phases. The XRD analysis shows that the flashed sample fully retained its initial cubic fluorite structure, shown in Fig. 4-40 (a). The reduced cations (Ce^{3+}) therefore accommodate in solid solution in the parent fluorite phase.

Fig. 4-40 (b) shows the Ce 3d XPS spectrum before and after FS in air. The relative intensity of the spectral line associated with Ce^{3+} increases after flash. This might be not very evident due to the presence of multiple peaks and the complex nature of the Ce XPS spectrum. However, the Ce^{3+} lines at 884 and 903 eV suggest that the relative intensity of Ce^{3+} rises after the sample flashed. A deconvolution of the spectra allows to point out a modification of the ratio between the intensities of the Ce^{3+} and Ce^{4+} components. The $Ce^{3+}/(Ce^{4+} + Ce^{3+})$ ratio passing from 0.26 (before flash) to 0.34 (after flash). This indicates that the sample is indeed partly reduced during the flash process. The results were also confirmed by a shift in the maximum XPS O 1s signal, which moves toward higher energies after the sample flashed (Figure 4-40 (d)). Such shift is consistent with a partial reduction of the oxide [200].
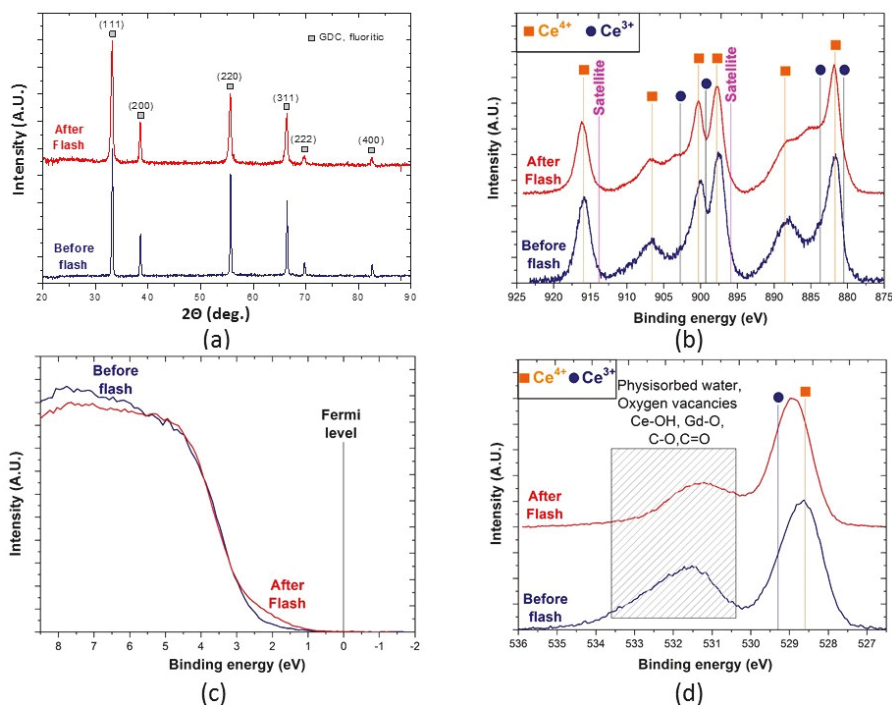
Figure 4-40 : Comparison between GDC10 samples before and after flash in air: (a) XRD spectra (b) XPS spectra of Ce 3d (c) valance band edge; and (d) O 1s XPS spectra (note that the signal at 531-533 eV is mainly related to surface impurities) [199].

Additionally, Figure 4-40 (c) shows the XPS spectra of the valance band edge region before and after flash. It is evident that the flash process caused a small shift of the valance band edge at higher energy, thus resulting closer to the Fermi level. This suggests that flash might be responsible for a decrease of the band gap due to the formation of donor levels connected with formation of oxygen vacancies upon flash. To verify the change in the band gap energy that was induced by the flash process, diffuse reflectance spectroscopy (DRS) measurements were carried out [201].

Figure 4-41 (a) shows that the reflectance after flash was drastically reduced, pointing out the activation of new absorption mechanisms. This suggests an enhanced absorption of the flashed sample at low energy that may be due to donor defects in the band gap region. Moreover, flash appears responsible for a decrease of the band gap, about 0.1 eV, as observed by drawing the tangent to the inflection point of the Kubelka-Munk plot (Figure 4-41 (b)).
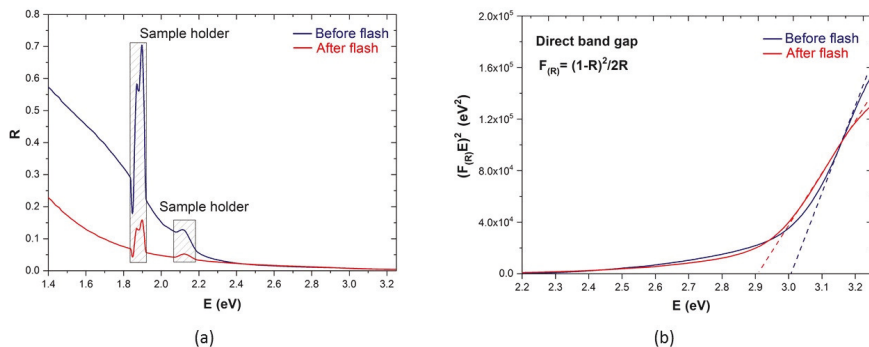
Figure 4-41 : (a) Diffuse reflectance (R); and (b) $(F_{(R)}E)^2$ vs. photon energy (*E) plot* for the determination of optical band gap of GDC10 before and after flash sintering [199].

It is worth mentioning that the results were measured at room temperature after cooling down from the flash event. Schmerbauch et. al. studied the evolution of point defects during flash sintering of ZnO by macro photoluminescence. This study reveal that the point defects (either cation or anion) are often modified during the flash state [194]. Therefore, a quantification of the band gap (E_g) change in the flash state remains an open question to be answered in the next future. However, the results clearly shows that: (i) the electronic properties of GDC10 are modified upon flash and (ii) these alterations are partially retained after the flash. The introduction of defects by flash could be useful to develop new out-of-equilibrium materials.

GDC10 in the reduced state, in GDC10 oxygen vacancies and electrons are generated to maintain the charge neutrality. Part of these extra electrons are located on the cations, which reduce their oxidation state form 4+ to 3+. Since $V_O^{..}$ concentration is pinned by the loading of the substitution element Gd, a reduction in P(O_2) mainly results in an increase of electrons concentration and Ce^{3+} species, enhancing the electronic *n-type* conductivity. Flash sintering experiment of GDC10 under Ar/5%H_2 was carried out to reduce the sample thereby increase in the bulk electronic conductivity.
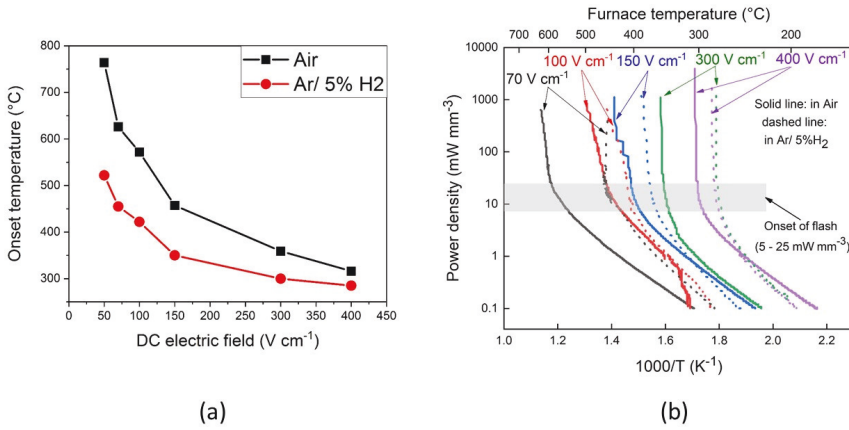
Figure 4-42 :(a) Onset temperature for FS in pre-sintered GDC10 specimen as a function of the electric field in air and Ar/5%H$_2$ (b) Arrhenius plots of power density for GDC10 pre-sintered specimen in air and Ar/5%H$_2$ showing the transition to non-linear rise in conductivity. Experiments were carried out at a heating rate 10°C/min and the maximum current density was set to 100 mA mm^{-2}. "T" in (b) represents the furnace temperature [199].

The onset flash temperature for pre-sintered GDC10 samples (relative density $\approx$ 61%) decreases in reducing atmosphere, i.e. Ar/5%H$_2$ (Figure 4-42 (a)). The effect is more pronounced at moderate values of the electric field i.e. < 150 V/ cm. Even though the flash occurred over a wide range of temperature and P(O$_2$) the power density required for the flash transition lies within a narrow range (5- 25 mW mm^{-3}). The said relation between atmosphere and flash temperature can be understood considering the higher electric conductivity of GDC10 in reducing environments. This can be easily observed in Figure 4-42 (b), which points out that the power dissipation (and so also the conductivity) in Ar/H$_2$ surpasses the one in air during the incubation of flash sintering at given values of electric field and furnace temperature.

The above findings suggest that the application of a DC electrical field changes the conduction mechanism of GDC10 from ionic to electronic in air. The electronic conductivity is associated with the partial reduction of the sample, which originated from the cathodic regions and propagates towards the anodic region as shown in the blackening experiments (Fig. 4-39). This moving reduction front often heterogeneous in nature at the microscopic scale, even though on macroscopic scale it seems homogeneous [202]. A large similarity between the onset behaviour of flash and resistive switching in the memristive device is being suggested during the 4th SPP

1959 convention in Weimar, 18-19th November 2019 [203]. The change in the electrochemical properties of the material upon application of electric field appears to play a key role in the onset of flash.

4.4.4. Effect of Processing Parameters on the Densification and Development of Processing Map for Safe Flash Sintering of GDC10

In this section, the effect of different flash parameters on the densification of GDC10 materials was systematically studied. The material was flash sintered at different combination of initial DC electric fields, current densities and holding time after flash. A processing map for flash sintering of GDC10 indicated at which parameters flash sintering can be safely conducted and at which parameters the sample failed.

First, the densification behavior of GDC10 as a function of electrical field is investigated. Pre-sintered dog-bone shaped samples (dog-bone-1 sample type, relative density around 60%, see section 3.2.1) were used for all experiments. Constant heating rate experiments were carried out using an electric field ranging from 0 V cm^{-1} to 4000 V cm^{-1}. The maximum current density for this set of experiment was limited to 100 mA mm^{-2}. Electric fields beyond 1500Vcm^{-1} were achieved by wrapping the platinum electrode in the gage section to reduce the length. However, the samples flashed above 300 Vcm^{-1} shows cracks and above 500 Vcm^{-1}, the samples splintered. Which is in accordance with the study relating to the Debye temperature of dense GDC10 samples [120].

The onset temperature as a function of applied electric field for the pre-sintered dog bone shaped samples are shown in Fig. 4-43 (a). The higher electrical field lower the furnace temperature for initiating the flash event for GDC10 sample, which is a universal behavior for all the materials reported in the literature. However, the important finding from this study is that cracking of the sample occurred if electric field exceeds a distinct value. For GDC10, the cracking of the sample took place above an electrical field of 300 V cm^{-1}. At higher electric fields the onset temperature for flash was below 400 ºC, an abrupt change in the temperature due to the Joule heating may cause the samples to crack. Also, It may be related to the non-uniform lattice expansion from non-uniform defect generation. The microstructure of the cracked sample will be discussed later in this section.
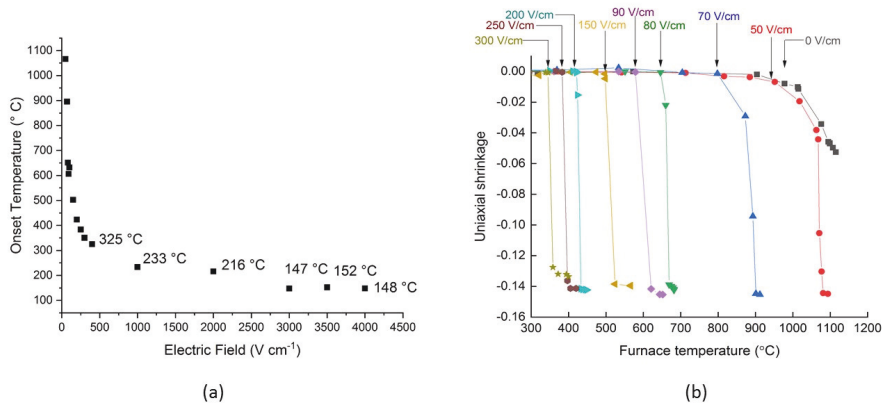
Figure 4-43 : (a) The furnace temperature for the onset of flash as a function of electric field and (b) Uniaxial shrinkage during the constant heating rate experiments at different electric fields.

Fig. 4-43 (b) shows the uniaxial linear shrinkage strain plots with applied electric field ranging from 0 V cm^{-1} to 300 V cm^{-1}. Shrinkage at higher electric fields (above 300 V cm^{-1}) was not monitored due to cracking of the samples. The shrinkage behavior of GDC10 at an applied field of 50 Vcm^{-1} coincides with the conventional densification rate until the flash occurred at around 1100 ºC. At fields above 70 V cm^{-1} a rapid shrinkage can be observed in mere seconds, which is one of the signatures of flash sintering. The relative density of all the samples was around 88%, which was measured by Archimedes' principle. These results suggest that the current density of 100 mA mm^{-2} is not enough to fully densify the GDC10 material, whereas near full density was achieved at 100 mA mm^{-2} for YSZ materials [124].

With the constant heating rate experiments, the optimum furnace temperature for flash sintering at specific electrical fields was found. In the present work, iso-thermal experiments at a furnace temperature of 680 ºC and a moderate electric field of 90 V cm^{-1} was selected as next step of investigation. Here, the effect of current density on the degree of densification by limiting the maximum current density was studied.
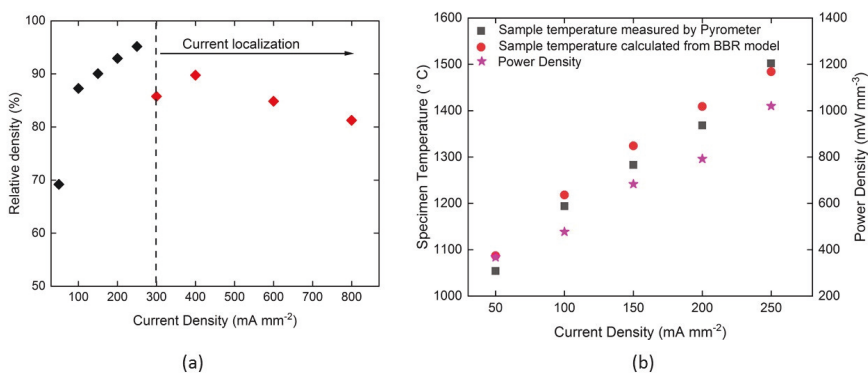
Figure 4-44 : (a) The influence of current density on the degree of densification and (b) specimen temperature measured by the pyrometer, calculated from the BBR model and the power density at stage III for different current density, at a constant electric field (90 Vcm^{-1}) and furnace temperature (680 °C).

Figure 4-44 (a) shows the influence of the current density at a constant electric field and furnace temperature. The current density obviously influences the degree of densification for GDC10. Current density higher than 200 mA mm^{-2} is required to achieve above 95% relative density. If exceeding a current density of 250 mA mm^{-2}, the current starts to channel through a preferential path in the samples (also called hotspot formation). This results in partial densification of the dog-bone shaped specimen, where the densification only occurred in a small area and the other area remains un-sintered. Usually, this effect is accompanied by melt formation in the densified areas. The microstructural effects of the failed specimens will be discussed later in this section.

The specimen temperature during flash have been measured with an optical pyrometer and estimated by a black body radiation (BBR) model for the current study on GDC10. In a steady state of flash (Stage III in voltage-to-current experiments) the estimated sample temperature by BBR model match quite well with the measured sample temperature by an optical pyrometer. Furthermore, direct measurement of the sample temperature with a platinum standard during *in-situ* experiments at APS and BNL synchrotrons for TiO_2 and YSZ [136,153] also are in good agreement with the BBR model and pyrometer measured values. The steady state BBR model assumes that the power consumption is equal to the radiation loss. The BBR model used in this study to estimate the sample temperature is reported in the literature [150], which is derived from the Stefan-Boltzmann law and modified for the flash experiment condition (Eq. 4.6).

$$\frac{T}{T_0} = \left[1 + \frac{1000*W_v\,(mW*mm^{-3})}{\sigma T_0^4}\left(\frac{V}{A}\,(mm)\right)\right]^{1/4} \qquad\qquad \text{Eq. (4.6)}$$

In eq. 4.6, T is the sample temperature (K), T_0 the furnace temperature (K), A is the surface area (mm²), V is the volume of the sample (mm³), W_v is the normalized power dissipated in the sample with respect to the volume of the sample (W mm⁻³), σ = 5.670374419...×10⁻⁸ W*m⁻²*K⁻⁴ is the Stefan–Boltzmann constant and α is a correction factor to account the emissivity of the sample, in the current experiments assuming the emissivity of GDC10 to be 0.9.

Figure 4-44 (b) shows the specimen temperature measured by optical pyrometer and estimated from the BBR modal at the steady state (stage III). Furthermore, the figure includes the corresponding power density at the stage III. These results reveal that the increment in the temperature is directly related to the power dissipated by the specimen. The specimen temperature estimated from the BBR model is in good agreement with the temperature measured by the optical pyrometer. Furthermore, the remarkable result from this analysis is that how accurately the sample temperature and the degree of densification of GDC10 matches with the conventional sintering result, which shown in Fig. 4-8. A temperature of 1400 ºC is required to achieve a relative density of approximately 95% in conventional sintering, the sample temperature was achieved by Joule heating by applying a current density of 200 mA mm⁻², which results in a densification of around 95% by flash sintering process. Nevertheless, it is important to consider in conventional sintering the sintering rate is very low and dwell time quite long as compared to the sintering kinetics during the flash sintering. Therefore, it is important to consider additional effects for the enhanced sintering rate in addition to the thermal effect.

In addition to the above mentioned voltage-to-current experiments with constant heating rate and iso-thermal mode, different sets of iso-thermal experiments were carried out, which revealed the suitable parameters for safe flash sintering of GDC10, shown in Fig. 4-45.
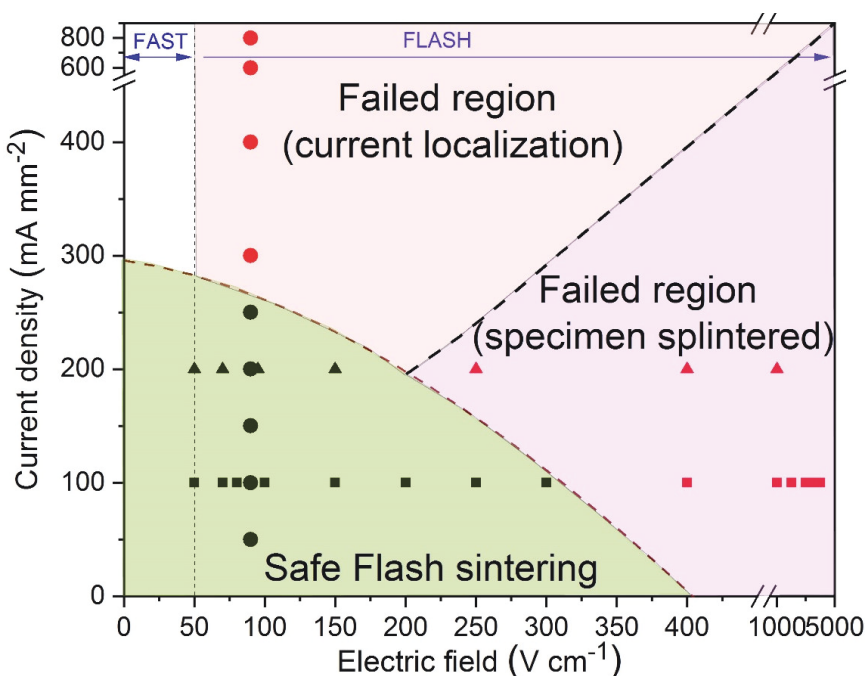
Figure 4-45 : Processing map for safe voltage-to-current flash sintering of GDC10.

The failure of flash sintered samples due to unsuitable flash parameters can be categorized in two regions. (i) in the case of current localization, the degree of densification depends on the current density. However, at very high current density the current seems to find a preferential path in the specimen, which is known as current localization or hotspot generation. Example of such flash sintered samples with current localization is shown in Fig. 4-46 (c), for comparison images of the pre-sintered samples before flash and safe flash sintered sample is shown in Fig. 4-46 (a) and (b) respectively. (ii) in the case of higher electric fields, the onset temperature but does not affect the degree of densification. However, when a high electric fields in the range $300 - 1000$ V cm^{-1} was applied the GDC10 samples are still intact but cracked (Fig. 4-46 (d)), further increment of the electric field (above 1000 Vcm-1), the specimen splinters into many small pieces.
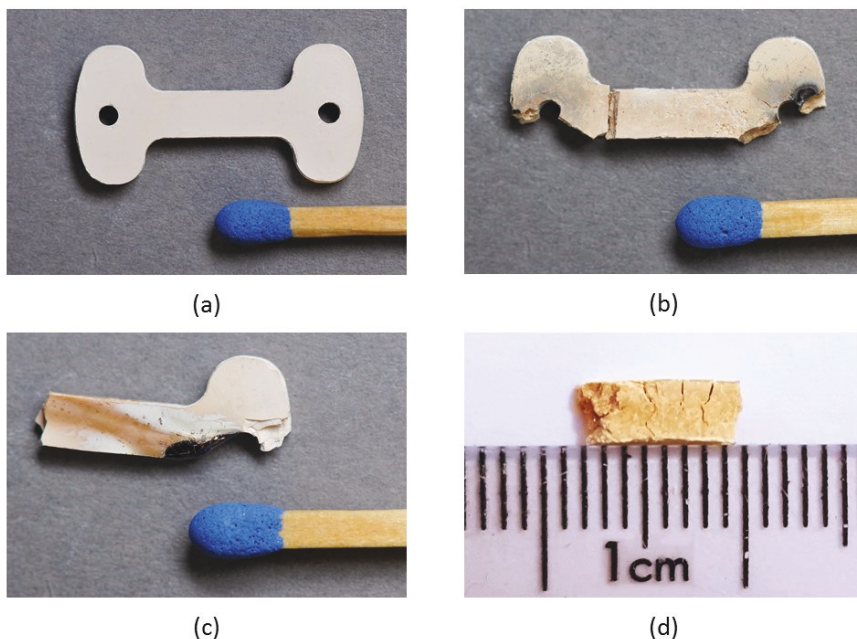
Figure 4-46 : Images of the dog-bone shaped GDC10 samples (a) pre-sintered, (b) safe flash sintered (constant heating rate, 10 ºC/min, 150 Vcm^{-1} and 200 mA mm^{-2}), (c) failed sample showing current localization due to higher current density (iso-thermal, 680 ºC, 90 Vcm^{-1} and 800 mA mm^{-2}) and (d) failed sample showing cracking of the sample due to higher electric field (constant heating rate, 10 ºC/min, 500 Vcm^{-1} and 200 mA mm^{-2}).

Figure 4-47 shows SEM micrographs at different positions of the flash sintered sample with unsuitable parameters. The microstructure of the samples with higher electrical fields shows partial densification, where the un-sintered area of the sample has many pores and the sintered area undergone full densification and significant grain growth, Fig. 4-47 (a). The microstructure of failed samples at higher electric field shows the local damage of the sample. The grain size distribution of the sample was highly inhomogeneous at a distance as close as 100 μm.
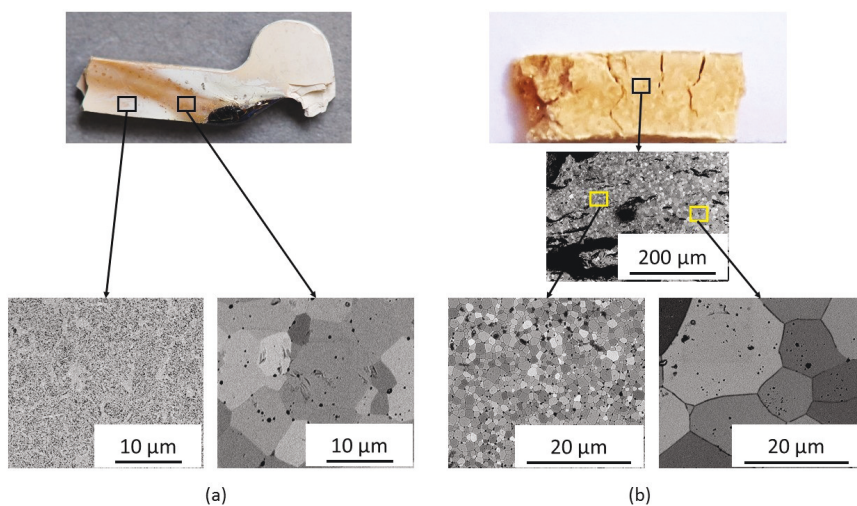
Figure 4-47 : SEM micrographs of two different failed conditions of the flash sintered samples (a) at higher current density and (b) at higher electric fields.
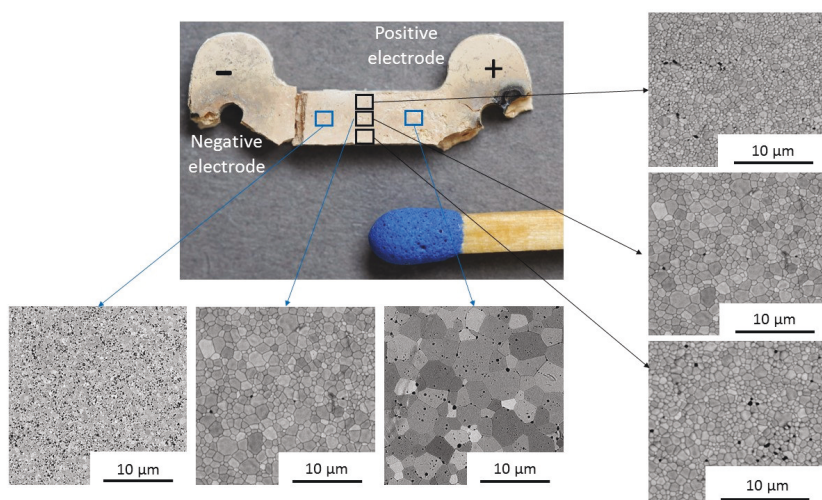

Figure 4-48 : SEM micrographs at different positions of a sample belonging to the safe region.

The microstructure of the flash sinter sample with safe parameters (constant heating rate, 10 ºC/min, 150 Vcm^{-1} and 200 mA mm^{-2}) was investigated at different positions along the gage section and across the gage section. The microstructure across the gage section that is transverse to the direction of the current flow has a small deviation of grain size. Where the grain size close to the surface are finer as compared to the grains in the middle section of the sample. This microstructure hints on the formation of a filament like in the resistive switching, as shown in the progression of the electrochemical blackening at the centre of the sample. However, the grain size along the current flow direction showed a large deviation with respect to the electrode's polarity. The average grain size near the anode was approximately 3±1.1 μm, in the center 0.70±0.35 μm and at the cathode 0.40±0.23 μm; thus, the grain size changed over a factor of ten along the gage section. The non-uniformity of the average grain size in voltage-to-current experiments are reported in the literature [144,204–206]. However, for some materials coarser grains are observed near to the cathode side, while for some materials the coarser grains are located near the anode side.

The abnormal grain growth is often related to electrochemical effects induced by the application of DC electric field [142]. Charalambous and co-workers [207] proposed the abnormal grain growth in Titania near anode due to the Peltier effect, which causes heating at the anode-electrode junction and cooling at the cathode. GDC10 material shows significant electrochemical reduction at the cathode side which propagates to the anode side. The enhanced grain growth at the positive electrode side in GDC10 may be due to the temperature effect. As the cathode side is more reduced than the anode side, the cathode side will be more electrical conductive than the anode side, which resulted in higher heating due to higher resistance between the metal electrode and sample at the anode side as compared to the cathode side. The inhomogeneity in the microstructure during voltage-to-current flash sintering can be avoided by optimizing the processing parameters. For example Biesuz et. al. [142] reported by using AC current for the flash sintering experiments, the electrochemical effects can be minimized. Additionally, different electrode materials act differently at the electrode and sample interface, by using alternate electrode material the homogeneity of the sample can also be improved [123,145].

4.4.5. Summary

To summarize, fundamental study to understand the mechanism responsible for flash sintering was done. Constant heating rate experiments at different electric fields ranging from 50 Vcm^{-1}

to 4000 Vcm^{-1} for GDC 10 material have been carried out. Both powder pressed green and dense sample was considered in this study. The onset temperature for the flash event is a function of both the electric field and the specimen temperature, which is quite similar to the same as the furnace temperature before the flash event. The flash-onset temperature for GDC10 saturates electric field ≥ 1000 V cm^{-1}. The present study confirms previous findings on YSZ and titania [119] and supports the thesis that Debye temperature is indeed the lower bound temperature to initiate flash.

It became obvious that the onset of flash was triggered due to the electronic conduction generated under DC field. The application of DC field generates oxygen vacancies that are accumulated near the cathode side. Since this effect took place in air, its electrochemical nature becomes obvious. The oxygen vacancy concentration increases during the incubation period (stage I) and propagate towards anode side. Therefore, it activates *n-type* electronic conductivity which is associated to an electrochemical reduction process. This process is coupled with the growth of a microscopic filament as in memristive switching. Additionally, by using reducing atmosphere the onset temperature for initiating flash can be lowered significantly, which further supports the onset of flash due to the enhanced electronic conductivity if oxygen deficit became stronger pronounced.

Influence of different flash parameters on the densification behavior of GDC10 was extensively studied. It was found that while the higher electric field lowered the onset temperature for flash, the current density is responsible for the degree of densification for GDC10. A current density of 200 mA mm^{-2} is required to obtain near full density for GDC10 as compared to 100 mA mm^{-2} required for YSZ [34]. Specimen temperature that was measured by optical pyrometer and estimated by using BBR model showed that at the maximum current density (200 mA mm^{-2}) was approximately 1400 ºC. Different sets of voltage-to-current flash experiments were carried out to identify processing parameters, which are suitable electrical parameters for densifying GDC10. Two distinct failed zones have been identified, where at higher current density current localization occurred in the sample and at higher electric field the sample splinters.

The voltage-to-current flash sintering of GDC10 under DC current results in non-uniform microstructure along the gage section of the sample. The grain size near the anode side is larger by a factor of 10 that the grain size near the cathode side.

4.5. A Step Beyond: Current Rate Flash Sintering

4.5.1. Overview

The voltage and current control is a fundamental feature of the flash sintering method. Most of the flash sintering experiments are carried out in the voltage-to-current mode. The onset of flash is signaled by a sharp rise in the conductivity of the sample and rapid increase of the current flowing through the sample results in rapid densification of the green specimen. However, the main challenges in the voltage-to-current flash sintering is that the densification and microstructure of the specimen cannot be controlled in an defined way (e.g. see Fig. 4-48). Moreover, due to the inertia of the power supply the power density curve usually shows a spike during the transition from voltage to current control. This rapid spike in the power enhances the risk of forming localized current paths (called hot spots) in the sample.

Very recently Kumar et. al. [122] reported a novel way of flash sintering where the current is controlled from the beginning of the experiment and raised at a constant rate, known as current rate (CR) flash sintering. It was found that after exceeding a certain current density (incubation time), the self-generated voltage of the sample drops rapidly and then remains almost constant for the complete duration of the CR flash sintering. The onset of flash is induced already at low current densities which to some extent avoid the uncontrolled reduction of the sample at the cathode. The power density profile shows a monotonous gradual increase as the current increases without any spike.

In this section, densification behavior of GDC10 by CR flash sintering mode is studied. All the CR flash experiments were carried out with pre-sintered dog bone shaped samples (Dog-bon-1 as dicussed in section 3.2.1). The hypothesis of this approach is to achieve a controlled densification and tailoring of the microstructure of the GDC10 sample by using CR flash sintering. Therefore, the current rate was varied over a factor of twenty from 50 to 1000 mA min^{-1}. In this way, the total time for the experiment ranged from about 1 minute to 28 min. The furnace was held at a constant temperature of 680° C. The onset phenomenon and the densification of GDC10 in CR flash sintering process was studied. The influence of the current rate on the densification and grain growth investigated. An analytical model for the "energy deficit" that was observed during the CR flash experiments was developed in this work. The energy deficit, that is, the difference between the temperature predicted by the black body radiation model and the temperature measured with the pyrometer, estimates a huge

concentrations of defects may be introduced and contribute to the sintering in the CR flash process.

4.5.2. Control Parameters for CR Flash Sintering

Current rate flash sintering experiments are carried out at an iso-thermal furnace temperature of 680 ºC. The sample were placed inside the hot zone of the furnace for 15 minutes to achieve homogeneous temperature distribution in the sample before the current was applied. Seven different CR flash sintering experiments were carried out at the following current rates 50, 100, 200, 400, 600, 800 and 1000 mA min^{-1}. The maximum current for all CR flash experiments was limited to 200 mA mm^{-2} therefore, the power to the specimen was stopped when the current density reached 200 mA mm^{-2}.

By varying the current rates, the total duration of the flash experiments was varied, where at the lowest current rate (50 mA min^{-1}) the experiment lasted for 28 minutes and at the highest current rate (1000 mA min^{-1}) the experiment lasted for only 1 minute. The increment of current density as a function of time for is shown in Fig. 4-49 and the total duration for all the CR experiments at different current rates are summarized in the Table 4-5.
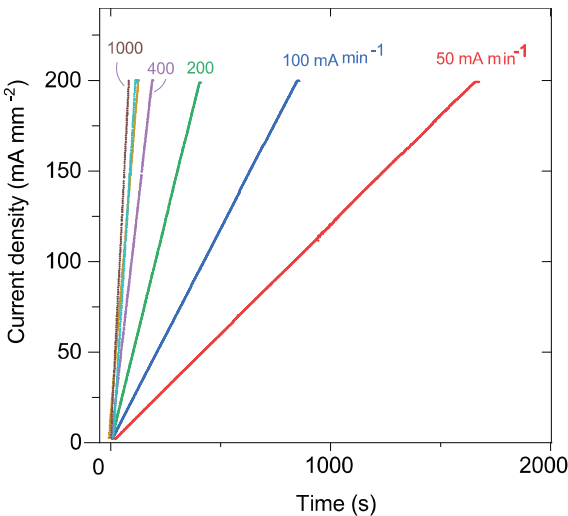

Figure 4-49 : The CR flash sintering experiments at different current-rates, experiment time ranging from 28 minutes to 1 minute [208].

143

Table 4-5: Total time of the experiment for different current-rate flash sintering experiments

Experiment number	Current-rate (mA mm^{-2})	Time for completion of the experiment (minutes)
1	50	28
2	100	14
3	200	7
4	400	3.2
5	600	2.3
6	800	1.8
7	1000	1.3

4.5.3. Onset of Flash, Power Dissipation and Sample Temperature in CR Flash Sintering

In conventional voltage-to-current flash sintering, the onset of flash is signaled by a nonlinear rise in the sample conductivity. This effect is observed from the increase in the current profile as well as a drop in the voltage profile. In CR flash sintering this behavior is different as the current is controlled from the beginning of the experiment and raised continuously at a constant rate. During CR flash experiment, the self-generated voltage due to the electrical resistance of the sample drops abruptly already at low current density. The peak in the voltage/electric field signaled the onset of flash. Afterwards, the self-generated voltage of the sample then saturated and stays mostly constant for the rest of the experiment

The onset of flash for the different current rate experiments is shown in Fig. 4-50 (a). The peaks in the electric field profile are quite distinct in the range of current-rates from 200 to 1000 mA min^{-1}. At lower current-rates they are less pronounced but still discernible. Surprisingly, in all instances the flash initiates at current densities in the range of 7-9 mA mm^{-2}. Unlike in the voltage-to-current flash sintering method, where the applied electric field defines the onset temperature of the material, in CR flash sintering method the onset temperature remains constant for different current rates. Hence, the onset in the CR flash mode is probably a material property. However, more work is needed to verify the findings.
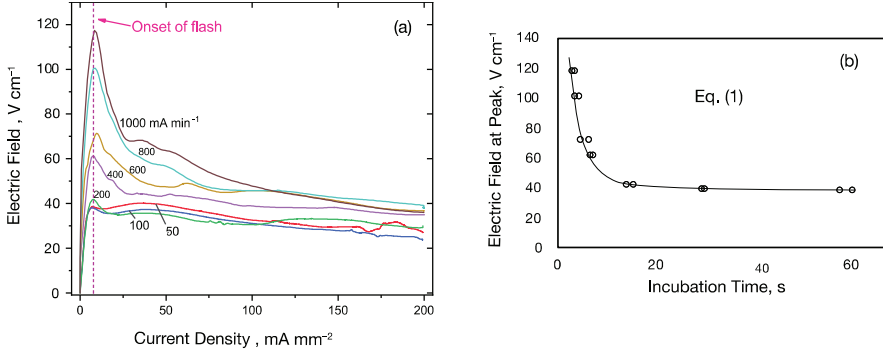
Figure 4-50 : (a) Electric field generated across the specimen when driven by different values of the constant current-rate. (b) The incubation time, given by the peak in the voltage profile, as a function of the voltage at the peak [208].

The onset of flash in CR flash occurred after an incubation time, which depends on the current density. If the current-rate is $\dot{J}$ (mA mm^{-2} min^{-1}) and the current-density at the onset of flash (i.e. the peak in the voltage) is J_{flash} (mA mm^{-2}), then the incubation time is given by

$$t_{inc} = \frac{J_{flash}}{\dot{j}}$$

Eq. (4.7)

A plot of the electric field at the peak (as measured from Fig. 4-50 (a)) and the incubation time, as calculated from Eq. (4.7) are shown in Fig. 4-50 (b). The incubation time lengthens significantly at lower electric fields which is consistent with the conventional voltage-to-current flash experiments.

The power density (P_W) dissipation in the specimen, per unit volume is given by

$$P_W = \rho J^2$$

Eq. (4.8)

where ρ is the resistivity of the sample, which was self-generated and J is the current density. The power density curves for the full span of the experiments are given in Fig. 4-51. Figure 4-51 (a) shows data representation for current density in the range of $0 - 20$ mA mm^{-2} and Figure 4-51 (b) gives the full data set up to the upper limit of current density of 200 mA mm^{-2}.
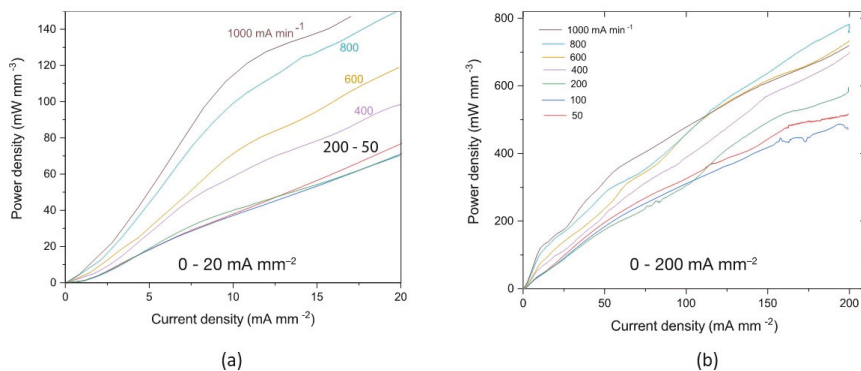
145

Figure 4-51 :(a) Power density profile as a function of current density in the range between $0 – 20$ mA mm^{-2} and (b) Power density for the full span of the experiment up to 200 mA mm^{-2} [208].

Prior to the onset of flash, the rate of the power density increases became higher with increasing current rate. After the onset of flash the conductivity of the specimen increases, by trend, this led to a reduction of the power density rate. The decline in resistance may be explained by the rise of specimen temperature with current density. An increase in conductivity with temperature is consistent with ionic transport. The power expenditure is somewhat higher at higher current-rates in the post-flash regime. This suggests a higher rate of sintering at higher current-rates, but later it is shown that the densification behaviour is essentially independent of the current-rate.

After the onset of flash, the sample temperature rise above the furnace temperature by Joule heating. The extent of Joule heating depends on the electrical power density dissipated in the sample. Direct measurement of sample temperature during the flash event is still a challenge. Generally, Black Body Radiation (BBR) model is used to estimate the sample temperature during the steady state (stage III) in voltage-to-current control flash experiments, which was discussed in section 4.4.4. However, in CR flash sintering, the power density changes continuously with the increase in the current density (Fig. 4-51), which suggests that the sample temperature also changes continuously. This makes the temperature measurement by pyrometer more reliable.

In order to estimate the sample temperature for CR flash sintering, where the energy that is being stored as specific heat was also considered, a modified BBR model was developed by Kumar & Raj [122]. Therefore, the power density (Pw) which was expended in the sample was

divided into two quantities, the energy required by the specific heat (ω_W) and the energy lost in the blackbody radiation(φ_W). The complete analysis for this amended BBR model is given in [122]. The model was applied to the current experiments assuming the emissivity of GDC to be 0.9, and the specific heat to be 900 J kg^{-1} K^{-1} as reported by Stelzer et. al for GDC10 [209]. Note that the surface area of the specimen was updated continuously while the sample sintered, which was also considered in the modified BBR model. Accordingly, the input power density was equated to the sum of two terms as below

$$\int_t^{t+\Delta t} P_W dt = \int_t^{t+\Delta t} \omega_W(t)\, dt + \int_t^{t+\Delta t} \varphi_W(t,T) dt \qquad \text{Eq. (4.9)}$$

(a)   (b)
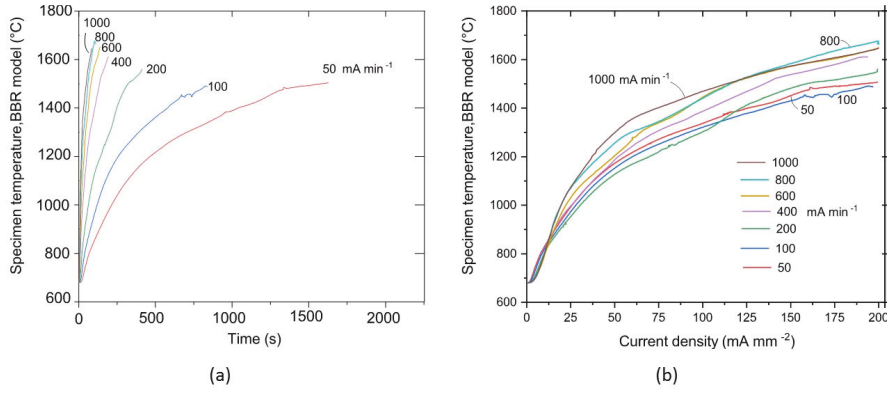
Figure 4-52 : Specimen temperature estimated from the black body radiation model as a function of (a) time and (b) current density [208].

Figure 4-52 shows the sample temperature estimated by the modified BBR model as a function of time and current density. The change of the sample temperature is almost independent of current rate (within a range of ± 100°C) but depends on the current density, which is responsible for the change of the power density after the onset of flash where the electric field saturates (see Fig. 4-51). The estimation of the sample temperature by the modified BBR model shows the maximum sample temperature at the maximum current density (i.e. 200 mA mm^{-2}) was approximately 1550±100 °C for different CR flash experiments.
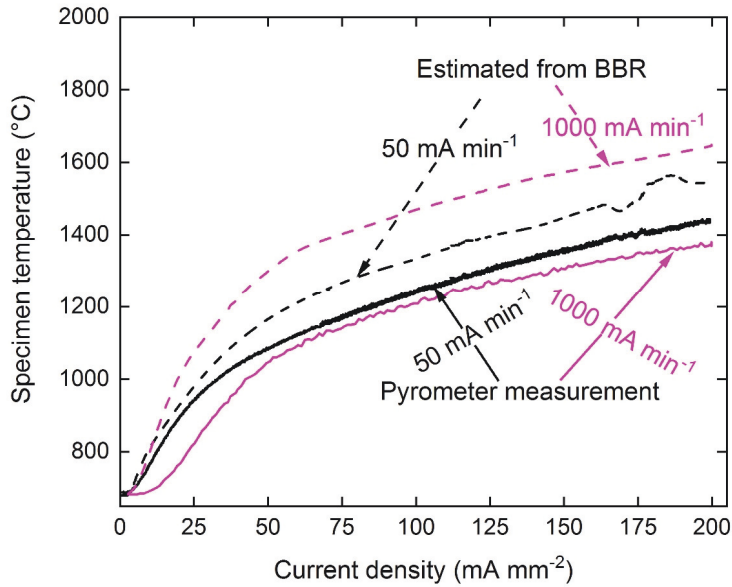
Figure 4-53 : Specimen temperature profile in current rate flash experiments for current rates 50 and 1000 mA min^{-1}, measured by an optical pyrometer and estimated from the modified BBR model.

To verify the calculated sample temperature, an optical pyrometer was used for measuring the sample temperature during the CR flash experiments, which measurement results shows in a good agreement with the BBR model in voltage-to-current flash experiments in stage III. The measurement from the pyrometer compared with the estimated temperature by modified BBR model for two different CR flash experiments with the lowest current rate (50 mA min-1) and at the highest current rate (1000 mA min-1) is shown in Fig. 4-53. The energy deficit that is, the difference between the estimated power input corresponding to the temperature, which was measured with a pyrometer and the actual power consumption. A preliminary analysis of the energy deficit and use it to estimate the concentration of defects with the assumption that the endothermic reaction of defect generation absorbs this excess enthalpy is introduced in this work that enables to draw some conclusions on the sintering mechanism, which will be discussed later in this section.

4.5.4. Densification and Grain Growth Behaviour of GDC10 in CR Flash Sintering

The uniaxial linear shrinkage strain was measured continuously from photographs taken at 1 s intervals. The linear shrinkage strain, ε, is given by equation 4.10.

$$\varepsilon = \ell n \left(\frac{L}{L_o} \right)$$

Eq. (4.10)

where L_0 and L are the initial and the time dependent gage lengths. Note that the strain is a negative quantity.

The uniaxial shrinkage is plotted against the time in Fig. 4-54 (a) and as a function of the instantaneous values of the current density in Fig. 4-54 (b) for all current rates. The interesting findings is that the densification is independent of the current rates and depends only on the current density. This result has practical value, in the voltage-to-current experiments sintering occurs in just a few seconds that makes it difficult to obtain in-situ experimental data, for example in live X-ray experiments. However, CR flash sintering experiments can stretch out the shrinkage to several minutes simply by slowing down the current rate. This behavior was found to be similar for 3YSZ material [122], which opens the possibility to produce not only dense but also materials with controlled porosity by the CR flash sintering mode.
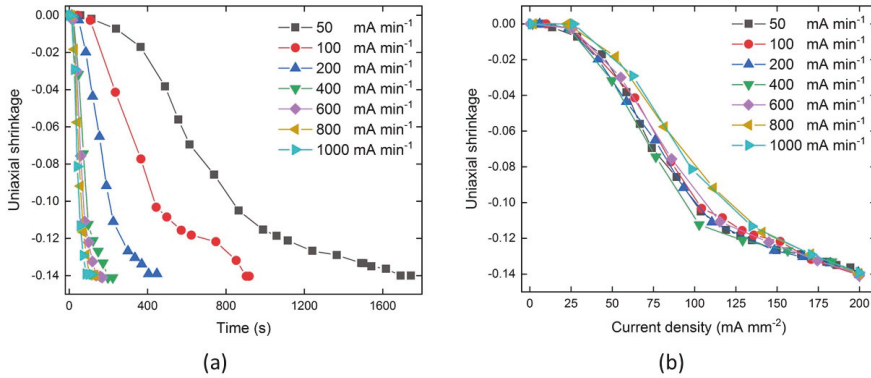

Figure 4-54 : (a) Variation of shrinkage as a function of real time for GDC10 at different current-rates, (b) Shrinkage as a function of current density for different current-rates [208].

149

Equation (4.11) gives the relationship between the linear shrinkage and the change in relative density [210].

$$\ell n\left(\frac{\rho}{\rho_g}\right) = 3\varepsilon$$

Eq. (4.11)

Earlier experiments have shown the shrinkage strains to be the same in the length width and the thickness directions of the dog-bone specimens [211]. Further confirmation is obtained by comparing the final density calculated from Eq. (4.11) with the final density measured by the Archimedes' method. The Archimedes' density measured with distilled water as a liquid medium was 95.6±0.45% (average value for all the CR flashed samples), assuming a theoretical density for GDC10 of 7.22 g/cm3. The relative density values of all current control flash sintered specimens are summarized in the Supplementary Table 4-5. Since ρ_g for the current experiments was equal to 0.62 and the finish linear shrinkage seen in Fig. (4-54) is approximately 0.14, the finish relative density is estimated (equation 4.11) to have been roughly 95%. The degree of densification was found to be independent of the current rates.

Table 4-5: Relative density of the current control flash sintered specimens measured by the Archimedes' method with distilled water as a liquid medium; the values for the relative densities were calculated assuming a theoretical density for GDC10 of 7.22 g/cm^3.

Current-rate (mA min^{-1})	Relative density (%)
50	95.88
100	95.62
200	95.17
400	96.36
600	95.7
800	94.74
1000	95.57

The crystal lattice of the pre-sintered and the CR flash sintered samples were analyzed by X-ray diffraction method. The XRD diffraction pattern suggested the CR flashed samples retains their original cubic fluorite structure. The crystallite size of the pre-sintered specimens were around 60 nm whereas the CR flashed sinter specimen has a crystallite size > 200 nm, suggesting densification and grain growth. These X-ray data are included in Fig. 4-55.
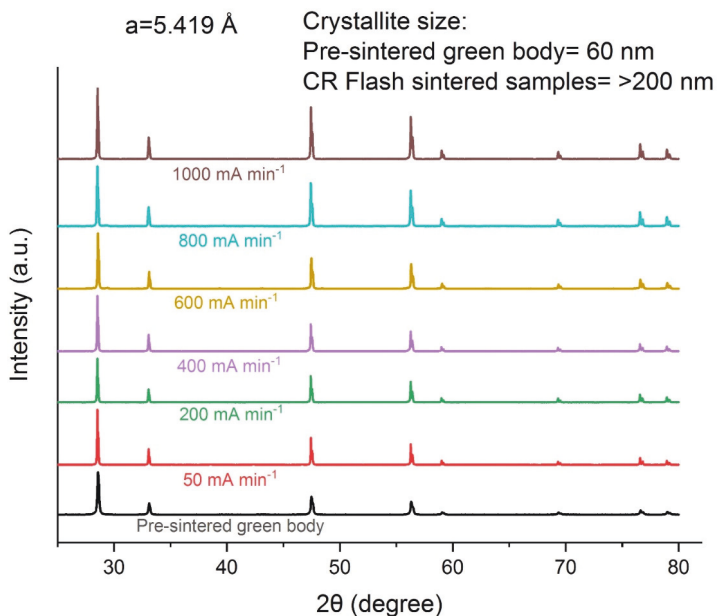
Figure 4-55 : X-ray diffraction of the starting pre-sintered sample and CR flash sintered samples showing increased in the crystallite size [208].

In voltage-to-current flash sintering, the sintering occurs abruptly (usually in less than 5 s) immediately after the onset of flash [33]. Such rapid densification makes it difficult to control the densification and tune the microstructure of the dense sample. For some materials like ZnO and TiO_2, voltage-to-current flash sintering process resulted inhomogeneous grain size distributions with respect to the polarity of the electrodes [118,212]. The different microstructure evolution at the electrodes suggests that a strong electrochemical gradient may influence the densification and grain growth along the gage section of the sample. The non-uniform grain size distribution along the gage section was also observed in this work, when the GDC10 sample has densified by voltage-to-current flash sinter mode (Fig. 4-48). Recent studies showed that CR flash sintered samples had a homogeneous grain size distribution along the gage section of the sample [122,204,205].

For studying the uniformity in the grain size distribution of the CR flash sintered GDC10 samples, SEM micrographs were taken at 15 different positions of the sample (Fig. 4-56 (a)), which was sintered at a current rate of 50 mA min^{-1}. The average grain size at these positions is summarized in Figure 4-56 (b).
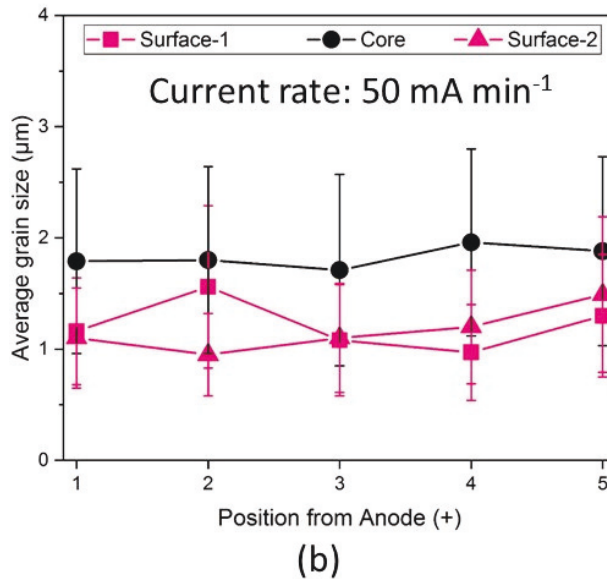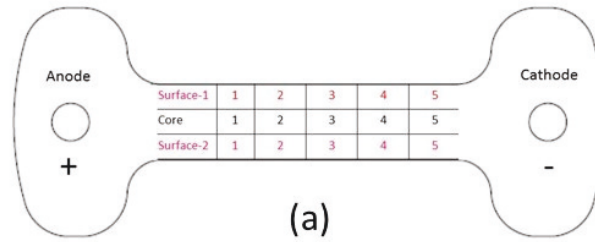
Figure 4-56 : (a) Position at the gage section where the SEM micrographs were taken for estimating the average grain size and (b) average grain size at different position of the gage section as shown in (a), the sample was flash sintered in current rate (CR) flash mode, at a current-rate of 50 mA min^{-1} [208].

The grain size analysis suggest that the microstructure along the gage section (from anode to cathode) of the sample is uniform nonetheless, a slightly coarser grain size was measured at the core of the sample as compared to the near surface area of the sample. The large grain sizes distribution at the core of the sample suggest a slightly higher temperature in this region during the flash event.

Sample temperature during the flash state rises above the furnace temperature due to Joule heating [114,121]. Therefore, it may be possible that the heat loss by radiation from the surfaces

of the sample during the CR flash sintering process is higher than the core of the sample. Thereby, a higher temperature at the core relative to the surfaces of the sample experience a higher temperature. Pereira da Silva et. al. studied the temperature distribution of 8 mol% yttria stibilized zirconia during voltage-to-current controlled flash sintering by Finite Element Method [213]. They found significant temperature gradients from the surface to the core of the sample. Additionally, the FEM simulation shows a higher temperature at the core section of the sample as compared to the top and bottom surface of the sample. They suggested the temperature difference can possibly cause by the heat loss from the surface of the sample by radiation. The microstructure characteristics seems to be in a good agreement with the FEM simulation results. While the non-uniform grain size distribution along the transverse direction could be due to the heat loss from the specimen in both the voltage-to-current and current rate control flash sintering mode, the abnormal grain growth at the anode side in voltage-to-current control mode can be prevented by CR flash sintering method. In future CR flash sintering experiments with thermal insulations of the samples is planned to avoid the heat loss from the surface of the sample.

The most remarkable result of the present study is the fact that the average grain size of CR flash sintered GDC10 samples can be tailored by controlling the current rate. If decreasing the current rate from 1000 mA min^{-1} to 50 mA min^{-1}, the grain size increased from sub-micrometer to several micrometers without any indication of abnormal grain growth, as shown in Fig. 4-57. On the other hand, the degree of densification mainly depends on the current density and is almost independent from the current rate.
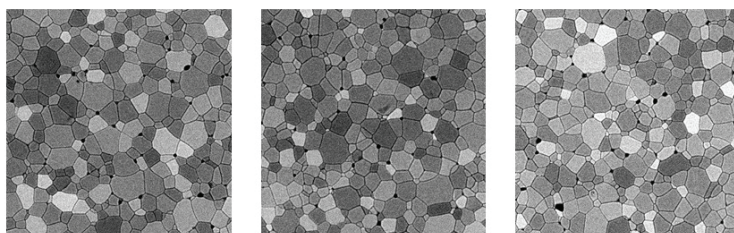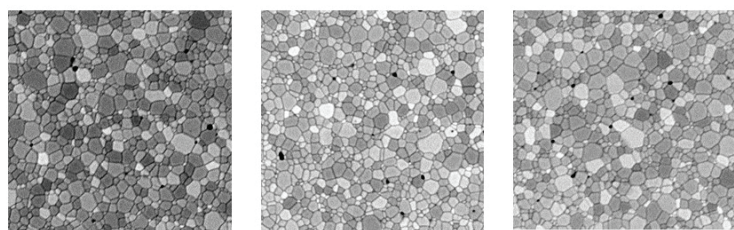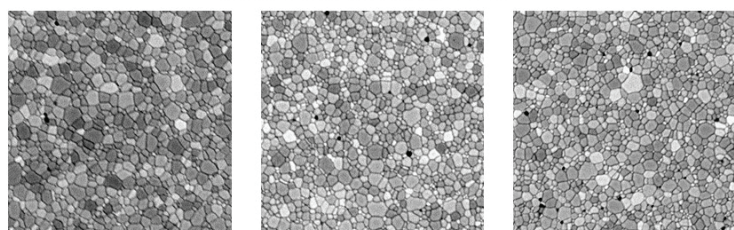
(a)
Current rate: 50 mA min^{-1}
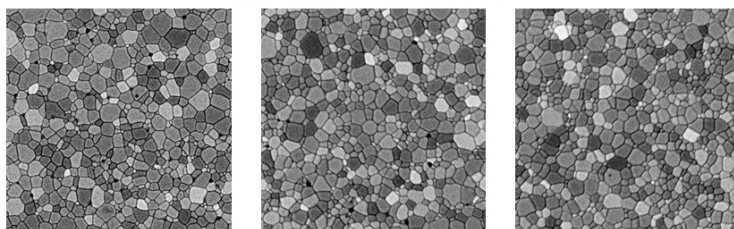
(b)
Current rate: 100 mA min^{-1}

20 μm

(c)
Current rate: 200 mA min^{-1}
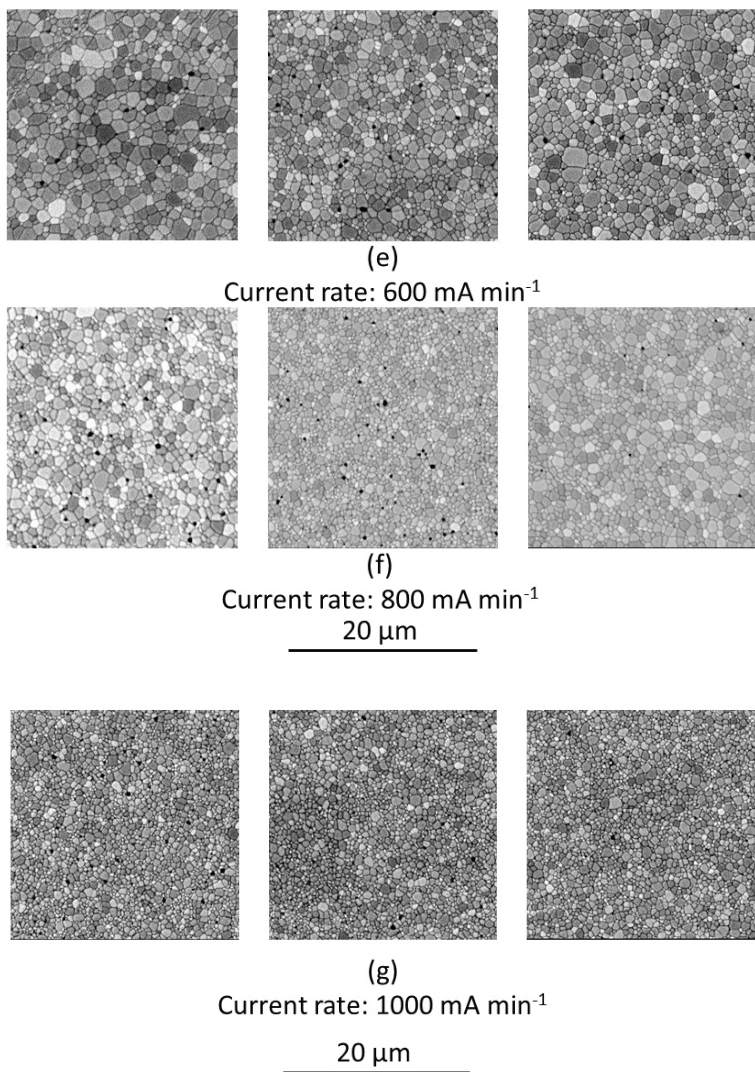

(d)
Current rate: 400 mA min^{-1}

20 μm

Figure 4-57 : SEM micrographs at three different positions, the positions could be visualized from the Fig. 4-56 (a) (i.e. left image: near the anode (core 1), middle image: at the center (core 3) of the sample and right image: near the cathode (core 5)) of the CR Flash sintered samples at seven different current rates, showing that higher current rates resulted in finer grain size and homogeneous grain size distribution along the gage section of the sample [208].

It is well known from conventional free sintering that diffusion controlled densification and grain growth are competing processes [41]. To achieve fine grained microstructure and to reliably avoid abnormal grain growth, activation energy of grain growth should remain lower than activation energy of densification until the end of the sintering cycle. In the case of low heating rates and long dwell times at sintering temperature it might become difficult to reliably control this relationship of activation energies, especially if the powder compact shows microstructural in-homogeneities from non-optimum powder processing [214]. A promising way to avoid excessive grain growth in conventional sintering is the application of high heating rates [215] or two-step sintering [187]. Recently, it has been demonstrated that electric field enhanced sintering is another powerful technique to reduce grain growth [216].

CR flash sintering is a step beyond to overcome these limitations. The grain size from all the above measurements are plotted in Fig. 4-58. It decreases steadily as the current-rate is increased, from ~3 □m at 50 mA min^{-1} down to ~0.5 □m at 1000 mA min^{-1}.
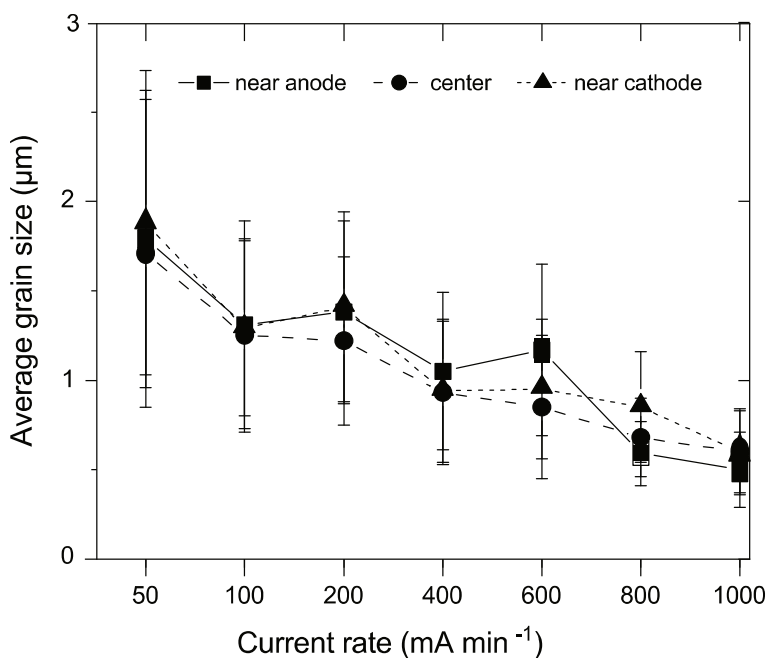

Figure 4-58 : Change in the average and the grain size distribution obtained from three locations along the gage length, as a function of the current-rate [208].

Microstructures shown in Figure 4-57 indicate that at all current rate flash experiments, densification and grain growth are well-balanced during the whole cycle. All samples had achieved almost the same density (around 96 %) and all residual pores were still connected to the grain boundaries, which hints on that final density could be further increased e.g. by adapting the maximum current density. Similar results were reported by Charalambous et. al., where slower current rate resulted in coarser grain size for ZnO material [205]. On the other hand, Kumar and Raj et al.[122], did similar experiments on YSZ samples not finding any related relationship. The influence of the electrical control parameter in flash sintering on grain size remains an open question. More studies with different material are necessary to draw a more general conclusion.

4.5.5. The Energy Deficit Model

In a private conversation with Jean-Marie and Rishi Raj, It was discussed that in current rate flash sintering the pyrometer temperature was often lower than the temperature estimated from the modified black body radiation (BBR) model [217]. In the current work it was also observed that the pyrometer temperature always shows lower temperature that the BBR model, as shown in Fig. 4-53. The systematic experiments in the present work permitted us to explore that observation rigorously. Here we explored the answer of this observation, assuming that the Frenkel pairs are being generated in the sample during the flash. A new model is developed to account for the energy deficit to explain the enhanced densification kinetics during the CR flash sintering. The differences between the voltage-to-current and current rate flash sintering mode are a key to better understand the observed behavior.

(i) In voltage-to-current flash sintering mode, the densification occurs abruptly at the onset of flash (stage II) during the transition from voltage control to current control. Afterwards, the flashing sample kept in a steady state under current control, where the voltage and current remains constant. During the steady state the heat loss from the sample due to the radiation is equal to the heat generated in the sample due to the power dissipation. In such a steady state the result from the BBR model has been shown to match (deviations are < 50°C) the temperature measured with the platinum standard measured in synchrotron [153]. Additionally, our own findings from the voltage-to-current flash experiments for GDC10 shows that the sample temperature measured by pyrometer and BBR model are in good agreement as well (see Fig. 4-44). From these results it was concluded that in voltage-to-current

experiments at the steady state the rate of defect generation is almost equal to the rate of defect recombination.

(ii)   The CR flash sintering mode has a fundamental different characteristic, here sintering occurs continuously as the current density is increased. The rate of sintering can be stretched out by slowing the current rate. If indeed excess defects are the reason for flash sintering then these excess defects are being produced continuously during the whole duration of the experiment.

The generation of defects in crystal lattice is an endothermic process. Therefore, it is expected that a portion of the power input is consumed by defect generation, while the rest got lost due to radiation.

To proof this assumption, the actual electrical power consumption was compared to the energy input that would be sufficient to heat the sample to the temperature measured by pyrometer according to the modified BBR model. The difference is the energy deficit, which can be translated into excess defect concentration.

The way, how to conduct the analysis is given below. We specify the electrical power consumption as $W(t)$, in Watt, and the power that can account for the temperature measured with the pyrometer as $W^*(t)$. The energy deficit, as a function of time, is then given by

$$\Delta H^*(t) = \int_0^t (W(t) - W^*(t))dt \qquad \text{Eq. (4.12)}$$

Unit of $\Delta H^*(t)$ is Joule and the calculated volume refers to the specific specimen. For more general conclusion, it is useful to relate the energy deficit to mol, as follows

$$\Delta H^*_{mol} = \frac{\Delta H^*}{V_{spec} / V_{molar}} \qquad \text{Eq. (4.13)}$$

Here V_{spec} refers to the volume of the matter only in the gage section of the specimen and V_{molar} is the molar volume of GDC. The molar volume is $V_{molar} = 2.36*10^4$ mm^3 mol^{-1}. The specimen volume, equal to the weight of the specimen divided by the density of ceria, was equal to $V_{spec} = 61.4$ mm^3. Thus, ΔH^*_{mol} is equal to the energy deficit per mole of GDC.

If the enthalpy of formation per one mole of Frenkel pairs is ΔH_{Fr}, then the mole fraction of defects, $X_{Frenkels}$ created in the GDC is given by

$$x_{Frenkels} = \frac{\Delta H^*_{mol}}{\Delta H_{Fr}}$$

<div align="right">Eq. (4.14)</div>

It remains now to calculate $W^*(t)$ in Eq. (4.12). It is related to the pyrometer temperature (which we write as) $T^p_K(t)$ through the BBR model [150], plus the heat absorbed in specific heat, so that

$$W^*(t) = \varepsilon_m S \sigma \left(\left[T^p_K \right]^4 - T^4_F \right) + m C_p \frac{dT^p_K}{dt}$$

<div align="right">Eq. (4.15)</div>

Here S is the surface area of the gage section of the specimen; it is corrected with time as the specimen shrinks. σ is the Stephan Boltzmann's constant, and ϵ_m is the emissivity. The furnace temperature is T_F, m is the mass of the specimen, equal to 0.443 g. and C_p is the specific heat, equal to 900 J kg^{-1} K^{-1} [209]. The nominal value for the emissivity of GDC is 0.8-1.0. We note that higher value of the emissivity increases W^* and therefore decreases the energy deficit. Thus, we set $\varepsilon = 1$ which gives the lower bound for the energy deficit.

One mole of Frenkel pairs is the sum of two anions and one cation. The enthalpy for one anion is 3.2 eV and 15.9 eV for the cation [218,219], Therefore the enthalpy of formation of one mole of Frenkel pairs (two anions and one cation) is 22.3 eV, which translates into $\Delta H_{Fr} = 2150$ kJ mol^{-1} of Frenkel pairs.

Plots of W and W^* (for the case of 1000 mA min^{-1}) are given in Fig. 4-59 (a), and the mole fraction of Frenkel pairs calculated as above are given in the upper curve in Fig. 4-59 (b). The mole fraction of Frenkel pairs rises to very large values, in the range of 20-30 mol%. If we assume that the pyrometer is underestimating the specimen temperature by 100 °C then the lower curve is obtained. Even then the Frenkel pairs concentrations are more than 10%. These are very large numbers. We present these results with caution due to the accuracy of the measured temperature by pyrometer but with some confidence that the energy deficits as described here are factual.

The concentration of Frenkel pairs calculated above are those that survive. Defects are excluded that are recombine (e.g. ionize into charge neutral defects and electron-hole pairs) during the experiment returning the enthalpy they consumed when they were formed. Our hypothesis is that, these surviving Frenkel pairs are contributing in the sintering process, by the vacancies becoming incorporated into grain boundaries, and the interstitials into the pores. The shrinkage of the pores reduces free energy of the system however, its magnitude is much

smaller than measured here. The energy of the grain boundaries is unlikely to change by absorption of vacancies. It is therefore possible that the large Frenkel pairs concentrations we calculate are simply equal to those absorbed into the sintering process. Further experiments with dense polycrystals and single crystals are needed to clarify this point.
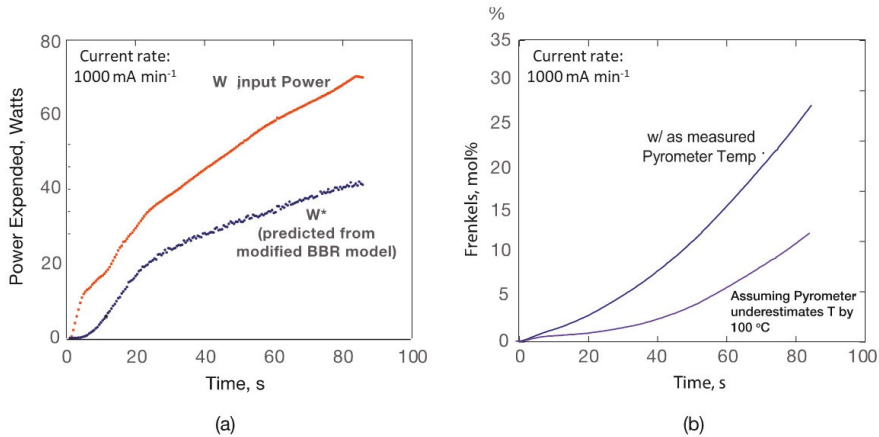

(a)

(b)

Figure 4-59 : (a) Energy deficit as given by Eq. (4-.12). (b) Mole fraction of Frenkel pairs estimated from the energy deficit, as given by Eq. (4.14). CR flash experiment at a current rate of 1000 mA min^{-1} [208].

It is possible that the energy deficit is not simply being accounted for the formation of Frenkel pairs. There can be also other endothermic reactions such as phase transformations that are far from equilibrium. Indeed new phases and heavy distortions in the X-ray diffraction peaks [135], and large atom displacements in TiO_2 measured by pair distribution function analysis of total X-ray scattering data from Brookhaven [136] are examples of such events. It is possible that defect generation is responsible for triggering these unusual effects.

4.5.6. Summary

Current rate experiments are a new research topic in the field of flash sintering; in CR mode, the power supply is always held under current control while the current is increased at a constant rate. CR experiments have significant differences with respect to conventional voltage-to-current experiments, where the voltage is applied from the beginning, and the power supply is switched to current control at the onset of the flash. In the CR experiments the onset of flash is signaled by a self-generated voltage maximum due to the resistance of the specimen,

which occurs at current densities that are far below the current limits used in the voltage-to-current experiments.

The densification behavior of GDC10 by current rate flash sintering has been studied. It is distinguished from the conventional voltage-to-current flash mode by two specific effects, (i) densification occurs continuously as the current is increased, while in voltage-to-current flash mode densification occurs abruptly when the power is switched from voltage control to current control, (ii) the extent of sintering in both instances depends on the current density. However, in CR mode the degree of densification depends on the instantaneous current density. Therefore, the degree of densification, can be tuned by the maximum value of current density at which the experiment is terminated. The current rate does not influence the degree of densification.

The current rate experiment is a non-steady state phenomenon whereas in the voltage-to-current experiments a quasi-steady state is achieved under constant current at stage III. The microstructures of the flash sintered samples in current rate mode are much more uniform from one electrode to the other, which is difficult to achieve in voltage-to-current flash sintering. Estimate of temperature from the modified BBR model in current-rate experiments is higher than measured with a pyrometer whereas in voltage-to-current experiments excellent agreement is achieved at least during Stage III.

A preliminary analysis of the "energy deficit", which is indicated by the temperature difference between the estimated specimen temperature using the modified BBR model and the specimen temperature measured by pyrometer, is attributed to the endothermic nature of defect generation. For GDC10, concentration in the range of 10-30 mol% were estimated. It is of course possible that other endothermic phenomena such as the formation of secondary phases that are far from equilibrium or reversible material decomposition are absorbing a part of this energy deficit. Another explanation can be that these Frenkel pairs are absorbed at grain boundaries and pores which enhance the sintering kinetics, which does not have a significant enthalpy ramification. Experiments with dense polycrystals and single crystals are underway to explore this possibility.

4.6. In-situ Flash Sintering of GDC10 in Synchrotron

4.6.1. Overview

Flash sintering is a highly dynamic and nonlinear phenomenon, In voltage-to-current flash sintering mode, a nonlinear rise in the sample conductivity and rapid densification is observed at the onset of flash. Voltage-to-current flash sintering of GDC10 shows an inhomogeneous grain size distribution along the gage section of the sample, as in detail discussed in section 4.4. The average grain size near the anode was approximately 3 ± 1.1 μm, in the center 0.70 ± 0.35 μm and at the cathode 0.40 ± 0.23 μm; thus the grain size changed over a factor of ten across the gage section. On the other hand, CR flash sintering shows a different densification behavior, where the sintering occurs continuously as the current density increases. Remarkably, the CR flash sintered samples has a much more homogeneous grain size distribution along the gage length and grain size can be tuned by the current rate.

In situ flash experiments at synchrotron are useful to study the highly nonlinear behavior during the flash sintering experiments. For example, Terauds et. al. [153] measured the in situ lattice expansion of the dense 3YSZ sample during the flash experiment and used this data to calculate the sample temperature in situ. Similarly, Yoon et. al. [136] performed in situ flash experiments on TiO_2 at the synchrotron. They analyzed the pair distribution function of the total X-ray scattering to measure the mean-square displacements of the ions. During flash event, a large mean square displacement of the oxygen ions was observed when, the mean square displacement of oxygen was compared at higher temperature under equilibrium conditions. Recently Jha et. al. [39] showed an abnormal lattice expansion during flash sintering of powder compact Ceria under DC current, which disappeared when conducting flash sintering experiment under AC current .

In the current study, in situ flash sintering experiments (DC electric field) for pre-sintered GDC10 samples, were carried out in air at NSLS-II at Brookhaven National Laboratory (BNL). Total scattering (Bragg and diffuse) measurements during the flash sintering experiments were done in both voltage-to-current and current rate flash mode. Total scattering analysis utilizes both Bragg scattering and diffuse scattering from a material to measure both average structure and local or short-range structure. The flash experiments in different modes were conducted in close proximity to the cathode and anode side separately. The goal of the in-situ experiments at the synchrotron was to measure the actual sample temperature with respect to the electrode polarity of GDC10 in the case of voltage-to-current mode and current rate flash mode.

4.6.2. Control Parameters for Flash Sintering Experiments

Total scattering (Bragg and Diffuse) measurements were done on GDC10 pre-sintered (relative density around 60%) samples during flash sintering event. Data were recorded with a time interval of 1 second. In total, four in situ flash sintering experiments were conducted aiming on to compare change of lattice parameters near the electrodes in voltage-to-current and CR flash mode. All the experiments were conducted at a iso-thermal furnace temperature of 680°C.

  (a) Voltage-to-current flash sintering near anode
  (b) Voltage-to-current flash sintering near cathode
  (c) Current rate flash sintering near anode
  (d) Current rate flash sintering near cathode

For more details on the experimental set up, we refer to the work of Terauds et al. [153] and the sample preparation process was explained in the section 3.1. Pre-sintered rectangular bar shaped samples (Rectangle bar-1) were used for the synchrotron experiments.
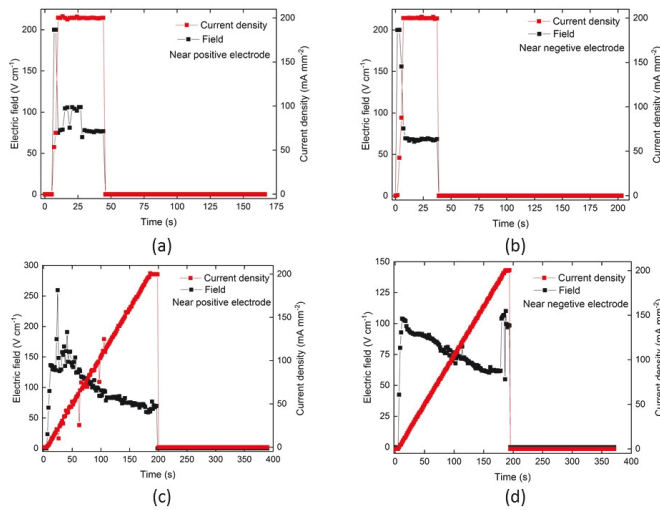

Figure 4-60 : Electric field and current density (a) during the voltage-to-current flash experiment near positive electrode, (b) during the voltage-to-current flash experiment near negative electrode (c) current rate flash sintering experiment near positive electrode and (d) current rate flash sintering experiment near negative electrode (current rate 200 mA min^{-1}). All the experiments were done at furnace temperature of 680°C.

The electric field and current density profile for the four flash sintering experiments is shown in Fig. 4-60. The voltage-to-current flash sintering experiments were conducted in iso-thermal flash condition, where the furnace temperature was at 680°C. The sample was placed inside the furnace for 15 minutes before switching the power supply on. The electrical field applied was 200 V cm^{-1} and the maximum current density was limited to 200 mA mm^{-2}. The current rate flash experiment was done at furnace temperature of 680°C as well. The current was raised at a rate of 200 mA min^{-1} up to a maximum current density of 200 mA mm^{-2}. The experiment at the cathode sides for both flash sintering mode are conducted with same electrical parameters. Please note that the deviation in the electric field during the CR flash sintering experiment near the cathode (Fig. 4-60 (d)) at around 200 s is due to the bad electrode contacts.

The power dissipated by the sample was calculated as a product of voltage and current, and then normalized with respect to the volume of the sample. It is expressed as power density in unit of mW mm^{-3}. The real time data for the power density profile during the flash sintering experiments for GDC10 specimens are shown in Fig. 4-61.
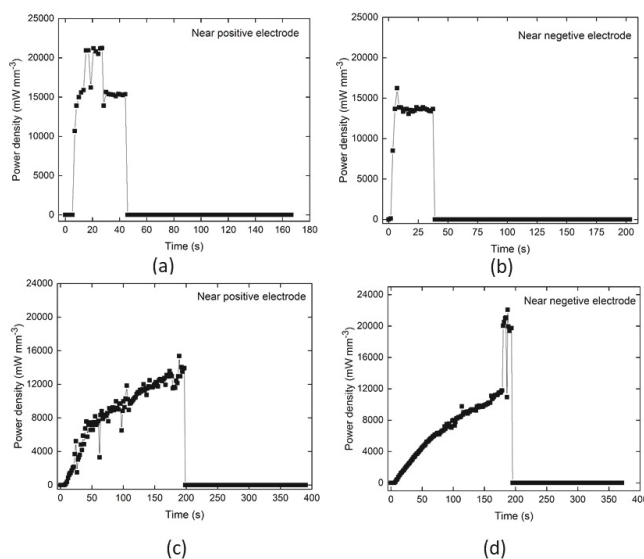

Figure 4-61 : The data for the change in power density with time: (a) during the voltage-to-current flash experiment near positive electrode, (b) during the voltage-to-current flash experiment near negative electrode (c) current rate flash sintering experiment near positive electrode and (d) current rate flash sintering experiment near negative electrode. All the experiments were done at furnace temperature of 680°C.

164

The evolution of the specimen temperature during the flash sintering process depends on the total power dissipation in the sample. In voltage-to-current flash experiments (Fig. 4-61 (a) and (b)), an abrupt rise in the power dissipation in the sample can be observed, which is a signature effect in the flash (voltage-to-current) experiments. On the other hand, the power dissipation in the specimen under CR flash condition shows and gradual increase with time.

4.6.3. In situ Measurements of the Specimen Temperature

The time resolved (at 1 second interval) diffraction peaks are obtained continuously during the four flash sintering experiments. The diffraction peak position and their widths, defined as the "full width half maximum" were measured. Rietveld analysis of the data was performed using the TOPAS program V4.2 (Bruker AXS) [220]. For calibration purpose, measurement of the lattice parameters as a function of temperature without an electric field was done at IEK-1, Forshungszentrum Juelich GmbH. The GDC10 sample was prepared under same conditions as in case of synchrotron. The pre-sintered GDC10 sample was then heated up to 1200°C under a heating rate of 10°C/min. As the temperature rises, the lattice expands, and the diffraction peaks are obtained at a temperature interval of 100°C. The lattice expansion of GDC10 at higher temperature was observed in terms of the peak shift to lower energies since the interplanar spacing is inversely proportional to the energy of the diffraction wavelength according to the Bragg's law given in Eq. 4.15:

$$E = \frac{hc}{2\sin\theta}\left(\frac{1}{d_{hkl}}\right) \qquad\qquad \text{Eq. (4.15)}$$

In summary, the baseline data for the lattice parameters as a function of only temperature without electrical field, which was measured in Juelich was used for estimation of the sample temperature during flash experiments at the synchrotron.

The base line data, that is the lattice expansion as a function of sample temperature is shown in Fig. 4-62.
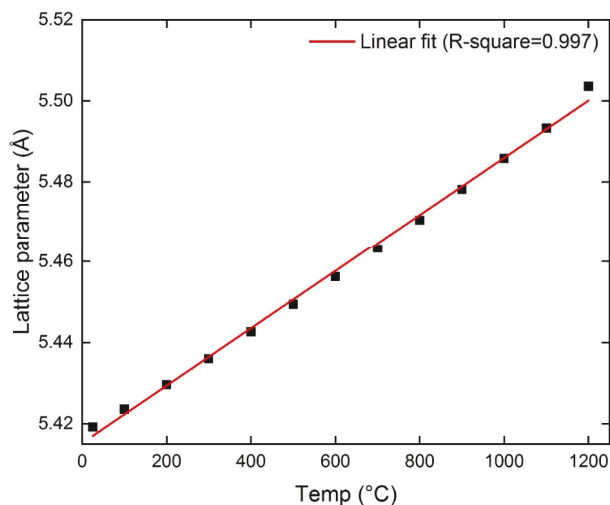
Figure 4-62 : Lattice parameter as a function of temperature for GDC10 in air measured by high temperature X-ray diffraction (measured at IEK-1, Forschungszentrum Juelich).

The change of the lattice parameters during the flash sintering was obtained from in-situ flash sintering experiments (Fig. 4-63). For the temperature above 1200°C, an extrapolation of the base line data was used. At the onset of flash, a nonlinear rise in the lattice expansion is observed in the voltage-to-current flash experiments. The full width half maxima (FWHM) of the peaks remained almost unchanged during the flash sintering at stage III. When turning off the power source, lattice contraction occurred and immediately lattice parameters went back to the starting condition. where lattice expansion is related to the furnace temperature of 680°C. Contrary to the voltage-to-current flash sintering, in current rate flash sintering the lattice expansion occurred gradually as a function of time, which is due to the increment of current density.
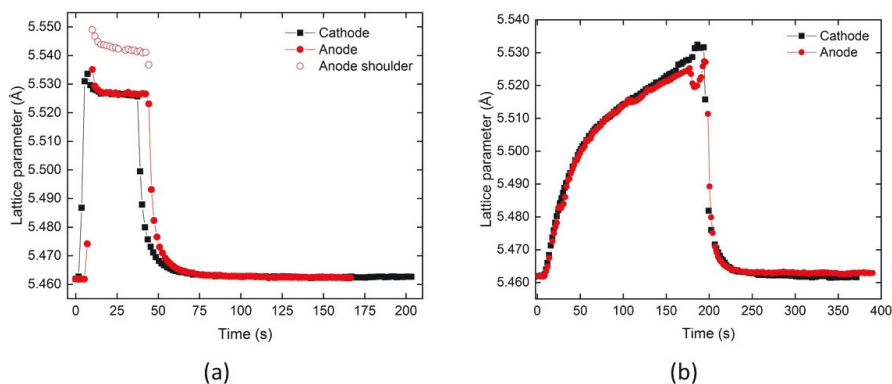
Figure 4-63 : Change in lattice parameters during flash sintering experiment in real time: (a) voltage-to-current flash sintering, occurrence of peak splitting on anode side and (b) current rate flash sintering.

During the analysis of the Bragg's peak, we observed that at the positive electrode (anode side), the peaks in addition to their shift broadened and split into two peaks, which generally corresponds to a second effect with respect to the lattice parameters. The peak splitting, which was indicated by the formation of a shoulder can be attributed to the different cation valance state due to the oxygen defects and reduction of some adjacent unit cells. Surprisingly, the peak splitting and the shoulder formation was not observed near the cathode side. The expanded view of the shape of the diffraction peaks before flash, during flash and after flash at different electrodes are shown in Fig. 4-64.
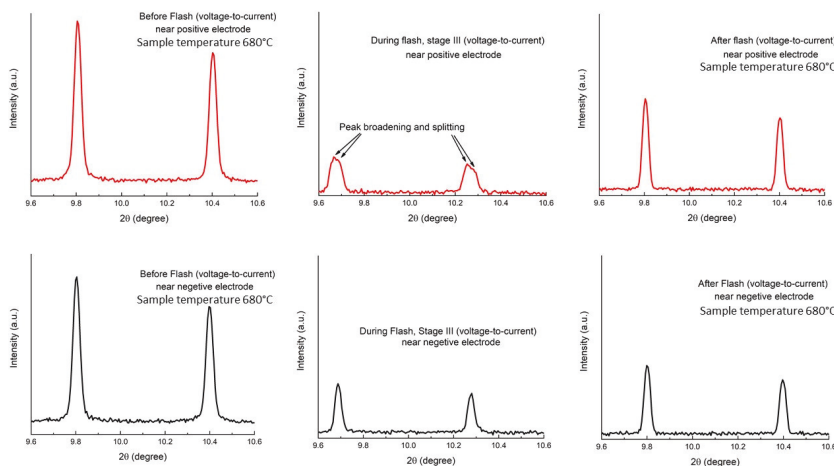
Figure 4-64 : Expanded view of the diffraction peaks before flash (at 680°C), during flash (at stage III) and after flash (at 680°C) near the positive and negative electrode, indicating a second effect in the lattice during flash in addition to the lattice expansion.

Interestingly, under similar processing conditions when flash sintering was carried out in current rate mode, no abnormal peak broadening observed at the electrodes. The lattice expansion increased similarly for both electrodes. This result suggests that the current rate flash sintering eliminates the inhomogeneous segregation of the oxygen deficiency and the temperature evolution is homogeneous in the full length of the sample.
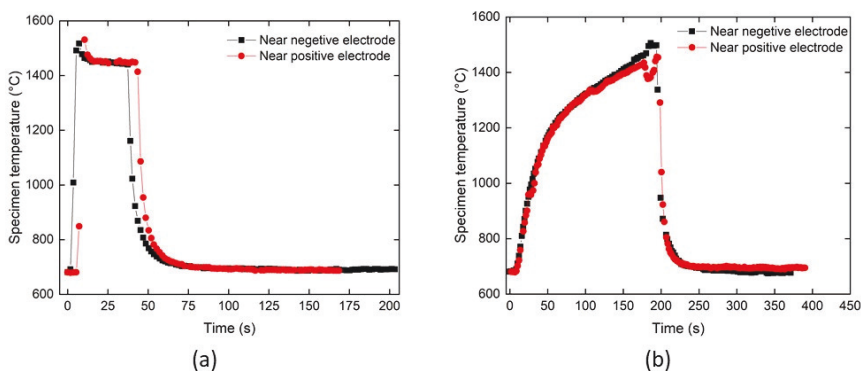

Figure 4-65 : Evolution of the sample temperature calculated from the lattice expansion during flash sintering: (a) voltage-to-current flash and (b) current rate flash. The base line peak as shown in Fig. 4-62 was used for calculation of the actual sample temperature.

Fig. 4-65 shows the evolution of the sample temperature in (a) voltage-to-current and (b) current rate flash sintering experiments. In voltage-to-current flash sintering conditions, a abrupt change in the sample temperature at the onset of flash is observed, whereas the temperature evolution in current rate flash sintering is gradual, which depends on the instantaneous current density. In both flash sintering mode, the maximum current density used was 200 mAmm^{-2}. From the sample temperature profile, it is observed that at the maximum current density the sample temperature could achieve approximately 1500°C. That again reconfirmed the previous findings that the degree of densification depends only on the current density not on the applied electric fields [123–125,131].

4.6.4. Summary

In situ flash sintering experiments in both voltage-to-current and CR flash mode at was carried out in a synchrotron comparing the lattice expansion behavior near different electrodes. The lattice expansion measurement of GDC10 near the positive electrode shows abnormal lattice expansion. The abnormal lattice expansion at the positive electrode was attributed to the generation of different non-stoichiometry in the lattice and defect generation due to the inhomogeneous reduction of the GDC10 under DC electric field. The abnormal lattice expansion at the positive electrode is vanished when the power is turned off. Surprisingly, flash sintering in current rate mode shows no abnormal lattice expansion and change of the lattice expansion was homogeneous in the sample.

The temperature of the sample during the flash sintering was calculated from the diffraction peak. The results reveal that the maximum temperature depends on the current density. For GDC10, a temperature of approximately 1500°C appeared if flash sintering was done at a current density of 200 mA mm^{-2}. This temperature is quite similar to the temperature required for conventional sintering GDC10. However, enhanced sintering kinetics under flash sintering conditions could be due to the formation of point defects that were generated during the flash sintering.

In our future work, the mean square displacement of the ions will be analyzed, which will provide information about the mobility of the individual ions during the flash state. Furthermore, the domain size evolution in the sample during the flash sintering experiments will be analyzed to study the grain boundary mobility depending on flash sintering mode and position, in the sample.

Chapter 5 Conclusions and Outlook

In this dissertation work, sintering and densification of 10 mol% Gadolinium-doped Ceria (GDC10) under the influence of reducing atmosphere and electric field was studied. The dissertation work contains three main sections:

(i) Conventional sintering of GDC10 under reducing condition: In this part, densification, microstructure evolution and chemical expansion of GDC10 under reducing conditions were investigated. The results act as reference for other sections.

(ii) Field assisted Sintering Technology/Spark Plasma Sintering of GDC10: A systematic study aimed on how to handle chemical expansion in a FAST/SPS device, operated with low electric fields.

(iii) Flash sintering of GDC10: Here, introduction to high electric field, where the current was forced to flow through the sample. Systematic studies were carried out to elucidate the mechanisms behind the onset of flash, densification and grain growth of GDC10 under flash condition. A novel mode of flash sintering, current rate flash sintering was introduced demonstrating the ability to control the densification and to tune the microstructure of GDC10 during flash sintering. Furthermore, in situ flash sintering of GDC10 was performed in a synchrotron facility at Brookhaven National Lab to measure the specimen temperature accurately during flash sintering experiment. A detailed summary of the main results is concluded below.

In the beginning of the dissertation work, benchmarking of four different commercially available GDC10 powders was carried out (FuellCellMaterials, CerpoTech, Treibacher and DKKK). The uniaxial compaction and conventional sintering studies of the different powders shows that the primary particle size and morphology can significantly influence the degree of densification and resulting microstructure of the sintered sample. It was found that the GDC10 powder from FuelCellMaterial, which has mostly unimodal particle size distribution and homogeneous powder morphology showed the most promising densification behavior among all the powders. Whereas the GDC10 powder from CerPoTech, which has a wide range of primary particle size distribution in the range from nanometer scale to several hundred

micrometer scale with a nonuniform particle morphology showed lowest degree of densification and nonuniform microstructure.

Conventional sintering of GDC10 material under reducing atmosphere (Ar/2.9%H$_2$) showed an enhanced densification of the material. Such enhanced densification behaviour of GDC10 under low oxygen partial pressure of oxygen (P(O$_2$) < 10^{-12} atm) was activated by high volume diffusion due to the formation of a large concentration of oxygen vacancies ($V_O^{\bullet\bullet}$) and associated cation defects (Ce'_{Ce}) due to the reduction of Ce^{4+} to Ce^{3+}. Maximum densification rate of GDC10 under reducing atmosphere was achieved by 200°C lower than in the air atmosphere. Nevertheless, the conventional sintered samples under reducing atmosphere showed high concentration of micro-cracks in the microstructure. These micro-cracks are generated in the sample due to the reduction of GDC10 under reducing atmosphere and abrupt change in the volume when expose to the air atmosphere at room temperature. Re-oxidation generates high internal stress in the sample.

Fundamental studies on the chemical expansion behaviour of the GDC10 material due to the generation of oxygen vacancies was carried out. Therefore, series of thermogravimetric and high temperature X-ray diffraction experiments were conducted. The quantification of the oxygen non-stoichiometry and the chemical expansion shows that the GDC10 sample may experience a volume change of above 4% at 1000°C under the reducing environment. The volume change inversely depends on the oxygen partial pressure and directly on the temperature. Therefore, the volume change of the sample was higher than 4% during the sintering experiments in this work. In conventional sintering an enhanced densification at a lower temperature (< 200°C) under reducing atmosphere than air is advantageous. However, samples which were sintered entirely under reducing atmosphere had several cracks in the microstructure. For taking advantage of the reducing atmosphere (Ar/2.9%H$_2$) effect at the same time avoiding the micro-cracks in the sample was obtained by a re-oxidation at 800°C during the cooling cycle.

Densification behaviour and grain growth of GDC10 by conventional FAST/SPS, which is a low electric field and high current technique, were investigated. Maximum densification rate of GDC10 was lowered by approximately 200°C in FAST/SPS set up. Sintering of GDC10 under reducing atmosphere with conventional, pressure assisted tool configuration (PA) shows a negligible effect. Additionally, the conventional tool setup (PA) has several challenges for fabrication of stable and crack free samples by FAST/SPS. The samples were splintered into

many small pieces while ejecting form the tool, which was primarily due to the uncontrolled reduction of the sample due to the direct contact with the tool material. Furthermore, in conventional tool configuration the sample is almost completely isolated from the external atmosphere, which hinder exchange of processing gas to reach to the sample. FAST/SPS of GDC10 sample in a conventional tool set up results in macroscopic cracking of the sample into many small pieces and the microstructure showed in addition high concentration of micro cracks. The cracking of the sample was caused by uncontrolled reduction of the material due to the processing conditions in FAST/SPS and associated volume changes.

The challenge of processing of the GDC10 samples in FAST/SPS was overcome by developing an alternative tool configuration, where no load was applied on the sample (pressure less, PL). The alternative tool had a cavity, where the uniaxially pressed green compact was placed and no load was applied from the punches. Therefore, the chemical expansion during heating and contraction during cooling of the sample in the FAST/SPS cycle was accommodated. This results in dense, stable and macroscopically crack free samples. However, the microstructures still showed micro-cracks. These micro-cracks were eliminated by an atmosphere change during the FAST/SPS cycle enabling re-oxidation of the sample at 800°C.

Flash sintering emerges as an important processing technique in the category of electric current assisted sintering technique (ECAS). Flash sintering utilizes moderate to high electric field and small current, which was forced to flow through a green ceramic body. A typical flash sintering process is carried out by applying a constant electric field to the green body specimen from the beginning. Generally, the flash sintering experiments are carried out in voltage-to-current control mode, where a constant electric field to the green body specimen from the beginning. At a critical furnace temperature (i.e. onset temperature) specific for the applied electric field a sharp rise in the conductivity of the sample leads to an uncontrolled flow of current in the sample. The electrical power to the specimen is then switched from voltage control to current control, which is set to a maximum current density in order to prevent electrical /thermal runaway.

A wide range of ceramics, which include semiconductors, electronic conductors, ionic conductors and insulators shows flash phenomenon. The onset temperature for flash however can vary depending on the material. However, the exact mechanism responsible for the onset phenomenon and rapid sintering rate is still unknown. In this work, fundamental studies to understand the onset phenomenon and mechanism of densification were done in voltage-to-

current mode. Later, flash sintering of GDC10 was also studied under current rate (CR) mode. In CR flash sintering, the current is applied from the beginning of the experiment and raised at a constant rate until a maximum predefined current density is reached.

The onset of flash that is the non-linear rise in conductivity as a function of the applied electric field and the furnace temperature. Higher electric field lowers the furnace temperature for initiating the onset of flash. In this dissertation work, we seek to investigate what would be the lowest possible onset temperature for initiating flash. Therefore, constant heating rate experiments at different electric fields ranging from 50 Vcm^{-1} to 4000 Vcm^{-1} for GDC 10 material (both porous and dense) have been carried out. It was found that the Debye temperature of the material is the lower bound temperature for initiation of flash for GDC10. The onset temperature from the current study together with the onset temperature data from the literature for YSZ and TiO$_2$, used to develop a universal onset plot, where the onset temperature of the material was normalized to their respective Debye temperature. A general conclusion could be drawn that the Debye temperature is indeed the lower bound temperature for initiating the flash. This finding is currently regarded as a fourth characteristics associated with the flash sintering. The other three characteristics of flash sintering are: (i) sharp rise in the sample conductivity (ii) a bright light emission and (iii) rapid densification (in couple of seconds)

Second, the mechanism behind the triggering of the onset of flash in GDC10 was studied. It was demonstrated that in air the onset of flash is triggered by the electronic conduction generated under DC field in GDC10. The application of DC field generates oxygen vacancies that are accumulated near the cathode side. The oxygen vacancy concentration increases during the incubation period (stage I) and propagate towards anode side. Therefore, it activates *n-type* electronic conductivity in air which is associated with the occurrence of an electrochemical reduction process. The reduction of GDC10 results in enhanced electronic conductivity of the material. Therefore, by conducting flash sintering of GDC10 under reducing atmosphere (i.e. Ar/5%H$_2$) the onset temperature for initiating flash was lowered significantly. That is in a good agreement with the experimental finding that the electronic conductivity in the GDC10 under DC electric field in air is responsible for the onset of flash.

In addition, systematic investigation of the influence of different flash parameters on the densification behavior of GDC10 was carried out. It was found that while the higher electric field lowered the onset temperature for flash, the current density is responsible for the degree of densification of GDC10. A current density of 200 mA mm^{-2} was required to obtain near full

density for GDC10 as compared to 100 mA mm^{-2} required for YSZ. Measurement of the specimen temperature at the steady state of flash (stage III) in voltage-to-control flash and the estimation of the specimen temperature by BBR model are in good agreement. In both cases, the specimen temperature was at current density of 200 mA mm^{2} was approximately 1400 ℃. Different sets of voltage-to-current flash experiments were carried out to develop a processing map, which shows suitable electrical parameters for safe sintering of GDC10 by flash sintering process. Of course, the degree of densification depends on the maximum current density. Two distinct failure modes have been identified, where at higher current density, current localization (so called hot spot formation) occurred in the sample. The current localization in the sample leads to inhomogeneous densification and in worst case partial melting of the sample. On the other hand, at higher electric fields the sample splinters. However, the voltage-to-current flash sintering of GDC10 under DC current tend to result in non-uniform microstructure along the gage section of the sample. The grain size near the anode side is larger over a factor of 10 times to the grain size near the cathode side.

Current rate (CR) flash sintering is a new development in the field of flash sintering. In CR flash sintering, the power supply was always held under current control while the current is increased at a constant rate to densify GDC10 material. The densification was found to be independent from the current rate and depended only on the instantaneous value of the current density. This mode of flash sintering allows to control the densification of the sample and provide opportunity to even fabricate samples with controlled porosity. The microstructure of all CR flash sintered sample had a uniform grain size along the complete length of the sample. Surprisingly, the average grain size of the CR flash sintered GDC10 samples showed a finer grain size as higher current rates. Therefore, it was demonstrated in this dissertation for the first time that current rate flash sintering technique has the potential to fabricate samples with controlled densification and microstructure for engineering applications. We believe that this is the key to scale up flash sintering to large dimensions.

A preliminary analysis of the "energy deficit" model is developed in this work, which is indicated by the temperature difference between the estimated specimen temperature using the modified BBR model and the specimen temperature measured during the CR flash experiment by pyrometer, is attributed to the endothermic nature of defect generation. For GDC10, concentration in the range of 10-30 mol% were estimated. Based on this model, we proposed a hypothesis for explaining the mechanism for the flash sintering. Our hypothesis suggests that

these Frenkel pairs are continuously fill in the pores at the grain boundaries, which enhance the sintering kinetics during flash sintering.

Last but not the least, one of the major challenges in the flash sintering experiments is the direct measurement of the actual sample temperature during the flash sintering experiment. In this work, in situ flash sintering experiments in both voltage-to-current and CR flash mode at was carried out in a synchrotron measuring the lattice expansion. In addition, reference measurement of the lattice expansion of GDC10 was measured (at Juelich) as a function of temperature without electric field. The synchrotron data are matched with the reference data to translate the lattice expansion into the specimen temperature during the flash sintering experiments. The result showed that the sample temperature (GDC10) during the flash sintering experiment at a current density of 200 mA mm $^{-2}$ was approximately 1500°C.

Outlook

Although fundamental study of the flash sintering was carried out to understand the mechanism for flash sintering, further investigations with different materials are necessary. The generality of the Debye temperature as the onset for flash is shown only for three oxides, future experiments with different materials are required to further justify the universality of the Debye temperature for the onset of flash. The current rate flash shows a huge potential to control the densification and tuning of the microstructure of the sintered sample. While in literature experiments with ZnO and the current work with GDC10 show an influence of the current rate on the grain size, YSZ samples sintered by CR flash did not showed this effect. Therefore, CR experiments with different material is necessary to draw a sound conclusion about the effect of current rates on the microstructure evolution in the samples. CR flash experiments with dense polycrystals and single crystals are underway to explore the possibility of the generation of the point defects and diffusion at grain boundaries and pores to enhance the sintering kinetics to support the hypothesis of the energy deficit model. This would probably give a new direction in explaining the enhanced densification during flash sintering.

Up to now, flash sintering is successfully demonstrated only on small samples. The primary reasons that limit the application of flash sintering on a larger scale is the generation of hot spots. We believe the challenge of formation of hot spots on large dimension samples could be overcome by utilizing current rate flash sintering. In CR flash sintering, the onset of flash

occurred at a very low current density, which could be beneficial for achieving a homogeneous current distribution on the surface area of the sample. The feasibility study for scaling up of flash sintering process will be done utilizing a unique hybrid FAST/SPS device, which has a 1000 V power source that allows to conduct flash sintering experiments at IEK-1, Forschungszentrum Juelich GmbH. The experimental work will be complimented by modelling and simulation work on the flash sintering of large dimensions samples. Development of material-specific numerical models (considering different sintering mechanisms) for the prediction of densification and grain growth during current rate flash sintering. Methods of integrated computational materials engineering (ICME) will be developed to achieve this target. Furthermore, the temperature evolution of the sample during flash sintering will be simulated.

References

[1] EIA projects nearly 50% increase in world energy usage by 2050, led by growth in Asia - Today in Energy - U.S. Energy Information Administration (EIA), (n.d.). https://www.eia.gov/todayinenergy/detail.php?id=41433 (accessed October 18, 2019).

[2] N. Mahato, A. Banerjee, A. Gupta, S. Omar, K. Balani, Progress in material selection for solid oxide fuel cell technology: A review, Progress in Materials Science. 72 (2015) 141–337. https://doi.org/10.1016/j.pmatsci.2015.01.001.

[3] I. Staffell, D. Scamman, A.V. Abad, P. Balcombe, P.E. Dodds, P. Ekins, N. Shah, K.R. Ward, The role of hydrogen and fuel cells in the global energy system, Energy Environ. Sci. 12 (2019) 463–491. https://doi.org/10.1039/C8EE01157E.

[4] Citeseer - Full Text PDF, (n.d.). http://citeseerx.ist.psu.edu/viewdoc/download;jsessionid=AC7AB3720378D549A173D3 736E24C5D6?doi=10.1.1.476.6374&rep=rep1&type=pdf (accessed October 22, 2019).

[5] C. Sun, H. Li, L. Chen, Nanostructured ceria-based materials: synthesis, properties, and applications, Energy Environ. Sci. 5 (2012) 8475. https://doi.org/10.1039/c2ee22310d.

[6] H. Inaba, H. Tagawa, Ceria-based solid electrolytes, Solid State Ionics. 83 (1996) 1–16. https://doi.org/10.1016/0167-2738(95)00229-4.

[7] J. Kašpar, P. Fornasiero, M. Graziani, Use of CeO2-based oxides in the three-way catalysis, Catalysis Today. 50 (1999) 285–298. https://doi.org/10.1016/S0920-5861(98)00510-0.

[8] N. Izu, W. Shin, N. Murayama, S. Kanzaki, Resistive oxygen gas sensors based on CeO2 fine powder prepared using mist pyrolysis, Sensors and Actuators B: Chemical. 87 (2002) 95–98. https://doi.org/10.1016/S0925-4005(02)00224-1.

[9] H.-J. Beie, A. Gnörich, Oxygen gas sensors based on CeO2 thick and thin films, Sensors and Actuators B: Chemical. 4 (1991) 393–399. https://doi.org/10.1016/0925-4005(91)80141-6.

[10] X. Yin, L. Hong, Z.-L. Liu, Oxygen permeation through the LSCO-80/CeO2 asymmetric tubular membrane reactor, Journal of Membrane Science. 268 (2006) 2–12. https://doi.org/10.1016/j.memsci.2005.06.005.

[11] K. Eguchi, T. Setoguchi, T. Inoue, H. Arai, Electrical properties of ceria-based oxides and their application to solid oxide fuel cells, Solid State Ionics. 52 (1992) 165–172. https://doi.org/10.1016/0167-2738(92)90102-U.

[12] V. Esposito, D.W. Ni, Z. He, W. Zhang, A.S. Prasad, J.A. Glasscock, C. Chatzichristodoulou, S. Ramousse, A. Kaiser, Enhanced mass diffusion phenomena in highly defective doped ceria, Acta Materialia. 61 (2013) 6290–6300. https://doi.org/10.1016/j.actamat.2013.07.012.

[13] B.C.H. Steele, Appraisal of Ce1−yGdyO2−y/2 electrolytes for IT-SOFC operation at 500°C, Solid State Ionics. 129 (2000) 95–110. https://doi.org/10.1016/S0167-2738(99)00319-7.

[14] M. Asher, O. Diéguez, A computational study of gadolinium-doped ceria: Relationship between atomic arrangement and electrostriction, APL Materials. 7 (2019) 041109. https://doi.org/10.1063/1.5091840.

[15] L. Rose, M. Menon, K. Kammer, O. Kesler, P.H. Larsen, Processing of $Ce_{1-x}Gd_xO_{2-\delta}$ (GDC) Thin Films from Precursors for Application in Solid Oxide Fuel Cells, AMR. 15–17 (2006) 293–298. https://doi.org/10.4028/www.scientific.net/AMR.15-17.293.

[16] J.C. De Vero, K. Develos-Bagarinao, H. Kishimoto, T. Ishiyama, K. Yamaji, T. Horita, H. Yokokawa, Influence of $La_{0.6}Sr_{0.4}Co_{0.2}Fe_{0.8}O_{3-\delta}$ Microstructure on GDC Interlayer Stability and Cation Diffusion across the LSCF/GDC/YSZ Interfaces, J. Electrochem. Soc. 163 (2016) F1463–F1470. https://doi.org/10.1149/2.0021614jes.

[17]   M. Brandner, M. Bram, J. Froitzheim, H.P. Buchkremer, D. Stöver, Electrically Conductive Diffusion barrier layers for Metal-Supported SOFC, Solid State Ionics. 179 (2008) 1501–1504. https://doi.org/10.1016/j.ssi.2008.03.002.

[18]   C. Chatzichristodoulou, M. Søgaard, J. Glasscock, A. Kaiser, S.P.V. Foghmoes, P.V. Hendriksen, Oxygen Permeation in Thin, Dense Ce0.9Gd0.1O1.95-δ Membranes II. Experimental Determination, J. Electrochem. Soc. 158 (2011) F73–F83. https://doi.org/10.1149/1.3559189.

[19]   A. Caravaca, S. Picart, M. Aouine, B. Arab-Chapelet, P. Vernoux, T. Delahaye, Development of Highly Nano-Dispersed NiO/GDC Catalysts from Ion Exchange Resin Templates, Catalysts. 7 (2017) 368. https://doi.org/10.3390/catal7120368.

[20]   D.W. Ni, J.A. Glasscock, A. Pons, W. Zhang, A. Prasad, S. Sanna, N. Pryds, V. Esposito, Densification of Highly Defective Ceria by High Temperature Controlled Re-Oxidation, J. Electrochem. Soc. 161 (2014) F3072–F3078. https://doi.org/10.1149/2.0121411jes.

[21]   S.H. Jo, P. Muralidharan, D.K. Kim, Electrical characterization of dense and porous nanocrystalline Gd-doped ceria electrolytes, Solid State Ionics. 178 (2008) 1990–1997. https://doi.org/10.1016/j.ssi.2007.12.076.

[22]   M. Caisso, R. Boulesteix, S. Picart, A. Maître, T. Delahaye, A. Ayral, Investigation of the sintering mechanisms of GDC pellets obtained by the compaction of nanostructured oxide microspheres, Journal of the American Ceramic Society. 100 (2017) 4450–4460. https://doi.org/10.1111/jace.14993.

[23]   T. Zhang, L. Kong, Z. Zeng, H. Huang, P. Hing, Z. Xia, J. Kilner, Sintering behavior and ionic conductivity of Ce0.8Gd0.2O1.9 with a small amount of MnO2 doping, J Solid State Electrochem. 7 (2003) 348–354. https://doi.org/10.1007/s10008-002-0337-0.

[24]   S. Grasso, Y. Sakka, G. Maizza, Electric current activated/assisted sintering (ECAS): a review of patents 1906–2008, Sci. Technol. Adv. Mater. 10 (2009) 053001. https://doi.org/10.1088/1468-6996/10/5/053001.

[25]   Eugene A. Olevsky, Dina V. Dudina - Field-Assisted Sintering_ Science and Applications-Springer International Publishing (2018).pdf, (n.d.).

[26]   O. Guillon, J. Gonzalez-Julian, B. Dargatz, T. Kessel, G. Schierning, J. Räthel, M. Herrmann, Field-Assisted Sintering Technology/Spark Plasma Sintering: Mechanisms, Materials, and Technology Developments: FAST/SPS: Mechanisms, Materials, and Technology Developments, Adv. Eng. Mater. 16 (2014) 830–849. https://doi.org/10.1002/adem.201300409.

[27]   M. Cologna, B. Rashkova, R. Raj, Flash Sintering of Nanograin Zirconia in <5 s at 850°C, Journal of the American Ceramic Society. 93 (2010) 3556–3559. https://doi.org/10.1111/j.1551-2916.2010.04089.x.

[28]   M. Biesuz, V.M. Sglavo, Flash sintering of ceramics, Journal of the European Ceramic Society. 39 (2019) 115–143. https://doi.org/10.1016/j.jeurceramsoc.2018.08.048.

[29]   O. Guillon, J. Gonzalez-Julian, B. Dargatz, T. Kessel, G. Schierning, J. Räthel, M. Herrmann, Field-Assisted Sintering Technology/Spark Plasma Sintering: Mechanisms, Materials, and Technology Developments, Advanced Engineering Materials. 16 (2014) 830–849. https://doi.org/10.1002/adem.201300409.

[30]   A. Prasad, L. Malakkal, L. Bichler, J. Szpunar, Challenges in Spark Plasma Sintering of Cerium (IV) Oxide, in: Processing, Properties, and Design of Advanced Ceramics and Composites II, John Wiley & Sons, Ltd, 2018: pp. 217–224. https://doi.org/10.1002/9781119423829.ch19.

[31]   C.E.J. Dancer, Flash sintering of ceramic materials, Mater. Res. Express. 3 (2016) 102001. https://doi.org/10.1088/2053-1591/3/10/102001.

[32]   M. Biesuz, V.M. Sglavo, Flash sintering of ceramics, Journal of the European Ceramic Society. 39 (2019) 115–143. https://doi.org/10.1016/j.jeurceramsoc.2018.08.048.

[33]   M. Cologna, B. Rashkova, R. Raj, Flash Sintering of Nanograin Zirconia in <5 s at 850°C: Rapid Communications of the American Ceramic Society, Journal of the American Ceramic Society. 93 (2010) 3556–3559. https://doi.org/10.1111/j.1551-2916.2010.04089.x.

[34]   M. Yu, S. Grasso, R. Mckinnon, T. Saunders, M.J. Reece, Review of flash sintering: materials, mechanisms and modelling, Advances in Applied Ceramics. 116 (2017) 24–60. https://doi.org/10.1080/17436753.2016.1251051.

[35]   M.Z. Becker, N. Shomrat, Y. Tsur, Recent Advances in Mechanism Research and Methods for Electric-Field-Assisted Sintering of Ceramics, Advanced Materials. 30 (2018) 1706369. https://doi.org/10.1002/adma.201706369.

[36]   T. Jiang, Z. Wang, J. Zhang, X. Hao, D. Rooney, Y. Liu, W. Sun, J. Qiao, K. Sun, Understanding the Flash Sintering of Rare-Earth-Doped Ceria for Solid Oxide Fuel Cell, Journal of the American Ceramic Society. 98 (2015) 1717–1723. https://doi.org/10.1111/jace.13526.

[37]   L. Spiridigliozzi, M. Biesuz, G. Dell'Agli, E. Di Bartolomeo, F. Zurlo, V.M. Sglavo, Microstructural and electrical investigation of flash-sintered Gd/Sm-doped ceria, J Mater Sci. 52 (2017) 7479–7488. https://doi.org/10.1007/s10853-017-0980-2.

[38]   X. Hao, Y. Liu, Z. Wang, J. Qiao, K. Sun, A novel sintering method to obtain fully dense gadolinia doped ceria by applying a direct current, Journal of Power Sources. 210 (2012) 86–91. https://doi.org/10.1016/j.jpowsour.2012.03.006.

[39]   S.K. Jha, H. Charalambous, H. Wang, X.L. Phuah, C. Mead, J. Okasinski, H. Wang, T. Tsakalakos, In-situ observation of oxygen mobility and abnormal lattice expansion in ceria during flash sintering, Ceramics International. 44 (2018) 15362–15369. https://doi.org/10.1016/j.ceramint.2018.05.186.

[40]   R.M. German, History of sintering: empirical phase, Powder Metallurgy. 56 (2013) 117–123. https://doi.org/10.1179/1743290112Y.0000000025.

[41]   M.N. Rahaman, Sintering of Ceramics, CRC Press, 2007.

[42]   R.K. Bordia, S.-J.L. Kang, E.A. Olevsky, Current understanding and future research directions at the onset of the next century of sintering science and technology, Journal of the American Ceramic Society. 100 (2017) 2314–2352. https://doi.org/10.1111/jace.14919.

[43]   S.-J.L. Kang, Sintering, Elsevier, 2005. https://doi.org/10.1016/B978-0-7506-6385-4.X5000-6.

[44]   M.E. Fine, Introduction to Chemical and Structural Defects in Crystalline Solids, in: N.B. Hannay (Ed.), The Chemical Structure of Solids, Springer US, Boston, MA, 1921: pp. 283–333. https://doi.org/10.1007/978-1-4684-2661-8_5.

[45]   M. Itoh, CHAPTER 2 - The Role of Lattice Defects in Oxides, in: H. Hosono, Y. Mishima, H. Takezoe, K.J.D. MacKenzie, K. MacKenzie, Y. Mishima, H. Takezoe (Eds.), Nanomaterials, Elsevier Science Ltd, Oxford, 2006: pp. 62–98. https://doi.org/10.1016/B978-008044964-7/50004-2.

[46]   P.-L. Chen, I.-W. Chen, Role of Defect Interaction in Boundary Mobility and Cation Diffusivity of CeO2, Journal of the American Ceramic Society. 77 (1994) 2289–2297. https://doi.org/10.1111/j.1151-2916.1994.tb04596.x.

[47]   F.A. Kröger, H.J. Vink, Relations between the Concentrations of Imperfections in Crystalline Solids, in: Solid State Physics, Elsevier, 1956: pp. 307–435. https://doi.org/10.1016/S0081-1947(08)60135-6.

[48]   J. Pelleg, Imperfections (Defects) in Ceramics, in: Mechanical Properties of Ceramics, Springer International Publishing, Cham, 2014: pp. 173–279. https://doi.org/10.1007/978-3-319-04492-7_3.

[49]   C.-J. Ting, H.-Y. Lu, Defect Reactions and the Controlling Mechanism in the Sintering of Magnesium Aluminate Spinel, Journal of the American Ceramic Society. 82 (1999) 841–848. https://doi.org/10.1111/j.1151-2916.1999.tb01844.x.

[50]   R.B. Atkin, R.M. Fulrath, Point Defects and Sintering of Lead Zirconate-Titanate, Journal of the American Ceramic Society. 54 (1971) 265–270. https://doi.org/10.1111/j.1151-2916.1971.tb12286.x.

[51]   R.L. Coble, Sintering Alumina: Effect of Atmospheres, Journal of the American Ceramic Society. 45 (1962) 123–127. https://doi.org/10.1111/j.1151-2916.1962.tb11099.x.

[52]   Mohamed N. Rahaman - Sintering of Ceramics-CRC Press (2007).pdf, (n.d.).

[53]   W. Wang, Z. Fu, H. Wang, R. Yuan, Influence of hot pressing sintering temperature and time on microstructure and mechanical properties of TiB2 ceramics, Journal of the European Ceramic Society. 22 (2002) 1045–1049. https://doi.org/10.1016/S0955-2219(01)00424-1.

[54]   H.B. Li, J.T. Luo, Y.F. Gu, Y.X. Xu, Hot Press Sintering Behavior of Nano-Sized AlN Powders, AMR. 105–106 (2010) 720–722. https://doi.org/10.4028/www.scientific.net/AMR.105-106.720.

[55]   J.M. Lonergan, W.G. Fahrenholtz, G.E. Hilmas, Sintering Mechanisms and Kinetics for Reaction Hot-Pressed ZrB2, Journal of the American Ceramic Society. 98 (2015) 2344–2351. https://doi.org/10.1111/jace.13544.

[56]   R.M. German, Sintering With External Pressure, in: Sintering: From Empirical Observations to Scientific Principles, Elsevier, 2014: pp. 305–354. https://doi.org/10.1016/B978-0-12-401682-8.00010-0.

[57]   R.M. German, Chapter Ten - Sintering With External Pressure, in: R.M. German (Ed.), Sintering: From Empirical Observations to Scientific Principles, Butterworth-Heinemann, Boston, 2014: pp. 305–354. https://doi.org/10.1016/B978-0-12-401682-8.00010-0.

[58]   S.-X. Wu, R.J. Brook, Kinetics of densification in stabilized zirconia, Solid State Ionics. 14 (1984) 123–130. https://doi.org/10.1016/0167-2738(84)90086-9.

[59]   J. Langer, M.J. Hoffmann, O. Guillon, Direct comparison between hot pressing and electric field-assisted sintering of submicron alumina, Acta Materialia. 57 (2009) 5454–5465. https://doi.org/10.1016/j.actamat.2009.07.043.

[60]   J. Langer, M.J. Hoffmann, O. Guillon, Electric Field-Assisted Sintering in Comparison with the Hot Pressing of Yttria-Stabilized Zirconia, Journal of the American Ceramic Society. 94 (2011) 24–31. https://doi.org/10.1111/j.1551-2916.2010.04016.x.

[61]   J. Chang, O. Guillon, J. Rödel, S.-J.L. Kang, Uniaxial viscosity of gadolinium-doped ceria determined by discontinuous sinter forging, Journal of the European Ceramic Society. 27 (2007) 3127–3133. https://doi.org/10.1016/j.jeurceramsoc.2007.01.003.

[62]   R. Zuo, E. Aulbach, J. Rödel, Experimental determination of sintering stresses and sintering viscosities, Acta Materialia. 51 (2003) 4563–4574. https://doi.org/10.1016/S1359-6454(03)00293-3.

[63]   H.V. Atkinson, S. Davies, Fundamental aspects of hot isostatic pressing: An overview, Metall and Mat Trans A. 31 (2000) 2981–3000. https://doi.org/10.1007/s11661-000-0078-2.

[64]   S. Grasso, Y. Sakka, G. Maizza, Electric current activated/assisted sintering (ECAS): a review of patents 1906–2008, Science and Technology of Advanced Materials. 10 (2009) 053001. https://doi.org/10.1088/1468-6996/10/5/053001.

[65]   M. Oghbaei, O. Mirzaee, Microwave versus conventional sintering: A review of fundamentals, advantages and applications, Journal of Alloys and Compounds. 494 (2010) 175–189. https://j.jallcom.2010.01.068.

[66]   M. Yu, S. Grasso, R. Mckinnon, T. Saunders, M.J. Reece, Review of flash sintering: materials, mechanisms and modelling, Advances in Applied Ceramics. 116 (2017) 24–60. https://doi.org/10.1080/17436753.2016.1251051.

[67]   O. Guillon, C. Elsässer, O. Gutfleisch, J. Janek, S. Korte-Kerzel, D. Raabe, C.A. Volkert, Manipulation of matter by electric and magnetic fields: Toward novel synthesis and processing routes of inorganic materials, Materials Today. 21 (2018) 527–536. https://doi.org/10.1016/j.mattod.2018.03.026.

[68]   R. Orrù, R. Licheri, A.M. Locci, A. Cincotti, G. Cao, Consolidation/synthesis of materials by electric current activated/assisted sintering, Materials Science and Engineering: R: Reports. 63 (2009) 127–287. https://doi.org/10.1016/j.mser.2008.09.003.

[69]   S. Grasso, Y. Sakka, G. Maizza, Electric current activated/assisted sintering (ECAS): a review of patents 1906–2008, Science and Technology of Advanced Materials. 10 (2009) 053001. https://doi.org/10.1088/1468-6996/10/5/053001.

[70]   O. Guillon, J. Gonzalez-Julian, B. Dargatz, T. Kessel, G. Schierning, J. Räthel, M. Herrmann, Field-Assisted Sintering Technology/Spark Plasma Sintering: Mechanisms, Materials, and Technology Developments, Advanced Engineering Materials. 16 (2014) 830–849. https://doi.org/10.1002/adem.201300409.

[71]   E.A. Olevsky, D.V. Dudina, Field-Assisted Sintering: Science and Applications, Springer, 2018.

[72]   E.A. Olevsky, W.L. Bradbury, C.D. Haines, D.G. Martin, D. Kapoor, Fundamental Aspects of Spark Plasma Sintering: I. Experimental Analysis of Scalability, Journal of the American Ceramic Society. 95 (2012) 2406–2413. https://doi.org/10.1111/j.1551-2916.2012.05203.x.

[73]   Z. Shen, M. Johnsson, Z. Zhao, M. Nygren, Spark Plasma Sintering of Alumina, Journal of the American Ceramic Society. 85 (2002) 1921–1927. https://doi.org/10.1111/j.1151-2916.2002.tb00381.x.

[74]   J. Hong, L. Gao, S.D.D.L. Torre, H. Miyamoto, K. Miyamoto, Spark plasma sintering and mechanical properties of ZrO2(Y2O3)–Al2O3 composites, Materials Letters. 43 (2000) 27–31. https://doi.org/10.1016/S0167-577X(99)00225-6.

[75]   J. Raethel, J. Hennicke, Y. Dyatlova, M. Herrmann, V. Rumyantsev, New Developments of FAST/SPS Tool Materials, AST. 88 (2014) 37–42. https://doi.org/10.4028/www.scientific.net/AST.88.37.

[76]   A.M. Laptev, H. Zheng, M. Bram, M. Finsterbusch, O. Guillon, High-pressure field assisted sintering of half-cell for all-solid-state battery, Materials Letters. 247 (2019) 155–158. https://doi.org/10.1016/j.matlet.2019.03.109.

[77]   Z.-H. Zhang, Z.-F. Liu, J.-F. Lu, X.-B. Shen, F.-C. Wang, Y.-D. Wang, The sintering mechanism in spark plasma sintering – Proof of the occurrence of spark discharge, Scripta Materialia. 81 (2014) 56–59. https://doi.org/10.1016/j.scriptamat.2014.03.011.

[78]   K. Biswas, A.S. Sharma, B. Basu, On the densification mechanisms and properties of Cu–Pb and Cu–Pb–TiB2 nanocomposites densified using spark plasma sintering, Scripta Materialia. 69 (2013) 122–126. https://doi.org/10.1016/j.scriptamat.2013.02.046.

[79]   M. Jaafar, H. Reveron, C. Esnouf, G. Fantozzi, Highly creep-resistant alumina–SiC nanocomposites processed by spark plasma sintering, Scripta Materialia. 68 (2013) 134–137. https://doi.org/10.1016/j.scriptamat.2012.10.001.

[80]   M. Gendre, A. Maître, G. Trolliard, A study of the densification mechanisms during spark plasma sintering of zirconium (oxy-)carbide powders, Acta Materialia. 58 (2010) 2598–2609. https://doi.org/10.1016/j.actamat.2009.12.046.

[81]   B.V. Neamţu, I. Chicinaş, O. Isnard, I. Ciascai, F. Popa, T.F. Marinca, Consolidation and DC magnetic properties of nanocrystalline Supermalloy/iron composite cores prepared by spark plasma sintering, Journal of Magnetism and Magnetic Materials. 353 (2014) 6–10. https://doi.org/10.1016/j.jmmm.2013.10.021.

[82]   O.A. Graeve, M.S. Saterlie, R. Kanakala, S.D. de la Torre, J.C. Farmer, The kinetics of devitrification of amorphous alloys: The time–temperature–crystallinity diagram describing the spark plasma sintering of Fe-based metallic glasses, Scripta Materialia. 69 (2013) 143–148. https://doi.org/10.1016/j.scriptamat.2013.02.019.

[83]   J.R. Groza, A. Zavaliangos, Sintering activation by external electrical field, Materials Science and Engineering: A. 287 (2000) 171–177. https://doi.org/10.1016/S0921-5093(00)00771-1.

[84]   K.A. Khor, X.J. Chen, S.H. Chan, L.G. Yu, Microstructure-property modifications in plasma sprayed 20 wt.% yttria stabilized zirconia electrolyte by spark plasma sintering (SPS) technique, Materials Science and Engineering: A. 366 (2004) 120–126. https://doi.org/10.1016/j.msea.2003.08.119.

[85]   D.M. Hulbert, A. Anders, J. Andersson, E.J. Lavernia, A.K. Mukherjee, A discussion on the absence of plasma in spark plasma sintering, Scripta Materialia. 60 (2009) 835–838. https://doi.org/10.1016/j.scriptamat.2008.12.059.

[86]   D.M. Hulbert, A. Anders, D.V. Dudina, J. Andersson, D. Jiang, C. Unuvar, U. Anselmi-Tamburini, E.J. Lavernia, A.K. Mukherjee, The absence of plasma in "spark plasma sintering," Journal of Applied Physics. 104 (2008) 033305. https://doi.org/10.1063/1.2963701.

[87]   R. Chaim, Densification mechanisms in spark plasma sintering of nanocrystalline ceramics, Materials Science and Engineering: A. 443 (2007) 25–32. https://doi.org/10.1016/j.msea.2006.07.092.

[88]   Z.A. Munir, U. Anselmi-Tamburini, M. Ohyanagi, The effect of electric field and pressure on the synthesis and consolidation of materials: A review of the spark plasma sintering method, J Mater Sci. 41 (2006) 763–777. https://doi.org/10.1007/s10853-006-6555-2.

[89]   J. Langer, M.J. Hoffmann, O. Guillon, Direct comparison between hot pressing and electric field-assisted sintering of submicron alumina, Acta Materialia. 57 (2009) 5454–5465. https://doi.org/10.1016/j.actamat.2009.07.043.

[90]   E.A. Olevsky, S. Kandukuri, L. Froyen, Consolidation enhancement in spark-plasma sintering: Impact of high heating rates, Journal of Applied Physics. 102 (2007) 114913. https://doi.org/10.1063/1.2822189.

[91]   A.M. Okoro, S.S. Lephuthing, S.R. Oke, O.E. Falodun, M.A. Awotunde, P.A. Olubambi, A Review of Spark Plasma Sintering of Carbon Nanotubes Reinforced Titanium-Based Nanocomposites: Fabrication, Densification, and Mechanical Properties, JOM. 71 (2019) 567–584. https://doi.org/10.1007/s11837-018-3277-2.

[92]   R.H.R. Castro, K. van Benthem, eds., Sintering: mechanisms of convention nanodensification and field assisted processes, Springer, Berlin ; New York, 2013.

[93]   正雄鎬田, Sps放電プラズマ焼結法の最近の技術動向, 粉体工学会誌. 30 (1993) 790–804. https://doi.org/10.4164/sptj.30.11_790.

[94]   S. Deng, R. Li, T. Yuan, P. Cao, S. Xie, Electromigration-Enhanced Densification Kinetics During Spark Plasma Sintering of Tungsten Powder, Metall and Mat Trans A. 50 (2019) 2886–2897. https://doi.org/10.1007/s11661-019-05201-4.

[95]   Z. Trzaska, J.-P. Monchoux, Electromigration experiments by spark plasma sintering in the silver–zinc system, Journal of Alloys and Compounds. 635 (2015) 142–149. https://doi.org/10.1016/j.jallcom.2015.02.122.

[96] R. Raj, M. Cologna, J.S.C. Francis, Influence of Externally Imposed and Internally Generated Electrical Fields on Grain Growth, Diffusional Creep, Sintering and Related Phenomena in Ceramics, Journal of the American Ceramic Society. 94 (2011) 1941–1965. https://doi.org/10.1111/j.1551-2916.2011.04652.x.

[97] J. Langer, M.J. Hoffmann, O. Guillon, Electric Field-Assisted Sintering in Comparison with the Hot Pressing of Yttria-Stabilized Zirconia, Journal of the American Ceramic Society. 94 (2011) 24–31. https://doi.org/10.1111/j.1551-2916.2010.04016.x.

[98] O. Guillon, Effects of Applied Stress and Heating Rate in Field Assisted Sintering, in: R. Castro, K. van Benthem (Eds.), Sintering: Mechanisms of Convention Nanodensification and Field Assisted Processes, Springer, Berlin, Heidelberg, 2013: pp. 195–213. https://doi.org/10.1007/978-3-642-31009-6_9.

[99] M.-Y. Chu, M.N. Rahaman, L.C.D. Jonghe, R.J. Brook, Effect of Heating Rate on Sintering and Coarsening, Journal of the American Ceramic Society. 74 (1991) 1217–1225. https://doi.org/10.1111/j.1151-2916.1991.tb04090.x.

[100] L.A. Stanciu, V.Y. Kodash, J.R. Groza, Effects of heating rate on densification and grain growth during field-assisted sintering of α-Al2O3 and MoSi2 powders, Metall and Mat Trans A. 32 (2001) 2633–2638. https://doi.org/10.1007/s11661-001-0053-6.

[101] E.A. Olevsky, L. Froyen, Impact of Thermal Diffusion on Densification During SPS, Journal of the American Ceramic Society. 92 (2009) S122–S132. https://doi.org/10.1111/j.1551-2916.2008.02705.x.

[102] A.M. Laptev, M. Bram, K. Vanmeensel, J. Gonzalez-Julian, O. Guillon, Enhancing efficiency of field assisted sintering by advanced thermal insulation, Journal of Materials Processing Technology. 262 (2018) 326–339. https://doi.org/10.1016/j.jmatprotec.2018.07.008.

[103] L. Wang, V. Pouchly, K. Maca, Z. Shen, Y. Xiong, Intensive particle rearrangement in the early stage of spark plasma sintering process, Journal of Asian Ceramic Societies. 3 (2015) 183–187. https://doi.org/10.1016/j.jascer.2015.02.004.

[104] E. Olevsky, L. Froyen, Constitutive modeling of spark-plasma sintering of conductive materials, Scripta Materialia. 55 (2006) 1175–1178. https://doi.org/10.1016/j.scriptamat.2006.07.009.

[105] R.L. Coble, Diffusion models for hot pressing with surface energy and pressure effects as driving forces, Journal of Applied Physics. 41 (1970) 4798–4807. https://doi.org/10.1063/1.1658543.

[106] G. Bernard-Granger, C. Guizard, Spark plasma sintering of a commercially available granulated zirconia powder: I. Sintering path and hypotheses about the mechanism(s) controlling densification, Acta Materialia. 55 (2007) 3493–3504. https://doi.org/10.1016/j.actamat.2007.01.048.

[107] A.M. Thompson, M.P. Harmer, Influence of Atmosphere on the Final-Stage Sintering Kinetics of Ultra-High-Purity Alumina, Journal of the American Ceramic Society. 76 (1993) 2248–2256. https://doi.org/10.1111/j.1151-2916.1993.tb07761.x.

[108] H. Yoshida, K. Hiraga, T. Yamamoto, Densification Behavior of Ti-Doped Polycrystalline Alumina in a Nitrogen-Hydrogen Atmosphere, Materials Transactions. 50 (2009) 1032–1036. https://doi.org/10.2320/matertrans.MC200829.

[109] Y.-K. Paek, K.-Y. Eun, S.-J.L. Kang, Effect of Sintering Atmosphere on Densification of MgO-Doped Al2O3, Journal of the American Ceramic Society. 71 (1988) C-380-C–382. https://doi.org/10.1111/j.1151-2916.1988.tb06398.x.

[110] J.G. Noudem, S. Quetel-Weben, R. Retoux, G. Chevallier, C. Estournès, Thermoelectric properties of Ca0.9Yb0.1MnO3−x prepared by spark plasma sintering in air atmosphere, Scripta Materialia. 68 (2013) 949–952. https://doi.org/10.1016/j.scriptamat.2013.02.059.

[111]   T. Ibn-Mohammed, C.A. Randall, K.B. Mustapha, J. Guo, J. Walker, S. Berbano, S.C.L. Koh, D. Wang, D.C. Sinclair, I.M. Reaney, Decarbonising ceramic manufacturing: A techno-economic analysis of energy efficient sintering technologies in the functional materials sector, Journal of the European Ceramic Society. 39 (2019) 5213–5235. https://doi.org/10.1016/j.jeurceramsoc.2019.08.011.

[112]   J.G.P. da Silva, H.A. Al-Qureshi, F. Keil, R. Janssen, A dynamic bifurcation criterion for thermal runaway during the flash sintering of ceramics, Journal of the European Ceramic Society. 36 (2016) 1261–1267. https://doi.org/10.1016/j.jeurceramsoc.2015.11.048.

[113]   J. Narayan, A new mechanism for field-assisted processing and flash sintering of materials, Scripta Materialia. 69 (2013) 107–111. https://doi.org/10.1016/j.scriptamat.2013.02.020.

[114]   R.I. Todd, E. Zapata-Solvas, R.S. Bonilla, T. Sneddon, P.R. Wilshaw, Electrical characteristics of flash sintering: thermal runaway of Joule heating, Journal of the European Ceramic Society. 35 (2015) 1865–1877. https://doi.org/10.1016/j.jeurceramsoc.2014.12.022.

[115]   R. Chaim, Liquid Film Capillary Mechanism for Densification of Ceramic Powders during Flash Sintering, Materials. 9 (2016) 280. https://doi.org/10.3390/ma9040280.

[116]   K.S. Naik, V.M. Sglavo, R. Raj, Flash sintering as a nucleation phenomenon and a model thereof, Journal of the European Ceramic Society. 34 (2014) 4063–4067. https://doi.org/10.1016/j.jeurceramsoc.2014.04.043.

[117]   M. Biesuz, P. Luchi, A. Quaranta, V.M. Sglavo, Theoretical and phenomenological analogies between flash sintering and dielectric breakdown in α-alumina, Journal of Applied Physics. 120 (2016) 145107. https://doi.org/10.1063/1.4964811.

[118]   Y. Zhang, J.-I. Jung, J. Luo, Thermal runaway, flash sintering and asymmetrical microstructural development of ZnO and ZnO–Bi2O3 under direct currents, Acta Materialia. 94 (2015) 87–100. https://doi.org/10.1016/j.actamat.2015.04.018.

[119]   D. Yadav, R. Raj, Two unique measurements related to flash experiments with yttria-stabilized zirconia, Journal of the American Ceramic Society. 100 (2017) 5374–5378. https://doi.org/10.1111/jace.15114.

[120]   T.P. Mishra, V. Avila, R.R.I. Neto, M. Bram, O. Guillon, R. Raj, On the role of Debye temperature in the onset of flash in three oxides, Scripta Materialia. 170 (2019) 81–84. https://doi.org/10.1016/j.scriptamat.2019.05.030.

[121]   R. Raj, Analysis of the Power Density at the Onset of Flash Sintering, Journal of the American Ceramic Society. 99 (2016) 3226–3232. https://doi.org/10.1111/jace.14178.

[122]   P.K.M. K, D. Yadav, J.-M. Lebrun, R. Raj, Flash sintering with current rate: A different approach, Journal of the American Ceramic Society. 102 (2019) 823–835. https://doi.org/10.1111/jace.16037.

[123]   M. Biesuz, V.M. Sglavo, Flash sintering of alumina: Effect of different operating conditions on densification, Journal of the European Ceramic Society. 36 (2016) 2535–2542. https://doi.org/10.1016/j.jeurceramsoc.2016.03.021.

[124]   J.S.C. Francis, R. Raj, Influence of the Field and the Current Limit on Flash Sintering at Isothermal Furnace Temperatures, Journal of the American Ceramic Society. 96 (2013) 2754–2758. https://doi.org/10.1111/jace.12472.

[125]   J.-M. Lebrun, R. Raj, A First Report of Photoemission in Experiments Related to Flash Sintering, Journal of the American Ceramic Society. 97 (2014) 2427–2430. https://doi.org/10.1111/jace.13130.

[126]   M. Biesuz, P. Luchi, A. Quaranta, A. Martucci, V.M. Sglavo, Photoemission during flash sintering: An interpretation based on thermal radiation, Journal of the European

Ceramic Society. 37 (2017) 3125–3130. https://doi.org/10.1016/j.jeurceramsoc.2017.03.050.

[127] S.K. Jha, R. Raj, Electric Fields Obviate Constrained Sintering, Journal of the American Ceramic Society. 97 (2014) 3103–3109. https://doi.org/10.1111/jace.13136.

[128] S.K. Jha, K. Terauds, J.-M. Lebrun, R. Raj, Beyond flash sintering in 3 mol % yttria stabilized zirconia, J. Ceram. Soc. Japan. 124 (2016) 283–288. https://doi.org/10.2109/jcersj2.15248.

[129] M. Cologna, J.S.C. Francis, R. Raj, Field assisted and flash sintering of alumina and its relationship to conductivity and MgO-doping, Journal of the European Ceramic Society. 31 (2011) 2827–2837. https://doi.org/10.1016/j.jeurceramsoc.2011.07.004.

[130] R. Muccillo, M. Kleitz, E.N.S. Muccillo, Flash grain welding in yttria stabilized zirconia, Journal of the European Ceramic Society. 31 (2011) 1517–1521. https://doi.org/10.1016/j.jeurceramsoc.2011.02.030.

[131] R. Baraki, S. Schwarz, O. Guillon, Effect of Electrical Field/Current on Sintering of Fully Stabilized Zirconia, Journal of the American Ceramic Society. 95 (2012) 75–78. https://doi.org/10.1111/j.1551-2916.2011.04980.x.

[132] S. Grasso, T. Saunders, H. Porwal, O. Cedillos-Barraza, D.D. Jayaseelan, W.E. Lee, M.J. Reece, Flash Spark Plasma Sintering (FSPS) of Pure ZrB2, Journal of the American Ceramic Society. 97 (2014) 2405–2408. https://doi.org/10.1111/jace.13109.

[133] L.W. Hartman., A Spectrophotometric Study of the Luminous Radiation from the Nernst Lamp Glower under Varying Current Density, Phys. Rev. (Series I). 17 (1903) 65–90. https://doi.org/10.1103/PhysRevSeriesI.17.65.

[134] V. Avila, B. Yoon, R.R. Ingraci Neto, R.S. Silva, S. Ghose, R. Raj, L.M. Jesus, Reactive flash sintering of the complex oxide Li0.5La0.5TiO3 starting from an amorphous precursor powder, Scripta Materialia. 176 (2020) 78–82. https://doi.org/10.1016/j.scriptamat.2019.09.037.

[135] J.-M. Lebrun, T.G. Morrissey, J.S.C. Francis, K.C. Seymour, W.M. Kriven, R. Raj, Emergence and Extinction of a New Phase During On–Off Experiments Related to Flash Sintering of 3YSZ, Journal of the American Ceramic Society. 98 (2015) 1493–1497. https://doi.org/10.1111/jace.13476.

[136] B. Yoon, D. Yadav, R. Raj, E. Sortino, S. Ghose, P. Sarin, D. Shoemaker, Measurement of O and Ti atom displacements in TiO2 during flash sintering experiments, Journal of the American Ceramic Society. 101 (2018) 1811–1817. https://doi.org/10.1111/jace.15375.

[137] G. Liu, D. Liu, J. Liu, Y. Gao, Y. Wang, Asymmetric temperature distribution during steady stage of flash sintering dense zirconia, Journal of the European Ceramic Society. 38 (2018) 2893–2896. https://doi.org/10.1016/j.jeurceramsoc.2018.02.012.

[138] J.S.C. Francis, M. Cologna, R. Raj, Particle size effects in flash sintering, Journal of the European Ceramic Society. 32 (2012) 3129–3136. https://doi.org/10.1016/j.jeurceramsoc.2012.04.028.

[139] J.V. Campos, I.R. Lavagnini, R.V. de Sousa, J.A. Ferreira, E. Pallone, Influence of 3YSZ sample height at the onset temperature of flash sintering, Electric Field Enhanced Processing of Advanced Materials II: Complexities and Opportunities. (2019). https://dc.engconfintl.org/efe_advancedmaterials_ii/34.

[140] V. Avila, R. Raj, Flash sintering of ceramic films: The influence of surface to volume ratio, Journal of the American Ceramic Society. 102 (2019) 3063–3069. https://doi.org/10.1111/jace.16298.

[141] D. Yadav, R. Raj, The onset of the flash transition in single crystals of cubic zirconia as a function of electric field and temperature, Scripta Materialia. 134 (2017) 123–127. https://doi.org/10.1016/j.scriptamat.2017.02.015.

[142] M. Biesuz, L. Pinter, T. Saunders, M. Reece, J. Binner, V.M. Sglavo, S. Grasso, Investigation of Electrochemical, Optical and Thermal Effects during Flash Sintering of 8YSZ, Materials. 11 (2018) 1214. https://doi.org/10.3390/ma11071214.

[143] J. Janek, C. Korte, Electrochemical blackening of yttria-stabilized zirconia – morphological instability of the moving reaction front, Solid State Ionics. 116 (1999) 181–195. https://doi.org/10.1016/S0167-2738(98)00415-9.

[144] W. Qin, H. Majidi, J. Yun, K. van Benthem, Electrode Effects on Microstructure Formation During FLASH Sintering of Yttrium-Stabilized Zirconia, J. Am. Ceram. Soc. 99 (2016) 2253–2259. https://doi.org/10.1111/jace.14234.

[145] L.B. Caliman, R. Bouchet, D. Gouvea, P. Soudant, M.C. Steil, Flash sintering of ionic conductors: The need of a reversible electrochemical reaction, Journal of the European Ceramic Society. 36 (2016) 1253–1260. https://doi.org/10.1016/j.jeurceramsoc.2015.12.005.

[146] Y. Zhang, J. Luo, Promoting the flash sintering of ZnO in reduced atmospheres to achieve nearly full densities at furnace temperatures of <120°C, Scripta Materialia. 106 (2015) 26–29. https://doi.org/10.1016/j.scriptamat.2015.04.027.

[147] J.S.C. Francis, R. Raj, Flash-Sinterforging of Nanograin Zirconia: Field Assisted Sintering and Superplasticity, Journal of the American Ceramic Society. 95 (2012) 138–146. https://doi.org/10.1111/j.1551-2916.2011.04855.x.

[148] M. Biesuz, J. Dong, S. Fu, Y. Liu, H. Zhang, D. Zhu, C. Hu, S. Grasso, Thermally-insulated flash sintering, Scripta Materialia. 162 (2019) 99–102. https://doi.org/10.1016/j.scriptamat.2018.10.042.

[149] J.-M. Lebrun, S.K. Jha, S.J. McCormack, W.M. Kriven, R. Raj, Broadening of Diffraction Peak Widths and Temperature Nonuniformity During Flash Experiments, Journal of the American Ceramic Society. 99 (2016) 3429–3434. https://doi.org/10.1111/jace.14326.

[150] R. Raj, Joule heating during flash-sintering, Journal of the European Ceramic Society. 32 (2012) 2293–2301. https://doi.org/10.1016/j.jeurceramsoc.2012.02.030.

[151] R. Chaim, G. Chevallier, A. Weibel, C. Estournès, Flash sintering of dielectric nanoparticles as a percolation phenomenon through a softened film, Journal of Applied Physics. 121 (2017) 145103. https://doi.org/10.1063/1.4980853.

[152] J. Narayan, Grain growth model for electric field-assisted processing and flash sintering of materials, Scripta Materialia. 68 (2013) 785–788. https://doi.org/10.1016/j.scriptamat.2013.01.008.

[153] K. Terauds, J.-M. Lebrun, H.-H. Lee, T.-Y. Jeon, S.-H. Lee, J.H. Je, R. Raj, Electroluminescence and the measurement of temperature during Stage III of flash sintering experiments, Journal of the European Ceramic Society. 35 (2015) 3195–3199. https://doi.org/10.1016/j.jeurceramsoc.2015.03.040.

[154] M. Jongmanns, R. Raj, D.E. Wolf, Generation of Frenkel defects above the Debye temperature by proliferation of phonons near the Brillouin zone edge, New J. Phys. 20 (2018) 093013. https://doi.org/10.1088/1367-2630/aadd5a.

[155] S. Jo, R. Raj, Transition to electronic conduction at the onset of flash in cubic zirconia, Scripta Materialia. 174 (2020) 29–32. https://doi.org/10.1016/j.scriptamat.2019.07.043.

[156] J. Frenkel, On Pre-Breakdown Phenomena in Insulators and Electronic Semi-Conductors, Phys. Rev. 54 (1938) 647–648. https://doi.org/10.1103/PhysRev.54.647.

[157] J.A. Downs, Mechanisms of Flash Sintering in Cubic Zirconia, phd, University of Trento, 2013. http://eprints-phd.biblio.unitn.it/976/ (accessed April 9, 2020).

[158] M. Biesuz, L. Pinter, T. Saunders, M. Reece, J. Binner, V.M. Sglavo, S. Grasso, Investigation of Electrochemical, Optical and Thermal Effects during Flash Sintering of 8YSZ, Materials (Basel). 11 (2018). https://doi.org/10.3390/ma11071214.

[159] C. Manière, G. Lee, E.A. Olevsky, All-Materials-Inclusive Flash Spark Plasma Sintering, Sci Rep. 7 (2017) 1–8. https://doi.org/10.1038/s41598-017-15365-x.

[160] S. Grasso, T. Saunders, H. Porwal, B. Milsom, A. Tudball, M. Reece, Flash Spark Plasma Sintering (FSPS) of α and β SiC, Journal of the American Ceramic Society. 99 (2016) 1534–1543. https://doi.org/10.1111/jace.14158.

[161] D. Demirskyi, O. Vasylkiv, Hot-spots generation, exaggerated grain growth and mechanical performance of silicon carbide bulks consolidated by flash spark plasma sintering, Journal of Alloys and Compounds. 691 (2017) 466–473. https://doi.org/10.1016/j.jallcom.2016.08.234.

[162] O. Vasylkiv, H. Borodianska, Y. Sakka, D. Demirskyi, Flash spark plasma sintering of ultrafine yttria-stabilized zirconia ceramics, Scripta Materialia. 121 (2016) 32–36. https://doi.org/10.1016/j.scriptamat.2016.04.031.

[163] K.E. Haque, Microwave energy for mineral treatment processes—a brief review, International Journal of Mineral Processing. 57 (1999) 1–24. https://doi.org/10.1016/S0301-7516(99)00009-5.

[164] P.R. Matli, R.A. Shakoor, A.M. Amer Mohamed, M. Gupta, Microwave Rapid Sintering of Al-Metal Matrix Composites: A Review on the Effect of Reinforcements, Microstructure and Mechanical Properties, Metals. 6 (2016) 143. https://doi.org/10.3390/met6070143.

[165] P. Yadoji, R. Peelamedu, D. Agrawal, R. Roy, Microwave sintering of Ni–Zn ferrites: comparison with conventional sintering, Materials Science and Engineering: B. 98 (2003) 269–278. https://doi.org/10.1016/S0921-5107(03)00063-1.

[166] K.I. Rybakov, E.A. Olevsky, E.V. Krikun, Microwave Sintering: Fundamentals and Modeling, Journal of the American Ceramic Society. 96 (2013) 1003–1020. https://doi.org/10.1111/jace.12278.

[167] Agglomerate and Particle Size Effects on Sintering Yttria-Stabilized Zirconia - RHODES - 1981 - Journal of the American Ceramic Society - Wiley Online Library, (n.d.). https://ceramics.onlinelibrary.wiley.com/doi/abs/10.1111/j.1151-2916.1981.tb09552.x (accessed January 24, 2020).

[168] duramax_b-1000.pdf, (n.d.). https://nshosting.dow.com/doc-archive/business/pmat/duramax/duramax_b-1000/tds/duramax_b-1000.pdf (accessed January 24, 2020).

[169] Evacuable Dies for IR Spectroscopy and X-ray Spectroscopy, (n.d.). https://www.msscientific.de/dies.htm (accessed January 24, 2020).

[170] Labor, Home - Nabertherm Industrieofenbau. (n.d.). //www.nabertherm.de/produkte/labor/de (accessed January 25, 2020).

[171] X. Shi, S. Ghose, E. Dooryhee, Performance calculations of the X-ray powder diffraction beamline at NSLS-II, J Synchrotron Rad. 20 (2013) 234–242. https://doi.org/10.1107/S0909049512049175.

[172] J.-M. Lebrun, C.S. Hellberg, S.K. Jha, W.M. Kriven, A. Steveson, K.C. Seymour, N. Bernstein, S.C. Erwin, R. Raj, In-situ measurements of lattice expansion related to defect generation during flash sintering, Journal of the American Ceramic Society. 100 (2017) 4965–4970. https://doi.org/10.1111/jace.15071.

[173] E. Gregorová, W. Pabst, I. Bohačenko, Characterization of different starch types for their application in ceramic processing, Journal of the European Ceramic Society. 26 (2006) 1301–1309. https://doi.org/10.1016/j.jeurceramsoc.2005.02.015.

[174] Mineral Slurry On-Stream Particle Size Analysis, Filtration & Separation. 40 (2003) 36–37. https://doi.org/10.1016/S0015-1882(03)00730-4.

[175] D. Louër, Powder X-Ray Diffraction, Applications, in: J.C. Lindon (Ed.), Encyclopedia of Spectroscopy and Spectrometry, Elsevier, Oxford, 1999: pp. 1865–1875. https://doi.org/10.1006/rwsp.2000.0242.

[176] S.P.S. Badwal, D. Fini, F.T. Ciacchi, C. Munnings, J.A. Kimpton, J. Drennan, Structural and microstructural stability of ceria – gadolinia electrolyte exposed to reducing environments of high temperature fuel cells, J. Mater. Chem. A. 1 (2013) 10768–10782. https://doi.org/10.1039/C3TA11752A.

[177] grain and particle analysis with line intersection method - File Exchange - MATLAB Central, (n.d.). https://www.mathworks.com/matlabcentral/fileexchange/35203 (accessed January 27, 2020).

[178] Effect of Change of Scale on Sintering Phenomena: Journal of Applied Physics: Vol 21, No 4, (n.d.). https://aip.scitation.org/doi/10.1063/1.1699658 (accessed January 28, 2020).

[179] Hydrothermal synthesis and sintering of ultrafine CeO2 powders | Journal of Materials Research | Cambridge Core, (n.d.). https://www.cambridge.org/core/journals/journal-of-materials-research/article/hydrothermal-synthesis-and-sintering-of-ultrafine-ceo2-powders/90CAE4620229522CF9F5B2D2283ED80E (accessed January 28, 2020).

[180] Effects of Particle-Size Distribution in Initial-Stage Sintering - COBLE - 1973 - Journal of the American Ceramic Society - Wiley Online Library, (n.d.). https://ceramics.onlinelibrary.wiley.com/doi/abs/10.1111/j.1151-2916.1973.tb12524.x (accessed January 28, 2020).

[181] F. Teocoli, V. Esposito, Viscoelastic properties of doped-ceria under reduced oxygen partial pressure, Scripta Materialia. 75 (2014) 82–85. https://doi.org/10.1016/j.scriptamat.2013.11.027.

[182] V. Pouchly, K. Maca, Master sintering curve: A practical approach to its construction, Science of Sintering. 42 (2010) 25–32.

[183] T.P. Mishra, A.M. Laptev, M. Ziegner, S.K. Sistla, A. Kaletsch, C. Broeckmann, O. Guillon, M. Bram, Field-Assisted Sintering/Spark Plasma Sintering of Gadolinium-Doped Ceria with Controlled Re-oxidation for Crack Prevention, Materials. 13 (2020) 3184. https://doi.org/10.3390/ma13143184.

[184] D. Udomsilp, D. Roehrens, N.H. Menzler, A.K. Opitz, O. Guillon, M. Bram, Novel processing of La0.58Sr0.4Co0.2Fe0.8O3−δ cathodes for metal-supported fuel cells, Materials Letters. 192 (2017) 173–176. https://doi.org/10.1016/j.matlet.2016.12.027.

[185] M.F. Yan, Grain Growth in Fe3O4, Journal of the American Ceramic Society. 63 (1980) 443–447. https://doi.org/10.1111/j.1151-2916.1980.tb10209.x.

[186] P.-L. Chen, I.-W. Chen, Role of Defect Interaction in Boundary Mobility and Cation Diffusivity of CeO2, Journal of the American Ceramic Society. 77 (1994) 2289–2297. https://doi.org/10.1111/j.1151-2916.1994.tb04596.x.

[187] I.-W. Chen, X.-H. Wang, Sintering dense nanocrystalline ceramics without final-stage grain growth, Nature. 404 (2000) 168–171. https://doi.org/10.1038/35004548.

[188] M.-B. Choi, S.-Y. Jeon, H.-N. Im, S.-J. Song, Thermodynamic quantities and oxygen nonstoichiometry of undoped BaTiO3−δ by thermogravimetric analysis, Journal of Alloys and Compounds. 513 (2012) 487–494. https://doi.org/10.1016/j.jallcom.2011.10.096.

[189] A. Kabir, S. Santucci, N. Van Nong, M. Varenik, I. Lubomirsky, R. Nigon, P. Muralt, V. Esposito, Effect of oxygen defects blocking barriers on gadolinium doped ceria (GDC) electro-chemo-mechanical properties, Acta Materialia. 174 (2019) 53–60. https://doi.org/10.1016/j.actamat.2019.05.009.

[190] S. K. Sistla, Electric Field-Assisted Sintering of Gadolinium-Doped Ceria: Sintering and Grain Growth Kinetics, J. Ceram. Sci. Technol. (2019). https://doi.org/10.4416/JCST2019-00045.

[191] Defect Dynamics in Doped Ceria Electrolytes, (n.d.). https://ufdc.ufl.edu/UFE0051019/00001 (accessed April 11, 2020).

[192] M. Bram, A.M. Laptev, T.P. Mishra, K. Nur, M. Kindelmann, M. Ihrig, J.G.P. da Silva, R. Steinert, H.P. Buchkremer, A. Litnovsky, F. Klein, J. Gonzalez-Julian, O. Guillon, Application of Electric Current-Assisted Sintering Techniques for the Processing of Advanced Materials, Advanced Engineering Materials. n/a (n.d.) 2000051. https://doi.org/10.1002/adem.202000051.

[193] P. Debye, Zur Theorie der spezifischen Wärmen, Annalen Der Physik. 344 (1912) 789–839. https://doi.org/10.1002/andp.19123441404.

[194] C. Schmerbauch, J. Gonzalez-Julian, R. Röder, C. Ronning, O. Guillon, Flash Sintering of Nanocrystalline Zinc Oxide and its Influence on Microstructure and Defect Formation, Journal of the American Ceramic Society. 97 (2014) 1728–1735. https://doi.org/10.1111/jace.12972.

[195] C. Cao, R. Mücke, O. Guillon, Effect of AC field on uniaxial viscosity and sintering stress of ceria, Acta Materialia. 182 (2020) 77–86. https://doi.org/10.1016/j.actamat.2019.10.035.

[196] T. Hisashige, Y. Yamamura, T. Tsuji, Thermal expansion and Debye temperature of rare earth-doped ceria, Journal of Alloys and Compounds. 408–412 (2006) 1153–1156. https://doi.org/10.1016/j.jallcom.2004.12.190.

[197] S. Wang, T. Kobayashi, M. Dokiya, T. Hashimoto, Electrical and Ionic Conductivity of Gd-Doped Ceria, J. Electrochem. Soc. 147 (2000) 3606–3609. https://doi.org/10.1149/1.1393946.

[198] M. Mogensen, Physical, chemical and electrochemical properties of pure and doped ceria, Solid State Ionics. 129 (2000) 63–94. https://doi.org/10.1016/S0167-2738(99)00318-5.

[199] T.P. Mishra, R.R.I. Neto, G. Speranza, A. Quaranta, V.M. Sglavo, R. Raj, O. Guillon, M. Bram, M. Biesuz, Electronic conductivity in gadolinium doped ceria under direct current as a trigger for flash sintering, Scripta Materialia. 179 (2020) 55–60. https://doi.org/10.1016/j.scriptamat.2020.01.007.

[200] M. Romeo, K. Bak, J.E. Fallah, F.L. Normand, L. Hilaire, XPS Study of the reduction of cerium dioxide, Surface and Interface Analysis. 20 (1993) 508–512. https://doi.org/10.1002/sia.740200604.

[201] R. López, R. Gómez, Band-gap energy estimation from diffuse reflectance measurements on sol–gel and commercial TiO2: a comparative study, J Sol-Gel Sci Technol. 61 (2012) 1–7. https://doi.org/10.1007/s10971-011-2582-9.

[202] R. Kirchheim, Incubation time for flash sintering as caused by internal reactions, exemplified for yttria stabilized zirconia, Acta Materialia. 175 (2019) 361–375. https://doi.org/10.1016/j.actamat.2019.06.030.

[203] N. Ahr, M. Martin, Kinetic Unmixing and Kinetic Decomposition of Oxides in External Electric Fields, (2019). https://www.fieldsmatter.de (accessed April 14, 2020).

[204] X.L. Phuah, H. Wang, H. Charalambous, S.K. Jha, T. Tsakalakos, X. Zhang, H. Wang, Comparison of the grain growth behavior and defect structures of flash sintered ZnO with and without controlled current ramp, Scripta Materialia. 162 (2019) 251–255. https://doi.org/10.1016/j.scriptamat.2018.11.009.

[205] H. Charalambous, S.K. Jha, K.H. Christian, R.T. Lay, T. Tsakalakos, Flash Sintering using Controlled Current Ramp, Journal of the European Ceramic Society. 38 (2018) 3689–3693. https://doi.org/10.1016/j.jeurceramsoc.2018.04.003.

[206] D. Demirskyi, O. Vasylkiv, Hot-spots generation, exaggerated grain growth and mechanical performance of silicon carbide bulks consolidated by flash spark plasma

sintering, Journal of Alloys and Compounds. 691 (2017) 466–473. https://doi.org/10.1016/j.jallcom.2016.08.234.

[207] H. Charalambous, S.K. Jha, H. Wang, X.L. Phuah, H. Wang, T. Tsakalakos, Inhomogeneous reduction and its relation to grain growth of titania during flash sintering, Scripta Materialia. 155 (2018) 37–40. https://doi.org/10.1016/j.scriptamat.2018.06.017.

[208] T.P. Mishra, R.R.I. Neto, R. Raj, O. Guillon, M. Bram, Current-rate flash sintering of gadolinium doped ceria: Microstructure and Defect generation, Acta Materialia. 189 (2020) 145–153. https://doi.org/10.1016/j.actamat.2020.02.036.

[209] N. Stelzer, J. Nölting, I. Riess, Phase Diagram of Nonstoichiometric 10 mol% Gd2O3-Doped Cerium Oxide Determined from Specific Heat Measurements, Journal of Solid State Chemistry. 117 (1995) 392–397. https://doi.org/10.1006/jssc.1995.1290.

[210] R. Raj, Separation of Cavitation-Strain and Creep-Strain During Deformation, Journal of the American Ceramic Society. 65 (1982) C-46-C–46. https://doi.org/10.1111/j.1151-2916.1982.tb10397.x.

[211] F. Shikhar, A study on Flash Sintering and Related Phenomena in Titania and its Composites with Alumina, (n.d.) 171.

[212] R. Muccillo, E.N.S. Muccillo, Electric field-assisted flash sintering of tin dioxide, Journal of the European Ceramic Society. 34 (2014) 915–923. https://doi.org/10.1016/j.jeurceramsoc.2013.09.017.

[213] Temperature Distributions During Flash Sintering of 8% Yttria-Stabilized Zirconia - Pereira da Silva - 2015 - Journal of the American Ceramic Society - Wiley Online Library, (n.d.). https://ceramics.onlinelibrary.wiley.com/doi/full/10.1111/jace.13786 (accessed February 12, 2020).

[214] A. Roosen, H.K. Bowen, Influence of Various Consolidation Techniques on the Green Microstructure and Sintering Behavior of Alumina Powders, Journal of the American Ceramic Society. 71 (1988) 970–977. https://doi.org/10.1111/j.1151-2916.1988.tb07567.x.

[215] D.E. García, D. Hotza, R. Janssen, Building a Sintering Front through Fast Firing, International Journal of Applied Ceramic Technology. 8 (2011) 1486–1493. https://doi.org/10.1111/j.1744-7402.2011.02609.x.

[216] R. Raj, M. Cologna, J.S.C. Francis, Influence of Externally Imposed and Internally Generated Electrical Fields on Grain Growth, Diffusional Creep, Sintering and Related Phenomena in Ceramics, Journal of the American Ceramic Society. 94 (2011) 1941–1965. https://doi.org/10.1111/j.1551-2916.2011.04652.x.

[217] J.-M. Lebrun, R. Raj, Private conversation, University of Colorado Boulder, n.d.

[218] A. Walsh, S.M. Woodley, C.R.A. Catlow, A.A. Sokol, Potential energy landscapes for anion Frenkel-pair formation in ceria and india, Solid State Ionics. 184 (2011) 52–56. https://doi.org/10.1016/j.ssi.2010.08.010.

[219] T. Zacherle, A. Schriever, R.A. De Souza, M. Martin, Ab initio analysis of the defect structure of ceria, Phys. Rev. B. 87 (2013) 134104. https://doi.org/10.1103/PhysRevB.87.134104.

[220] Y.J. Sohn, G. Mauer, G. Roth, O. Guillon, R. Vaßen, Crystal structure analysis and high-temperature phase transitions of complex rare-earth perovskite, La2(Al1/2MgTa1/2)O6, Journal of the American Ceramic Society. 103 (2020) 1404–1413. https://doi.org/10.1111/jace.16740.

Acknowledgements

Undertaking this Ph.D. has been a truly life-changing experience for me. I owe gratitude towards several people without whom it would not have been possible to complete my Ph.D. thesis successfully. Their continuous support, guidance, encouragement, and trust have indeed contributed over the past three years. Though it will not be enough to express my gratefulness in words to all those people, I still would like to give my sincere appreciation to them. Thank you! Vielen Dank! धन्यवाद! ધન્યબાદ્!

First and foremost, I would like to express my sincerest gratitude to my distinguished supervisor PD Dr. Martin Bram for offering me this opportunity to carry out my dissertation work at IEK-1, Forschungszentrums Jülich GmbH. His constant guidance, encouragement and support throughout the period of my Ph.D. enabled me to develop an understanding of the subject. I have been amazingly fortunate to have him as an advisor who gave me the freedom and opportunity to explore.

I cordially thank to the members of my PhD examination committee, Prof. Dr.-Ing. Viktor Scherer for chairing my PhD examination. PD Dr. Martin Bram and Prof. Robert Vassen for evaluating my dissertation and giving me helpful suggestions to improve my thesis.

I am deeply grateful to Prof. Dr. Olivier Guillon for following the progression of my work very closely. He was always been there in times of need and gave his insights during my Ph.D. work. Thanks to his profound knowledge in the area of field assisted sintering technology, from which I have benefited a lot.

I gratefully acknowledge the financial support from the German Research Foundation (DFG) within the Priority Program on "manipulation of matter controlled by an electric and magnetic field, SPP 1959 under the Grant No. BR 3418/1-1". This work was done in close collaboration with colleagues from the Institute for Materials Applications in Mechanical Engineering, RWTH Aachen. I extend my thanks to my project partners, Mr. Sree Koundinya Sistla, Dr.-Ing. Anke Kaletsch and Prof. dr.-ing. christoph broeckmann for a wonderful collaboration.

I would like to express my gratefulness to Prof. Rishi Raj, University of Colorado Boulder, USA for providing me a unique opportunity to work at his esteemed research group on the topic of Flash sintering. Prof. Raj's has a big contribution to this Ph.D. work specifically, on the flash sintering studies. He gave an uninterrupted support during the last one and half years,

List of Publications

- **Published Articles**

[1] **T.P. Mishra**, V. Avila, R.R.I. Neto, M. Bram, O. Guillon, R. Raj, On the role of Debye temperature in the onset of flash in three oxides, Scripta Materialia. 170 (2019) 81–84. https://doi.org/10.1016/j.scriptamat.2019.05.030.

[2] **T.P. Mishra**, R.R.I. Neto, G. Speranza, A. Quaranta, V.M. Sglavo, R. Raj, O. Guillon, M. Bram, M. Biesuz, Electronic conductivity in gadolinium doped ceria under direct current as a trigger for flash sintering, Scripta Materialia. 179 (2020) 55–60. https://doi.org/10.1016/j.scriptamat.2020.01.007.

[3] **T.P. Mishra**, R.R.I. Neto, R. Raj, O. Guillon, M. Bram, Current-rate flash sintering of gadolinium doped ceria: Microstructure and Defect generation, Acta Materialia. 189 (2020) 145–153. https://doi.org/10.1016/j.actamat.2020.02.036.

[4] **T.P. Mishra**, A.M. Laptev, M. Ziegner, S.K. Sistla, A. Kaletsch, C. Broeckmann, O. Guillon, M. Bram, Field-Assisted Sintering/Spark Plasma Sintering of Gadolinium-Doped Ceria with Controlled Re-oxidation for Crack Prevention, Materials. 13 (2020) 3184. https://doi.org/10.3390/ma13143184.

[5] S. K. Sistla, **T. Mishra**, Y. Deng, A. Kaletsch, M. Bram, C. Broeckmann, Electric Field-Assisted Sintering of Gadolinium-Doped Ceria: Sintering and Grain Growth Kinetics, J. Ceram. Sci. Technol. (2019). https://doi.org/10.4416/JCST2019-00045.

[6] M. Bram, A.M. Laptev, **T.P. Mishra**, K. Nur, M. Kindelmann, M. Ihrig, J.G.P. da Silva, R. Steinert, H.P. Buchkremer, A. Litnovsky, F. Klein, J. Gonzalez-Julian, O. Guillon, Application of Electric Current-Assisted Sintering Techniques for the Processing of Advanced Materials, Advanced Engineering Materials. n/a (n.d.) 2000051. https://doi.org/10.1002/adem.202000051.

- **Manuscript in Preparation**

[7] Development of a processing map for SAFE sintering of Gadolinium Doped Ceria.

[8] In situ study of flash sintering of Gadolinium Doped Ceria in synchrotron; comparative study between voltage-to-current and current rate flash.

[9] Electric field/current effect on the microstructure of Gadolinium Doped Ceria sintered in FAST/SPS.

Curriculum Vitae

Personal Information

Name: Tarini Prasad Mishra

Date of Birth: 28.05.1988

Place of Birth: Keonjhar Town

Nationality: Indian

Education

2016 – 2020	**PhD Candidate**, Mechanical Engineering, Ruhr-University Bochum,
	Dissertation: "Field Assisted Sintering of Gadolinium-doped Ceria"
	Institute of Energy and Climate Research Materials Synthesis and Processing (IEK-1), Forschungszentrum Jülich GmbH
2018	Guest Researcher, Department of Mechanical Engineering, University of Colorado at Boulder, CO, US
2012 – 2016	**Master of Science**, Materials Science, Technical University Darmstadt, Germany
2015	Master Thesis, "Process optimization of Aerosol Deposition Method for thick Ceramic coating at Room Temperature", IEK-1, Forschungszentrum Jülich GmbH
2008 – 2012	**Bachelor of Technology**, Metallurgical and Materials Engineering, Jawaharlal Nehru Technological University (JNTU), India
2012	Bachelor Thesis, "Characterizing and optimization of best parameter for tungsten carbide powders coating on structural steel by detonation spray technique.", International Advanced Research Centre for Powder Metallurgy and New Materials, India
2011	Guest Researcher, Max-Planck-Institut für Plasmaphysik, Garching
2002 – 2005	**Diploma in Engineering**, Metallurgical Engineering,
	Indira Gandhi Institute of Technology, India

Band / Volume 496
**Tomographic observations of gravity waves
with the infrared limb imager GLORIA**
I. Krisch (2020), vii, 187 pp
ISBN: 978-3-95806-481-2

Band / Volume 497
**Aquisition of temporally and spatially highly resolved data sets of relevant
trace substances for model development and model evaluation purposes
using a mobile measuring laboratory**
D. Klemp, R. Wegener, R. Dubus, U. Javed (2020), 110 pp
ISBN: 978-3-95806-465-2

Band / Volume 498
**Charakterisierung des Werkstoffverhaltens während des Kosinterns
einer neuartigen, inert gestützten Festoxidbrennstoffzelle**
F. Grimm (2020), ix, 168 pp
ISBN: 978-3-95806-482-9

Band / Volume 499
**WEGE FÜR DIE ENERGIEWENDE
Kosteneffiziente und klimagerechte Transformationsstrategien
für das deutsche Energiesystem bis zum Jahr 2050**
M. Robinius et al (2020), VIII, 141 pp
ISBN: 978-3-95806-483-6

Band / Volume 500
**Mechanical Behavior of Solid Electrolyte Materials
for Lithium-ion Batteries**
G. Yan (2020), x, 139 pp
ISBN: 978-3-95806-484-3

Band / Volume 501
**Retrieval of atmospheric quantities from remote sensing measurements of
nightglow emissions in the MLT region**
Q. Chen (2020), 208 pp
ISBN: 978-3-95806-485-0

Band / Volume 502
Auswirkungen der Energiewende auf das deutsche Gastransportsystem
B. Gillessen (2020), XVII, 186
ISBN: 978-3-95806-487-4

Schriften des Forschungszentrums Jülich
Reihe Energie & Umwelt / Energy & Environment

Band / Volume 503
Lagrangian Simulation of Stratospheric Water Vapour: Impact of Large-Scale Circulation and Small-Scale Transport Processes
L. Poshyvailo (2020), 126 pp
ISBN: 978-3-95806-488-1

Band / Volume 504
Water Management in Automotive Polymer-Electrolyte-Membrane Fuel Cell Stacks
S. Asanin (2020), XVIII, 172 pp
ISBN: 978-3-95806-491-1

Band / Volume 505
Towards a new real-time irrigation scheduling method: observation, modelling and their integration by data assimilation
D. Li (2020), viii, 94 pp
ISBN: 978-3-95806-492-8

Band / Volume 506
Modellgestützte Analyse kosteneffizienter CO_2-Reduktionsstrategien
P. M. Lopion (2020), XIV, 269 pp
ISBN: 978-3-95806-493-5

Band / Volume 507
Integration of Renewable Energy Sources into the Future European Power System Using a Verified Dispatch Model with High Spatiotemporal Resolution
C. Syranidou (2020), VIII, 242 pp
ISBN: 978-3-95806-494-2

Band / Volume 508
Solar driven water electrolysis based on silicon solar cells and earth-abundant catalysts
K. Welter (2020), iv, 165 pp
ISBN: 978-3-95806-495-9

Band / Volume 509
Electric Field Assisted Sintering of Gadolinium-doped Ceria
T. P. Mishra (2020), x, 195 pp
ISBN: 978-3-95806-496-6

Weitere *Schriften des Verlags im Forschungszentrum Jülich* unter
http://wwwzb1.fz-juelich.de/verlagextern1/index.asp

JÜLICH
Forschungszentrum